UNIVERSITAT POLITÈCNICA DE VALÈNCIA

Department of Mechanical and Materials Engineering

PhD Thesis

Contact problem modelling using the Cartesian grid Finite Element Method

Presented by: José Manuel Navarro Jiménez

Supervised by: Dr. Juan José Ródenas García

Dr. Manuel Tur Valiente

València, June 2019

PhD Thesis

Contact problem modelling using the Cartesian grid Finite Element Method

for the degree of

Doctor in Industrial Engineering and Production

presented by

José Manuel Navarro Jiménez

at the

Department of Mechanical and Materials Engineering

of Universitat Politècnica de València

Supervised by

Dr. Juan José Ródenas García
Dr. Manuel Tur Valiente

València, June 2019

PhD Thesis

Contact problem modelling using the Cartesian grid Finite Element Method

Presented by: José Manuel Navarro Jiménez

Supervised by: Dr. Juan José Ródenas García

Dr. Manuel Tur Valiente

QUALIFYING TRIBUNAL

President: Dr. _____

Vocal: Dr. _____

Secretary: Dr. _____

València, June 2019

Abstract

The contact interaction between elastic solids is one of the most complex phenomena in the computational mechanics research field. The solution of such problem requires robust algorithms to treat the geometrical non-linearities characteristic of the contact constrains. The Finite Element Method (FE) has become one of the most popular options for the mechanical components design, including the solution of contact problems. In this method the computational cost of the generation of the discretization (mesh generation) is directly related to the complexity of the analysis domain, namely its boundary. This complicates the introduction in the numerical simulations of complex surfaces (for example NURBS), which are being increasingly used in the CAD industry.

This thesis is grounded on the Cartesian grid Finite Element Method (cgFEM). In this methodology, which belongs to the family of *Immersed Boundary* methods, the problem at hand is extended to an approximation domain which completely embeds the analysis domain, and its meshing is straightforward. The decoupling of the boundary definition and the discretization mesh results in a great reduction of the mesh generation's computational cost. Is for this reason that the cgFEM is a suitable tool for the solution of problems that require multiple geometry modifications, such as shape optimization problems or wear simulations.

The cgFEM is also capable of automatically generating FE models from medical images without the intermediate step of generating CAD entities. The introduction of the contact interaction would open the possibility to consider different states of the union between implant and living tissue for the design of optimized implants, even in a patient-specific process.

Hence, in this thesis a formulation for solving 3D contact problems with the cgFEM is presented, considering both frictionless and Coulomb's friction problems. The absence of nodes along the boundary in cgFEM prevents the enforcement of the contact constrains using the standard procedures. Thus, we develop a stabilized formulation that makes use of a recovered stress field, which ensures the stability of the method.

The analytical definition of the contact surfaces (by means of NURBS) has been included in the proposed formulation in order to increase the accuracy of the solution.

In addition, the robustness of the cgFEM methodology is increased in this thesis in two different aspects: the control of the numerical problem's ill-conditioning by means of a stabilized method, and the enhancement of the stress recovered field, which is used in the error estimation procedure.

The proposed methodology has been validated through several numerical examples, showing the great potential of the cgFEM in these type of problems.

Resumen

La interacción de contacto entre sólidos deformables es uno de los fenómenos más complejos en el ámbito de la mecánica computacional. La resolución de este problema requiere de algoritmos robustos para el tratamiento de no linealidades geométricas. El Método de Elementos Finitos (MEF) es uno de los más utilizados para el diseño de componentes mecánicos, incluyendo la solución de problemas de contacto. En este método el coste asociado al proceso de discretización (generación de malla) está directamente vinculado a la definición del contorno a modelar, lo cual dificulta la introducción en la simulación de superficies complejas, como las superficies NURBS, cada vez más utilizadas en el diseño de componentes.

Esta tesis está basada en el *Cartesian grid Finite Element Method* (cgFEM). En esta metodología, encuadrada en la categoría de métodos *Immersed Boundary*, se extiende el problema a un dominio de aproximación (cuyo mallado es sencillo de generar) que contiene al dominio de análisis completamente en su interior. Al desvincular la discretización de la definición del contorno del problema se reduce drásticamente el coste de generación de malla. Es por ello que el método cgFEM es una herramienta adecuada para la resolución de problemas en los que es necesario modificar la geometría múltiples veces, como el problema de optimización de forma o la simulación de desgaste.

El método cgFEM permite también crear de manera automática y eficiente modelos de Elementos Finitos a partir de imágenes médicas. La introducción de restricciones de contacto habilitaría la posibilidad de considerar los diferentes estados de integración implante-tejido en procesos de optimización personalizada de implantes.

Así, en esta tesis se desarrolla una formulación para resolver problemas de contacto 3D con el método cgFEM, considerando tanto modelos de contacto sin fricción como problemas con rozamiento de Coulomb. La ausencia de nodos en el contorno en cgFEM impide la aplicación de métodos tradicionales para imponer las restricciones de contacto, por lo que se ha desarrollado una formulación estabilizada que hace uso de un campo de tensiones recuperado para asegurar la estabilidad del método. Para

una mayor precisión de la solución, se ha introducido la definición analítica de las superficies en contacto en la formulación propuesta.

Además, se propone la mejora de la robustez de la metodología cgFEM en dos aspectos: el control del mal condicionamiento del problema numérico mediante un método estabilizado, y la mejora del campo de tensiones recuperado, utilizado en el proceso de estimación de error.

La metodología propuesta se ha validado a través de diversos ejemplos numéricos presentados en la tesis, mostrando el gran potencial de cgFEM en este tipo de problemas.

Resum

La interacció de contacte entre sòlids deformables és un dels fenòmens més complexos en l'àmbit de la mecànica computacional. La resolució d'este problema requerix d'algoritmes robustos per al tractament de no linealitats geomètriques. El Mètode dels Elements Finits (MEF) és un dels més utilitzats per al disseny de components mecànics, incloent la solució de problemes de contacte. En este mètode el cost associat al procés de discretització (generació de malla) està directament vinculat a la definició del contorn a modelar, la qual cosa dificulta la introducció en la simulació de superfícies complexes, com les superfícies NURBS, cada vegada més utilitzades en el disseny de components.

Esta tesi està basada en el *Cartesian grid Finite Element Method* (cgFEM). En esta metodologia, enquadrada en la categoria de mètodes *Immersed Boundary*, s'estén el problema a un domini d'aproximació (el mallat del qual és senzill de generar) que conté al domini d'anàlisi completament en el seu interior. Al desvincular la discretització de la definició del contorn del problema es reduïx dràsticament el cost de generació de malla. És per això que el mètode cgFEM és una ferramenta adequada per a la resolució de problemes en què és necessari modificar la geometria múltiples vegades, com el problema d'optimització de forma o la simulació de desgast. El mètode cgFEM permet també crear de manera automàtica i eficient models d'Elements Finits a partir d'imatges mèdiques. La introducció de restriccions de contacte habilitaria la possibilitat de considerar els diferents estats d'integració implant-teixit en processos d'optimització personalitzada d'implants.

Així, en esta tesi es desenvolupa una formulació per a resoldre problemes de contacte 3D amb el mètode cgFEM, considerant tant models de contacte sense fricció com a problemes amb fregament de Coulomb. L'absència de nodes en el contorn en cgFEM impedix l'aplicació de mètodes tradicionals per a imposar les restriccions de contacte, per la qual cosa s'ha desenvolupat una formulació estabilitzada que fa ús d'un camp de tensions recuperat per a assegurar l'estabilitat del mètode. Per a una

millor precisió de la solució, s'ha introduït la definició analítica de les superfícies en contacte en la formulació proposada.

A més, es proposa la millora de la robustesa de la metodologia cgFEM en dos aspectes: el control del mal condicionament del problema numèric per mitjà d'un mètode estabilitzat, i la millora del camp de tensions recuperat, utilitzat en el procés d'estimació d'error.

La metodologia proposada s'ha validat a través de diversos exemples numèrics presentats en la tesi, mostrant el gran potencial de cgFEM en este tipus de problemes.

Preface

The work presented in this thesis has been carried out at the Research Centre for Mechanical Engineering at the Universitat Politècnica de València, under the supervision of Professor Juan José Ródenas García and Dr. Manuel Tur Valiente. This thesis consists of a summary report and the following appended papers:

A M. Tur, J. Albelda, J.M. Navarro-Jiménez, and J.J. Ródenas. *A modified perturbed Lagrangian formulation for contact problems*, Computational Mechanics, **55**(4), 737-754, (2015).

B J.M. Navarro-Jiménez, M. Tur, J. Albelda, and J.J. Ródenas. *Large deformation frictional contact analysis with immersed boundary method*. Computational Mechanics, **62**(4), 853–870, (2018).

C J.M. Navarro-Jiménez, M. Tur, F.J. Fuenmayor, and J.J. Ródenas. *On the effect of the contact surface definition in the Cartesian grid finite element method*. Advanced Modeling and Simulation in Engineering Sciences, **5**(1), 12, (2018).

D J.M. Navarro-Jiménez, E. Nadal, M. Tur, J.J. Ródenas, and J. Martínez. *On the use of stabilization techniques in the cgFEM framework for iterative solvers*. Preprint submitted to International Journal for Numerical Methods in Engineering.

E J.M. Navarro-Jiménez, H. Navarro-García, M. Tur and J.J. Ródenas. *Superconvergent patch recovery with constrains for 3D contact problems within the Cartesian grid Finite Element Method*. Preprint submitted to International Journal for Numerical Methods in Engineering.

Acknowledgements

To my supervisors, Prof. Juan José Ródenas and Dr. Manuel Tur. Not only they have patiently shared all their knowledge and guided me through this years, but they have created the best working environment I can ever expect, based on trust, freedom and joy.

To Dr. Rubén Sevilla, for embracing me during my stage in the Zienkiewicz Centre for Computational Engineering at Swansea University, and whose help has been crucial for the development of this thesis.

To all members of the Research Centre for Mechanical Engineering and the Department of Mechanical and Material Engineering at Universitat Politécnica de Valéncia. Fellow MSc. and PhD. students, researchers, lecturers, administration and technical support staffm for all the help, advice, support and good moments I had with you all. I am proud to say that I must ommit giving names because the list would be huge.

To the spanish public education system, because although there is always margin for improvement, it has provided me with the necessary resources to become what I am. Hopefully I will have the opportunity to return some to the spanish society with my performing.

And finally to Isabel, who is always by my side; to Maria, because being my sister is quite a task itself; and to my parents, who insistently encouraged their bashful son to go beyond.

To all of you, thank you so much.

Contents

Part I

Thesis report

Chapter 1

Introduction

1.1. Motivation

The contact phenomenon is present in almost all mechanical or structural systems. The forces appearing when two or more solids become in contact are the basic principles considered in many classical mechanical applications such as gear or clutch transmissions, wheel-rail and tyre-road systems, all kinds of interference fits (i.e. bearing-shaft), impact dynamics and wear problems. The contact interaction is relevant not only in purely industrial applications but also in relatively new fields like biomedical engineering. The applications in this context are very interesting because of their potential for high impact for the society. One example of contact in this field is the prosthetic device design strategy, where the contact interaction between living tissues and implant can be used to analyze the performance of the implant and to optimize its shape for a certain group of patients or even to obtain *patient-specific* optimum designs.

The solution of contact problems is highly challenging due to the different non-linearities that must be considered. First, the contact area when solids are in equilibrium is not known *a priori* and depends on the solution of the problem. Moreover, if frictional contact is considered it is not possible to use the classical approach of minimizing an energy function, since the frictional contact force is non-conservative, this is, the work of such force depends on the path followed. Finally, in contact problems is frequent to consider other sources of non-linearity, including large displacements and rotations, finite strains or hyperelastic and plastic material behavior. Although there exist analytical solutions for a few academic problems, the solution of com-

plex contact problems is nowadays obtained with numerical methods such as discrete methods, boundary elements and the finite element method. Only the latter will be considered in this Thesis.

The Finite Element Method (FEM) [1] has become the standard method for solving mechanical problems in general, and contact problems between elastic solids in particular. The commercial FEM implementations include a contact module for solving such problems. However, it still remains a challenge to find a robust and efficient strategy suitable for any application. In the standard version of the method, the same discretization is used for both the approximation of the solution and the analysis domain representation, including its boundary. An immediate consequence of this is the fact that the complexity of the FEM mesh is directly linked to that of the analysis domain. Furthermore, in the case of contact problems the loss of *smoothness* in the discretized surfaces can affect the accuracy of the solution or compromise the robustness of the contact algorithm.

To reduce the cost and complexity associated to the mesh generation process, several methods, alternative to the standard FEM, have been developed in recent years under the names of *Immersed Boundary*, *Fictitious domain* or *Embedded domain* methods [2]. All of them share a common idea: the choice of an auxiliary domain that completely covers the analysis domain and is easier to mesh. Among these methods we find the Cartesian grid Finite Element Method (cgFEM) presented in [3] for 2D linear elasticity and extended to 3D problems in [4]. The method makes use of a hierarchical data structure based on a set of Cartesian grids with h-adaptive refinement. This structure eases the data reuse between calculations, the projection of information through the refinement process, the introduction of parallel computation and, in conclusion, results in a high efficiency in terms of computational cost. The cgFEM is able to consider the CAD definition of the analysis boundary (by means of NURBS or T-Splines) in the numerical integration, and has been also extended for the automatic creation of FE models from medical images [5], exploiting the topological similarities between the Cartesian grids and the voxel-based structure present in 3D images.

These features seem promising for the solution of contact applications such as patient specific implant-tissue interaction simulation and contact wear simulations. The generation of the FEM model represents the bottleneck in terms of human time in both cases, first due to the complexity involving the model generation from an image, and second because of the need to modify the discretization when the analysis domain changes. Furthermore, it is straightforward that the availability of the CAD definition of the boundaries would allow more accurate measures of the gap between bodies in contact, which is of great interest when solving contact problems.

1.2. Objective

The aim of this thesis is to develop a methodology for the solution of 3D contact problems within the cgFEM framework. In the context of this thesis we will consider frictionless and frictional problems, assuming a Coulomb's model for the latter case. We will also take into account small and large slidings, as well as linear elastic and hyper-elastic material behavior. Following this objective, two partial objectives are defined:

1. **Develop a formulation to solve 3D frictional contact problems using the Cartesian grid Finite Element Method.** The use of immersed boundary (IB) methods entails some shortcomings, one of them being the complexity to enforce Dirichlet boundary conditions due to the lack of nodes located on the boundary. This also concerns the enforcing of contact constrains, thus a special treatment of the boundary conditions is needed in the formulation. These issues are addressed in papers A and B. The cgFEM enables the inclusion of the NURBS boundaries in the definition of the contact kinematic variables such as the gap between bodies, its implementation and influence study is presented in papers B and C.

2. **Enhance the robustness and efficiency of the 3D implementation of the cgFEM methodology for the solution of non-linear problems using *h*-adapted meshes.** The robustness of the solution algorithms in contact problems is a key element due to all the different non-linearities that take part. In the present thesis we aim to enhance the robustness and accuracy of the methodology in two different aspects: the reduction of the system ill-conditioning and the enhancement of the recovered stress field.
   One drawback related to IB appears when a discretization element in the mesh contains a very small portion of material volume. This situation greatly increases the ill-conditioning of the system of equations and it may cause a loss of convergence of the solution algorithm as the mesh is refined. In paper D we propose a stabilization strategy to keep the ill-conditioning of the system under control.
   Finally, the cgFEM includes an h-adaptive refinement strategy based on the Zienkiewicz and Zhu error estimator and the Superconvergent Patch Recovery technique (SPR). It is expected that the introduction of already known information of the contact mechanics to the SPR problem might increase the accuracy of the recovered stress field. This possibility is explored in paper E.

1.3. Outline of the thesis

This document is divided in two parts, Thesis report and Articles. Following this brief introduction, the first part presents the state of the art in Chapter 2. A complete description of the problem at hand is introduced in Chapter 3, including the continuum and discretized contact formulation, together with some features of the cgFEM and NURBS notation. Chapter 4 summarizes the work developed with this Thesis, together with an illustrative application example of implant simulation. Finally, Chapter 5 contains some conclusions of the present work and proposes further research lines.

The second part consists in a compilation of five articles that emerged from this Thesis. Papers A, B and C have been already published in peer review journals whereas papers D and E are currently undergoing a peer review process. All contributions are presented in this document without journal editing, and each paper is preceded by a cover page with a citation of the corresponding journal.

Paper A presents a stabilized Lagrangian formulation for 3D frictionless contact problems. In paper B the previous contact formulation is extended to 3D frictional contact with large sliding and finite deformations, and included in the cgFEM with consideration of the CAD geometry through the use of NURBS. The influence of the contact surface definition in this framework is studied in paper C. Finally, the performance and efficiency of the developed methodology is enhanced in two different aspects: paper D presents a stabilized method to keep the ill-conditioning of the system of equations under control, and in paper E contact constrains are included into the Superconvergent Patch Recovery technique to improve the accuracy of the smooth stress field, which result in the enhancement of the error estimator and, consequently, a more efficient h-refinement process.

Chapter 2

State of the art

2.1. Immersed boundary FEM

The introduction of CAD tools in the design process of structural components has allowed the use of splines, Bézier surfaces or NURBS models to define complex geometries. In this context, the generation of standard body-fitted FEM meshes becomes a critical phase of the structural analysis workflow, and it is considered to be the most demanding task in terms of man-hours. These difficulties have encouraged part of the scientific community to develop alternative methods in which the discretization mesh is somehow decoupled from the analysis boundary definition.

The work by Peskin [6], related to fluid-structure interaction, is considered the first immersed boundary approach. The first attempts in solid mechanics can be found in the eXtended FEM (XFEM) [7,8] and the Generalized FEM (GFEM) [9]. In both cases, enrichment functions containing already known information of the solution are included at specific locations of the analysis domain by means of the Partition of Unity Method (PUM) [10]. In particular, in the XFEM the cracks are embedded in the discretization mesh and the PUM is used to add enrichment functions to numerically represent the singular stress field around the crack tip. The main advantage of this approach is that no re-meshing is needed when the crack tip advances.

Since then, a wide variety of methods have been developed with different names such as *Immersed Boundary, Fictitious Domain, Embedded Domain or Fixed grid FEM*. A review on these methods by Bordas *et al.* [2] suggests the term *Finite Elements in ambient space* to group them. Among all contributions we can cite the Finite Cell Method (FCM) [11, 12], which combines a structured cell mesh with high order approximation basis and integration schemes to accurately capture the analysis

boundary, together with $p-/hp-$refinement strategies; cutFEM [13], which employs a background mesh of tetrahedrons non-conforming with the geometry, and the Cartesian grid Finite Element Method (cgFEM) [3, 4] which is the basis of this thesis, and combines the use of hierarchical structured Cartesian grids with a high order integration scheme and low order approximation bases with h-adaptive refinement strategies.

The common idea to all embedded domain methods is that of embedding the analysis domain Ω in an auxiliary domain $\Omega^{'}$ with a simple shape (for instance a parallelepiped) so that its meshing is straightforward. This somehow decouples the definition of the analysis domain from the FE discretization mesh in which the solution is approximated. The freedom in the geometry definition without increasing the mesh complexity makes these methods very well suited for applications such as structural topology and shape optimization, where the re-meshing during the optimization process is avoided. For example, the embedded domain approach was combined with genetic algorithms in [14] and gradient-based algorithms in [15–17] to solve shape optimization problems, the FCM was applied to topology optimization in [18], and in refs. [19, 20] the cgFEM was used to solve 2D and 3D shape optimization problems. The embedded domain methods seem also an ideal framework to solve problems in which the geometry is given with a voxel structure, like CT scans of porous materials or medical images. Applications of embedded domain methods for image-based analysis are found in [21, 22] for XFEM, using Composite Finite Elements in [23], the FCM [24, 25] and the cgFEM [5].

Since the discretization mesh is non conforming with the analysis domain, there are some issues which are common to all embedded methods, namely the treatment of the analysis boundary for the numerical integration and the proper enforcement of the Dirichlet boundary conditions. The latter will be discussed in the following section due to the similarities with the contact constrains enforcement.

Once the auxiliary domain $\Omega^{'}$ is meshed, there may be elements whose nodes are all inside the domain, thus they can be treated like standard FEM. However, the elements cut by the analysis boundaries require a special integration scheme so that only the material part of the element is considered during the numerical integration (see Figure 2.1). In this regard, the definition of Γ determines the quality of the geometry approximation. There are several alternatives in the literature. The simplest method is the construction of linear approximations using the intersections of the geometry with the mesh edges, e.g. [13, 26], which is equivalent to the isoparametric linear definition typically used in low order body-fitted meshes. A geometry error is introduced, which can be relevant in interface problems such as contact or fluid-structure interaction. High order surface definitions as in [27] or the *smart octrees* for the FCM [28] result in a considerably lower geometry error compared to linear approximations, at the cost of more complex algorithms to build the integration rules. However, the geometry error still depends on the complexity of the domain, and the consideration of sharp features usually requires specific procedures.

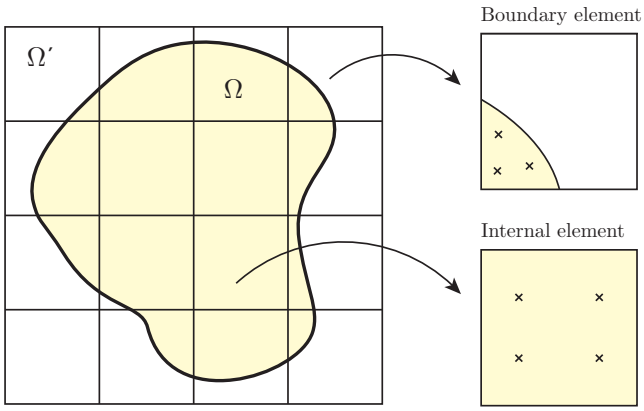

Figure 2.1: *Scheme of the integration process in 2D immersed boundary methods. Internal elements can be treated as standard FEM, whereas a special integration scheme is used for each boundary element.*

In recent years some standard body-fitted methods have been developed with the aim of eliminating the geometric error associated to the mesh generation process using the CAD definition of the analysis boundary. Among them we remark the Isogeometric Analysis (IGA) [29] and the NURBS-enhanced Finite Element Method (NEFEM) [30, 31]. In NEFEM the NURBS surface definition is introduced only in the numerical integration process of the boundary elements, whereas the IGA requires a 3D NURBS or T-Spline parametrization of the entire domain. However, the standard CAD programs used in industry only provide a parametric representation of the boundary (B-Rep) and the 3D parametrization must be obtained by post-processing the given model [32]. The IGA and NEFEM techniques have been combined with the FCM [33] and cgFEM [4] respectively.

A relevant issue that is still being addressed within the IB methods is the uncontrolled ill-conditioning caused by small cuts between the discretization mesh and the geometry, which are arbitrary [34, 35]. This problem hinders the scalability of such methods because systems with a large number of degrees of freedom must be solved with iterative solvers, and those solvers may lose convergence due to severe ill-conditioning. Some works towards the reduction of the system ill-conditioning are the penalization of the gradient jumps between boundary elements in cutFEM [13], and the cell aggregation in [26]. In this thesis we propose a stabilized method to control the condition of the system by penalizing the solution at the nodes external to the geometry with a smoothed displacement obtained with a local recovery technique, while keeping the Cartesian structure of the discretization mesh. This is presented in Paper D and section 4.3.1.

The development of accurate error estimators to assess the quality of the approximated solution provided by the Finite Element method has always been a research field of interest. In this sense, the *a posteriori* error estimators [36] are very useful not

only to evaluate the overall accuracy of the solution, but also to estimate the error in quantities of interest [37] or to guide an adaptive refinement of the discretization mesh [38].

Zienkiewicz and Zhu presented in [39] a simple error estimator (usually named *ZZ-estimator* after the authors). Some adaptations of this estimator for contact problems can be found in [40] using the global version of the ZZ-estimator and mixed with multigrid methods in [41]. The ZZ-estimator makes use of a smooth stress field $\boldsymbol{\sigma}^*$ which is usually computed using the superconvergent patch recovery technique (SPR) [42]. After its publication, there have been attempts to increase the quality of the SPR technique, see [43] for a detailed revision. These techniques were included in cgFEM to guide an automatic h-adaptive refinement [44]. In section 4.3.2 and paper E we present a modified version of the SPR technique in which the boundary equilibrium around the contact area is weakly enforced, with the objective of increasing the accuracy of $\boldsymbol{\sigma}^*$ for contact problems solved with cgFEM.

2.2. Contact formulations with immersed boundary methods

In the last decades contact formulations based on the mortar method [45] have been thoroughly developed, see [46–53] to cite some. Its advantages with respect to classical *node-to-node* formulations are the ability to deal with non-conforming meshes, together with the consideration of large sliding and deformations. Furthermore, the mortar-based formulations fulfill the *InfSup* condition [54], thus guaranteeing the optimal FE convergence rate, which is the main flaw of the *node-to-segment* formulations. Nevertheless, the mortar method cannot be directly implemented in the immersed boundary framework, because the definition of a Lagrange multipliers field that fulfills the *InfSup* condition is not straightforward. This problem is common for the enforcement of both Dirichlet boundary conditions and frictionless contact constrains, as the latter can be seen as a non-linear variation of the first. In both cases the weak enforcement is usually performed by means of Lagrange multipliers, but the naive choice of the intersection points between the FE mesh and the boundary for the multiplier space leads to non-infsup formulations, thus lacking optimal convergence and prone to locking problems.

Regarding immersed boundary methods there are several works in the XFEM framework. For example the frictional sliding between crack faces is combined in [55, 56] with the LATIN method [57], and ref. [58] proposes a frictionless formulation based on the augmented Lagrange method [59] for elastic-plastic crack growth problems. The contact problem has also been included in the finite cell method for 2D unilateral contact [60] and 3D frictionless contact using a fictitious material [61] and regularized penalty method in [62]. Refs. [63, 64] present a weak form for the enforcement of 3D

frictional contact with small and large slidings. However it is stated that the *InfSup* condition may be violated for some situations. The instability issue due to the *InfSup* condition was described in a review by Laursen and Sanders [65] where two different alternatives were suggested to ensure stability. The first consists in the proper choice of the Lagrange multipliers space e.g. with the Vital Vertex method [66, 67]. There are works for 2D large sliding contact [68] but the extension to 3D problems is still a challenge (although Dirichlet boundary conditions were imposed in [69]). The second alternative is the addition of stabilizing terms to the formulation. Several works in this direction have been presented. A polynomial projection stabilization for low order interpolations in XFEM is presented in [70]. In the context of immersed boundaries, ref. [71] includes a global polynomial multiplier stabilization for 2D small slidings. In [72] a similar stabilized formulation with local definition of the multipliers is developed for frictionless contact. Similar stabilized formulations based on the Nitsche's method [73] have been adapted to immersed boundary methods for small sliding in 2D [74] and 3D [75]. These stabilized formulations include the FE traction in the stabilizing term and, as a consequence, the penalty parameter of the stabilization term may fail the *InfSup* condition if is not chosen locally (e.g. a local eigenvalue problem [72] or as a function of the surface/volume ratio in the element [74]). A major contribution of this thesis is a stabilized formulation suitable for immersed boundary methods in which the stability is ensured with a penalty parameter independent of the mesh. This is presented in section 4.1 and paper A for frictionless contact and in section 4.1.3 and paper B for Coulomb's frictional contact.

Another key aspect for the accuracy and robustness of contact algorithms is the definition of the contact surfaces. The classical approach is the use of isoparametric linear elements. In this case the continuity on the normal vector field is lost, and the robustness of contact detection algorithms and convergence of the solution may be compromised. To alleviate this problem, several *smoothing* techniques have been proposed using Bézier splines, Hermite splines and NURBS interpolations [76–79] as well as Nagata and Gregory patches ([80] and [81] respectively). The use of IGA-based methods represents a step further in this direction, as it allows the use of the CAD geometry in the contact formulation (e.g. [52, 53, 82]). In the work of Corbett and Sauer [83, 84] the isogeometric basis are introduced in the model as enrichment functions only at the contact region, so that simple linear elements are used for the rest of the domain. In immersed boundary methods there is a natural decoupling of the solution and surface interpolations, so there is more freedom in the choice for the surface definition. For instance, ref. [62] presents a modification of the marching cubes algorithm [85] using high order triangle patches with an increased accuracy in the simulation results. Another contribution found in this thesis is the inclusion in the contact kinematic variables of the exact CAD boundary definition through the use of NURBS. In section 4.2 and paper C two different alternatives are proposed, and the quality of the solution is compared with a simple definition of the surface with linear interpolations.

Chapter 3

Problem description

3.1. Continuum formulation

In this section we will set the notation and the equations that govern the problem of interest in this thesis, which is the 3D contact problem between elastic solids. Figure 3.1 shows the scheme of two elastic bodies $\Omega^{(i)} \in \mathbb{R}^3; i = 1, 2$ becoming in contact. We divide the boundaries $\Gamma^{(i)}$ of each body in three non-overlapping parts: the Dirichlet boundary Γ_D, Neumann boundary Γ_N and the area where contact may occur Γ_C. The initial configuration of any point in $\Omega^{(i)}$ is depicted as $\mathbf{X}^{(i)}$, and the motion is described with the following mapping:

$$\boldsymbol{\varphi} : \Omega \longrightarrow \mathbb{R}^3 \; ; \qquad \mathbf{x}^{(i)} = \boldsymbol{\varphi}\left(\mathbf{X}^{(i)}\right) \tag{3.1}$$

where we assume a quasi-static hypothesis. Then the displacement of a point is defined as the difference between the deformed and the initial configuration: $\mathbf{u} = \mathbf{x} - \mathbf{X}$. The differential formulation of the elastic problem can be written as:

$$\begin{aligned} &\operatorname{div} \boldsymbol{\sigma} + \mathbf{b} = 0 \\ &\boldsymbol{\sigma} = \boldsymbol{\sigma}(\boldsymbol{\epsilon}) \\ &\boldsymbol{\epsilon} = \boldsymbol{\epsilon}(\mathbf{u}) \\ &\mathbf{u}(\mathbf{X}) = \mathbf{u}_d(\mathbf{X}) \qquad \mathbf{X} \in \Gamma_D \\ &\mathbf{n} \cdot \boldsymbol{\sigma} = \hat{\mathbf{t}} \qquad \mathbf{X} \in \Gamma_N \end{aligned} \tag{3.2}$$

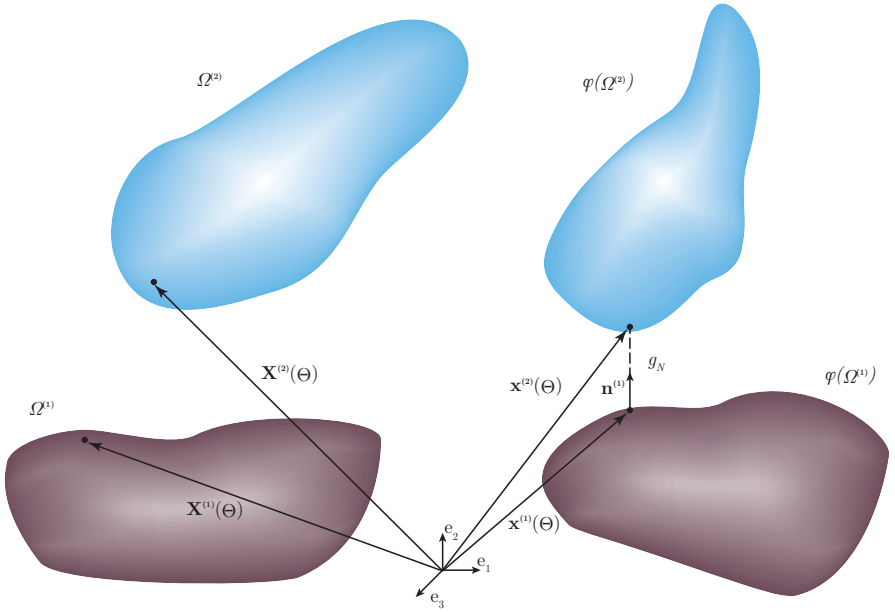

Figure 3.1: *Sketch of two deformable solids getting in contact.*

where $\boldsymbol{\sigma}$ is the Cauchy stress tensor, $\mathbf{b}$ are the volume forces, $\boldsymbol{\epsilon}$ is the strain tensor, $\mathbf{u}_d$ the Dirichlet boundary conditions and $\hat{\mathbf{t}}$ the prescribed traction along the Neumann boundary. For the sake of simplicity we will assume that there are no volumetric forces acting in $\Omega^{(i)}$. The definition of the material constitutive relation and the displacement-strain relation will depend on the hypothesis considered in the analysis [86]. In this thesis we will consider elastic and hyperelastic material, together with small and finite deformations and displacements. This problem is usually solved by minimizing a weak form of the total potential energy Π_p, so the problem is stated as finding $\mathbf{u}$ as follows:

$$\begin{aligned} &\min \left\{ \Pi_{\mathrm{p}}(\mathbf{u}) = \sum_{i=1,2} \left(\Pi_e^{(i)}(\mathbf{u}) - \int_{\Gamma_N^{(i)}} \mathbf{u} \cdot \hat{\mathbf{t}} \, d\Gamma \right) \right\} \\ &\text{subject to } \mathbf{u} = \mathbf{u}_d \qquad \text{in } \Gamma_D \end{aligned} \tag{3.3}$$

with $\Pi_e^{(i)}$ being the strain energy stored in each deformed body.

Frictionless contact. Once the elasticity problem is stated we define the distance between bodies likely to be in contact with the variable g_N. To measure that distance, a pairing between points of the bodies in contact must be established. There is not a unique solution to this problem and there are different strategies such as the closest

point projection [86, 87] or the ray-tracing [49, 64], which is the used in this thesis, and is depicted in Figure 3.1. Given a point $\mathbf{x}^{(1)}$ the contact pair $\mathbf{x}^{(2)}$ is defined as:

$$\mathbf{x}^{(2)}\left(\boldsymbol{\Theta}^{(2)}\right) = g_N \mathbf{n}^{(1)} + \mathbf{x}^{(1)}; \qquad \mathbf{x}^{(1)} \in \Gamma_c^{(1)}, \quad \mathbf{x}^{(2)} \in \Gamma_c^{(2)} \tag{3.4}$$

where $\boldsymbol{\Theta}^{(i)} \equiv (\xi, \eta)^{(i)}$ are the convective coordinates of $\Gamma_c^{(i)}$ and $\mathbf{n}^{(i)}$ is the normal vector to the surface $\Gamma_C^{(i)}$. Equation (3.4) has the unknowns $\boldsymbol{\Theta}^{(2)}$ and g_N, and the method for solving it will depend on the definition of $\mathbf{x}^{(2)}(\boldsymbol{\Theta}^{(2)})$, which will be discussed in section 4.1.1.

The condition of impenetrability between solids $g_N \geq 0$ transforms the formulation (3.3) into a minimization problem with inequality constrains. Among all methods to solve this type of problems we find the Lagrange multiplier method, used in several FE formulations including the presented in this thesis. We define the Lagrange multiplier as λ_N, an additional term is included in (3.3), and the new formulation must be optimized, this is, minimize $\mathbf{u}$ and maximize λ_N

$$\begin{gathered} \operatorname{opt}\left\{\Pi_{\mathrm{p}}(\mathbf{u}) + \int_{\Gamma_C^{(1)}} \lambda_N g_N \, d\Gamma\right\} \\ \text{subject to} \begin{cases} g_N \geq 0 \\ \lambda_N \leq 0 \\ g_N \lambda_N = 0 \end{cases} \quad \text{in } \Gamma_C^{(1)} \end{gathered} \tag{3.5}$$

where we find the classical Karush-Khun-Tucker contact conditions [88]. The contact integral in (3.5) is evaluated at $\Gamma_C^{(1)}$, which is usually called the *slave body*. However, the contact surface is not known *a priori*, as the gap is a function of the displacements, which are the unknown of the contact problem itself. This non-linearity is addressed introducing the active set strategy, in which Γ_C is assumed to be known, problem (3.5) is solved and the new contact active set is defined, until convergence is achieved. In this thesis we will use the Newton-Raphson algorithm as the solution method for solving the non-linear problem.

In section 4.1.2 we use the Finite Element method to solve the problem defined in (3.5). The choice of the Lagrange multipliers field based on the intersections between the Cartesian grid and the boundary fails to fulfill the *InfSup* condition in the discretized problem [67], so some modifications are needed to obtain the optimal convergence rate of the FE solution. In this thesis we will explore the option of adding extra terms to equation (3.5) to obtain the so-called "stabilized" or "perturbed" Lagrangian formulations [89].

Frictional contact. In the previous formulation we have assumed that the sliding between bodies is not constrained, thus the surface traction has only normal component along Γ_C. To consider frictional contact we must first define the components of

the traction vector $\mathbf{t} = \mathbf{n} \cdot \boldsymbol{\sigma}$ along Γ_C as shown in Figure 3.2. The contact pressure, denoted with the scalar p_N is the projection of $\mathbf{t}$ on the vector normal to the surface $\mathbf{n}$, this is, $p_N = \mathbf{n} \cdot \boldsymbol{\sigma}\mathbf{n}$. Then the tangent component of the traction can be defined as

$$\mathbf{p}_T = \mathbf{t} - p_N \, \mathbf{n} \tag{3.6}$$

We can define $\mathbf{T}_n$ as the projection operator onto the tangent plane at a given point with normal vector $\mathbf{n}$ and the tangent pressure is rewritten as

$$\mathbf{p}_T = \mathbf{T}_n \cdot \mathbf{t}; \qquad \mathbf{T}_n = \left(\mathbb{I} - \mathbf{n}^{(1)} \otimes \mathbf{n}^{(1)} \right) \tag{3.7}$$

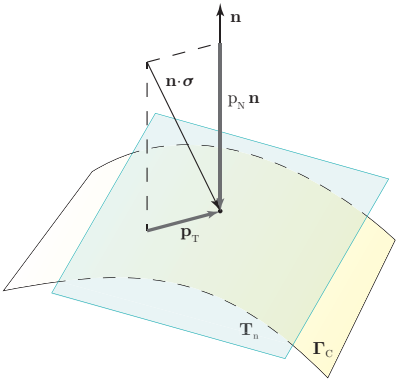

Figure 3.2: *Surface traction along the contact boundary. Decomposition in* p_N, $\boldsymbol{p}_T$

In the scope of this thesis we will consider a Coulomb frictional model, which defines two different contact states: adhesion and frictional sliding. Setting μ as the friction coefficient between bodies, if the modulus of $\mathbf{p}_T$ is lower than μp_N there will be adhesion (*stick* condition), and if the tangent stress reaches that limit value there will be a relative movement $\dot{\mathbf{g}}$ between bodies without increasing that stress value (*slip* condition). Details on the definition of the relative sliding are provided in section 4.1.1. The behavior of the Coulomb's frictional stress can be written in a compact way using the operator $P_{B(n,s)}(\mathbf{x})$, presented in [64], which is defined as the projection of $\mathbf{x}$ both on the tangent plane $\mathbf{T}_n$ and on a circle of radius s, this is:

$$P_{B(n,\mu p_N)}(\mathbf{t}) = \begin{cases} \mathbf{T}_n \mathbf{t} & if \quad \|\mathbf{T}_n \mathbf{t}\| \leq \mu p_N \\ \\ \mu p_N \frac{\mathbf{T}_n \mathbf{t}}{\|\mathbf{T}_n \mathbf{t}\|} & if \quad \|\mathbf{T}_n \mathbf{t}\| > \mu p_N \end{cases} \tag{3.8}$$

As remarked in Chapter 1, the solution of frictional contact problems cannot be achieved by building an energy functional to minimize, since the frictional contact force is non-conservative. A common idea is to modify the functional obtained for

frictionless contact and include the chosen frictional model. In section 4.1.3 we present the strategy followed in this thesis to obtain a stabilized formulation for Coulomb's frictional contact.

3.2. The Cartesian grid Finite Element Method (cgFEM)

The Cartesian grid Finite Element Method (cgFEM) is an immersed boundary method for solving the elasticity problem (first developed for 2D problems [3] and recently for 3D [4]) which employs a hierarchical set of regular Cartesian grids to create FE discretization meshes independent of the geometry. The cgFEM has been developed with the aim of providing an efficient methodology that overcomes the high cost that standard body-fitted methods usually require in the meshing and re-meshing of the analysis domain, especially in terms of man-hours. The process of creating a non-conforming discretization mesh is summarized in Figure 3.3. The domain of interest Ω is embedded in an auxiliary domain Ω_h that consists in regular hexahedron. From this reference hexahedron an octree hierarchical structure of Cartesian grids is created. The mesh is intersected with the CAD model of the domain Ω to establish the status of each node as inside or outside the domain. Then, we can distinguish three different elements depending on their location with respect to Ω (Figure 3.3c): there can be elements completely internal to Ω (for now on *internal elements*), elements with all their nodes outside Ω (which will not be considered during the analysis) and elements that are intersected by the analysis boundary Γ (*boundary elements*).

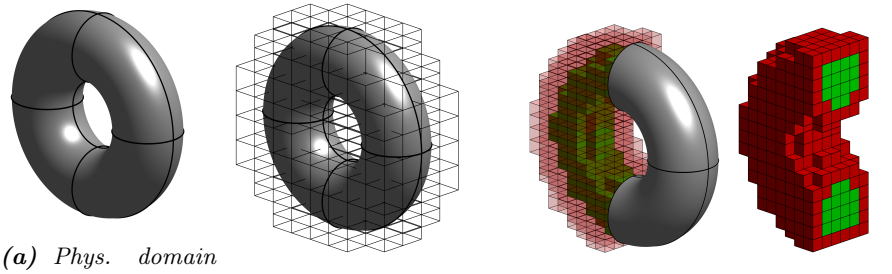

(a) *Phys. domain* Ω ***(b)*** *Discretization* Ω_h ***(c)*** *Internal and boundary elements*

Figure 3.3: *Disctretization mesh of a torus in cgFEM. In green, elements internal to the domain. In red, elements cut by the boundary (boundary elements). Elements completely outside the domain are not considered during the analysis.*

The internal elements can be treated like standard FEM elements, whereas the boundary elements require a special integration scheme so that only the material part of the element is considered during the numerical integration. In other words, an auxiliary mesh (named *integration mesh* to differentiate it from the discretization mesh) is built only for integration purposes at each boundary element, taking into account the intersection between the element and the analysis boundary. Note that, although those integration subdomains may have a significant distortion this will never affect the quality of the method. This is because FE interpolation functions are defined in the discretization mesh, which is built with regular hexahedrons, so the Jacobian is kept constant.

The cgFEM also features two different strategies for the h-adaptive refinement of the discretization mesh [44]: the first is based on the geometrical features of the CAD model, and can be performed as a preprocessing step. The second strategy is based on the Zienkiewicz and Zhu error estimator [39], which uses a smooth stress field $\boldsymbol{\sigma}^*$ obtained with the superconvergent patch recovery technique [42].

Besides the easier mesh generation, the hierarchical structure of Cartesian grids presents other advantages [20]. On the one hand, the nested structure of the Cartesian grids provides a natural framework to apply a subdomain decomposition. Using that information we can also obtain a reordering of the system of equations that reduces the computational cost when using direct solvers. On the other hand, all relations between elements in the different levels of the structure are known *a priori*, so the projection of information between meshes is highly efficient, including the projection of information between different domains in shape optimization processes.

3.2.1. Numerical integration: surface representation with NURBS

One important issue the immersed boundary methods must address is the numerical integration in the boundary elements. For example, in the Finite Cell Method an octree-based subdivision is performed in each element, where the newly created subdomains are conforming to the geometry [28]. The procedure followed in cgFEM for the numerical integration of boundary elements is presented in the 2D sketch of Figure 3.4. Once the location of the nodes with respect to the geometry is established, the Marching Cubes algorithm [85] classifies all intersected elements in 16 configurations. A decomposition in tetrahedrons and triangles for volume and surface integrals [44] is associated to each of these configurations, and only those entities inside the material part of each element are kept (Figure 3.4b). There may be boundary elements whose intersection pattern has no correspondence with the Marching Cubes classification (for example multiple surfaces inside an element). In this case a tailor-made subdivision is created.

The *boundary representation* or B-Rep method has been widely adopted by the CAD industry for the definition of geometries, being NURBS and trimmed-NURBS the most commonly used method for representing curves and surfaces. A key feature of the cgFEM is the inclusion of the CAD definition in the numerical integration so that the exact volume and surface inside the boundary elements is evaluated [4], as depicted in Figure 3.4c. This technique is based on the NURBS-enhanced Finite Element Method (NEFEM) of Sevilla *et al.* [30, 90]. In the NEFEM, developed for body-fitted meshes, the NURBS description is included at the elements laying on the boundary of the domain while the internal elements remain with the standard FE interpolation and integration methods. This represents an advantage with respect to the isogeometric analysis [29] in the sense that the NURBS basis functions are not extended into the bulk of the domain, and the simplicity of the piecewise polynomial FE interpolations is kept.

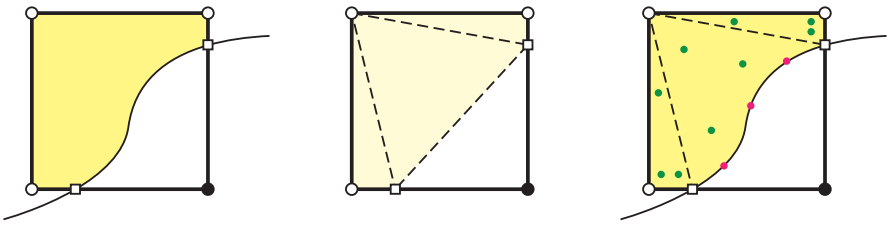

Figure 3.4: *Numerical integration for boundary elements in cgFEM. a) Boundary element and its intersections with the mesh. b) Integration subdomains provided by the Marching Cubes algorithm. c) The volume (green) and surface (red) quadratures account for the exact NURBS geometry.*

Since the surface integration quadratures in the cgFEM can use the NURBS definition of the analysis domain we present here the notation regarding the mathematical modelling of such surfaces. Given a 2D parametric space (ξ, η), a NURBS surface is defined as the transformation $\mathbf{Q} : (\xi, \eta) \longrightarrow \mathbb{R}^3$ in the following form

$$\mathbf{Q}(\xi,\eta) = \sum_{i=1}^{n}\sum_{j=1}^{m} \frac{N_i^{(p)}(\xi)\, M_j^{(q)}(\eta)\, w_{i,j}}{\sum_{i=1}^{n}\sum_{j=1}^{m} N_i^{(p)}(\xi)\, M_j^{(q)}(\eta)\, w_{i,j}} \mathbf{P}_{i,j} \tag{3.9}$$

Figure 3.5 shows an example of a simple NURBS geometry. The transformation is defined by a net of $n \times m$ control points with coordinates $\mathbf{P}_{i,j}$ and weights $w_{i,j}$ (the black circles in the figure), and two *knot vectors* of order p and q respectively, from which the 1D basis functions $N_i^{(p)}$ and $M_j^{(q)}$ are built in a recursive way, see e.g. [91] for further details. Despite the rational nature of the NURBS basis functions, equation (3.9) can be interpreted as an interpolation of the control points $\mathbf{P}_{i,j}$ with the basis $S_{i,j}(\xi, \eta)$, defined as:

$$S_{i,j}(\xi,\eta) = \frac{N_i^{(p)}(\xi)\, M_j^{(q)}(\eta)\, w_{i,j}}{\sum_{i=1}^{n}\sum_{j=1}^{m} N_i^{(p)}(\xi)\, M_j^{(q)}(\eta)\, w_{i,j}} \tag{3.10}$$

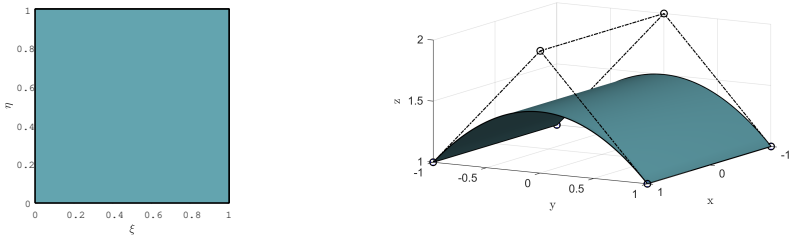

(a) Parametric space (ξ, η). *(b) NURBS in the physical domain* $\mathbb{R}^3$.

Figure 3.5: *Example of a surface defined with NURBS. Definition in the parametric space (a) and its corresponding transformation into* $\mathbb{R}^3$.

In fact, we can rewrite this transformation in matrix form if we rearrange the indexation of the control points from (i, j) to a unique index k:

$$\mathbf{Q}(\xi, \eta) = \sum_{k=1}^{n \times m} S_k(\xi, \eta) \mathbf{P}_k = \mathbf{S}(\xi, \eta) \cdot \mathbf{P} \tag{3.11}$$

This compact form will be useful for the definition of the contact kinematic variables and their variation in 4.1.1.

3.2.2. Error estimation: the Superconvergent Patch Recovery

To asses the error of the approximated FE solution of problems involving linear elastic materials and guide an automatic h-adaptive refinement process, the cgFEM makes use of the well-known Zienkiewicz and Zhu's error estimator (ZZ-estimator) [39] which is written as:

$$\|\mathbf{e}_{es}\| = \int_\Omega \left(\boldsymbol{\sigma}^* - \boldsymbol{\sigma}^h\right)^t \mathbf{D}^{-1} \left(\boldsymbol{\sigma}^* - \boldsymbol{\sigma}^h\right) \, d\Omega \tag{3.12}$$

where $\boldsymbol{\sigma}^*$ is the so-called *smooth* stress field and D is the material constitutive relation. Note that if $\boldsymbol{\sigma}^*$ were the exact solution of the stress field, equation (3.12) would coincide with the exact error in energy norm. The idea of the estimator is to use as reference a stress field with better convergence properties than the FE field $\boldsymbol{\sigma}^h$. For this purpose, Zienkiewicz and Zhu presented the superconvergent patch recovery technique [42] to create a smooth stress field from the FE solution.

The technique is summarized as follows. A patch Ω_p^k is created (Figure 3.6) for each node k of the discretization mesh with all the elements attached to the node

itself. Then a minimization problem, formulated in equation (3.13), is solved for each component i of the stress tensor.

$$\min \left[\sum_{g}^{\Omega_p^k} \left(\sigma_i^{*,k} - \sigma_i^h \right)^2 d\Omega \right] \tag{3.13}$$

where the subscript g denotes every quadrature point in Ω_p^k. The smooth stress is defined as a polynomial $\sigma_i^{*,k}(\mathbf{x}) = \mathbf{p}(\mathbf{x})\ \mathbf{a}_i^k$, where $\mathbf{p}(\mathbf{x})$ contains the monomials of the same degree as the FE interpolation and $\mathbf{a}_i^k$ are the unknown coefficients of the problem. The sum in (3.13) implies that the information of each quadrature point is evenly weighted. This can be somehow problematic within the cgFEM, because the boundary elements have a higher density of quadrature points than the internal elements due to the special numerical integration along the boundary. Instead, an integral approach of the minimization problem (3.13) is presented in [3] so that each quadrature point is weighted with its own integration weight. Then the problem is rewritten as:

$$\min \left[\int_{\Omega_p^k} \left(\sigma_i^{*,k} - \sigma_i^h \right)^2 d\Omega \right] \tag{3.14}$$

After operating, the minimization problem yields a linear system of equations per component $\mathbf{M}\mathbf{a}_i^k = \mathbf{H}_i$ with the following definitions:

$$\mathbf{M}_i = 2 \int_{\Omega_p^k} \mathbf{p}(\mathbf{x})^T\, \mathbf{p}(\mathbf{x}) d\Omega\ ; \qquad \mathbf{H}_i = 2 \int_{\Omega_p^k} \mathbf{p}(\mathbf{x})^T\, \sigma_i^h d\Omega \tag{3.15}$$

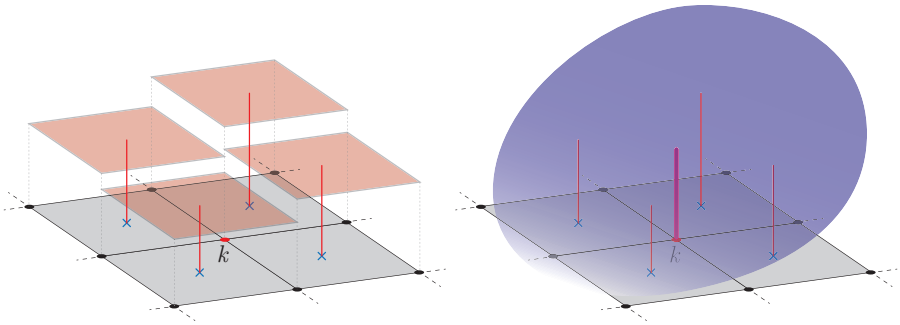

(a) *(b)*

Figure 3.6: *2D representation of an SPR patch Ω_p^k, with the node k assembly in red. The FE stress $\boldsymbol{\sigma}^h$ is evaluated at the elements in the patch (left) and a polynomial is fitted to obtain the smooth stress $\boldsymbol{\sigma}^*$ (right).*

Note that the size of the systems to solve is small, so the impact of this method in the global computational cost of the analysis is relatively low. When all nodal patches are solved, the smooth field $\boldsymbol{\sigma}^*$ is evaluated at any point $\mathbf{x} \in \Omega$ as:

$$\sigma_i^*(\mathbf{x}) = \sum_j N_j(\mathbf{x}) \sigma_i^{*,j}(\mathbf{x}_j) \tag{3.16}$$

where the interpolation employs the FE linear shape functions $N_j(\mathbf{x})$ associated to the j vertices of the element. Instead, the cgFEM makes use of the *conjoint polynomials Enhancement* technique [92], which provides an improved field by interpolating not only the nodal patch value $\sigma_i^{*,j}(\mathbf{x}_k)$ but the whole polynomial evaluated at $\mathbf{x}$, with the shape functions $N_j^v(\mathbf{x})$ associated to the element's vertices. This is written as:

$$\sigma_i^*(\mathbf{x}) = \sum_j N_j^v(\mathbf{x}) \sigma_i^{*,j}(\mathbf{x}) \tag{3.17}$$

A special case arises when using the SPR technique with immersed boundary methods. Figure 3.7a shows the patch associated to a node outside the domain (in red), whose only connected element has a low ratio between material and element volume. This situation involves two issues: *(i)* the stiffness associated to the red node is very small. This induces an ill-conditioning of the FE problem, and at a local level the quality of the FE stress field is poor compared to that of internal elements. This second issue is discussed in section 4.3.1 where we propose a solution to control the ill-conditioning of the FE formulation. *(ii)* The available domain in the patch to make the SPR fitting might be too small, compromising the accuracy of the fitted smooth stress. In order to overcome this problem we propose the enlargement of these problematic patches based on a volume ratio measure. This is, if the ratio between material volume and element volume in the patch is below a fixed threshold the neighbor elements are included in the new patch domain $\Omega_p^{'k}$ (Figure 3.7b). A threshold value of 25% has been used in this thesis with acceptable results, although a study of the influence of this parameter in the quality of $\boldsymbol{\sigma}^*$ should be performed.

(a) *Original patch* ***(b)*** *Enlarged patch*

Figure 3.7: *Example of boundary patch enhancement. The patch Ω_p^k associated to the red node has a low material/element volume ratio. Hence a bigger patch $\Omega_p^{'k}$ is considered with the surrounding elements.*

The structured nature of the cgFEM can be exploited to increase the computational efficiency of the SPR technique. In h-adapted cgFEM meshes the adjacent elements with a size difference are non conforming. Therefore, there exist *hanging nodes*, and we use multi-point constraints (MPCs) [93] to ensure C^0 continuity between elements. Nevertheless only one level of difference is allowed between adjacent elements, so the range of different shapes for SPR patches Ω_p^k possible in cgFEM is (at least) finite. Indeed, the number of different patch topologies for the 2D case is reduced to 19, shown in Figure 3.8a.

Now we recall the coefficient matrix $\mathbf{M}$ in (3.15). If we normalize the coordinates of the integration points inside the patch with the nodal coordinates $\mathbf{x}_N$ and a representative size of the patch h_p:

$$\mathbf{x}_{local} = \frac{\mathbf{x} - \mathbf{x}_N}{h_p} \tag{3.18}$$

then, $\mathbf{M}$ only depends on the integration points distribution inside the patch. All internal elements in cgFEM have identical quadrature rules, therefore all patches containing only internal elements (called *internal patches*) with the same topology will share the same $\mathbf{M}$ as well. So given a discretization mesh, we can detect all different patch topologies, pre-compute their coefficient matrix $\mathbf{M}$ and, with only one matrix inversion for each different topology, we can solve all SPR problems for the internal patches. Finally, the patches containing boundary elements (*boundary patches*) are evaluated individually because each boundary element has its specific quadrature rule. This feature is analogous to the numerical integration of the FE stiffness matrix for linear elasticity. Since all internal elements are affine, their stiffness matrices are proportional with a scale factor depending on the size difference. Therefore we can pre-compute only one stiffness matrix and scale it to obtain all the elemental matrices in the bulk. These features somehow reduce the computational cost of the method in one dimension, since the cost is proportional only to the elements on the boundary.

The number of possible topologies in 3D cgFEM meshes scales up to several hundreds (two configurations are shown in Figure 3.8b). However, there is no need to manually classify and code each topology. Instead we have designed an automatic coding based on the level difference of the elements in the patch. Two examples of this coding are given in Figure 3.9. Having fixed the order of the elements in the patch, the biggest element is considered as level 0, and the relative level of each element compared to the 0 level is written as a digit. Finally all digits are concatenated and form the number associated to the patch. This numeration is not compact, but allows to automatically search for all the different topologies existing in a 3D mesh, and then only the matrices $\mathbf{M}$ belonging to those configurations are evaluated.

In section 4.3.2 we explore the introductions of additional constrains into (3.13) to enhance the quality of the recovered stress field. This was first studied for elastic problems in [43], and in this thesis we propose the addition of the contact boundary equilibrium in the SPR problem.

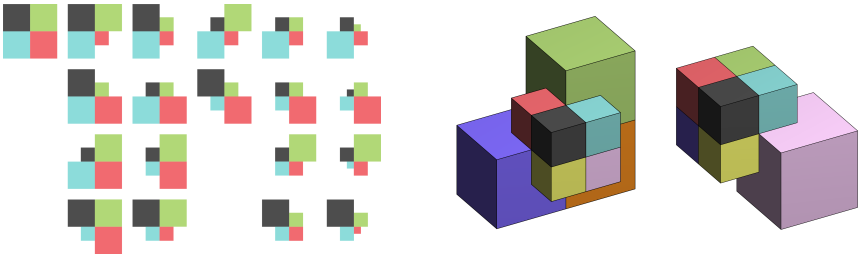

Figure 3.8: *Patch topologies that can appear in a cgFEM analysis. All possible configurations for cgFEM 2D (a), and examples of possible configurations for cgFEM 3D (b).*

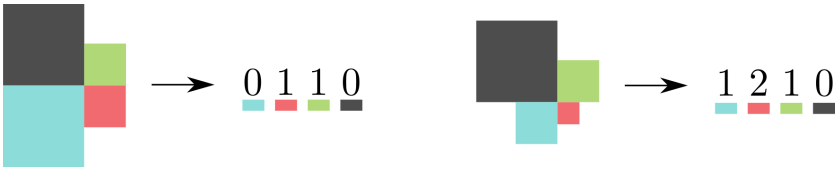

Figure 3.9: *2D example of SPR patch coding. The patch on the left has code number* 0110 *and the patch on the right is number* 1210.

Chapter 4

Contributions

In this Chapter a summary of the thesis contributions is presented, emphasizing the novelties introduced in each publication. The contributions are divided in three sections, each of them focused in a different aspect of the thesis. First, the stabilized frictional contact formulation is presented in 4.1. The aspects regarding the surface definition in cgFEM are discussed in 4.2. Then in section 4.3 we present different strategies to enhance the robustness and accuracy of the method. Finally an illustrative example of an engineering application of this thesis is shown in section 4.4.

4.1. A stabilized augmented Lagrangian contact formulation

The first objective of this thesis is to develop a formulation to solve 3D contact problems using the cgFEM. A stabilized augmented Lagrangian formulation is presented in paper A for frictionless contact, and then extended to Coulomb frictional contact in paper B. In this section we set the kinematic variables involved in the solution of contact problems. Then the main features of this formulation are presented, first for the frictionless case and finally for friction problems.

4.1.1. Contact kinematic variables

In this section we will set the kinematic variables that take part in frictionless and frictional contact problems, together with its variation. As it was stated in section 3.1 we use a ray-tracing scheme to determine the contact point pairs. We will name $\Gamma_C^{(1)}$, from which the normal vector is evaluated, as the *slave* surface, and the corresponding contact *master* surface, $\Gamma_C^{(2)}$. Now we rewrite here the relation defined in section 3.1:

$$\mathbf{x}^{(2)}\left(\boldsymbol{\Theta}\right) = g_N \mathbf{n}^{(1)} + \mathbf{x}^{(1)}; \qquad \mathbf{x}^{(1)} \in \Gamma_c^{(1)}, \quad \mathbf{x}^{(2)} \in \Gamma_c^{(2)} \tag{4.1}$$

where the convective coordinates of the *slave* surface are omitted because they remain fixed, thus we introduce the simplified notation $\boldsymbol{\Theta} \equiv \boldsymbol{\Theta}^{(2)}$. The unit normal vector to the surface $\mathbf{n}^{(1)}$ is obtained with the cross product of the tangent vectors of the surface, which are defined as the partial derivatives of x with respect to the convective coordinates:

$$\mathbf{n}^{(1)} = \frac{\mathbf{x}_{,\xi}^{(1)} \times \mathbf{x}_{,\eta}^{(1)}}{\left\| \mathbf{x}_{,\xi}^{(1)} \times \mathbf{x}_{,\eta}^{(1)} \right\|}; \qquad \mathbf{x}_{,\xi}^{(1)} = \frac{\partial \mathbf{x}^{(1)}}{\partial \xi}, \qquad \mathbf{x}_{,\eta}^{(1)} = \frac{\partial \mathbf{x}^{(1)}}{\partial \eta} \tag{4.2}$$

with the components of the convective coordinates written as $\boldsymbol{\Theta} \equiv (\xi, \eta)$. If we multiply equation (4.1) by $\mathbf{n}^{(1)}$, and taking into account that $\mathbf{n}^{(1)} \cdot \mathbf{n}^{(1)} = 1$, we obtain the definition of the normal gap:

$$g_N = \left(\mathbf{x}^{(2)}\left(\boldsymbol{\Theta}\right) - \mathbf{x}^{(1)} \right) \cdot \mathbf{n}^{(1)} \tag{4.3}$$

This will be the variable used in the formulation for frictionless problems. However, the solution of frictional contact includes an additional kinematic variable that represents the relative velocity between bodies, which was defined as $\dot{\mathbf{g}}\, dt$ for the continuum in section 3.1. In this thesis we will solve the frictional contact problem by solving a sequence of quasi-static time increments. In ref. [49] the approximation $\Delta^t \mathbf{g}$ for the FE discretization was presented for 2D problems. This incremental definition is similar to that presented in [47], and it was proven to be frame independent in [94]. In paper B we extended this approximation to the 3D case, which we reproduce here.

Figure 4.1 shows the contact situation for a point that is sliding between time increments t and $t+1$. Let $\mathbf{x}_t^{(1)}$ be a point on the slave surface, which is in contact with point $\mathbf{x}_t^{(2)}(\boldsymbol{\Theta}_t)$ at time t. If there is no sliding we have a *sticking* state and the gap vector is simply defined as:

$$\mathbf{g} = \mathbf{x}^{(2)}\left(\boldsymbol{\Theta}\right) - \mathbf{x}^{(1)} \tag{4.4}$$

Now assume that a relative sliding between the bodies in contact occurred at time $t+1$. This means that the contact pair on the master surface changes from $\boldsymbol{\Theta}_t$ to a new location $\boldsymbol{\Theta}_{t+1}$. Then the relative increment velocity is defined as:

$$\dot{\mathbf{g}}\, dt \approx \Delta^t \mathbf{g} = \left(\mathbf{x}_{t+1}^{(2)}(\boldsymbol{\Theta}_t) - \mathbf{x}_{t+1}^{(2)}(\boldsymbol{\Theta}_{t+1}) \right) \tag{4.5}$$

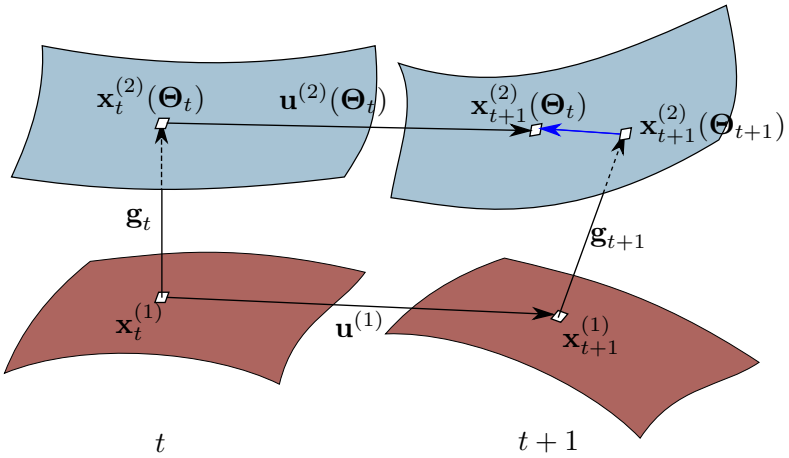

Figure 4.1: *Sliding between bodies. At time step t, there is a pair of points* $\left[\boldsymbol{x}_t^{(1)}, \boldsymbol{x}_t^{(2)}(\boldsymbol{\Theta}_t)\right]$ *in adhesive contact. At time* $t+1$ *sliding occurs, and the same point* $\boldsymbol{x}_{t+1}^{(1)}$ *is now contacting with the point* $\boldsymbol{x}_{t+1}^{(2)}(\boldsymbol{\Theta}_{t+1})$*. The slip increment* $\Delta^t \boldsymbol{g}$ *is represented by the blue arrow.*

We are interested in the projection of the relative velocity onto the tangent plane at the current step to evaluate the tangent forces due to relative sliding. Using the operator $\mathbf{T}_n$, defined in (3.7), this is written as:

$$\mathbf{T}_n \Delta^t \mathbf{g} = \mathbf{T}_n \left(\mathbf{x}_{t+1}^{(2)}(\boldsymbol{\Theta}_t) - \mathbf{x}_{t+1}^{(2)}(\boldsymbol{\Theta}_{t+1}) \right) \tag{4.6}$$

Note that only $\boldsymbol{\Theta}_t$ is needed from the previous step's data, since all terms are evaluated in the current configuration. An alternative definition of (4.6) is obtained if we consider the following relation:

$$\mathbf{x}_{t+1}^{(2)}(\boldsymbol{\Theta}_{t+1}) = \mathbf{x}_{t+1}^{(1)} + \mathbf{g}_{t+1} \tag{4.7}$$

and since $\mathbf{g}_{t+1}$ is in the direction of $\mathbf{n}^{(1)}$, then $\mathbf{T}_n \mathbf{g}_{t+1} = 0$, so:

$$\mathbf{T}_n \, \mathbf{x}_{t+1}^{(2)}(\boldsymbol{\Theta}_{t+1}) = \mathbf{T}_n \, \mathbf{x}_{t+1}^{(1)} \tag{4.8}$$

and finally we obtain:

$$\mathbf{T}_n \Delta^t \mathbf{g} = \mathbf{T}_n \left(\mathbf{x}_{t+1}^{(2)}(\boldsymbol{\Theta}_t) - \mathbf{x}_{t+1}^{(2)}(\boldsymbol{\Theta}_{t+1}) \right) = \mathbf{T}_n \left(\mathbf{x}_{t+1}^{(1)} - \mathbf{x}_{t+1}^{(2)}(\boldsymbol{\Theta}_t) \right) \tag{4.9}$$

The definition in 4.9 has only one term containing the convective coordinates. Note that if there is no change in the convective coordinates in the case of adhesive contact, then $\boldsymbol{\Theta}_{t+1} = \boldsymbol{\Theta}_t$ and adding (4.9) and (4.3) in normal direction we have:

$$g_n \mathbf{n}^{(1)} - \mathbf{T}_n \Delta^t \mathbf{g} = \mathbf{x}^{(2)}(\boldsymbol{\Theta}) - \mathbf{x}^{(1)} = \mathbf{g} \tag{4.10}$$

which proves the continuity of the kinematic variables between the *slip* and *stick* states. This relation will be useful to simplify the contact formulation for frictional adhesion in section 4.1.3

Variation of kinematic variables. Starting with the normal gap g_N, if we take variations in equation (4.1) we have:

$$\delta\mathbf{x}^{(2)}(\xi,\eta) = \delta g_N \mathbf{n}^{(1)} + g_N \delta\mathbf{n}^{(1)} + \delta\mathbf{x}^{(1)} \tag{4.11}$$

and projecting again on $\mathbf{n}^{(1)}$, with the additional consideration $\delta\mathbf{n}^{(1)} \cdot \mathbf{n}^{(1)} = 0$ we obtain δg_N expressed as:

$$\delta g_N = \left(\delta\mathbf{x}^{(2)}(\xi,\eta) - \delta\mathbf{x}^{(1)}\right) \cdot \mathbf{n}^{(1)} \tag{4.12}$$

Now we need the variations of $\mathbf{x}^{(1)}$ and $\mathbf{x}^{(2)}$. Note that only the convective coordinates of the master surface are involved in the variation, as the convective coordinates of the slave body remain fixed in the ray-tracing algorithm. Therefore we write the variations as:

$$\begin{aligned} \delta\mathbf{x}^{(1)} &= \mathbf{x}^{(1)}_{,u}\ \delta\mathbf{u} \\ \delta\mathbf{x}^{(2)} &= \left(\mathbf{x}^{(2)}_{,\xi}\delta\xi + \mathbf{x}^{(2)}_{,\eta}\delta\eta + \mathbf{x}^{(2)}_{,u}\right)\ \delta\mathbf{u} \end{aligned} \tag{4.13}$$

The definitions $\mathbf{x}_{,u}, \mathbf{x}_{,\xi}, \mathbf{x}_{,\eta}$ depend on the surface and interpolations considered in the FE analysis. In paper C, and section 4.2 we explore different definitions and compare them in terms of quality of the solution and efficiency of the method. We can build a small system of equations to find the terms $\delta\xi$ and $\delta\eta$. If we project equation (4.11) into $\mathbf{x}^{(1)}_{,\xi}$ and $\mathbf{x}^{(1)}_{,\eta}$, and considering now that $\mathbf{x}^{(1)}_{,\xi} \cdot \mathbf{n}^{(1)} = 0, \mathbf{x}^{(1)}_{,\eta} \cdot \mathbf{n}^{(1)} = 0$ we end up with the following system:

$$\begin{bmatrix} \mathbf{x}^{(2)}_{,\xi}\cdot\mathbf{x}^{(1)}_{,\xi} & \mathbf{x}^{(2)}_{,\eta}\cdot\mathbf{x}^{(1)}_{,\xi} \\ \mathbf{x}^{(2)}_{,\xi}\cdot\mathbf{x}^{(1)}_{,\eta} & \mathbf{x}^{(2)}_{,\eta}\cdot\mathbf{x}^{(1)}_{,\eta} \end{bmatrix} \begin{Bmatrix} \delta\xi \\ \delta\eta \end{Bmatrix} = \begin{Bmatrix} g_N\delta\mathbf{n}^{(1)}\cdot\mathbf{x}^{(1)}_{,\xi} - (\mathbf{x}^{(2)}_{,u} - \mathbf{x}^{(1)}_{,u})\cdot\mathbf{x}^{(1)}_{,\xi} \\ g_N\delta\mathbf{n}^{(1)}\cdot\mathbf{x}^{(1)}_{,\eta} - (\mathbf{x}^{(2)}_{,u} - \mathbf{x}^{(1)}_{,u})\cdot\mathbf{x}^{(1)}_{,\eta} \end{Bmatrix} \tag{4.14}$$

which can be solved analytically. This system includes also the variation of the normal vector $\delta\mathbf{n}^{(1)}$. Finally, we take variations in (4.2) and the variation of the normal gap is completely defined:

$$\begin{aligned} \delta\mathbf{n}^{(1)} &= \mathbf{n}^{(1)}_{,u}\delta\mathbf{u} \\ \mathbf{n}^{(1)}_{,u} &= \frac{\mathbf{x}^{(1)}_{,u,\xi}\times\mathbf{x}^{(1)}_{,\eta} + \mathbf{x}^{(1)}_{,\xi}\times\mathbf{x}^{(1)}_{,u,\eta}}{\left\|\hat{\mathbf{n}}^{(1)}\right\|} - \frac{\mathbf{n}^{(1)}}{\left\|\hat{\mathbf{n}}^{(1)}\right\|}\left[\mathbf{n}^{(1)}\cdot(\mathbf{x}^{(1)}_{,u,\xi}\times\mathbf{x}^{(1)}_{,\eta} + \mathbf{x}^{(1)}_{,\xi}\times\mathbf{x}^{(1)}_{,u,\eta})\right] \end{aligned} \tag{4.15}$$

The frictional contact formulation makes use of the variation of the gap vector (4.4) for the stick case. Note that when assuming adhesion there is no change in the contact point, so the variation is expressed as:

$$\delta \mathbf{g} = (\mathbf{x}^{(2)}_{,u} - \mathbf{x}^{(1)}_{,u})\delta \mathbf{u} \tag{4.16}$$

For this reason, and in order to keep the smooth transition between the *slip* and *stick* states, in the case of sliding contact we will omit the terms $\delta\xi$ and $\delta\eta$ for the evaluation of δg_N, then the variation will be written as:

$$\delta g_N|_{slip} = (\mathbf{x}^{(2)}_{,u}\delta \mathbf{u} - \mathbf{x}^{(1)}_{,u}\delta \mathbf{u}) \cdot \mathbf{n}^{(1)} \tag{4.17}$$

This choice ensures the smooth transition when sliding appears, at the cost of having a non-symmetric formulation, and a certain loss of angular momentum conservation. However, the Coulomb's frictional model will eventually lead to a non-symmetric system (section4.1.3) so this definition does not imply a loss of symmetry. Similar definitions of the term δg_N can be found in [64] and [46], where some ideas to maintain the angular momentum conservation are provided.

4.1.2. Frictionless contact

The lagrangian formulation in equation 3.5 can be solved with the Finite Element method replacing the continuum variables $\{\mathbf{u}, \lambda_N\}$ by suitable FE approximations $\mathbf{u}^h \in \mathscr{U}^h$ and $\lambda_N^h \in \mathscr{M}^h$. From now on we will omit the superscript h to denote FE variables for the sake of simplicity. The obtained formulation may lead to a loss of convergence of the FE solution as the mesh is refined. This is due to the increasing number of constrains included in the system, that eventually induces oscillations in the multipliers' values. The main principle of the stabilized formulations is the addition of a new term to the discretized formulation so that the multipliers' values are bounded. Simo, Wriggers and Taylor presented in [89] a perturbed Lagrangian formulation which includes a stabilizing term with a penalty parameter k. However, with this formulation the exact solution is not achieved when the mesh is refined, i.e. the formulation is not consistent. With our proposed modification of this perturbed Lagrangian formulation, presented in equation 4.18, the FE convergence to the exact solution is kept for a wide range in the values of the penalty parameter.

$$\text{opt}\left\{\Pi_{\text{p}}(\mathbf{u}) + \int_{\Gamma_C^{(1)}} \lambda_N g_N \, d\Gamma - \sum_{\forall e} \frac{h}{2E\kappa} \int_{\Gamma_C^{(1)}} (\lambda_N - p_N)^2 \, d\Gamma\right\} \tag{4.18}$$

In this thesis we propose the use of the Superconvergent Patch Recovery to compute the stabilizing stress: $p_N = \mathbf{n} \cdot \boldsymbol{\sigma}^* \mathbf{n}$. This was first presented in [95] for the weak imposition of Dirichlet conditions in immersed boundary methods. The main idea behind this choice is that the values of p_N at boundary elements with small cuts depend more on the solution of the internal nodes than that of the external ones.

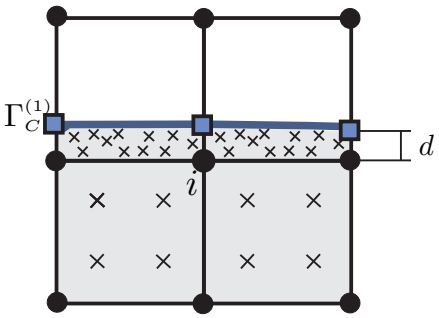

Figure 4.2: *Patch of elements for computing the smooth stress field of node i. The internal volume of the boundary elements depends on distance d.*

Furthermore, it was proven in [95] that with this choice the L^2 norm of p_N can be bounded with a constant $C > 0$ as:

$$\|p_N\|^2_{L^2(\Gamma_C)} \leq \frac{EC}{h}\|\mathbf{u}\|^2_E \tag{4.19}$$

being $\|\cdot\|_E$ the energy norm in the bulk. We have experienced that using a constant $C \geq 10$ is enough for linear and quadratic elements and any cut element pattern. This is crucial to ensure the stability of the method in situations with elements with very low volume/surface ratios, e.g. the mesh depicted in Figure 4.2. The material volume of the boundary elements in the Figure depends on the distance d whereas the surface remains constant. In this situation, typical of the immersed boundary methods, it is not possible to bound the L^2 norm of the FE tractions on the boundary (usually used in stabilized formulations) with the element's energy norm when $d \to 0$.

To solve the contact problem defined in (4.18) we have designed the following iterative procedure: the stabilizing stress p_N is fixed while solving the contact active set in (4.18). Then, when the contact problem has reached convergence, we update the value of p_N an solve again the problem until convergence in the stabilizing term is also reached. Therefore, if we take variations with respect to the displacements and multipliers we obtain the following variational form:

$$\begin{cases} \delta\Pi(\mathbf{u},\delta\mathbf{u}) + \displaystyle\int_{\Gamma_C^{(1)}} \lambda_N \delta g_N(\mathbf{u})\, d\Gamma = 0 \qquad \forall\delta\mathbf{u} \\ \displaystyle\int_{\Gamma_C^{(1)}} \delta\lambda_N\, g_N(\mathbf{u})\, d\Gamma - \frac{h}{E\kappa}\int_{\Gamma_C^{(1)}} \delta\lambda_N\, (\lambda_N - p_N)\, d\Gamma = 0 \qquad \forall\delta\lambda_N \end{cases} \tag{4.20}$$

Lagrange multipliers definition. We define λ_N at each quadrature point defined for the numerical integration of surface integrals on $\Gamma_C^{(1)}$, as first proposed in [96] for imposing Dirichlet boundary conditions in 2D elasticity problems. Although the contact integrals in (4.20) are defined on $\Gamma_C^{(1)}$ its contribution affects to both bodies

in contact due to the definition of the contact gap. Therefore to evaluate the exact integral it would be necessary to create a surface segmentation matching $\Gamma_C^{(1)}$ and $\Gamma_C^{(2)}$, as in the mortar method [97]. Instead we evaluate all the integrand at the quadrature points on $\Gamma_C^{(1)}$, as proposed also in [48,94]. In exchange of committing an integration error we obtain a faster and easier to implement method. At the same time we keep the optimal convergence for linear elements with uniform refinement, because the integration error decreases linearly with mesh refinement. The convergence rate can be compromised for quadratic elements, although the singularity that arises at the end of contact area in some problems also limits the optimal convergence rate for quadratic elements [98]. To reduce the integration error in the contact integrals we propose the use of a *double pass* strategy likewise in the penalty method, i.e. the duplication of the contact integrals in (4.18) also for $\Gamma_C^{(2)}$:

$$\begin{aligned} \text{opt} \Bigg\{ \Pi_{\text{p}}(\mathbf{u}) + \int_{\Gamma_C^{(1)}} \lambda_N g_N \, d\Gamma - \frac{h}{2E\kappa} \int_{\Gamma_C^{(1)}} \left(\lambda_N - \omega p_N\right)^2 \, d\Gamma \\ + \int_{\Gamma_C^{(2)}} \lambda_N g_N \, d\Gamma - \frac{h}{2E\kappa} \int_{\Gamma_C^{(2)}} \left(\lambda_N - (1-\omega)\, p_N\right)^2 \, d\Gamma \Bigg\} \end{aligned} \tag{4.21}$$

Note that in this case a weighting factor $\omega \in [0,1]$ multiplies the stabilizing stress p_N. This is to avoid the double imposition of such term, since each integral in (4.21) contributes to both bodies in contact. We have considered $\omega = 0.5$ for the numerical examples in this thesis where the double pass strategy is followed. For the sake of simplicity all the development of the contact formulation is presented considering only the integration on $\Gamma_C^{(1)}$, but the extension to a double pass strategy is straightforward.

Now we can simplify the stabilized formulation in a similar way as [99]. We can eliminate λ_N at each integration point thanks to the concentrated numerical integration, so for a given quadrature point g we obtain the following relation from the second equation in (4.20):

$$\lambda_{N\,g} = p_{N\,g} + \frac{\kappa E}{h} g_{N\,g} \tag{4.22}$$

and substituting this relation in the first equation in (4.20) the formulation is simplified:

$$\delta\Pi(\mathbf{u}, \delta\mathbf{u}) + \delta\Pi_{C_N}(\mathbf{u}, \delta\mathbf{u}) = 0 \tag{4.23}$$

where we have stated the contact contribution to the energy functional as

$$\delta\Pi_{C_N}(\mathbf{u}, \delta\mathbf{u}) = \sum_g \left(\frac{\kappa E}{h} g_{N\,g} + p_{N\,g} \right) \cdot \delta g_{N\,g} J_g H_g \tag{4.24}$$

with H_g the weight of the integration point and J_g the Jacobian of the transformation. We have obtained a stabilized formulation of the contact problem where the only unknowns are the displacements $\mathbf{u}$, so the system of equations is smaller compared to

the classical Lagrange multipliers method. In addition, the tangent matrix remains positive definite, allowing the use of faster solver algorithms. Some advantages of our proposal with respect to Nitsche-based formulations are the existence of less integrals in the variational form (4.20) and the easiness of introducing non-linear material behavior, since there are no terms involving the derivatives of the material constitutive relation.

Problem solution. The choice of computing p_N with a post-processing of the solution implies the creation of an extra iterative loop in exchange, which eventually results in more problem resolutions. The proposed solution sequence for small displacements and deformations is shown in Algorithm 1. We call the additional iteration *augmentation loop* because of the resemblance to the Uzawa algorithm present in the augmented Lagrange formulation [59], where the Lagrange multipliers are updated with the previous iteration values. When p_N and g_N are computed, the contact active set is found by minimizing the residual of equation (4.23) in the *contact loop*.

Algorithm 1 Small displacements frictionless contact.

```
Compute p_N from previous step (3.13)
while Residual > Tol do Augmentation loop
    λ_Ng ← p_Ng + (Eκ/h) g_Ng
    while Residual > Tol do Contact loop
        Check active quadrature points: λ_Ng < 0
        Evaluate frictionless contact, δΠ_{C_N} (4.24)
        Evaluate residual of (4.23)
        Solve u
    end while
    Update p_N (3.13)
    Evaluate residual of (4.23)
end while
```

The convergence of the augmentation loop is proved in paper A. Practice has shown that usually 2-3 iterations are enough to reach an acceptable result. This process is similar to that presented in [95] and implemented in the cgFEM, thus the same augmentation loop is used to update p_N at both boundaries and no additional loops are required. Finally, during an incremental load analysis the last value of p_N is used as initial guess with a considerable reduction of necessary iterations. This can also be applied during an h-adaptive refinement analysis, where p_N can be easily projected into the new discretization mesh thanks to the hierarchical structure available in the cgFEM.

After presenting the stabilized formulation for linear elasticity and small displacements we can extend it to deal with large deformations and displacements. In this case the contact point may change as the bodies are displaced and/or deformed, thus the contact gap becomes a non-linear function of the displacements. Equation (4.23) is now solved using a Newton-Raphson method, and the linearization of both terms

with respect to the displacements is required for the solution. The new strategy is finally presented in Algorithm 2, where the main difference with respect to a small displacements problem is that the contact gap must be updated for each iteration. The details on the computation of $\Delta\delta\Pi_{C_N}$, Δg_N and $\Delta\delta g_N$ are shown in paper A.

Algorithm 2 Large displacements frictionless contact.

```
Compute p_N from previous converged step (3.13)
while Residual > Tol do Augmentation loop
    while Residual > Tol do N-R loop
        λ_N ← (κE/h) g_N + p_N
        Check active quadrature points. (λ_N < 0)
        for all Active contact points do
            Evaluate frictionless contact, Δδ Π_{C_N}
        end for
        Evaluate residual of (4.23)
        Solve Δu
    end while
    Update p_N (3.13)
    Evaluate residual of (4.23)
end while
```

This formulation has been tested through several numerical examples in papers A and B, considering small and large deformations together with linear elastic, hyperelastic and elasto-plastic material behavior. The examples have been solved using the cgFEM and also standard body fitted meshes to show the suitability for all methods. The optimal convergence rates are obtained for linear elements, whereas the error integration may affect the convergence rate for quadratic elements. However, the examples show that the double pass strategy allows to obtain acceptable results from an engineering point of view.

4.1.3. Frictional contact

The stabilized formulation proposed for Coulomb's frictional contact is derived from a modification of the augmented Lagrangian functional presented by Alart and Curnier [100] and Pietrzak and Curnier [101] written as:

$$\begin{aligned} opt \Bigg\{ \Pi(\mathbf{u}) + \frac{1}{2\kappa_1} \int_{\Gamma_C^{(1)}} \left(\left[\boldsymbol{\lambda} \cdot \mathbf{n}^{(1)} + \kappa_1 g_N \right]_-^2 - \|\boldsymbol{\lambda}\|^2 \right) \, d\Gamma + \\ + \frac{1}{2\kappa_1} \int_{\Gamma_C^{(1)}} \| P_{B(n,s)} \left(\boldsymbol{\lambda} - \kappa_1 \dot{\mathbf{g}} \, dt \right) \|^2 \, d\Gamma \Bigg\} \end{aligned} \tag{4.25}$$

where we have used the projection operator $P_{B(n,s)}$ presented in section 3.1 and the negative part operator, defined as:

$$[x]_- = \begin{cases} -x & if \quad x \leq 0 \\ \\ 0 & if \quad x > 0 \end{cases} \tag{4.26}$$

The procedure followed in paper B, similar to [64], is as follows. First, a stabilization term is introduced in the weak form (4.25):

$$\begin{aligned} opt \Bigg\{ \Pi(\mathbf{u}) + \frac{1}{2\kappa_1} \int_{\Gamma_C^{(1)}} \left(\left[\boldsymbol{\lambda} \cdot \mathbf{n}^{(1)} + \kappa_1 g_N \right]_-^2 - \|\boldsymbol{\lambda}\|^2 \right) d\Gamma + \\ + \frac{1}{2\kappa_1} \int_{\Gamma_C^{(1)}} \| P_{B(n,s)} \left(\boldsymbol{\lambda} - \kappa_1 \Delta^t \mathbf{g} \right) \|^2 \, d\Gamma - \frac{1}{2\kappa_2} \int_{\Gamma_C^{(1)}} \| \boldsymbol{\lambda} - \mathbf{S}^* \|^2 d\Gamma \Bigg\} \end{aligned} \tag{4.27}$$

The additional term (the last in (4.27)) is similar to that in (4.18), but now we consider the recovered traction vector, $\mathbf{S}^* = \mathbf{n} \cdot \boldsymbol{\sigma}^*$, instead of the normal pressure. A weak form in (4.25) is derived and then the friction limit s is substituted by $\mu \left[\lambda_N + \kappa_1 g_N \right]_-$ to consider a Coulomb model. The final variational form of the problem is written as follows:

$$\begin{cases} \delta\Pi(\mathbf{u}, \delta\mathbf{u}) - \displaystyle\int_{\Gamma_C^{(1)}} \left(\left[\boldsymbol{\lambda} \cdot \mathbf{n}^{(1)} + \kappa_1 g_N \right]_- \delta g_N + P_B \left(\boldsymbol{\lambda} - \kappa_1 \Delta^t \mathbf{g} \right) \delta \mathbf{g} \right) d\Gamma = 0, \ \forall \delta \mathbf{u} \\ \\ -\frac{1}{\kappa_1} \displaystyle\int_{\Gamma_C^{(1)}} \left(\left[\boldsymbol{\lambda} \cdot \mathbf{n}^{(1)} + \kappa_1 g_N \right]_- \mathbf{n}^{(1)} + \boldsymbol{\lambda} - P_B \left(\boldsymbol{\lambda} - \kappa_1 \Delta^t \mathbf{g} \right) \right) \delta \boldsymbol{\lambda} \, d\Gamma \\ \\ -\frac{1}{\kappa_2} \displaystyle\int_{\Gamma_C^{(1)}} \left(\boldsymbol{\lambda} - \mathbf{S}^* \right) \delta \boldsymbol{\lambda} \, d\Gamma = 0, \ \forall \delta \boldsymbol{\lambda} \end{cases} \tag{4.28}$$

where the subindices of the operator P_B have been omitted for simplicity. Paper B proved that, for the case of frictionless contact, the variations (4.20) and (4.28) are equivalent. The Lagrange multipliers are condensed at each integration point as in (4.22) with the correspondence $\kappa = \kappa_1 + \kappa_2$.

The Lagrange multipliers can also be eliminated for the frictional case using the second equation in (4.28), however the procedure is more complex. First, we will assume a *stick* state, so the projection operator takes the value $P_B = \mathbf{T}_n \left(\boldsymbol{\lambda} - \kappa_1 \Delta^t \mathbf{g} \right)$ and the second equation in (4.28) is now written as:

$$-\frac{1}{\kappa_1} \left(\left[\boldsymbol{\lambda} \cdot \mathbf{n}^{(1)} + \kappa_1 g_N \right]_- \mathbf{n}^{(1)} + \boldsymbol{\lambda} - \mathbf{T}_n \left(\boldsymbol{\lambda} - \kappa_1 \Delta^t \mathbf{g} \right) \right) - \frac{1}{\kappa_2} \left(\boldsymbol{\lambda} - \mathbf{S}^* \right) = 0 \tag{4.29}$$

We can simplify (4.29) considering that $\boldsymbol{\lambda} = \left(\boldsymbol{\lambda}\cdot\mathbf{n}^{(1)}\right)\mathbf{n}^{(1)} + \mathbf{T}_n\boldsymbol{\lambda}$. Finally the multipliers can be condensed at each quadrature point denoted by the subindex g:

$$\boldsymbol{\lambda}_g = \mathbf{S}^*_g + \kappa_2\left(g_{N\,g}\mathbf{n}^{(1)} - \mathbf{T}_n\Delta^t\mathbf{g}_g\right) \tag{4.30}$$

and then substituting the multipliers in the first equation in (4.28) we obtain the contact contribution for the *stick* state:

$$\delta\Pi_{C_{St}}(\mathbf{u},\delta\mathbf{u}) = \sum_g\left(\frac{\kappa E}{h}\mathbf{g}_g + \mathbf{S}^*{}_g\right)\cdot\delta\mathbf{g}_g\,|J_g|\,H_g \tag{4.31}$$

Now we will eliminate the Lagrange multipliers for the *sliding* case. Replacing the operator P_B with the corresponding value, the second equation in (4.28) is now:

$$\begin{aligned}&-\tfrac{1}{\kappa_1}\left(\left[\boldsymbol{\lambda}\cdot\mathbf{n}^{(1)} + \kappa_1 g_N\right]_-\mathbf{n}^{(1)} + \boldsymbol{\lambda} + \mu\left(p_N + \tfrac{\kappa E}{h}g_N\right)\tfrac{\mathbf{T}_n\left(\boldsymbol{\lambda}-\kappa_1\Delta^t\mathbf{g}\right)}{\|\mathbf{T}_n\left(\boldsymbol{\lambda}-\kappa_1\Delta^t\mathbf{g}\right)\|}\right)\\ &\qquad -\tfrac{1}{\kappa_2}\left(\boldsymbol{\lambda}-\mathbf{S}^*\right) = 0\end{aligned} \tag{4.32}$$

We can now project (4.32) into $\mathbf{n}^{(1)}$ and $\mathbf{T}_n$ to account for the normal and tangential components respectively. The projection on $\mathbf{n}^{(1)}$ leads to the same equation discussed in the frictional formulation, and leads to the condensation of λ_N in (4.22). The projection of (4.32) on $\mathbf{T}_n$ yields the condition that forces $\mathbf{T}_n\boldsymbol{\lambda}$ to have the same direction as the relative sliding vector $\mathbf{T}_n\Delta^t\mathbf{g}$ in the first equation in (4.28). Therefore, we choose the stabilizing pressure $\mathbf{p}_T = \mathbf{T}_n\cdot\mathbf{S}^*$ in the direction of $\mathbf{T}_n\Delta^t\mathbf{g}$, and the following substitution is made:

$$\mathbf{T}_n\boldsymbol{\lambda} = \kappa_2\mathbf{T}_n\Delta^t\mathbf{g} + \mathbf{p}_T \tag{4.33}$$

This choice also ensures that the transition between *stick* and *slip* is continuous. This can be verified by comparing both sets of multipliers at the friction limit, where the sum of equations (4.33) and (4.22) is equivalent to (4.30). Now the same procedure is used to obtain the contact contribution for the sliding case:

$$\delta\Pi_{C_{Sl}}(\mathbf{u},\delta\mathbf{u}) = \sum_g\left[\left(\frac{\kappa E}{h}g_N + p_N\right)\delta g_N - \mu\left(\frac{\kappa E}{h}g_N + p_N\right)\Delta^t\mathbf{g}_t\cdot\delta\mathbf{g}\right]|J_g|\,H_g \tag{4.34}$$

where the following simplification has been included:

$$\Delta^t\mathbf{g}_t = \frac{\mathbf{p}_T - \frac{\kappa E}{h}\mathbf{T}_n\Delta^t\mathbf{g}}{\|\mathbf{p}_T - \frac{\kappa E}{h}\mathbf{T}_n\Delta^t\mathbf{g}\|} \tag{4.35}$$

Problem solution. The equation to solve can be written as in (4.23), replacing $\delta\Pi_{C_N}$ by $\delta\Pi_{C_{St}}$ or $\delta\Pi_{C_{St}}$ depending on the contact status of each quadrature point. The solution procedure can be obtained by including some features in Algorithm 2. First, at the beginning of each time step, in addition to projecting the values of p_N and $\mathbf{p}_T$ from the previous converged step, all points with an active contact condition are set to *stick*, and their convective coordinates from the previous step $\boldsymbol{\Theta}_t$ are saved. Then, for each iteration in the N-R loop the contact status is evaluated at each quadrature point. If sliding happens, the relative displacement $\Delta^t\mathbf{g}_t$ is evaluated using $\boldsymbol{\Theta}_t$. The details of the linearizations $\Delta\delta\Pi_{C_{Stick}}$ and $\Delta\delta\Pi_{C_{Slip}}$ are provided in paper B, and the final solution procedure is shown in Algorithm 3.

Algorithm 3 Large displacements frictional contact.

```
Compute p_N and p_T from previous converged step (3.13)
Set all previous contact points to stick state.
Θ_t ← Θ (from previous step)
while Residual > Tol do Augmentation loop
    while Residual > Tol do N-R loop
        λ_N ← (κE/h) g_N + p_N
        Check active quadrature points. (λ_N < 0)
        for all Active stick points do
            λ_T ← T_n ( (κE/h) g + S* )
            if ||λ_T|| ≥ μ |λ_N| then
                Change status to Slip
            else
                Evaluate stick contact, Δδ Π_{C_St}
            end if
        end for
        for all Active slip points do
            Evaluate Δ^t g_t
            Evaluate slip contact, Δδ Π_{C_Sl}
        end for
        Evaluate residual of (4.23)
        Solve Δu
    end while
    Update p_N and p_T (3.13)
    Evaluate residual of (4.23)
end while
```

We have obtained a stabilized formulation for frictional contact able to deal with immersed boundary methods. The numerical examples in paper B show that the method provides optimal convergence rates, and smooth transitions between adhesion and sliding contact. A numerical result from paper B is reproduced here to show the performance of the method. This example features the sliding contact between a hyperelastic squared block and a sphere, the last having a higher stiffness. This is

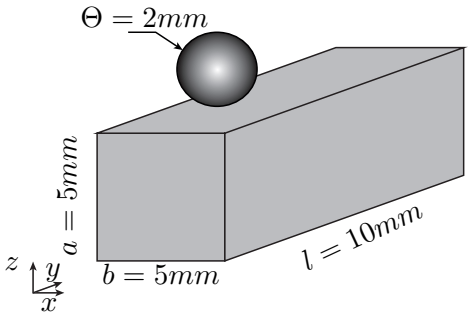

(a) Scheme of the ironing problem.

E_{Slab}	100 (GPa)
ν_{Slab}	0.3
E_{Sphere}	1000 (GPa)
ν_{Sphere}	0.3
Δu_z	-0.3 (mm)
Δu_y	5 (mm)
μ	0.3

(b) Parameter data

Figure 4.3: *Frictional contact example. Ironing problem.*

known in the research community as an *ironing problem*. The dimensions, material parameters and imposed displacements are shown in Figure 4.3.

The problem was solved using cgFEM with three different discretizations. Two uniform coarse meshes with element size $h = 0.675\,mm$ for the block and $h = 0.265\,mm$ for the sphere were created with 8-nodes linear $\mathscr{H}_8$ and 20-nodes quadratic $\mathscr{H}_{20}$ elements. Then, starting from the uniform $\mathscr{H}_{20}$ mesh, one element subdivision was performed at the block's contact surface, so the new discretization at that area is of size $h = 0.3375\,mm$. The same problem was also solved using ANSYS® with two different discretizations: the first, similar to the coarse mesh in cgFEM, and an *overkilled* mesh which serves as a reference, both with $\mathscr{H}_{20}$ elements. The results in Figure 4.4 show that the reaction forces obtained with cgFEM tend to the reference values, and for coarse discretizations the oscillations of the forces (which have a length equal to the mesh size) are lower. This level of accuracy is achieved because, despite the low resolution of the discretization mesh, the exact geometry is taken into account in the numerical integration in cgFEM. The inclusion of the exact geometry in the kinematic variables is analyzed in the following section.

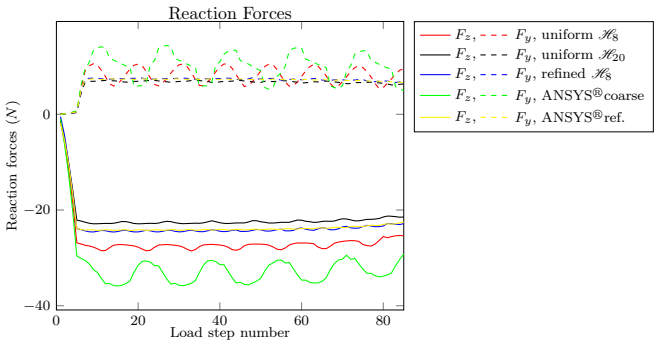

Figure 4.4: *Ironing problem. Reaction forces on the lower face of the block.*

4.2. Surface definition in cgFEM

This section summarizes the study presented in paper C, where the definition of the contact surface is analyzed. Section 4.1.1 defined the contact gap, sliding vector and their variations, leaving the definition of the position of a point $\mathbf{x} \in \Gamma_C$ open. In standard isoparametric FE formulations the same discretization is used for both the solution and the analysis domain. This means that, for linear FE interpolations the contact surface is discretized using linear facets (usually triangles or quadrilaterals). A linear discretization of the contact surface implies that the normal vector field is C^0 continuous, which may cause issues in the measurement of the contact gap, influences the convergence of the search algorithms (closest projection, ray-tracing) and eventually compromises the robustness of the contact formulation. A proof of that is the wide range of alternatives to obtain a smooth normal field, e.g. using interpolations with Hermite polynomials [76], Bezier splines [77, 78], NURBS [79], Gregory patches [81], Nagata patches [80] and enrichement functions based on the isogeometric analysis [83, 84].

The numerical integration procedure at the boundary elements in cgFEM allows to account for the exact CAD definition by means of NURBS surfaces, as presented in section 3.2.1. Therefore, in this framework, the discretization of the solution and the contact surface are decoupled in a natural way, so, the position of a point on the contact surface is defined as a combination of the NURBS transformation $\mathbf{Q}(\xi, \eta)$ (equation (3.11) in section 3.2.1) and the FE interpolation of the solution:

$$\mathbf{x} = \mathbf{Q}(\xi, \eta) + \mathbf{N}(\boldsymbol{\zeta}^e)\,\mathbf{u}, \qquad \mathbf{x} \in \Gamma_c \tag{4.36}$$

Note that the decoupling of the discretization comes with two different local coordinate systems: the convective coordinates of the surface (ξ, η) and the parametric coordinates of the reference element $\boldsymbol{\zeta}^e$. The three different coordinate systems that are present in equation (4.36) are put together in a 2D simplification in Figure 4.5 with the generic transformation $\mathbf{B}(\boldsymbol{\Theta})$ (which corresponds to $\mathbf{Q}(\xi, \eta)$ if the NURBS is considered). The only ingredient missing in that Figure is the backward mapping from the reference configuration $\mathbf{X} = \mathbf{Q}(\xi, \eta)$ to the reference hexaedron element $\square : [-1, 1]^3$. Thanks to the structured mesh in the cgFEM this mapping is the affine transformation:

$$\boldsymbol{\zeta}^e = \frac{\mathbf{Q}(\xi, \eta) - \mathbf{X}_e}{h/2} \tag{4.37}$$

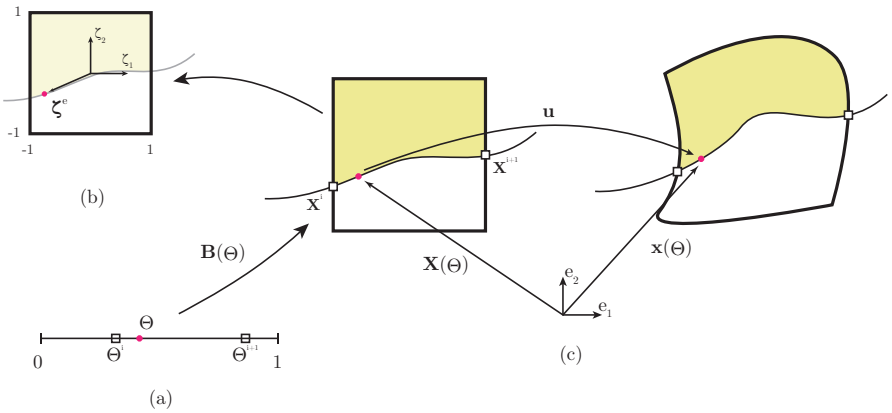

Figure 4.5: *Convective to local coordinates transformation. A point located at* $\boldsymbol{\Theta}$ *in the surface parametric space (a) is mapped to the reference configuration* $\boldsymbol{X}(\boldsymbol{\Theta})$ *on the global coordinates system (c) and then to the local element space (b) with coordinates* $\boldsymbol{\zeta}^e$*.*

The variation and the linearization of the contact kinematic variables make use of the partial derivatives of the position vector in (4.36), which are computed as:

$$\begin{aligned}
\mathbf{x}_{,u} &= \mathbf{N}\left(\boldsymbol{\zeta}^e\right) \\
\mathbf{x}_{,\xi} &= \mathbf{Q}_{,\xi}\left(\xi,\eta\right) + \mathbf{N}_{,\boldsymbol{\zeta}^e}\left(\boldsymbol{\zeta}^e\right)\frac{\partial \boldsymbol{\zeta}^e}{\partial \xi}\mathbf{u} \\
\mathbf{x}_{,u,\xi} &= \mathbf{N}_{,\boldsymbol{\zeta}^e}\left(\boldsymbol{\zeta}^e\right)\frac{\partial \boldsymbol{\zeta}^e}{\partial \xi} \\
\mathbf{x}_{,\xi,\xi} &= \mathbf{Q}_{,\xi,\xi}\left(\xi,\eta\right) + \mathbf{N}_{,\boldsymbol{\zeta}^e,\boldsymbol{\zeta}^e}\left(\boldsymbol{\zeta}^e\right)\frac{\partial \boldsymbol{\zeta}^e}{\partial \xi}\frac{\partial \boldsymbol{\zeta}^e}{\partial \xi}\mathbf{u} + \mathbf{N}_{,\boldsymbol{\zeta}^e}\left(\boldsymbol{\zeta}^e\right)\frac{\partial^2 \boldsymbol{\zeta}^e}{\partial \xi^2}\mathbf{u}
\end{aligned} \tag{4.38}$$

To complete the definitions in (4.38) we take derivatives in (4.37) with respect the convective coordinates:

$$\frac{\partial \boldsymbol{\zeta}^e}{\partial \xi} = \frac{2}{h}\mathbf{Q}_{,\xi}; \qquad \frac{\partial \boldsymbol{\zeta}^e}{\partial \eta} = \frac{2}{h}\mathbf{Q}_{,\eta} \tag{4.39}$$

and the partial derivatives of the NURBS transformation are obtained by differentiating equation (3.11):

$$\mathbf{Q}_{,\xi} = \frac{\partial \mathbf{S}\left(\xi,\eta\right)}{\partial \xi}\mathbf{P}; \qquad \mathbf{Q}_{,\eta} = \frac{\partial \mathbf{S}\left(\xi,\eta\right)}{\partial \eta}\mathbf{P} \tag{4.40}$$

The numerical experiments in paper C proved that the inclusion of the NURBS in the position definition has a considerable impact on the accuracy of the solution, specially in problems involving curved surfaces with small penetration (when the resulting stress is mainly due to the initial gap). The improved accuracy comes at the cost of an increased computational cost, since the terms in equations (4.36), (4.38) and the ray-tracing problem in (4.1) require more calculations than the use of linear contact facets. In paper C we explore an alternative approach in which a NURBS

surface is fitted to the solution of the contact problem $\mathbf{u}$ minimizing the following function:

$$\min \left[\frac{1}{2} \int_{\Gamma_C} \left(\mathbf{S}\left(\xi,\eta\right) \mathbf{V} - \mathbf{N}(\boldsymbol{\zeta}^e)\mathbf{u} \right)^2 d\xi d\eta \right] \tag{4.41}$$

where the $\mathbf{S}\left(\xi,\eta\right)$ are the NURBS basis functions used to define Γ_C (equation (3.11)) and $\mathbf{V}$ are the unknown displacements of the NURBS control points $\mathbf{P}$ from equation. Using the surface quadrature rules of cgFEM, the solution of problem (4.41) is written as:

$$\mathbf{V} = \mathbf{M}^{-1}\mathbf{G}\mathbf{u} \tag{4.42}$$

$$\mathbf{M} = \sum_i \mathbf{S}\left(\xi,\eta\right)_i^T \mathbf{S}\left(\xi,\eta\right)_i \left|\mathbf{J}\right|_i H_i \; ; \qquad \mathbf{G} = \sum_i \mathbf{S}\left(\xi,\eta\right)_i^T \mathbf{N}(\boldsymbol{\zeta}_i^e) \left|\mathbf{J}\right|_i H_i \tag{4.43}$$

We can rewrite the displacements of the control points as $\mathbf{V} = \mathbf{C}\mathbf{u}$, where the transformation $\mathbf{C} = \mathbf{M}^{-1}\mathbf{G}$ is independent of the solution, thus it can be precomputed for each NURBS surface in Γ_C. Using this approach the position vector and its partial derivatives are written as follows:

$$\begin{aligned}
&\mathbf{x} = \mathbf{S}\left(\xi,\eta\right)\left(\mathbf{P}+\mathbf{V}\right) = \mathbf{S}\left(\xi,\eta\right)\left(\mathbf{P}+\mathbf{C}\mathbf{u}\right), \qquad \mathbf{x} \in \Gamma_c \\
&\mathbf{x}_{,u} = \mathbf{S}\left(\xi,\eta\right)\mathbf{C} \\
&\mathbf{x}_{,\xi} = \mathbf{S}_{,\xi}\left(\xi,\eta\right)\left(\mathbf{P}+\mathbf{C}\mathbf{u}\right) \\
&\mathbf{x}_{,u,\xi} = \mathbf{S}_{,\xi}\left(\xi,\eta\right)\mathbf{C} \\
&\mathbf{x}_{,\xi,\xi} = \mathbf{S}_{,\xi,\xi}\left(\xi,\eta\right)\left(\mathbf{P}+\mathbf{C}\mathbf{u}\right)
\end{aligned} \tag{4.44}$$

With this approach the computation of the gap and the ray tracing algorithm are simplified, since it only involves evaluations of a single NURBS surface and its derivatives. It is worth to remark that although the position vector on the boundary is in this case completely defined using NURBS basis we have not included the NURBS control points as unknowns of the problem, and the standard FE interpolation is kept inside the domain.

With the last proposed approach the computational cost is associated with the transformation $\mathbf{C}$, which is a full matrix that couples the degrees of freedom of the elements cut by the contact surface and the control points of the NURBS defining it. Therefore, this approach only represents an advantage with respect to the combination of NURBS and FE interpolation in (4.36) if the size of $\mathbf{C}$ is small, this is, if the size of the mesh elements and the NURBS are similar.

4.3. Towards robust, efficient solvers for non-linear problems based in cgFEM

The last two contributions of this thesis have been developed in the context of the second objective (section 1.2), which is the enhancement of the robustness and efficiency of the cgFEM methodology. We have focused in two different aspects: the reduction of the ill-conditioning of the system to solve in cgFEM and the assessment of the finite element error in contact problems. These contributions are presented in sections 4.3.1 (paper D) and 4.3.2 (paper E) respectively.

4.3.1. Control of the system ill-conditioning through a displacement-based stabilization

The stabilization terms included in cgFEM at the contact formulation in paper A and in the imposition of Dirichlet boundary conditions [95] guarantee the finite element solution's convergence. However, the solution of the system of equations might be compromised due to ill-conditioning problems. An example of a problematical situation, common to all immersed boundary methods, is shown in Figure 4.6a. If there are elements with a very small cut of the geometry inside (like that on the right in Figure 4.6a) there will be nodes with a negligible associated stiffness, i.e. the displacements at those so-called *pathological* nodes become unbounded.

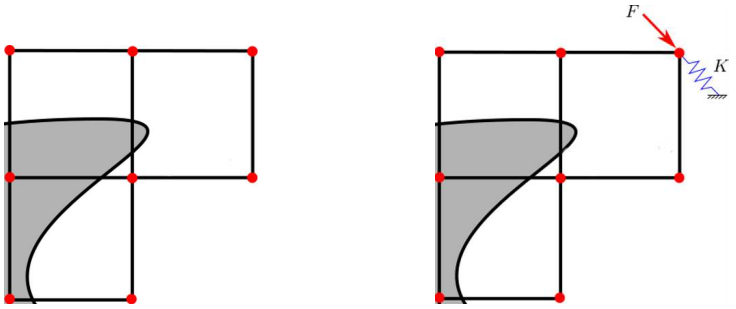

(a) *Ill-conditioning issue due to mesh-geometry intersection.*

(b) *Effect of the additional term.*

Figure 4.6: *Example of ill-conditioning problems due to small cuts of the geometry.*

This issue was already detected in [102], which introduced the *ghost penalty* stabilizing term. However, that penalty term required to build an L_2 projection of the solution in a patch of elements in Ω to a polynomial expansion, which is not common in FE. The aggregated unfitted finite element method [26] proposes the modification

of the Cartesian structure by building *aggregates* to add stiffness at the pathological nodes. In paper D we present a stabilization procedure using common FE procedures without modifying the Cartesian structure. The proposed technique consists in adding a term to the potential energy functional $\Pi_{\mathrm{p}}(\mathbf{u})$ as follows:

$$\Pi_{\mathrm{p}}(\mathbf{u}) - \frac{\alpha E}{h^2} \int_{\hat{\Omega}^h} (\mathbf{u} - \mathbf{u}^*)^2 \; d\Omega \tag{4.45}$$

where $\hat{\Omega}^h$ comprises all the elements in Ω^h containing at least one pathological node. The similarity of this term with that introduced in (4.18) is clear and, now, the penalty term features the user defined parameter $\alpha > 0$. Roughly speaking, the new term in (4.45) adds an artificial stiffness and force that are compensated in the solution and restrict the unbounded displacement at the pathological nodes.

Having stated the additional term we proceed in the same manner as in the Dirichlet boundary or contact stabilization procedures to obtain the problem to be solved: the field $\mathbf{u}^*$ is considered independent of the solution and is obtained with a displacement recovery, which is nothing but solving the minimization problem of the SPR technique (3.14) replacing $\boldsymbol{\sigma}^*$ by $\mathbf{u}^*$ and $\boldsymbol{\sigma}^h$ by $\mathbf{u}^h$. Note that in this case $\mathbf{u}^*$ is directly obtained as the solution of (3.14) and there is no need to apply the conjoint polynomials enhancement (3.17), since the stabilization term in (4.45) only makes use of the nodal values. Moreover, the stabilizing term can be constructed as a lumped mass, which is a highly efficient procedure, and the computation of $\mathbf{u}^*$ is carried out in the same augmentation loop presented in the previous solution algorithms. The work in paper D provides the following proofs: the new stabilizing term (i) does not affect the convergence of the FE solution, (ii) neither the Richardson iteration (augmentation loop) and (iii) the condition number grows with h^{-2}, which is the rate of body-fitted FE formulations.

Numerical example. The contribution in paper D has been developed for the elasticity problem and can be applied to contact problems without loss of generality, as in the case of the following numerical example. Figure 4.7 shows two toroidal volumes with major radius $R = 1.5\,cm$ and minor radius $r = 0.5\,cm$ that are becoming in contact. A constant displacement of $0.05\,cm$ is enforced on the orange colored surfaces. The blue surfaces have all displacements constrained. The material properties considered in this example are $E = 115\,GPa, \nu = 0.3$ and a Coulomb friction coefficient $\mu = 1$. Two different discretizations are considered, with uniform meshes of size $h = [0.255, 0.1275]\;cm$ respectively. For each mesh two analysis are performed, one with the addition of the displacement-based stabilization term and another one without it. The resulting condition number of the system is shown in Table 4.1. It is clear that the omission of the displacement-based stabilization would make the method unable to solve fine meshes, as the condition number scales dramatically with the mesh refinement.

The displacement-based stabilization completes, together with the Dirichlet and contact boundary stabilization, the set of analytical tools for a robust solver of the

contact problem in the cgFEM. All three terms are built with the same philosophy, the use of recovery techniques and an iteration procedure to update the recovered fields. It is worth to remark that, although using a single augmentation loop to update all terms, the consideration of a global convergence criterion of that loop may lead to some issues from a numerical point of view, i.e. some of the stabilizing terms may have not converged yet, because its contribution to the global residual is small. This issue has been addressed in this thesis by tuning the convergence criteria. The development of a generalized procedure to establish the criteria for the numerical convergence of all stabilization terms is left as a future work.

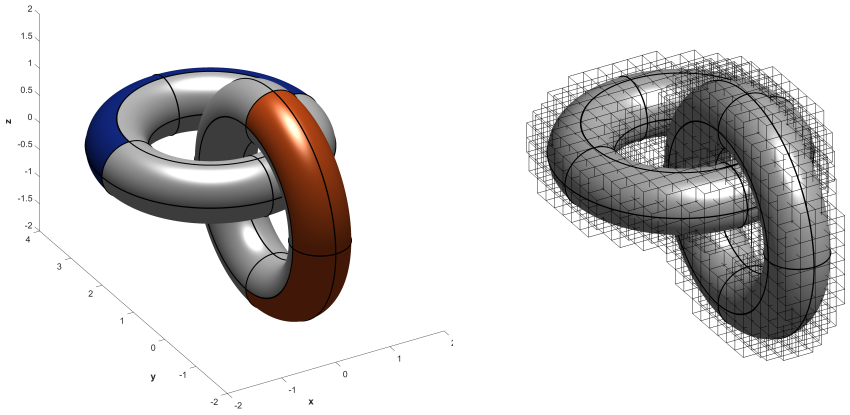

Figure 4.7: *Analysis of the condition number in a contact problem between toroidal volumes. Lengths in cm. (a) Problem definition. Surfaces in blue are clamped, and a constant displacement $u_y = -0.05cm$ is applied on the orange surfaces. (b) Discretization of the first analysis, uniform grid with $h = 0.255cm$.*

DOF	Without stabilization	With stabilization
6840	1.12×10^{13}	1.57×10^{5}
37872	4.86×10^{27}	3.06×10^{5}

Table 4.1: *Condition number of the system matrix for the contact problem between toroidal volumes.*

4.3.2. Improvement of the recovered stress field for contact problems

Adaptivity is an essential ingredient towards an efficient FE methodology. An optimal distribution of the degrees of freedom along the analysis domain, using *h*-, *p*- or *hp*-adaptivity, allows to have an increased accuracy with a reduced computational cost. Taking into account the hierarchical Cartesian structure in cgFEM, the implementation of *h*-adaptive refinement strategies seems the most convenient choice. Section 3.2.2 presented the tools currently available in cgFEM to guide the adaptive refinement [44], which are the ZZ-estimator [39] and the superconvergent patch recovery [42]. An interesting idea to improve this technique (and consequently the error estimator's accuracy) is to obtain a recovered field that satisfies the equilibrium equations. The contribution in this thesis is inspired by the SPR-C technique (SPR with constrains) [43], in which the internal, Neumann boundary equilibrium and compatibility equations were introduced as additional constrains to the SPR minimization problem. In paper E we present a modification of the SPR-C technique in which the traction equilibrium along the contact boundary is enforced.

The superconvergent patch recovery with constrains (SPR-C). Recalling the integral version of the SPR presented in section 3.2.2, the minimization problem (3.14) is modified into the following:

$$\min \left[\int_{\Omega_p^k} \left(\boldsymbol{\sigma}^{*,k} - \boldsymbol{\sigma}^h \right)^2 d\Omega \right] \qquad \text{subject to } \mathbf{C}\mathbf{A}^k = \boldsymbol{\Lambda} \tag{4.46}$$

Two differences are observed in this re-formulation of the SPR problem: (i) the minimization problem has now additional constrains, which contain known information that the stress field satisfies in the exact solution, like the internal equilibrium or the boundary equilibrium; and (ii) due to the nature of these constrains, all the components of the stress tensor $\{\sigma_1^{*,k}, ..., \sigma_6^{*,k}\}$ must be solved at once. This is addressed with the following compact definitions of recovered stress field:

$$\boldsymbol{\sigma}^{*,k}(\mathbf{x}) = \mathbf{P}(\mathbf{x})\mathbf{A}^k \tag{4.47}$$

$$\mathbf{P}(\mathbf{x}) = diag\left(\mathbf{p}(\mathbf{x}), ..., \mathbf{p}(\mathbf{x})\right) \ ; \qquad \mathbf{A}_k = \left\{\mathbf{a}_1^k, ..., \mathbf{a}_6^k\right\} \tag{4.48}$$

We have to identify the terms $\{\mathbf{C}, \boldsymbol{\Lambda}\}$ introduced in (4.46) to enforce the additional constrains. The constraint equations are obtained from the elasticity problem defined in Chapter 3.1, particularly the first and last equations in (3.2). The internal equilibrium equation is written as $\nabla\boldsymbol{\sigma} + \mathbf{b} = 0$, where $\mathbf{b}$ are the volume forces.

Taking into account the definition (4.47) and identifying terms we have the following constraint equation:

$$\nabla \cdot \mathbf{P}(\mathbf{x})\ \mathbf{A}^k = -\mathbf{b}(\mathbf{x}) \qquad \Rightarrow \qquad \mathbf{C}^{iee} = \nabla \cdot \mathbf{P}(\mathbf{x})\ ; \qquad \mathbf{\Lambda}^{iee} = -\mathbf{b}(\mathbf{x}); \qquad \mathbf{x} \in \Omega_p^k \tag{4.49}$$

Now, the same procedure is followed for the boundary equilibrium, which is written as $\mathbf{n} \cdot \boldsymbol{\sigma} = \hat{\mathbf{t}}$ in the elasticity problem, with the external traction vector $\hat{\mathbf{t}}$. The constraint equation in this case is written as:

$$\mathbf{R}(\mathbf{x})\mathbf{P}(\mathbf{x})\ \mathbf{A}^k - \hat{\mathbf{t}}(\mathbf{x}) = \mathbf{0} \qquad \Rightarrow \qquad \mathbf{C}^{ext} = \mathbf{R}(\mathbf{x})\mathbf{P}(\mathbf{x})\ ; \qquad \mathbf{\Lambda}^{ext} = \hat{\mathbf{t}}(\mathbf{x}); \qquad \mathbf{x} \in \Gamma_p^k \tag{4.50}$$

where we have included the operator $\mathbf{R}(\mathbf{x})$ which uses the normal $\mathbf{n}$ to transform the vector $\mathbf{P}(\mathbf{x})\ \mathbf{A}^k$ that contains the six stress tensor components into the traction vector $\mathbf{t}$. The constraint (4.49) is applied to all SPR patches in the mesh. However, the boundary constraint (4.50) is only enforced at those *boundary patches* that are cut by Γ_N.

Note that the polynomial field $\boldsymbol{\sigma}^{*,k}$ cannot fulfill the introduced constrains for all $\mathbf{x} \in \Omega_p^k$ in a general case. For example, a polynomial definition of degree p can only satisfy the internal equilibrium equation for volume forces defined as polynomials of degree $p-1$. Moreover, the boundary equilibrium cannot be satisfied even for constant enforced traction if the loaded surfaces are arbitrarily curved. In paper E we propose the weak enforcement of the constrains by using a pseudoinverse approach. The procedure is explained here for the boundary equilibrium and is likewise applied to the internal equilibrium constrain. The equation (4.50) is written for every surface quadrature point, so $\mathbf{C}^{ext}$ and $\mathbf{\Lambda}^{ext}$ become a matrix and a column vector respectively. The combination of linearly independent columns of that matrix (denoted by $\mathbf{C}^{*ext'}$) is extracted, and the set of constraint equations is obtained as:

$$\mathbf{C}^{*ext'}\mathbf{C}^{ext}\mathbf{A}_k = \mathbf{C}^{*ext'}\mathbf{\Lambda}^{ext} \tag{4.51}$$

Now applying the Lagrange multiplier method to solve (4.46) we obtain the following system in matrix form:

$$\begin{bmatrix} \mathbf{M} & \mathbf{C}^T \\ \mathbf{C} & \mathbf{0} \end{bmatrix} \begin{Bmatrix} \mathbf{A}^k \\ \boldsymbol{\lambda} \end{Bmatrix} = \begin{Bmatrix} \mathbf{H} \\ \mathbf{\Lambda} \end{Bmatrix} \tag{4.52}$$

where the $\mathbf{M}$ and $\mathbf{H}$ are built by concatenating the terms $\mathbf{M}_i$ (in a block diagonal) and $\mathbf{H}_i$ defined in (3.15), and the constraint terms $\{\mathbf{C}, \mathbf{\Lambda}\}$ are built by concatenation of the considered constrains. For instance, for the case of a boundary patch intersected by Γ_N the constrains are written as:

$$\mathbf{C} = \begin{Bmatrix} \mathbf{C}^{*iee'}\mathbf{C}^{iee} \\ \mathbf{C}^{*ext'}\mathbf{C}^{ext} \end{Bmatrix}\ ; \qquad \mathbf{\Lambda} = \begin{Bmatrix} \mathbf{C}^{*iee'}\mathbf{\Lambda}^{iee} \\ \mathbf{C}^{*ext'}\mathbf{\Lambda}^{ext} \end{Bmatrix} \tag{4.53}$$

SPR-C for contact problems. In the case of solving contact problems we can include an additional condition that the stress field satisfies in the exact solution, this is, the continuity of tractions along the contact surface. Let Γ_C be the contact surface in the exact solution, then for a point $\mathbf{x} \in \Gamma_C$ the contact equilibrium is written as:

$$\mathbf{t}^{(1)}(\mathbf{x}) + \mathbf{t}^{(2)}(\mathbf{x}) = \mathbf{0} \ , \qquad \forall \mathbf{x} \in \Gamma_C^{(i)d} \tag{4.54}$$

where $\mathbf{t}^{(1)}, \mathbf{t}^{(2)}$ are the traction vectors of the recovered field $\boldsymbol{\sigma}^*$, and are written as:

$$\mathbf{t}^{(i)}(\mathbf{x}) = \mathbf{R}^{(i)}(\mathbf{x})\boldsymbol{\sigma}^{*,(i)}(\mathbf{x}) = \mathbf{R}^{(i)}(\mathbf{x})\mathbf{P}^{(i)}(\mathbf{x})\ \mathbf{A}^{(i)} \tag{4.55}$$

so the additional constrain for contact problems is defined as:

$$\mathbf{R}^{(1)}(\mathbf{x})\mathbf{P}^{(1)}(\mathbf{x})\ \mathbf{A}^{(1)} + \mathbf{R}^{(2)}(\mathbf{x})\mathbf{P}^{(2)}(\mathbf{x})\ \mathbf{A}^{(2)} = \mathbf{0} \tag{4.56}$$

The main difference with respect to the previously presented constrains is that this constrain relates the recovered fields of both bodies. However, it is impossible to establish a unique correspondence between nodes of both bodies in contact in the framework of non-matching immersed boundary meshes. Instead, we propose the solution of the SPR-C problem for each body in contact as follows: let's assume that we are solving the SPR-C problem at node k of the so-called *main body* (in this example $\Omega_p^k \in \Omega^{(1)}$). Then we build a subdomain $\Omega_p^{aux} \in \Omega^{(2)}$ in the *auxiliary body* following the procedure depicted in Figure 4.8. First, we define the contact area at the main body as a convex polygon containing all active contact points in $\Gamma_C \cap \Omega_p^k$, and a projection direction is computed with the weighted average of the normal vectors of all those quadrature points with an active contact condition. Then the contact area is projected towards the interior of the auxiliary body and the auxiliary region Ω_p^{aux} is built with the boundary elements in $\Omega^{(2)}$ that lay inside that projection.

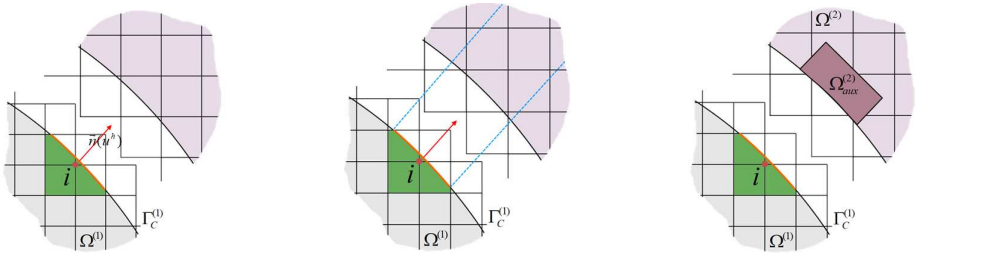

(a) *SPR patch with active contact condition. The contact area is depicted in red.*

(b) *Projection of the contact area towards the auxiliary body.*

(c) *The boundary elements inside the projection define the auxiliary domain.*

Figure 4.8: *Definition of the auxiliary domain $\Omega\star$.*

Once the auxiliary domain Ω_p^{aux} is created we build another SPR-C problem related to that region, with the unknown coefficients $\mathbf{A}^{(2)aux}$. Note that the solution

of the SPR-C problem at the auxiliary body is not related to any node of the mesh, thus it cannot be used to compute the recovered field. Then the problem to solve is written in the matrix system (4.57), where the blocks in red are the SPR-C system (4.53) computed at $\Omega_p^k \in \Omega^{(1)}$, the blocks in green represent the same problem evaluated at $\Omega_p^{aux} \in \Omega^{(2)}$ and the constraint blocks C^{cont} and $\boldsymbol{\lambda}^{cont}$ are obtained with the same procedure in (4.51).

$$\begin{bmatrix} \mathbf{M}^{(1)} & \mathbf{C}^{(1)T} & \mathbf{0} & & \mathbf{C}^{cont\ T} \\ \mathbf{C}^{(1)} & \mathbf{0} & & & \\ & \mathbf{0} & \mathbf{M}^{(2)} & \mathbf{C}^{(2)T} & \\ & & \mathbf{C}^{(2)} & \mathbf{0} & \\ & \mathbf{C}^{cont} & & & \mathbf{0} \end{bmatrix} \begin{Bmatrix} \mathbf{A}^{(1)} \\ \boldsymbol{\lambda}^{(1)} \\ \mathbf{A}^{(2)aux} \\ \boldsymbol{\lambda}^{(2)} \\ \boldsymbol{\lambda}^{cont} \end{Bmatrix} = \begin{Bmatrix} \mathbf{H}^{(1)} \\ \boldsymbol{\Lambda}^{(1)} \\ \mathbf{H}^{(2)} \\ \boldsymbol{\Lambda}^{(2)} \\ \mathbf{0} \end{Bmatrix} \tag{4.57}$$

With the solution of system (4.57) we obtain the coefficients $\mathbf{A}^{(1)}$ to compute the recovered field at the main body, and the coefficients $\mathbf{A}^{(2)aux}$ are disregarded. After solving all patches in $\Omega^{(1)}$ the roles of *main* and *auxiliary* are exchanged to evaluate the recovered field at $\Omega^{(2)}$.

Since the solution of the SPR-C patches is performed in a decoupled manner, there will always be a lack of equilibrium along the contact boundary at a patch level. However, the numerical tests performed in paper E show that both the quality of $\boldsymbol{\sigma}^*$ and the traction equilibrium along the contact boundary is greatly improved with the proposed technique. The non-smooth behavior characteristic contact pressure around the end-of-contact area is not properly captured since we use a single polynomial to represent the recovered field. Nevertheless, the accuracy of the contact pressure evaluated with the SPR-C technique is also higher in the end-of-contact area than that obtained with the classic SPR technique.

Moreover, it is shown that the effectivity of the ZZ-estimator (3.12) is considerably increased around the contact area when the SPR-C recovered field is used. This allows to perform an accurate automatic h-adaptive refinement procedure which increases the efficiency of the method for the solution of 3D contact problems, in the sense that the same error level can be obtained with less degrees of freedom.

4.4. Application example: patient-specific dental implant simulation

With the contributions presented in this Chapter we have developed a framework for solving contact problems with cgFEM. In this section we present a conceptual example of an engineering application in which the advantages of the cgFEM can be

exploited: the patient-specific simulation of the interaction between living tissues and prosthetic devices, particularly a dental implant simulation.

When the dental implant is inserted, the contact forces between the bone and the implant hold it in place. This first stage is followed by a bone remodeling process and a osseointegration process, accompanied by a progressive reduction of the contac forces. The analysis of the contact stresses at this first stage is relevant for the optimization of immediate-load dental implants, where the devices can be exposed to the chewing forces immediately after implantation. The contact interaction also influences the local evolution of the osseointegration and bone remodeling processes. Hence, these contact forces are relevant for the success of the implant's performance. The heterogeneity of the living tissue at each patient, both in terms of geometry and material properties, prevents the analysis of these local effects using a generalized model of a mandible. Thus, an accurate pre-operative evaluation of the success of an implant involves creating a patient-specific FE model from the medical image provided by a CT scan, which usually involves a complex pre-processing segmentation phase.

Giovannelli *et al.* [103] presented an efficient method for the automatic creation of such models taking advantage of the high compatibility of the cgFEM mesh and the medical image structures. The voxels of the CT scan were directly introduced in the structured mesh without the usual intermediate step of creating geometrical models of the living tissue. Then the material properties were assigned to each voxel in the image for the numerical integration. This was done using the relations found in literature between the values of the voxel (in Hounsfield units), apparent mineral density and, finally, Young's modulus (see for instance [104, 105]). To avoid excessive homogeneization of the material inside each element in the mesh the method features an automatic h-adaptive refinement procedure based on the distribution of material properties in the elements. This technique was used in [103] to model the last phase of the process, i.e., to model the bone-implant interaction assuming a complete osseointegration, and therefore, the continuity of displacements between bone and implant. This continuity allowed the use of one single FE mesh to model bone and implant, simply taking into account different material properties at each of them. No remodeling was considered in this reference.

In the example shown in this thesis we will model the initial stage of the process, where the bone-implant interaction is driven by the contact forces. This implies considering two independent FE meshes, one for each body. Figure 4.9a shows the jaw model used in [103], from which a region is extracted (Figure 4.9b) for the simulation with a CAD model of a dental implant (Figure 4.10a) of titanium ($E = 110GPa, \nu = 0.3$). The Young's modulus considered for mandible model is a piece-wise linear interpolations of the values in Table 4.2, and a constant Poisson's ratio $\nu = 0.3$ [103]. The applied boundary conditions are depicted in Figure 4.9b: all displacements are constrained at the nodes located over the blue surfaces, and a distributed load $\sigma_{yy} = \sigma_{zz} = -2\ MPa$ is applied on the upper surface of the implant.

Both models are meshed independently, and all the image voxels located inside the CAD defining the implant are deactivated, i.e. its material properties are set to zero. The challenge now is to obtain the contact point pairs between both solids, as

the medical image does not define any explicit surface. We propose to duplicate the NURBS entities defining the implant and associate that copy to the image, this is, the new surface will move with the voxels in the image. We find this approach suitable for this application in which there are small displacements, but other methods should be explored otherwise, e.g. for the simulation of the implant insertion.

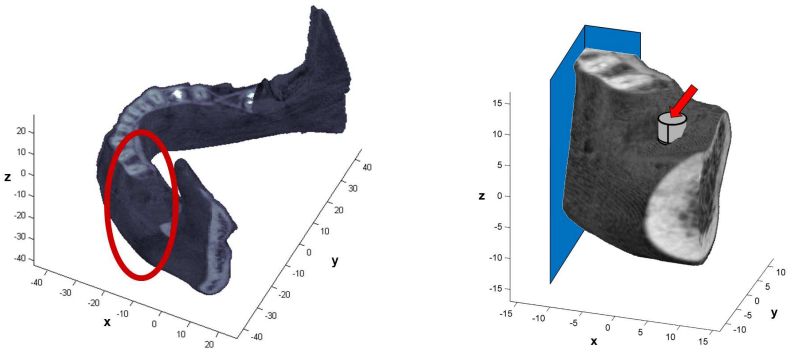

(a) *CAD model* ***(b)*** *FE model, 36k DOF*

Figure 4.9: *Example of implant simulation. CAD and mesh of the implant model.*

HU	0	227	228	1500	2000	4095
E $[GPa]$	10^{-4}	10^{-4}	0.5	1.5	7	30

Table 4.2: *Material properties associated to the mandible model.*

The contact formulation developed in this thesis allows the simulation of different states of the integration between implant and mandible. On one hand the previous stage to the implant's osseointegration is modeled with a Coulomb's friction model with $\mu = 0.36$. On the other hand, a simulation of complete osseointegration is performed considering only adhesive contact. Figures 4.12 and 4.13 show the results corresponding to the FE stress σ^h_{zz} and the von Mises stress of the recovered field $\boldsymbol{\sigma}^*$ at the implant, respectively. Although these results cannot be interpreted from an engineering point of view, there are appreciable differences on the stress field around the contact surface depending on the assumptions made. Therefore, a unique model can be used to analyze the initial stage (considering frictional contact interaction between bone and implant) and the stationary regime, once osseointegration has taken place (considering adhesive contact). Hence, we also believe that the presented method is promising for the definition of patient-specific optimal implant designs, which maximize the long-term implant stability taking into account the contact interaction with the living tissues.

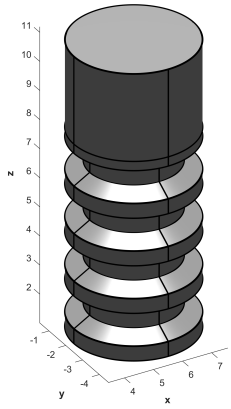

(a) CAD model

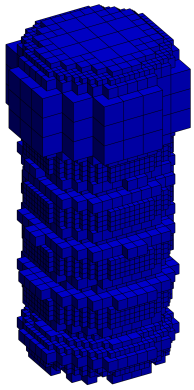

(b) FE model, 36k DOF

Figure 4.10: *Example of implant simulation. CAD and mesh of the implant model.*

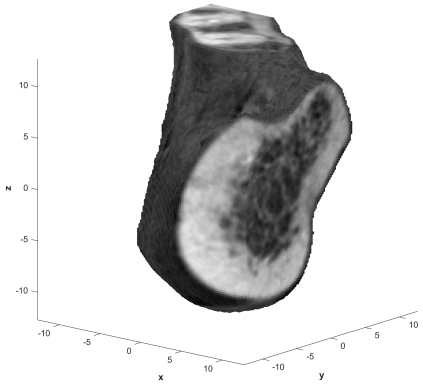

(a) Analysis domain

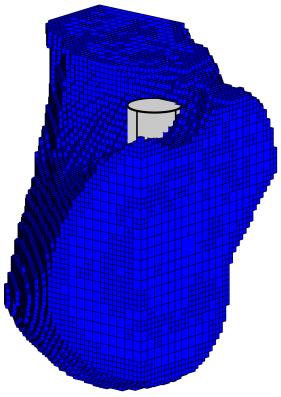

(b) FE model, 270k DOF

Figure 4.11: *Example of implant simulation. Image and mesh of the mandible model.*

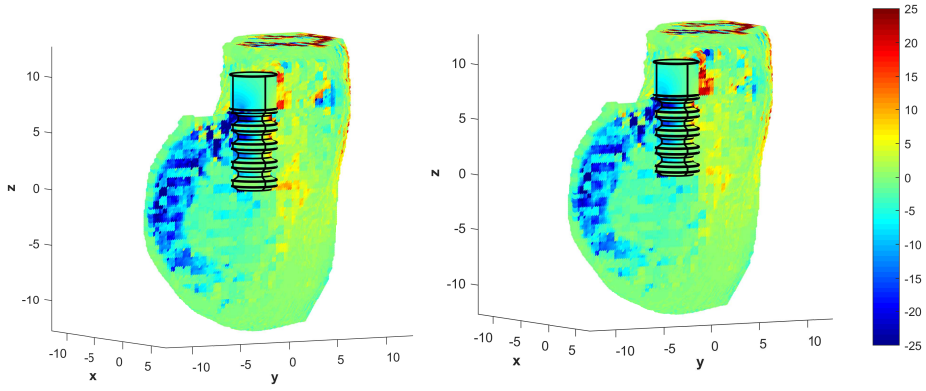

(a) Friction contact *(b) Adhesion contact*

Figure 4.12: *Example of implant simulation. Values of stress σ_{zz}^h corresponding to the assumptions of frictional and adhesion contact.*

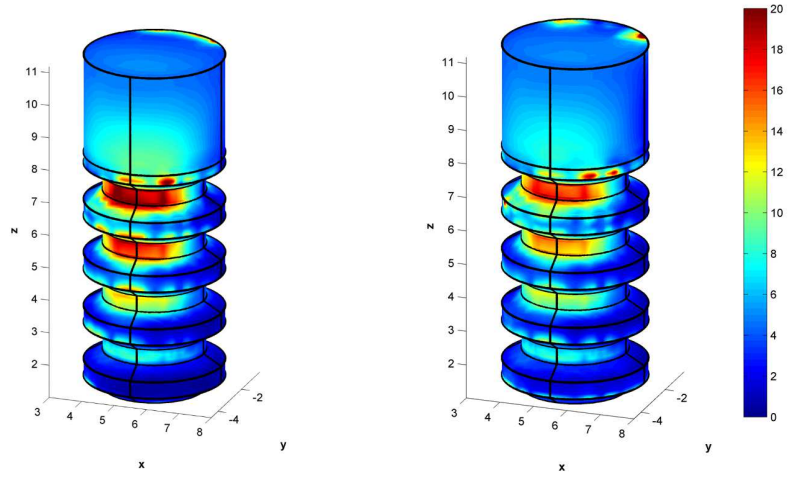

(a) Friction contact *(b) Adhesion contact*

Figure 4.13: *Example of implant simulation. Von Misses stress of the recovered field $\boldsymbol{\sigma}^*$ at the implant corresponding to the assumptions of frictional and adhesion contact.*

Chapter 5

Closure

5.1. Summary

In this thesis we have presented a framework for solving 3D frictional contact problems within the Cartesian grid Finite Element Method (cgFEM). The main contributions of this thesis are summarized as follows:

- A stabilized Lagrangian formulation for 3D frictional contact has been presented. In this formulation the stabilizing stress is computed by means of the superconvergent patch recovery technique. The FE optimal convergence rates are kept regardless of the arbitrary cuts between the Cartesian grids and the geometry and there are no additional unknowns in the elasticity problem. This is achieved at the cost of including an *augmentation* loop in which the stabilizing term is updated. However, the experience has shown that usually 2-3 iterations are enough to obtain accurate results and optimal convergence.

- The NURBS definition of the contact boundary, available in cgFEM, has been included in the kinematic variables definition. As a result, the measurement of the contact gap is greatly improved, with an overall impact on the accuracy of the method. In particular, it has been shown that the results obtained with coarse meshes and NURBS are comparable to those obtained with finer meshes and linear facets.

- An alternative definition of the contact surface involving a NURBS fitting problem has been studied. With this approach the evaluation of the kinematic variables and the ray-tracing algorithm are simplified. This may be suitable for meshes where the size of the elements is comparable to that of the surfaces. However, as the mesh is refined there is an increasing in the coupling of degrees of freedom, which eventually ends in an inadmissible computational cost.

- Following the same idea of the stabilizing term in the contact formulation we have presented a technique to address the ill-conditioning problems typical of immersed boundary methods by adding a stabilizing term for the *pathological* nodes. In this case the stabilizing term is computed with a displacements recovery, and the same *augmentation* loop of the contact iteration is used to update the new term. The performed tests show that the proposed approach eliminates the condition number dependence on the cuts between mesh and geometry.

- Finally, we have proposed a modification of the superconvergent patch recovery with constrains (SPR-C) for the recovery of stresses from the FE solution that includes the boundary equilibrium at the contact area. This modification results in an enhanced recovered stress field around the contact area, which leads to a better error estimation through the well known ZZ-estimator. The combination of this estimator and the SPR-C has been successfully used to guide an h-adaptive refinement process in contact problems with cgFEM.

5.2. Future developments

With this thesis we have established the basis for solving contact problems within the cgFEM methodology. This opens some research lines where the capabilities of the cgFEM are exploited in the context of contact problems:

- The combination between a technique that takes into account the specific features of the patient's bone present in the medical image and efficient shape optimization procedures seems very promising for the development of patient-specific optimized prosthetic devices. The contact formulation developed in this thesis allows to simulate different stages of the implant by switching between frictional and adhesive contact. We also believe that the osseointegration process can be modeled with the techniques presented in this thesis. To do this it will be necessary to develop a criterion that defines, for any given pair of points in contact, the transition between frictional and adhesive model. Finally, the combination of this methodology with a bone remodeling model will allow to run the complete evolution of a patient-specific implant simulation.

- cgFEM is a suitable framework for solving problems in which multiple geometry modifications must be performed, such as shape optimization. In this sense, the contribution in this thesis opens the possibility to simulate contact wear problems. For that, it is necessary to develop a strategy to modify the geometry of the bodies in contact using the resulting contact stresses.

- Up to this moment the contact search algorithm represents one of the most expensive tasks in terms of computational cost. A rudimentary algorithm has been implemented, but we believe that there is room for improvement with the combination of cgFEM's hierarchically structured data and optimized search algorithms currently available.

Bibliography

[1] O. C. Zienkiewicz, R. L. Taylor, and J. Z. Zhu, *The finite element method: its basis and fundamentals*. Elsevier Butterworth-Heinemann, 2005.

[2] S. Bordas, T. Rabczuk, J.-J. Rodenas, P. Kerfriden, M. Moumnassi, and S. Belouettar, "Recent Advances Towards Reducing the Meshing and Re-Meshing Burden in Computational Sciences," *Computational Technology Reviews*, vol. 2, pp. 51–82, 2010.

[3] E. Nadal Soriano, *Cartesian grid FEM (cgFEM): High performance h-adaptive FE analysis with efficient error control. Application to structural shape optimization.* PhD thesis, Universitat Politècnica de València, Valencia (Spain), 2014.

[4] O. Marco, R. Sevilla, Y. Zhang, J. J. Ródenas, and M. Tur, "Exact 3D boundary representation in finite element analysis based on Cartesian grids independent of the geometry," *International Journal for Numerical Methods in Engineering*, vol. 103, no. 6, pp. 445–468, 2015.

[5] L. Giovannelli, *Direct creation of patient-specific Finite Element models from medical images and preoperative prosthetic implant simulation using h-adaptive Cartesian grids.* PhD thesis, Universitat Politècnica de València, Valencia (Spain), 2018.

[6] C. S. Peskin, "Numerical analysis of blood flow in the heart," *Journal of Computational Physics*, vol. 25, no. 3, pp. 220–252, 1977.

[7] N. Moës, J. Dolbow, and T. Belytschko, "A finite element method for crack growth without remeshing," *International Journal for Numerical Methods in Engineering*, vol. 46, pp. 131–150, 1999.

[8] J. Dolbow, N. Moës, and T. Belytschko, "Discontinous enrichment in finite element with a partition of unity method," *Finite Elements in Analysis and Design*, vol. 36, pp. 235–260, 2000.

[9] T. Strouboulis, I. Babuška, and K. Copps, "The design and analysis of the Generalized Finite Element Method," *Computer Methods in Applied Mechanics and Engineering*, vol. 181, pp. 43–69, 2000.

[10] J. Melenk and I. Babuška, "The partition of unity finite element method: Basic theory and applications," *Computer Methods in Applied Mechanics and Engineering*, vol. 139, pp. 289–314, 1996.

[11] J. Parvizian, A. Düster, and E. Rank, "Finite cell method," *Computational Mechanics*, vol. 41, no. 1, pp. 121–133, 2007.

[12] A. Düster, J. Parvizian, Z. Yang, and E. Rank, "The finite cell method for three-dimensional problems of solid mechanics," *Computer Methods in Applied Mechanics and Engineering*, vol. 197, no. 45-48, pp. 3768–3782, 2008.

[13] E. Burman, S. Claus, P. Hansbo, M. G. Larson, and A. Massing, "CutFEM: Discretizing geometry and partial differential equations," *International Journal for Numerical Methods in Engineering*, vol. 104, no. 7, pp. 472–501, 2015.

[14] J. Haslinger and D. Jedelsky, "Genetic algorithms and fictitious domain based approaches in shape optimization," *Structural Optimization*, vol. 12, no. 4, pp. 257–264, 1996.

[15] K. Kunisch and G. Peichl, "Numerical Gradients for Shape Optimization Based on Embedding Domain Techniques," *Computational Optimization and Applications*, vol. 18, no. 2, pp. 95–114, 2001.

[16] A. R. Najafi, M. Safdari, D. A. Tortorelli, and P. H. Geubelle, "A gradient-based shape optimization scheme using an interface-enriched generalized FEM," *Computer Methods in Applied Mechanics and Engineering*, vol. 296, pp. 1–17, 2015.

[17] S. Riehl and P. Steinmann, "On structural shape optimization using an embedding domain discretization technique," *International Journal for Numerical Methods in Engineering*, vol. 109, no. 9, pp. 1315–1343, 2017.

[18] J. Parvizian, A. Düster, and E. Rank, "Topology optimization using the finite cell method," *Optimization and Engineering*, vol. 13, no. 1, pp. 57–78, 2012.

[19] E. Nadal, J. J. Ródenas, J. Albelda, M. Tur, J. E. Tarancón, and F. J. Fuenmayor, "Efficient Finite Element Methodology based on Cartesian grids: Application to structural shape optimization," *Abstract and Applied Analysis*, vol. 2013, pp. 1–19, 2013.

[20] O. Marco, J. J. Ródenas, J. Albelda, E. Nadal, and M. Tur, "Structural shape optimization using Cartesian grids and automatic h-adaptive mesh projection," *Structural and Multidisciplinary Optimization*, pp. 1–21, 2017.

[21] G. Legrain, P. Cartraud, I. Perreard, and N. Moës, "An X-FEM and level set computational approach for image-based modelling: Application to homogenization," *International Journal for Numerical Methods in Engineering*, vol. 86, no. 7, pp. 915–934, 2011.

[22] W. D. Lian, G. Legrain, and P. Cartraud, "Image-based computational homogenization and localization: comparison between X-FEM/levelset and voxel-based approaches," *Computational Mechanics*, vol. 51, no. 3, pp. 279–293, 2013.

[23] F. Liehr, T. Preusser, M. Rumpf, S. Sauter, and L. O. Schwen, "Composite Finite Elements for 3D Image Based Computing," *Computing in Visualization and Science*, vol. 12, pp. 171–188, 2009.

[24] M. Ruess, D. Tal, N. Trabelsi, Z. Yosibash, and E. Rank, "The finite cell method for bone simulations: verification and validation," *Biomechanics and Modeling in Mechanobiology*, vol. 11, no. 3-4, pp. 425–437, 2012.

[25] A. Düster, H.-G. Sehlhorst, and E. Rank, "Numerical homogenization of heterogeneous and cellular materials utilizing the finite cell method," *Computational Mechanics*, vol. 50, no. 4, pp. 413–431, 2012.

[26] S. Badia, F. Verdugo, and A. F. Martín, "The aggregated unfitted finite element method for elliptic problems," *Computer Methods in Applied Mechanics and Engineering*, vol. 336, pp. 533 – 553, 2018.

[27] T.-P. Fries and S. Omerović, "Higher-order accurate integration of implicit geometries," *International Journal for Numerical Methods in Engineering*, vol. 106, no. 5, pp. 323–371, 2016.

[28] L. Kudela, N. Zander, S. Kollmannsberger, and E. Rank, "Smart octrees: Accurately integrating discontinuous functions in 3D," *Computer Methods in Applied Mechanics and Engineering*, vol. 306, pp. 406–426, 2016.

[29] T. Hughes, J. Cottrell, and Y. Bazilevs, "Isogeometric analysis: CAD, finite elements, NURBS, exact geometry and mesh refinement," *Computer Methods in Applied Mechanics and Engineering*, vol. 194, no. 39-41, pp. 4135–4195, 2005.

[30] R. Sevilla, S. Fernández-Méndez, and A. Huerta, "NURBS-enhanced finite element method (NEFEM)," *International Journal for Numerical Methods in Engineering*, vol. 76, pp. 56–83, 2008.

[31] R. Sevilla, S. Fernández-Méndez, and A. Huerta, "NURBS-Enhanced Finite Element Method (NEFEM)," *Archives of Computational Methods in Engineering*, vol. 18, no. 4, pp. 441–484, 2011.

[32] L. Liu, Y. Zhang, T. J. R. Hughes, M. A. Scott, and T. W. Sederberg, "Volumetric T-spline construction using Boolean operations," *Engineering with Computers*, vol. 30, no. 4, pp. 425–439, 2014.

[33] E. Rank, M. Ruess, S. Kollmannsberger, D. Schillinger, and a. Düster, "Geometric modeling, isogeometric analysis and the finite cell method," *Computer Methods in Applied Mechanics and Engineering*, vol. 249-252, pp. 104–115, 2012.

[34] E. Burman and P. Hansbo, "Fictitious domain finite element methods using cut elements: II. A stabilized Nitsche method," *Applied Numerical Mathematics*, vol. 62, no. 4, pp. 328–341, 2012.

[35] M. Ruess, D. Schillinger, Y. Bazilevs, V. Varduhn, and E. Rank, "Weakly enforced essential boundary conditions for NURBS-embedded and trimmed NURBS geometries on the basis of the finite cell method," *International Journal for Numerical Methods in Engineering*, vol. 95, pp. 811–846, 2013.

[36] M. Ainsworth and J. T. J. T. Oden, *A posteriori error estimation in finite element analysis*. Wiley, 2000.

[37] T. Strouboulis, I. Babuŝka, D. Datta, K. Copps, and S. Gangaraj, "A posteriori estimation and adaptive control of the error in the quantity of interest. Part I: A posteriori estimation of the error in the von Mises stress and the stress intensity factor," *Computer Methods in Applied Mechanics and Engineering*, vol. 181, pp. 261–294, 2000.

[38] J. P. d. S. R. Gago, D. W. Kelly, O. C. Zienkiewicz, and I. Babuska, "A posteriori error analysis and adaptive processes in the finite element method: Part II - Adaptive mesh refinement," *International Journal for Numerical Methods in Engineering*, vol. 19, pp. 1593–1619, 1983.

[39] O. C. Zienkiewicz and J. Z. Zhu, "A simple error estimator and adaptive procedure for practical engineerng analysis," *International Journal for Numerical Methods in Engineering*, vol. 24, no. January 1986, pp. 337–357, 1987.

[40] A. Becheur, A. Tahakourt, and P. Coorevits, "An a posteriori error indicator for Coulomb's frictional contact," *Mechanics Research Communications*, vol. 35, no. 8, pp. 562–575, 2008.

[41] H. Liu, I. Ramière, and F. Lebon, "On the coupling of local multilevel mesh refinement and ZZ methods for unilateral frictional contact problems in elastostatics," *Computer Methods in Applied Mechanics and Engineering*, vol. 323, pp. 1–26, 2017.

[42] O. C. Zienkiewicz and J. Z. Zhu, "The superconvergent patch recovery and a posteriori error estimates. Part 1: The recovery technique," *International Journal for Numerical Methods in Engineering*, 1992.

[43] J. J. Ródenas, M. Tur, F. J. Fuenmayor, and A. Vercher, "Improvement of the superconvergent patch recovery technique by the use of constraint equations: The SPR-C technique," *International Journal for Numerical Methods in Engineering*, vol. 70, no. October 2006, pp. 705–727, 2007.

[44] O. Marco, J. Ródenas, J. Navarro-Jiménez, and M. Tur, "Robust h-adaptive meshing strategy considering exact arbitrary CAD geometries in a Cartesian grid framework," *Computers and Structures*, vol. 193, 2017.

[45] F. B. Belgacem, P. Hild, and P. Laborde, "The mortar finite element method for contact problems," *Mathematical and Computer Modelling*, vol. 28, no. 4-8, pp. 263–271, 1998.

[46] M. A. Puso and T. A. Laursen, "A mortar segment-to-segment frictional contact method for large deformations," *Computer Methods in Applied Mechanics and Engineering*, vol. 193, no. 45-47, pp. 4891–4913, 2004.

[47] B. Yang, T. A. Laursen, and X. Meng, "Two dimensional mortar contact methods for large deformation frictional sliding," *International Journal for Numerical Methods in Engineering*, vol. 62, no. 9, pp. 1183–1225, 2005.

[48] K. A. Fischer and P. Wriggers, "Mortar based frictional contact formulation for higher order interpolations using the moving friction cone," *Computer Methods in Applied Mechanics and Engineering*, vol. 195, no. 37-40, pp. 5020–5036, 2006.

[49] M. Tur, F. J. Fuenmayor, and P. Wriggers, "A mortar-based frictional contact formulation for large deformations using Lagrange multipliers," *Computer Methods in Applied Mechanics and Engineering*, vol. 198, no. 37-40, pp. 2860–2873, 2009.

[50] M. Gitterle, A. Popp, M. W. Gee, and W. A. Wall, "Finite deformation frictional mortar contact using a semi-smooth Newton method with consistent linearization," *International Journal for Numerical Methods in Engineering*, vol. 84, no. 5, pp. 543–571, 2010.

[51] L. De Lorenzis, P. Wriggers, and G. Zavarise, "A mortar formulation for 3D large deformation contact using NURBS-based isogeometric analysis and the augmented Lagrangian method," *Computational Mechanics*, vol. 49, no. 1, pp. 1–20, 2012.

[52] I. Temizer, P. Wriggers, and T. J. R. Hughes, "Three-dimensional mortar-based frictional contact treatment in isogeometric analysis with NURBS," *Computer Methods in Applied Mechanics and Engineering*, vol. 209-212, pp. 115–128, 2012.

[53] M. Dittmann, M. Franke, I. Temizer, and C. Hesch, "Isogeometric Analysis and thermomechanical Mortar contact problems," *Computer Methods in Applied Mechanics and Engineering*, vol. 274, pp. 192–212, 2014.

[54] F. Brezzi and M. Fortin, *Mixed and Hybrid Finite Element Methods*. Springer New York, 1991.

[55] J. Dolbow, N. Moës, and T. Belytschko, "An extended finite element method for modeling crack growth with frictional contact," *Computer Methods in Applied Mechanics and Engineering*, vol. 190, pp. 6825–6846, 2001.

[56] R. Ribeaucourt, M. C. Baietto-Dubourg, and A. Gravouil, "A new fatigue frictional contact crack propagation model with the coupled X-FEM/LATIN method," *Computer Methods in Applied Mechanics and Engineering*, vol. 196, pp. 3230–3247, 2007.

[57] P. Ladevèze, *Nonlinear Computational Structural Mechanics*. Mechanical Engineering Series, New York, NY: Springer New York, 1999.

[58] T. Elguedj, A. Gravouil, and A. Combescure, "A mixed augmented Lagrangian-extended finite element method for modelling elastic-plastic fatigue crack growth with unilateral contact," *International Journal for Numerical Methods in Engineering*, vol. 71, no. February, pp. 1569–1597, 2007.

[59] J. Simo and T. Laursen, "An augmented lagrangian treatment of contact problems involving friction," *Computers & Structures*, vol. 42, no. 1, pp. 97–116, 1992.

[60] A. Konyukhov, C. Lorenz, and K. Schweizerhof, "Various contact approaches for the finite cell method," *Computational Mechanics*, vol. 56, no. 2, pp. 331–351, 2015.

[61] T. Bog, N. Zander, S. Kollmannsberger, and E. Rank, "Normal contact with high order finite elements and a fictitious contact material," *Computers and Mathematics with Applications*, vol. 70, no. 7, pp. 1370–1390, 2015.

[62] T. Bog, N. Zander, S. Kollmannsberger, and E. Rank, "Weak imposition of frictionless contact constraints on automatically recovered high-order, embedded interfaces using the finite cell method," 2017.

[63] Y. Renard, "Generalized Newton's methods for the approximation and resolution of frictional contact problems in elasticity," *Computer Methods in Applied Mechanics and Engineering*, vol. 256, pp. 38–55, 2013.

[64] K. Poulios and Y. Renard, "An unconstrained integral approximation of large sliding frictional contact between deformable solids," *Computers and Structures*, vol. 153, pp. 75–90, 2015.

[65] T. A. Laursen and J. D. Sanders, "New Applications of Mortar Methodology to Extended and Embedded Finite Element Formulations," in *Recent Developments and Innovative Applications in Computational Mechanics*, pp. 1–8, Berlin, Heidelberg: Springer Berlin Heidelberg, 2011.

[66] N. Moës, E. Béchet, and M. Tourbier, "Imposing Dirichlet boundary conditions in the extended finite element method," *International Journal for Numerical Methods in Engineering*, vol. 67, no. 12, pp. 1641–1669, 2006.

[67] É. Béchet, N. Moës, and B. Wohlmuth, "A stable Lagrange multiplier space for stiff interface conditions within the extended finite element method," *International Journal for Numerical Methods in Engineering*, vol. 78, no. 8, pp. 931–954, 2009.

[68] I. Nistor, M. L. E. Guiton, P. Massin, N. Moës, and S. Géniaut, "An X-FEM approach for large sliding contact along discontinuities," *International Journal for Numerical Methods in Engineering*, vol. 78, pp. 1407–1435, 2009.

[69] M. Hautefeuille, C. Annavarapu, and J. E. Dolbow, "Robust imposition of Dirichlet boundary conditions on embedded surfaces," *International Journal for Numerical Methods in Engineering*, vol. 90, no. November 2011, pp. 40–64, 2012.

[70] F. Liu and R. I. Borja, "Stabilized low-order finite elements for frictional contact with the extended finite element method," *Computer Methods in Applied Mechanics and Engineering*, vol. 199, no. 37-40, pp. 2456–2471, 2010.

[71] P. Heintz and P. Hansbo, "Stabilized Lagrange multiplier methods for bilateral elastic contact with friction," *Computer Methods in Applied Mechanics and Engineering*, vol. 195, no. 33-36, pp. 4323–4333, 2006.

[72] P. Hansbo, A. Rashid, and K. Salomonsson, "Least-squares stabilized augmented Lagrangian multiplier method for elastic contact," *Finite Elements in Analysis and Design*, vol. 116, pp. 32–37, 2016.

[73] J. Nitsche, "Über ein Variationsprinzip zur Lösung von Dirichlet-Problemen bei Verwendung von Teilräumen, die keinen Randbedingungen unterworfen sind," *Abhandlungen aus dem Mathematischen Seminar der Universität Hamburg*, vol. 36, no. 1, pp. 9–15, 1971.

[74] C. Annavarapu, M. Hautefeuille, and J. E. Dolbow, "A Nitsche stabilized finite element method for frictional sliding on embedded interfaces. Part I: Single interface," *Computer Methods in Applied Mechanics and Engineering*, vol. 268, pp. 417–436, 2014.

[75] C. Annavarapu, R. R. Settgast, S. M. Johnson, P. Fu, and E. B. Herbold, "A weighted nitsche stabilized method for small-sliding contact on frictional surfaces," *Computer Methods in Applied Mechanics and Engineering*, vol. 283, pp. 763–781, 2015.

[76] P. Wriggers, L. Krstulovic-Opara, and J. Korelc, "Smooth C1-interpolations for two-dimensional frictional contact problems," *International Journal for Numerical Methods in Engineering*, vol. 51, no. 12, pp. 1469–1495, 2001.

[77] V. Padmanabhan and T. Laursen, "A framework for development of surface smoothing procedures in large deformation frictional contact analysis," *Finite Elements in Analysis and Design*, vol. 37, no. 3, pp. 173–198, 2001.

[78] M. Tur, E. Giner, F. Fuenmayor, and P. Wriggers, "2D contact smooth formulation based on the mortar method," *Computer Methods in Applied Mechanics and Engineering*, vol. 247-248, pp. 1–14, 2012.

[79] M. Stadler, G. A. Holzapfel, and J. Korelc, "Cn continuous modelling of smooth contact surfaces using NURBS and application to 2D problems," *International Journal for Numerical Methods in Engineering*, vol. 57, no. 15, pp. 2177–2203, 2003.

[80] D. Neto, M. Oliveira, L. Menezes, and J. Alves, "A contact smoothing method for arbitrary surface meshes using Nagata patches," *Computer Methods in Applied Mechanics and Engineering*, vol. 299, pp. 283–315, 2016.

[81] M. A. Puso and T. A. Laursen, "A 3D contact smoothing method using Gregory patches," *International Journal for Numerical Methods in Engineering*, vol. 54, no. 8, pp. 1161–1194, 2002.

[82] L. De Lorenzis, P. Wriggers, and T. J. Hughes, "Isogeometric contact: a review," *GAMM-Mitteilungen*, vol. 37, no. 1, pp. 85–123, 2014.

[83] C. J. Corbett and R. A. Sauer, "NURBS-enriched contact finite elements," *Computer Methods in Applied Mechanics and Engineering*, vol. 275, pp. 55–75, 2014.

[84] C. J. Corbett and R. A. Sauer, "Three-dimensional isogeometrically enriched finite elements for frictional contact and mixed-mode debonding," *Computer Methods in Applied Mechanics and Engineering*, 2015.

[85] W. E. Lorensen, H. E. Cline, W. E. Lorensen, and H. E. Cline, "Marching cubes: A high resolution 3D surface construction algorithm," in *Proceedings of the 14th annual conference on Computer graphics and interactive techniques - SIGGRAPH '87*, vol. 21, (New York, New York, USA), pp. 163–169, ACM Press, 1987.

[86] P. Wriggers, *Computational contact mechanics*. Springer, 2006.

[87] T. Laursen, *Computational Contact and Impact Mechanics: Fundamentals of Modelling Interfacial Phenomena In Nonlinear Finite Element Analysis*. Springer, 2003.

[88] N. Kikuchi and J. T. J. T. Oden, *Contact problems in elasticity : a study of variational inequalities and finite element methods*. SIAM, 1988.

[89] J. C. Simo, P. Wriggers, and R. L. Taylor, "A perturbed Lagrangian formulation for the finite element solution of contact problems," *Computer Methods in Applied Mechanics and Engineering*, vol. 50, no. 2, pp. 163–180, 1985.

[90] R. Sevilla and S. Fernández-Méndez, "Numerical integration over 2D NURBS-shaped domains with applications to NURBS-enhanced FEM," *Finite Elements in Analysis and Design*, vol. 47, no. 10, pp. 1209–1220, 2011.

[91] D. F. Rogers, *An introduction to NURBS : with historical perspective*. Morgan Kaufmann Publishers, 2001.

[92] T. Blacker and T. Belytschko, "Superconvergent patch recovery with equilibrium and conjoint interpolant enhancements*," *International Journal for Numerical Methods in Engineering*, vol. 37, no. December 1992, pp. 517–536, 1994.

[93] J. F. Abel and M. S. Shephard, "An algorithm for multipoint constraints in finite element analysis," *International Journal for Numerical Methods in Engineering*, vol. 14, no. 3, pp. 464–467, 1979.

[94] M. E. Hammer, "Frictional mortar contact for finite deformation problems with synthetic contact kinematics," *Computational Mechanics*, vol. 51, no. 6, pp. 975–998, 2013.

[95] M. Tur, J. Albelda, O. Marco, and J. J. Ródenas, "Stabilized method of imposing Dirichlet boundary conditions using a recovered stress field," *Computer Methods in Applied Mechanics and Engineering*, vol. 296, pp. 352–375, 2015.

[96] M. Tur, J. Albelda, E. Nadal, and J. J. Ródenas, "Imposing Dirichlet boundary conditions in hierarchical Cartesian meshes by means of stabilized Lagrange multipliers," *International Journal for Numerical Methods in Engineering*, vol. 98, pp. 399–417, 2014.

[97] M. A. Puso and T. A. Laursen, "A mortar segment-to-segment contact method for large deformation solid mechanics," *Computer Methods in Applied Mechanics and Engineering*, vol. 193, no. 6-8, pp. 601–629, 2004.

[98] B. I. Wohlmuth, "An a Posteriori Error Estimator for Two-Body Contact Problems on Non-Matching Meshes," *J Sci Comput*, vol. 33, pp. 25–45, 2007.

[99] R. Stenberg, "On some techniques for approximating boundary conditions in the finite element method," *ELSEVIER Journal of Computational and Applied Mathematics*, vol. 63, pp. 139–148, 1995.

[100] P. Alart and A. Curnier, "A mixed formulation for frictional contact problems prone to Newton like solution methods," *Computer Methods in Applied Mechanics and Engineering*, vol. 92, no. 3, pp. 353–375, 1991.

[101] G. Pietrzak and A. Curnier, "Large deformation frictional contact mechanics: continuum formulation and augmented Lagrangian treatment," *Computer Methods in Applied Mechanics and Engineering*, vol. 177, no. 3-4, pp. 351–381, 1999.

[102] E. Burman and P. Hansbo, "Fictitious domain finite element methods using cut elements: I. A stabilized Lagrange multiplier method," *Computer Methods in Applied Mechanics and Engineering*, vol. 199, no. 41-44, pp. 2680–2686, 2010.

[103] L. Giovannelli, J. Ródenas, J. Navarro-Jiménez, and M. Tur, "Direct medical image-based Finite Element modelling for patient-specific simulation of future implants," *Finite Elements in Analysis and Design*, vol. 136, 2017.

[104] C. Zannoni, R. Mantovani, and M. Viceconti, "Material properties assignment to finite element models of bone structures: a new method," *Medical Engineering & Physics*, vol. 20, no. 10, pp. 735–740, 1999.

[105] H. Wille, E. Rank, and Z. Yosibash, "Prediction of the mechanical response of the femur with uncertain elastic properties," *Journal of Biomechanics*, vol. 45, no. 7, pp. 1140–1148, 2012.

Part II

Articles

PAPER A

A modified perturbed Lagrangian formulation for contact problems

M. Tur, J. Albelda, J.M. Navarro-Jiménez and J.J. Ródenas

Computational Mechanics
Volume 55, Pages 737-754, 2015
DOI: 10.1007/s00466-015-1133-6

Abstract

The aim of this work is to propose a formulation to solve both small and large deformation contact problems using the finite element method. We consider both standard finite elements and the so-called immersed boundary elements. The method is derived from a stabilized Nitsche formulation. After introduction of a suitable Lagrange multiplier discretization the method can be simplified to obtain a modified perturbed Lagrangian formulation. The stabilizing term is iteratively computed using a smooth stress field. The method is simple to implement and the numerical results show that it is robust. The optimal convergence rate of the finite element solution can be achieved for linear elements.

Key words

Contact; Stabilized; Penalty; Large deformation; Perturbed Lagrangian

Contents

1. Introduction

The aim of this work is to propose a formulation to solve contact problems in the context of large and small deformations using the finite element method. We consider both standard finite elements and the so called immersed boundary elements in which an underlying Cartesian grid made of regular hexahedral elements is cut by the real geometry and integration is performed only in the internal part of the elements. In recent years segment-to-segment formulations like the mortar method [8] have been successfully applied to solving a wide variety of contact problems in 2D [27,35,55] and 3D [38,39], with linear and quadratic elements [28,53], in large and small deformations including Coulomb friction [17, 18, 20, 40–42, 50] and dynamic problems [24]. The theoretical basis of the mortar method is well known [15,28,30–32]. The compatibility of the displacement field and the contact stresses allows the Brezzi-Babuska-InfSup condition to be fulfilled, so the optimal convergence rate of the finite element solution can be achieved. The above references are only a part of the bibliography on the mortar method applied to contact problems.

In the case of immersed boundaries it is more difficult to find finite element spaces that fulfill the InfSup condition. To our knowledge only the Vital Vertex method, first proposed by Bechet *et al.* [7], can satisfy the compatibility between displacements and multipliers. This method has been used for imposing Dirichlet boundary conditions in 2D and 3D [2] immersed boundaries. However, its applicability to deal with large deformation contact problems is more involved, although there are some works in 2D [37]. For this reason, other techniques based on stabilized formulations have recently been proposed to solve contact problems. In these techniques the finite element spaces can be freely chosen at the price of adding new stabilizing terms to the formulation. Modifications of the Nitsche method have been applied to standard FEM [13, 26, 29, 57], X-FEM [3, 4, 21] and interface problems [1, 2, 12, 23, 45]. Other techniques use different stabilized formulations. For example [34] uses a polynomial stabilization valid for linear elements or [11] penalizes the jump in the multiplier linear elements. In other works the idea of extending the solution of internal elements to the intersected elements was explored [14,25]. In [19] the idea of condensing the Lagrange multipliers to obtain a simplified method for immersed boundaries was introduced. It was also used in [51] using the quadrature points. The same ideas were applied in [5] using a stabilizing field defined in the volume of the element instead of its surface. For Navier-Stokes equations in [46] a stabilization term that takes into account the jump in the derivative in the internal elements edges is used to overcome limitations of the Nitsche method in immersed boundaries.

In this work we propose a formulation derived from the stabilized Nitsche method. With the choice of finite element spaces, after simplifying the formulation, we obtain a formulation of the perturbed Lagrangian formulation proposed in [47]. From our analysis, an extra term due to contact is introduced to obtain a consistent formulation. The correction term can be iteratively computed using a smooth stress field. The

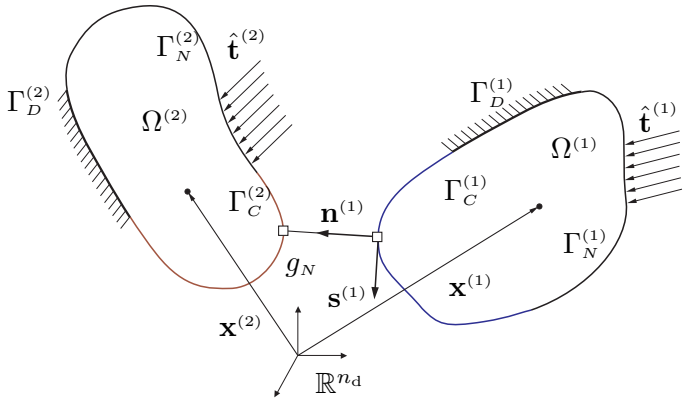

Figure 1: Scheme of two deformable bodies in contact.

same idea is used in [52] to impose the Dirichlet boundary conditions in immersed boundaries. It is demonstrated that the optimal convergence rate of the finite element solution can be achieved for linear and quadratic elements. This paper is organized as follows: Section 2 describes the formulation of the contact problem using Lagrange multipliers. In Section 3 we propose a stabilized formulation based on the Nitsche method. We propose an iterative method to solve the problem. In Section 4, the convergence of the iterative method is analyzed. In Section 5 the formulation is simplified and expressed as a modified penalty formulation with a suitable choice of the Lagrange multiplier field. We provide some details of the linearization for solving large deformation problems. In the last section some numerical examples are solved.

2. Contact problem formulation

In this part we introduce the contact problem formulation for small deformations. In Section 5 we will extend the formulation to deal with large deformations and large sliding problems. Fig. 1 shows a schematic representation of two deformable bodies labeled $^{(1)}$ and $^{(2)}$ that occupy volumes $\Omega^{(1)}$ and $\Omega^{(2)}$, respectively. The boundary of each body $\Gamma^{(i)}$ is divided into three non-overlapping surfaces, $\Gamma_D^{(i)}$ on which Dirichlet boundary conditions are imposed, $\Gamma_N^{(i)}$, the Neumann boundary, and $\Gamma_C^{(i)}$ the surface of the bodies on which contact can occur. We assume a linear elastic behavior of the materials and small deformations. With this setting, the contact problem can be formulated as a minimization of a functional [33,54], the total potential energy, under

the contact constraints, i.e.:

$$\min \left\{ \Pi_{\mathrm{p}}(\mathbf{u}) = \sum_{i=1,2} \left(\int_{\Omega^{(i)}} \boldsymbol{\sigma}(\mathbf{u}) : \boldsymbol{\epsilon}(\mathbf{u}) \, d\Omega - \int_{\Gamma_N^{(i)}} \mathbf{u} \cdot \hat{\mathbf{t}} \, d\Gamma \right) \right\} \quad \text{subject to} \quad g_N \geq 0 \qquad \text{in } \Gamma_C^{(1)} \tag{1}$$

where $\boldsymbol{\sigma}$ is the stress tensor, $\boldsymbol{\epsilon}$ linear strain tensor and $\hat{\mathbf{t}}$ are the tractions imposed at the Neumann boundary. The normal gap between the two contact surfaces is g_N. Here we assume that the contact constraint is satisfied for surface $\Gamma_C^{(1)}$. The gap is computed as the distance between the surface point $\mathbf{x}^{(1)}$ and the intersection of the other contact surface $\Gamma_C^{(2)}$ with the line emanating from the first point in the direction of the normal vector $\mathbf{n}^{(1)}$,

$$g_N = \left(\mathbf{x}^{(2)} \left(\boldsymbol{\xi}^{(2)} \right) - \mathbf{x}^{(1)} \right) \cdot \mathbf{n}^{(1)} \tag{2}$$

where $\boldsymbol{\xi}^{(2)}$ is the local coordinate of the intersection point on surface $\Gamma_C^{(2)}$ (in 3D it has 2 components). The position can be written as the sum of the initial position and the displacement, i.e. $\mathbf{x}^{(i)} = \mathbf{x}_0^{(i)} + \mathbf{u}^{(i)}$. In small deformations we assume that the contact point denoted by the surface coordinate $\boldsymbol{\xi}^{(2)}$ remains the same despite the deformation of the solids, i.e. it can be computed for the initial undeformed position. We can therefore write:

$$\begin{aligned} g_N &= \left(\mathbf{u}^{(2)} \left(\boldsymbol{\xi}^{(2)} \right) - \mathbf{u}^{(1)} \right) \cdot \mathbf{n}^{(1)} + \left(\mathbf{x}_0^{(2)} \left(\boldsymbol{\xi}^{(2)} \right) - \mathbf{x}_0^{(1)} \right) \cdot \mathbf{n}^{(1)} \\ &= \left(\mathbf{u}^{(2)} \left(\boldsymbol{\xi}^{(2)} \right) - \mathbf{u}^{(1)} \right) \cdot \mathbf{n}^{(1)} + g_{N0} \end{aligned} \tag{3}$$

The minimization problem under inequality constraints (1) can be solved using the Lagrange multiplier method, which is the basis of many finite element formulations for contact problems. A new variable, the Lagrange multiplier field λ_N is introduced and the following functional must be minimized with respect to the displacements and maximized with respect to the multipliers

$$\operatorname{opt} \left\{ \sum_{i=1,2} \int_{\Omega^{(i)}} \boldsymbol{\sigma}(\mathbf{u}) : \boldsymbol{\epsilon}(\mathbf{u}) \, d\Omega - \int_{\Gamma_N^{(i)}} \mathbf{u} \cdot \hat{\mathbf{t}} \, d\Gamma + \int_{\Gamma_C^{(1)}} \lambda_N g_N \, d\Gamma \right\} \quad \text{subject to} \quad \lambda_N \leq 0 \tag{4}$$

With this formulation the inequality constraint affects the multiplier λ_N. This restriction can be resolved by an active set strategy, assuming that the real contact surface is known, solving the problem and modifying the contact surface. From now onwards, for the analysis of convergence, we assume that the real contact surface is known and denoted as $\Gamma_C^{(1)}$. In Section 5 we provide details of the algorithm used to update the real contact surface.

As pointed out above, Equation (4) can be used to obtain a finite element formulation of the contact problem. The displacement and multiplier fields are replaced by a suitable finite element approximation $\mathbf{u}^h \in \mathscr{U}^h$ and $\lambda_N^h \in \mathscr{M}^h$.

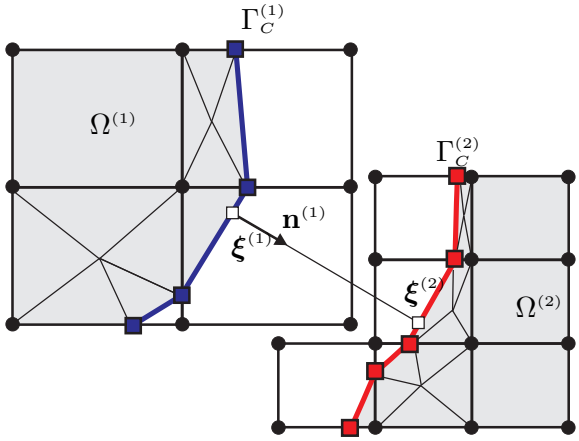

Figure 2: Cartesian grid finite elements in contact. The thick lines are the contact surfaces that follow the deformation of the boundary elements. Thin lines represent the subtriangulation of the boundary elements performed only for integration purposes.

In this work we use both 3D standard hexahedral finite elements and the so-called immersed boundary method with 8-node linear elements $\mathscr{H}_8$ and 20-node quadratic elements $\mathscr{H}_{20}$. Here we only describe the basic aspects of the immersed boundary method. A more detailed description can be found in [36, 49], for example. In the immersed boundary method, sometimes referred to as the Cartesian grid method, the underlying mesh consists of regular hexahedrals and this will be used in this work. Figure 2 schematically shows the Cartesian grids of two bodies that can come into contact. The thick lines represent the contact surface, which in general does not coincide with the edges of the elements. The shaded area represents the real domain of the bodies. For the boundary elements (elements cut by the real geometry of the problem) the integration is performed only in the part of the elements lying within the problem domain. Thus, a linear sub-triangulation of the internal part of the elements is defined only for integration purposes and the contact surface is approximately represented with straight segments, as depicted in Figure 2. Analogously, in the 3D case, the boundary elements are subdivided into tetrahedrals for integration and the contact surface is approximately represented by linear triangles.

The contact interaction between Cartesian meshes follows the same definition as the gap given in Equation (2) using the local coordinate in the contact surface $\boldsymbol{\xi}^{(1)}$ and normal vector $\mathbf{n}^{(1)}$. The position of the contact surface in the deformed configuration is defined by standard finite element interpolation using all the nodes of the boundary elements and not only the boundary nodes.

It is well known that in mixed formulations such as that of equation 4 a careful choice must be made of the discretization spaces for displacements and multipliers to achieve the optimal convergence rate. There are two conditions [9, 10] the ElKer and

the InfSup. As a solution for the compatibility of the spaces of Lagrange multipliers and displacements we find the mortar method, which has been successfully applied to 2D and 3D, large and small deformation contact problems using linear or quadratic elements, as pointed out in the Introduction. For immersed boundary methods the Vital Vertex method has been defined to fulfill the InfSup condition in the case of a Dirichlet boundary in 2D [7] and 3D [2].

The InfSup condition introduces many constraints in the case of immersed boundaries and it is by no means straightforward to derive a contact formulation that fulfills this condition. Stabilized methods can be used obtain greater freedom to choose the Lagrange multiplier space. This will be introduced in the following section and will form the basis of the proposed formulation.

3. Stabilized formulation

The difficulty in solving equation 4 by finite elements usually arises when the space of the multipliers is too rich, i.e. there are too many constraints in relation to the displacement degrees of freedom as the mesh is refined. Even though the problem can be solved, the convergence rate of the solution may be compromised. As the number of constraints increases, the constraint equations become more dependent and the value of the multiplier is unbounded. The idea of the stabilized formulations is to add a new term to the functional 4 that would prevent the multiplier from taking unbounded values.

In order to simplify the notation, from now on, we assume that the finite element variables are denoted without superscript h, i.e. $\mathbf{u} = \mathbf{u}^h$ and $\lambda_N = \lambda_N^h$.

The ideas of stabilizing the solution were used in [47]. Simo, Wriggers and Taylor proposed a perturbed Lagrangian formulation to solve contact problems as the optimization of the following functional

$$\text{opt}\left\{\Pi_{\text{p}}(\mathbf{u}) + \int_{\Gamma_C^{(1)}} \lambda_N g_N \, d\Gamma - \frac{1}{2k}\int_{\Gamma_C^{(1)}} \lambda_N^2 \, d\Gamma\right\} \tag{5}$$

The last integral in the functional is a penalty stabilizing term that allows the values of the multipliers to be bounded. As pointed out in [47], this penalized method is not consistent, in the sense that the exact solution of the contact problem is a solution of the above functional only at the limit, when the parameter $k \to \infty$, which is impossible in practice. In [47], after some simplifications, a structure of the problem as a pure penalty method was obtained in which the contact constraints are imposed in an average sense.

In this work we propose a new method that includes a modification of the perturbed Lagrangian formulation to make the formulation consistent, i.e. the finite

element solution converges to the exact solution as the mesh is refined for a wide range of bounded values of the penalty parameter k.

In what follows, we first introduce (Subsection 3.1) the modified functional used to stabilize the problem and analyze the similarities of the proposed formulation with the Nitsche method. In subsection 3.2 we introduce the stabilization field used in this work and show that the proposed field overcomes some limitations of the Nitsche method, particularly for immersed boundary meshes. The proof of convergence of the proposed formulation will be analyzed in Section 5 after introducing the iterative solution method.

3.1. Proposed stabilized functional

The proposed formulation can be derived from a modified version of the Barbosa-Hughes stabilization [6] in which the stabilizing term is replaced by a smooth stress field. Stenberg [48] demonstrated that the Barbosa-Hughes stabilization was equivalent to the Nitsche method, so that the proposed formulation can also be considered as a modified version of the Nitsche method. The functional reads as:

$$\text{opt} \left\{ \Pi_{\text{p}}(\mathbf{u}) + \int_{\Gamma_C^{(1)}} \lambda_N g_N \, d\Gamma - \sum_{\forall e} \frac{h}{2E\kappa} \int_{\Gamma_C^{(1)}} \left(\lambda_N - p_N\right)^2 \, d\Gamma \right\} \tag{6}$$

where E is the Young modulus, κ a user-defined penalty parameter that will be defined in the following sections and p_N is the stabilizing stress. The difference is found in the definition of the stabilizing stress p_N.

The last integral in Equation 6 is computed for each contact segment, as defined in the following section. The constant multiplying the stabilizing term includes E and a representative measure of the element size h. The former is needed to obtain a physical meaning of energy, since we have the product of stress multiplied by stress in the integral. Thus, dividing by E transforms the term into energy. The latter, h, is included to give the stabilizing term the same order of magnitude as the strain energy. As the element size is reduced, the variation of the element strains and stresses inside the element is also reduced. We can think on the limit as being constant in the entire element. Thus, the strain energy will be proportional to h^3, as it is a volume integral. The stabilizing term is a surface integral so it will be proportional to h^2. The additional h constant is introduced to have the same order of magnitude, as we need to bound the stabilizing term with the strain energy to achieve the convergence of the method (see following Section).

In the case of the Nitsche method p_N is the contact traction computed from the finite element solution, i.e. $p_N = \mathbf{n} \cdot \boldsymbol{\sigma}(\mathbf{u})\mathbf{n}$. This has been applied in [26,29] to derive the formulations to solve contact problems. With the same choice for p_N, the value of the constant can be adapted to deal with X-FEM problems [1,3,4,45].

The negative sign before the last integral is necessary, as the optimization of the functional is a maximization with respect to the multipliers. However, as the problem

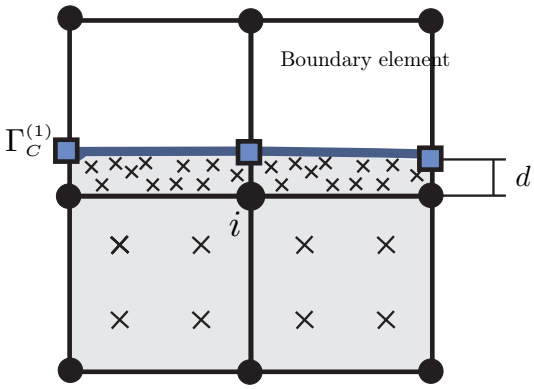

Figure 3: Patch of elements for computing the smooth stress field of node i. The internal volume of the boundary elements depends on distance d.

is a minimization with respect to the displacements and $\mathbf{n} \cdot \boldsymbol{\sigma}(\mathbf{u})\mathbf{n}$ linearly depends on this field, the negative sign may cause a non desired behavior of the stabilization term. A possible solution with standard finite elements is to bound this term by taking a sufficiently large value for κ so that this integral can be bounded by the strain energy [51]. In the case of immersed boundary elements there are some difficulties involved in bounding this term, particularly in meshes with cut elements that have a very small volume/surface ratio, as pointed out in [25].

To illustrate this problem two boundary elements with small internal volumes are shown in Figure 3. In general the L^2 norm of the stress on the boundary cannot be bounded by the energy norm of the element as its volume depends on distance d which can be very close to zero. Therefore, the stress $\mathbf{n} \cdot \boldsymbol{\sigma}(\mathbf{u})\mathbf{n}$ can only be bounded with very large values of the constant κ up to a geometric tolerance (see also [2, 45]). This can affect the convergence of the Nitsche method in this context, although from the engineering point of view, the results obtained using the tolerance seem to be acceptable. Appropriate choices for the stabilizing constant are proposed in the $\gamma-$Nitsche method [1, 45] for X-FEM applications. Schott and Wall [46] recently proposed an additional stabilization term that penalizes the jump in the derivative along internal element edges for fluid problems.

3.2. Smooth stress field

In this work we propose to define p_N as a smooth stress field obtained from the finite element solution, following the ideas introduced in [52] to apply Dirichlet boundary conditions in immersed boundaries. This choice is motivated from the observation that any variable having good convergence properties to the exact contact traction can be used as stabilizing term p_N in equation 6. The smooth stress field depends

not only on the solution of the boundary elements but also on the internal elements, where stresses are better estimated. The idea is close to that used in [14, 25], where the displacements of the internal elements are extended to the boundary cut elements. In [46] the solution of the internal elements is also used to stabilize the variables in the boundary elements.

The smooth stress field is based on the SPR (Superconvergent Patch Recovery) first proposed in [59] and improved in [43] to include constraint equations that must be fulfilled by the exact solution. Here we recall the main features of the smooth stress field calculation. The smooth stress field $\mathbf{S}_i = \{1\, x\, y\, xy\, ...\}\, \mathbf{a}_i$ is defined as a polynomial associated to each node i whose coefficients $\mathbf{a}_i$ are computed solving the following minimization problem:

$$\mathbf{a}_i = \text{argmin} \left\{ \int_{\Omega_i^{\text{patch}}} (\boldsymbol{\sigma}(\mathbf{u}) - \mathbf{S}_i) \cdot (\boldsymbol{\sigma}(\mathbf{u}) - \mathbf{S}_i)\ d\Omega \right\} \tag{7}$$

where $\boldsymbol{\sigma}(\mathbf{u})$ is the stress field computed from the finite element solution. The integral is extended in the volume of a so-called nodal patch Ω_i^{patch}. This volume includes all internal elements that contain node i and the internal volume of boundary elements that contain this node. For example, Figure 3 shows the patch of node i in a 2D case, that contains two internal and two boundary elements. With this choice, small-volume boundary elements (d close to zero, in which the finite element stress is poorly estimated, i.e. it has a large error) contribute less than the internal elements to the computation of the smooth stress field.

The stabilization term is computed as the normal traction of the smooth stress in the contact surface $p_N = \mathbf{n} \cdot \mathbf{Sn}$. With this definition it can be proved that the L^2 norm of p_N in the contact surface can be bounded with the energy norm [52], with a bounded positive constant C as follows

$$\|\mathbf{S}\|^2_{L^2(\Gamma_C)} \leq \frac{EC}{h} \|\mathbf{u}\|^2_E \tag{8}$$

where h is a representative measure of the element size and $\|\cdot\|_E$ is the energy norm in the volume. The value of C depends on the order of the interpolation and the nodal patches. For immersed boundaries the worst case appears for nodes whose elements are cut and have very small volume. Even in that case, as the smooth stress field depends on the solution of the internal elements, the constant C is bounded. In practice we found that we can use $C \geq 10$ for linear and quadratic elements.

4. Iterative solution method

The stabilization term p_N depends on the finite element solution $\mathbf{u}$. However, it is somewhat cumbersome to obtain an explicit formula for it, as its computation derives

from equation (7). Following the ideas presented in [52], we propose an iterative process to solve the optimization problem 6 in which the stabilization term p_N is assumed to be constant. After solving the problem, p_N is updated from the finite element solution, and problem 6 is solved again. The process begins with $p_N = 0$ and runs until convergence is achieved.

Assuming that the stabilization term p_N is known, we solve problem (6) taking variations with respect to the displacements and the multipliers to obtain a following variational equation. We have to find the iteration k solution, $[\mathbf{u}^k, \lambda_N^k]$, solving the following system

$$\begin{aligned}
&\sum_{i=1,2} G_{int}^{(i)}(\mathbf{u}^k, \delta\mathbf{u}) + \int_{\Gamma_C^{(1)}} \lambda_N \delta g_N(\mathbf{u}^k)\, d\Gamma = \sum_{i=1,2} G_{ext}^{(i)}(\delta\mathbf{u}) \qquad \forall \delta\mathbf{u} \\
&\int_{\Gamma_C^{(1)}} \delta\lambda_N^k\, g_N(\mathbf{u}^k)\, d\Gamma - \frac{h}{E\kappa} \int_{\Gamma_C^{(1)}} \delta\lambda_N\, \lambda_N^k\, d\Gamma = -\frac{h}{E\kappa} \int_{\Gamma_C^{(1)}} \delta\lambda_N\, p_N(\mathbf{u}^{k-1})\, d\Gamma \qquad \forall \delta\lambda_N
\end{aligned} \tag{9}$$

$G_{int}^{(i)}$ and $G_{ext}^{(i)}$ are the virtual work of internal and external forces of body i, respectively. The contact integral in the first equation is the virtual work of contact forces, and δg_N is the virtual gap computed by taking variations in equation (3). The smooth pressure is written as $p_N(\mathbf{u}^{k-1})$ to emphasize the dependence of this variable on the solution of a previous iteration $k-1$. In the second equation, the first integral contains the constraints imposed to fulfill the non-penetrability condition of contact. The other two integral terms in the second equation prevent the contact constraints from being exactly fulfilled but tend to compensate each other as the mesh is refined. At the limit, when the element size tends to zero, $\lambda_N = p_N$ and the exact constraint will be enforced.

Note that, compared with the Nitsche method used in [26], the proposed formulation has a lower number of integrals that need to be evaluate to obtain the tangent matrix of the system. In particular, all the terms of the Nitsche method that derive from the variation of the stabilization term p_N (which is here a function of $\mathbf{u}$) are avoided in the proposed formulation, at the cost of an iterative solution process. It is necessary to verify the conditions under which the iterative method converges to the solution and to check the stability of the system. This is done in the following Section after defining the Lagrange multiplier finite element space.

5. Lagrange multiplier interpolation: Penalty method

The stabilized formulation (9) gives greater freedom than the Lagrange formulation to choose the Lagrange multiplier finite element space. The displacement field

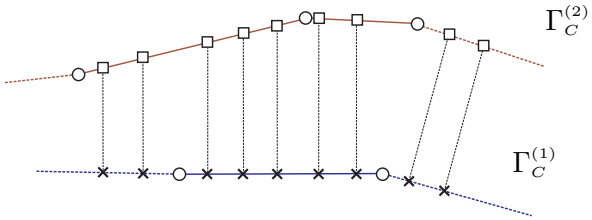

Figure 4: Concentrated inexact numerical integration. The integrands are only evaluated at the quadrature points (shown as x) defined in each contact slave surface segment. The circles are the nodes and the squares are the corresponding contact points on the master surface. Normal vectors are independently defined for each slave segment.

is defined in $\mathbf{u}^h \in H^1(\Omega)$ and the multiplier space $\lambda_N^h \in L^2(\Gamma_C)$. We choose for the displacement field linear 8-node $\mathscr{H}_8$ or quadratic 20-node $\mathscr{H}_{20}$ hexahedral elements, having degree of interpolation $p = 1$ and $p = 2$, respectively. As pointed out above, we deal with standard or cut (immersed boundary) elements.

The only requirement for the Lagrange multiplier space is that it must have adequate approximation properties. Stenberg [48] analyzes the approximation properties of the multiplier space used to impose the Dirichlet boundary conditions using the Nitsche method. From this analysis, if the solution is regular enough, the optimal convergence rate can be achieved [52] if the Lagrange multiplier space is at least a piecewise constant, not necessarily continuous, interpolation for linear elements $\mathscr{H}_8$ and a piecewise linear, not necessarily continuous, interpolation for quadratic elements $\mathscr{H}_{20}$.

In [51] an implicit definition of the multiplier field was introduced for 2D elements, based on the value of the multiplier at the quadrature points of the surface used to numerically evaluate the boundary integrals. The Dirichlet boundary conditions in immersed boundary elements problem was analyzed in this work. For 2D problems, the Dirichlet boundary was divided into segments defined in each cut element. It has been stated that $n_{pg} = 2$ quadrature points for linear elements define a piecewise linear interpolation for the multiplier $q = 1$ and can exactly integrate polynomials of degree 3. As the product of the multiplier and the displacement has degree 2, it is enough to exactly evaluate integrals with constant Jacobian. Similarly, in 2D for quadratic elements $n_{pg} = 3$ allows exact integration and good approximation properties of the multiplier field.

In the case of contact problems, the boundary integrals on the contact surface are more complex because they involve functions defined in the two bodies in contact. Exact evaluation of the contact surface integrals would need a segmentation of the surface, as proposed for the mortar method in [39,40,56]. Instead of looking for exact integration, in this work we use the same strategy proposed in [18,22,50] and depicted

in Figure 4. The approximate integration is performed evaluating the integrand at the quadrature points defined on the surface $\Gamma_C^{(1)}$ regardless of whether the integrand belongs to one or other body. Despite the inexact integration, this method has certain advantages. First, the evaluation has a lower computational cost and is easy to implement. Also, the optimal convergence rate of the finite element solution error can be achieved for linear elements if a uniform refinement is performed. The reason is that the error in the contact integral computation will decrease linearly as the mesh is refined.

The main drawback of this integration is that for quadratic elements the theoretical rate of convergence $p+1$ in energy norm is lost when the mesh is refined. The problem can be alleviated by increasing the number of quadrature points, so that the level of the integration error is reduced. Even though the rate is not improved, the optimal rates of convergence of the finite element error could be achieved for the first meshes when the discretization error is much higher than the integration error. Therefore, from the engineering point of view, the method is suitable for achieving an accurate finite element solution with a reasonable amount of degrees of freedom. It must be pointed out that in some contact problems the regularity of the solution itself limits the theoretical rate of convergence that could be achieved with quadratic elements.

Another alternative that is explored in the numerical examples in the present paper is to impose the contact constraints on both contact boundaries $\Gamma_C^{(1)}$, $\Gamma_C^{(2)}$ at the same time, which is possible due to the stabilized formulation. It can be seen as the double pass strategy defined in the classical penalty method. As the stabilization stress ${p_N}^{(1)}$ and ${p_N}^{(2)}$ are acting at the same time in the two bodies, $\lambda_N = {p_N}^{(1)} + {p_N}^{(2)}$ must be fulfilled. Any weight factor can be defined between 0 and 1 for the two pressures. In the examples we choose ${p_N}^{(1)} = {p_N}^{(2)} = \lambda_N/2$.

5.1. Penalty method

Once the Lagrange multiplier field is defined, the iterative method of equation (9) can be simplified by eliminating the Lagrange multipliers. As the interpolation is defined as a piecewise discontinuous function, the multiplier can be condensed element by element before the assembly. Indeed, due to the concentrated numerical integration, they can also be eliminated for every quadrature point. The value of the Lagrange multiplier at each quadrature point is:

$$\lambda_{Ng}^k = p_N(\mathbf{u}^{k-1}) + \frac{E\kappa}{h} g_{Ng} \tag{10}$$

where the subindex g is used to denote the value of the variable at the quadrature point.

Formally, we proceed as in [48, 52] to obtain a simplified stabilized problem. We can take the variation of the multiplier as the projection in L^2 of an appropriate displacement field in the second equation of the problem (9) to condense the multiplier

and then substitute in the first equation to obtain:

$$\sum_{i=1,2} G_{int}^{(i)}(\mathbf{u}^k, \delta\mathbf{u}) + \frac{E\kappa}{h} \int_{\Gamma_C^{(1)}} g_N(\mathbf{u}^k)\, \delta g_N \, d\Gamma = \sum_{i=1,2} G_{ext}^{(i)}(\delta\mathbf{u}) - \int_{\Gamma_C^{(1)}} \delta g_N \, p_N(\mathbf{u}^{k-1}) \, d\Gamma \tag{11}$$

Here we find a close similarity between the proposed formulation and the perturbed Lagrangian formulation [47]. In the first iteration, when $p_N = 0$, the formulation is a pure penalty method, but computed in a distributed sense. This coincides with the formulation in [47]. As far as the integral can be exactly evaluated, the penalty term in equation (11) is like a distributed spring that joins the two bodies in contact. As has been pointed out above, the number of quadrature points can be freely chosen, provided that they define a suitable interpolation of sufficient degree. Increasing the number of points only affects the numerical integration error. Although the number of constraints in the formulation (9) is increased, as we condense the Lagrange multipliers, the number of equations remains the same for the simplified formulation (11). On the right hand side of Equation (11) the smooth stress field has the effect of compensating the error introduced by the penalty method. This term is computed iteratively from the finite element solution (see Subsection 5.3). Another alternative followed in the literature in order to find stable contact formulations using springs without stabilizing terms (penalty formulation) is to properly choose the number of quadrature points and define a distributed integration [16, 58].

The system of Equation (11) can be written in matrix form using the standard finite element procedure to define the following residual:

$$\mathbf{r}^k = \left(\mathbf{K} + \frac{E\kappa}{h}\mathbf{M}\right)\mathbf{d}^k - \mathbf{f} - \mathbf{S}\,\mathbf{d}^{k-1} = 0 \tag{12}$$

where $\mathbf{d}^k$ is the nodal displacements vector in the iteration k, $\mathbf{K}$ is the stiffness matrix and $\mathbf{f}$ is the external force vector. For clarity of presentation we assume that the initial gap g_{N0} is zero. Matrix $\mathbf{M}$ is computed from the second integral of Equation (11) using the numerical integration presented above and the gap definition. Although, in general, h is included in the integral of each element for meshes with different element sizes, here we leave the factor to emphasize the dependence of this term on the element size. Matrix $\mathbf{S}$ is derived from the last integral of Equation (11) and points out the linear dependence of the smooth stress field with respect to the displacement field. In practice, this term is computed as the additional contact force vector $\mathbf{f}_N^{k-1}$ depending on the previous displacement field and $\mathbf{S}$ is not explicitly obtained.

5.2. Large deformations

The formulation proposed above for small deformations can be extended to deal with large deformations and large sliding problems. The virtual work of internal and

external forces can be evaluated in the standard way for all type of material behavior, including hyper-elasticity and plasticity. In addition to the contact iterations, another non-linear behavior due to contact has to be considered, i.e. the change of the contact point as the bodies deform. This makes the gap and the virtual gap, to be non-linear functions of the displacements. Equation (11) is now the residual of a non-linear equation that can be solved using a semi-smooth Newton method. After numerical integration the residual can be expressed as:

$$\delta\mathbf{u}\cdot\mathbf{r}^k = \delta\mathbf{u}\cdot\left(\mathbf{f}_{int}(\mathbf{u}^k)-\mathbf{f}_{ext}\right)+\sum_{\forall g} H_g\left(\frac{E\kappa}{h}g_{N\,g}(\mathbf{u}^k)+p_{N\,g}(\mathbf{u}^{k-1})\right)\delta g_{N\,g}J_g \tag{13}$$

where H_g is the weight of the quadrature point and J_g the Jacobian of the transformation. Here the sum is extended to the active quadrature points that will be discussed in the following subsection.

Here any definition found in the literature of the contact variables g_N and δg_N at the quadrature points could be used (based on closest point projection [33, 54] for example) although the aim of this paper is not to deal with the computation details of these contact variables for large deformation problems. We have chosen the definition given in a previous paper [50], to which we refer for details of linearizations. Also, we neglect the linearization of the Jacobian because it leads to a non-symmetric tangent matrix. An additional term could be included in the functional of the formulation to recover symmetry [17] and perform a consistent linearization. In practice, the convergence obtained without consistent linearization in the numerical problems analyzed seems to be acceptable.

We use the definition of the gap based on the ray tracing, so we follow the formulation proposed in [50] also used in [24] for 2D problems, but extended to 3D. We recall here the main steps of the derivation. Taking variations in expression (2), we have

$$\delta g_N = (\delta\mathbf{u}^{(2)}-\delta\mathbf{u}^{(1)})\cdot\mathbf{n}^{(1)}+\mathbf{s}_\xi^{(2)}\cdot\mathbf{n}^{(1)}\,\delta\xi+\mathbf{s}_\eta^{(2)}\cdot\mathbf{n}^{(1)}\,\delta\eta \tag{14}$$

where $\delta\xi$ and $\delta\eta$ are the variations of the contact point local coordinates and $\mathbf{s}_\xi^{(2)}$ and $\mathbf{s}_\eta^{(2)}$ are the tangent vectors. The variations of the contact point can be computed using the same procedure as in [50] to obtain the following system (2), we have

$$\begin{bmatrix} \mathbf{s}_\xi^{(1)}\cdot\mathbf{s}_\xi^{(2)} & \mathbf{s}_\xi^{(1)}\cdot\mathbf{s}_\eta^{(2)} \\ \mathbf{s}_\eta^{(1)}\cdot\mathbf{s}_\xi^{(2)} & \mathbf{s}_\eta^{(1)}\cdot\mathbf{s}_\eta^{(2)} \end{bmatrix}\begin{Bmatrix} \delta\xi \\ \delta\eta \end{Bmatrix} = \begin{Bmatrix} (\delta\mathbf{x}^{(2)}-\delta\mathbf{x}^{(1)})\cdot\mathbf{s}_\xi^{(1)}+g_N\delta\mathbf{n}^{(1)}\cdot\mathbf{s}_\xi^{(1)} \\ (\delta\mathbf{x}^{(2)}-\delta\mathbf{x}^{(1)})\cdot\mathbf{s}_\eta^{(1)}+g_N\delta\mathbf{n}^{(1)}\cdot\mathbf{s}_\eta^{(1)} \end{Bmatrix} \tag{15}$$

The tangent matrix is obtained taking the derivative with respect to the displacements. As pointed out above, we neglect the derivative of the Jacobian. The tangent matrix used in the numerical examples is:

$$\begin{aligned}\mathbf{K}_T = \mathbf{K} &+ \sum_{\forall g} H_g\frac{E\kappa}{h}\Delta g_{N\,g}(\mathbf{u}^k)\,\delta g_{N\,g}J_g \\ &+ \sum_{\forall g} H_g\left(\frac{E\kappa}{h}g_{N\,g}(\mathbf{u}^k)+p_{N\,g}(\mathbf{u}^{k-1})\right)\Delta\delta g_{N\,g}J_g\end{aligned} \tag{16}$$

where $\mathbf{K}$ is the directional derivative of the work of internal forces with respect to the displacements. For the derivative of the virtual gap $\Delta\delta g_N$ the procedure described above can be followed.

5.3. Solution algorithm

Algorithm 5.1: ()

Compute p_N from previous step (Subsection 3.2)
$\lambda_{Ng} \leftarrow p_{Ng} + \dfrac{E\kappa}{h} g_{Ng}$
while $residual > Tol$: Augmentation loop
do
- **while** $residual > Tol$: Contact loop
  - **do**
    - Check active quadrature points: $\lambda_{Ng} < 0$
    - Solve system of Equation (11)
    - Check residual. Equation (12)
- Update p_N
- Check residual. Equation (12)

The proposed method has certain similarities with the Uzawa algorithm used in the augmented Lagrangian formulation, in which updating the Lagrange multiplier is called augmentation. We use the same term for the updating performed in (10), using the smooth stress field. It also resembles the method used in [1] to solve contact problems. The algorithm for small deformation problems is shown in Table 5.1. For every load step, the smooth stress field p_{Ng} and the gap g_{Ng} are first obtained for each quadrature contact point from the previous solution.

In addition to the augmentation iterations, another iterative process is defined to resolve the contact surface, i.e. to determine which part of the potential contact surface is active and will be used to impose the impenetrability constraints. The contact check is performed at each quadrature point, using the value of the multiplier defined in Equation (10), so that $\lambda_{Ng} \leq 0$. It can be seen that the contact iterations are performed with a constant value of the smooth stress p_N, which acts as an external pressure on the contact surface, so that the contact iterations are similar to a pure penalty method. The contact iterations run until the active contact points are unchanged. In this work this is directly checked with the residual of Equation (12).

For large deformation problems, the structure of the algorithm is the same, the only changes being the computation of the residual, which is now defined in Equation (13), and the solution of the system of equations by a Newton method.

In terms of computational cost, the proposed method is equivalent to an augmented Lagrange formulation implemented by the Uzawa algorithm. The advantage of the proposed method is the freedom to choose the number of quadrature points at which the contact constraints are imposed as the method is stabilized. Compared with the Lagrange multiplier formulation (or augmented Lagrange in which the multipliers remain as variables of the system), in the proposed method the system of equations to be solved in each iteration is smaller in size. Another advantage is that the system matrix is positive definite, which usually reduces the solution time. On the other hand, the number of iterations is in general greater as there is a nested loop.

5.4. Convergence of the iterative method

The iterative process for augmentations defined above in Equation (12) can be viewed as the Richardson method of solving a system of equations. This system can be rewritten as:

$$\left(\mathbf{K} + \frac{E\kappa}{h}\mathbf{M}\right)\mathbf{d}^k = \mathbf{S}\,\mathbf{d}^{k-1} + \mathbf{f} \tag{17}$$

The convergence [44, 52] is then verified if the spectral radius of the iteration matrix $\left(\mathbf{K} + \frac{E\kappa}{h}\mathbf{M}\right)^{-1}\mathbf{S}$ is lower than 1 (equivalently, the modulus of any eigenvalue α is lower than 1), even if the set of active quadrature points changes from one iteration to another.

To prove this, we start with the definition of the eigenvalue problem. Any eigenvector $\mathbf{v}^*$ associated with an eigenvalue α of the iteration matrix fulfils

$$\mathbf{S}\,\mathbf{v}^* = \alpha\left(\mathbf{K} + \frac{E\kappa}{h}\mathbf{M}\right)\mathbf{v}^* \tag{18}$$

On the other hand, if the following equation is satisfied for any nodal displacement vector $\mathbf{v}$:

$$\mathbf{v}^T\mathbf{S}\,\mathbf{v} < \mathbf{v}^T\left(\mathbf{K} + \frac{E\kappa}{h}\mathbf{M}\right)\mathbf{v} \qquad \forall\mathbf{v} \tag{19}$$

then the modulus of α is necessarily lower than 1 and the convergence is proven.

To check Equation (19), we use the definition of the stabilization term $\mathbf{S}\,\mathbf{v}$:

$$\left|\mathbf{v}^T\mathbf{S}\,\mathbf{v}\right| = \left|\int_{\Gamma_C^{(1)}} g_N(\mathbf{v})\,p_N(\mathbf{v})\;d\Gamma\right|.$$

Applying the Cauchy-Schwarz inequality, using Equation (8), and taking into account that for two positive numbers x, y , it holds that $2\,x\,y \leq x^2 + y^2$, we have:

$$\begin{aligned} \left|\mathbf{v}^T \mathbf{S}\, \mathbf{v}\right| = \left| \int_{\Gamma_C^{(1)}} g_N(\mathbf{v})\, p_N(\mathbf{v})\, d\Gamma \right| \leq \|g_N(\mathbf{v})\|_{L^2,\Gamma_C^{(1)}} \|p_N(\mathbf{v})\|_{L^2,\Gamma_C^{(1)}} \leq \\ \|g_N(\mathbf{v})\|_{L^2,\Gamma_C^{(1)}} \sqrt{\frac{EC}{h}} \|\mathbf{v}\|_E \leq \frac{EC}{4h} \|g_N(\mathbf{v})\|^2_{L^2,\Gamma_C^{(1)}} + \|\mathbf{v}\|^2_E \end{aligned} \tag{20}$$

Now, taking $\kappa > C/4$ we obtain the bound of the stabilization term and the iterative process will converge.

Remark: The stabilization term is only computed on the active contact zone of the current iteration, even if the size of the contact surface $\Gamma_C^{(1)}$ has been modified. This ensures that Equation 20 is verified even in this case.

6. Numerical examples

Some academic examples have been solved to test the performance of the proposed formulation. We used standard finite elements and immersed boundary elements with linear $\mathscr{H}_8$ and quadratic $\mathscr{H}_{20}$ interpolation and different number of quadrature points. In the case of standard linear elements we tried $n_{pg} = 2 \times 2$, $n_{pg} = 3 \times 3$ and $n_{pg} = 16 \times 16$. For quadratic elements we tried $n_{pg} = 3x3$ and $n_{pg} = 16 \times 16$. For immersed boundary elements the number of quadrature points is based on the triangulation of the surface due to the intersection of the real geometry with the element. For integration purposes, we divide the hexahedral into tetrahedral and use the quadrature formulas for the surface triangles of the tetrahedral whose face coincides approximately with the contact surface.

6.1. Hollow sphere under internal pressure

The first example to be tested is a problem with an exact solution, so that the discretization error can be exactly computed. The problem is a hollow sphere under internal pressure. We define two volumes that are discretized using non-conforming meshes as depicted in Figure 5. A sequence of uniformly refined meshes is obtained by element subdivision. In this problem all the quadrature points of the potential contact surface are in contact, so there are no iterations due to changes in contact conditions.

The first test was performed to check the influence of the constant κ in the finite element solution using standard linear (L) and quadratic (Q) elements. In Figure 6 the energy norm error and the L^2 norm error of the finite element solution are plotted

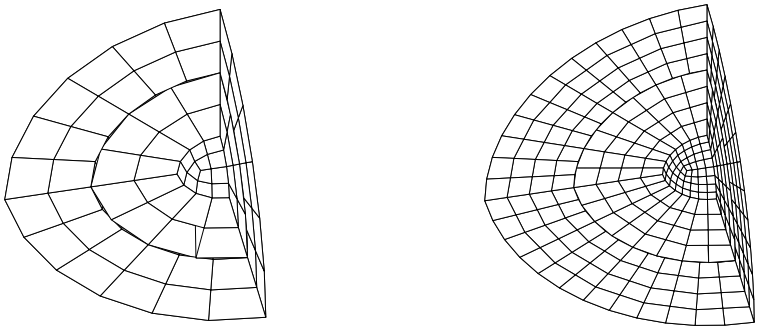

Mesh 1 Mesh 2

Figure 5: First two meshes of the sequence used to solve the problem of a hollow sphere under internal pressure. The hollow sphere is discretized into two volumes using non-conforming meshes.

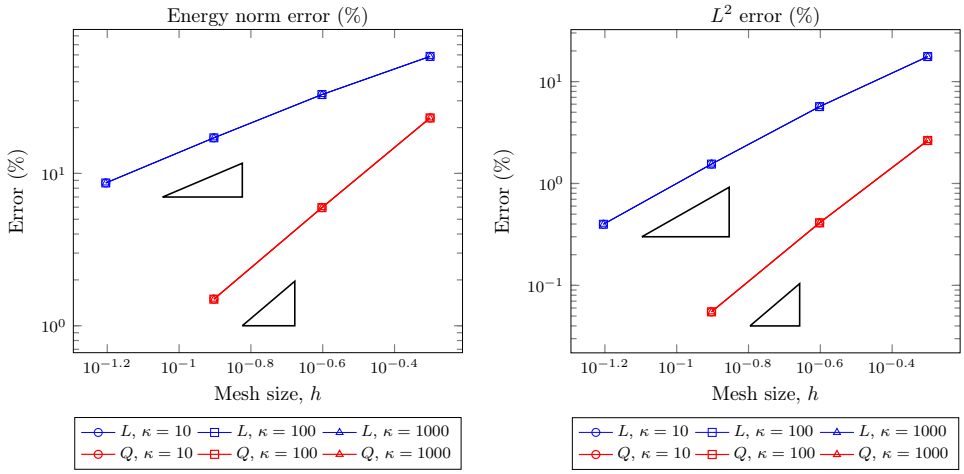

Figure 6: Hollow sphere under internal pressure problem. Analysis of the influence of parameter κ. Energy norm (left) and L^2 norm (right) error of the solution as a function of the element size.

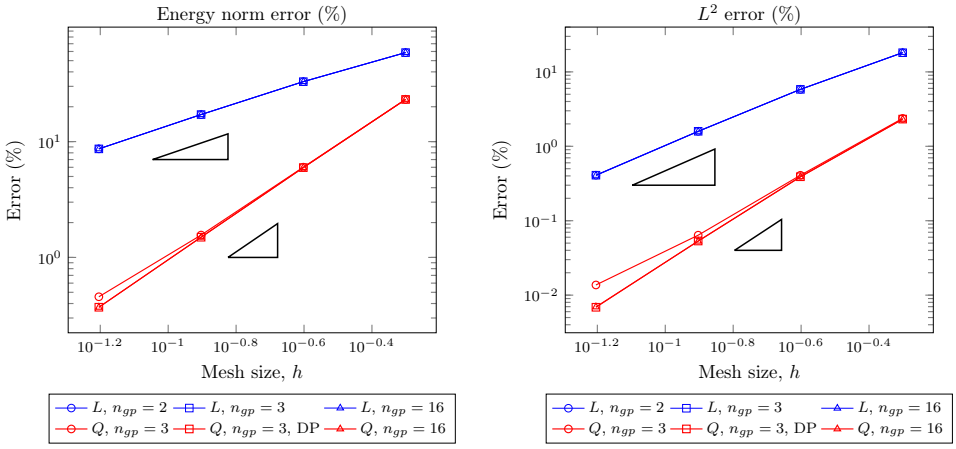

Figure 7: Analysis of the influence of the integration error for the hollow sphere under internal pressure problem. Energy norm (left) and L^2 norm (right) error of the solution as a function of the element size.

as a function of a representative element size. The triangles show the theoretical convergence rate that can be achieved in every case. These test were performed using $n_{pg} = 16x16$ quadrature points both for $\mathscr{H}_8$ and $\mathscr{H}_{20}$ elements to keep the integration error as small as possible. The theoretical convergence rate is obtained in all cases, at least for this level of error. The results show that the influence of the parameter κ is negligible in this example, as the curves for different values of κ perfectly overlap.

As pointed out above, it is not expected that the quadratic elements can achieve the theoretical rate of convergence of the finite element solution because of the integration error. However, if the meshes are not very refined (for example, the meshes shown in Figure 5), the level of the discretization error is much higher than the integration error. Despite the lower rate of convergence of the latter, the optimal convergence rate can be achieved. To test the influence of the integration error we solved the same problem using different number of quadrature points and different types of integration. For $\mathscr{H}_8$ linear elements we used $n_{pg} = 2 \times 2$, $n_{pg} = 3 \times 3$ and $n_{pg} = 16 \times 16$. For $\mathscr{H}_{20}$ quadratic elements we used $n_{pg} = 3 \times 3$, $n_{pg} = 3 \times 3$ with double pass integration (i.e. the surfaces of both bodies are considered at the same time as contact surfaces where the numerical integration is performed), and $n_{pg} = 16 \times 16$. The discretization error is shown in Figure 7 in energy and L^2 norms. The triangles show the theoretical rate of convergence. Optimal convergence is achieved for linear elements. However, for quadratic elements using $n_{pg} = 3 \times 3$ quadrature points, the integration error seems to affect the solution for the more refined meshes and the convergence rate is reduced. To alleviate this effect, using both a double pass strategy and more quadrature points seems to reduce the integration error and allows the optimal rate to be recovered in this case and for these element sizes.

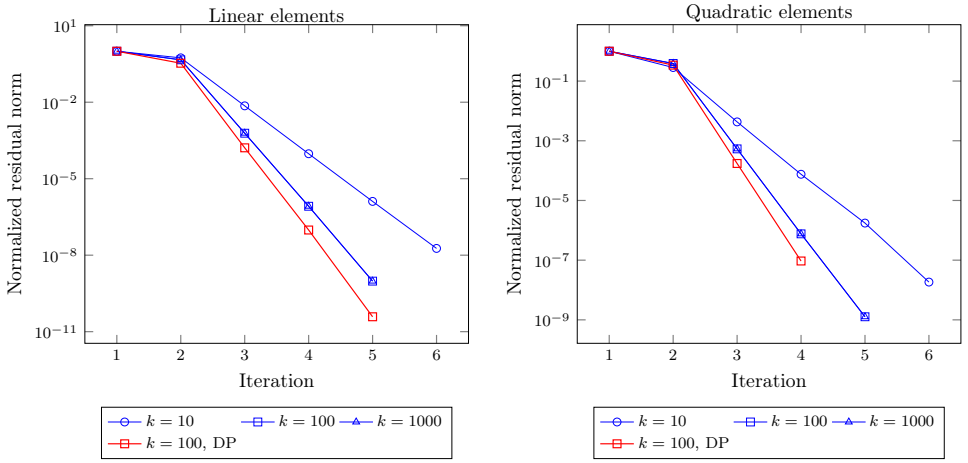

Figure 8: Hollow sphere under internal pressure problem. Convergence of the Richardson iteration of the system. The normalized norm of the residual is shown for linear and quadratic elements.

This linear example was used to test the convergence of the Richardson iterations of the system and the influence of parameter κ. In Figure 8 the normalized norm of the residual (equation (11)) is shown as a function of the number of iterations. The results are shown for linear $\mathscr{H}_8$ and quadratic $\mathscr{H}_{20}$ elements and different values of the parameter κ. Convergence is achieved between 4 and 6 iterations. This behavior is representative of all the tests ran for other numerical examples. In this case, the best convergence is achieved with a double pass strategy and $\kappa = 100$.

6.2. Rigid sphere in contact with a deformable block

In the second example a contact problem between a rigid sphere and an elastic solid is solved using an immerse boundary mesh. The geometry of the elastic solid is shown in Figure 9. It is a modified block with dimensions $2 \times 2 \times 2$ units of length, in which the upper face is a parabolic surface. The highest point of the parabolic surface is at 2.5 units of length. As it can be observed the elastic solid geometry is embedded in a uniform Cartesian Grid. The boundary elements are cut by the geometry and integration is only performed in the internal part of these elements. A sub-triangulation of the boundary elements using linear tetraedral is performed only for integration purposes. The number of quadrature points on the contact surface also depends on this sub-triangulation (7 quadrature points for each triangle).

The sphere is located above the curved surface of the block, and contact occurs at this curved face (see Figure 10). A rigid body motion towards the elastic solid is applied to the sphere causing a maximum theoretical penetration of $Dz = 0.15$ or

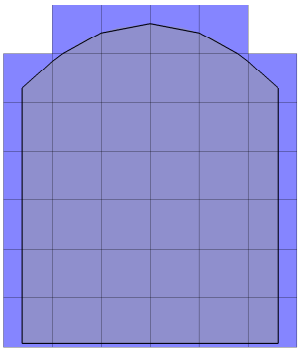

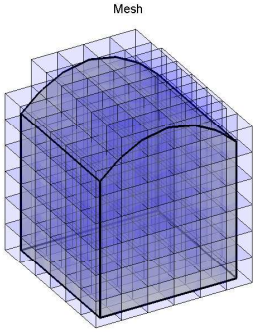

Geometry Cartesian Grid

Figure 9: Model of the rigid sphere contact with an immersed boundary mesh.

$Dz = 0.3$ units of length. The radius of the sphere is 2 units of length. Figure 10 shows the deformed configuration of the elastic block. The colormap values are related to the modulus of the displacement field. The contact traction at each quadrature point of the surface is also shown in the same figure. The convergence of the contact iterations and the augmentations is shown in Table 1 for different initial penetration Dz and penalty parameter κ values. We use a tolerance of 10^{-8} to determine if the solution has converged, both for the contact and Richardson iterations.

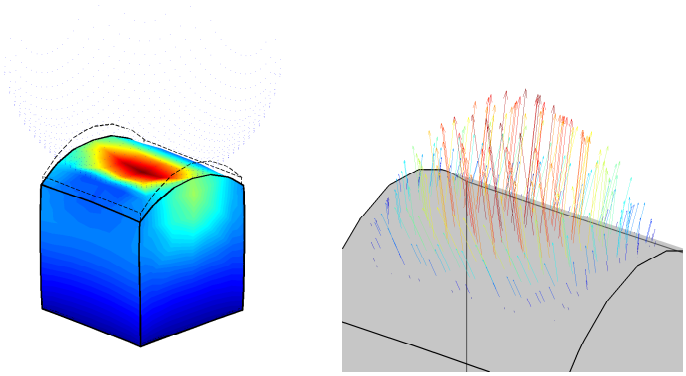

Figure 10: Contact traction of the rigid sphere contact with an immersed boundary mesh.

Table 1: Rigid sphere in contact with an immersed boundary mesh. Convergence of the contact and Richardson iterations. Normalized norm of the residual. The mark indicates that the stabilizing stress p_N was updated in the previous iteration.

Iter	$Dz = -0.15$, $\kappa = 10$	$Dz = -0.3$, $\kappa = 10$	$Dz = -0.3$, $\kappa = 100$
2	1.71E-01	1.16E-02	5.88E-03
3	5.68E-02	4.09E-03	1.75E-03
4	3.19E-02	2.03E-03	1.83E-03
5	2.22E-02	1.53E-03	4.56E-04
6	1.07E-02	4.00E-04	2.91E-04
7	3.16E-16	3.49E-16	7.21E-05
8	∗1.48E-02	∗1.38E-02	1.05E-05
9	3.11E-04	3.97E-16	1.50E-06
10	3.64E-16	∗2.90E-04	1.06E-16
11	∗2.79E-04	3.38E-16	∗5.12E-04
12	4.80E-16	∗6.01E-06	1.55E-05
13	∗5.72E-06	3.38E-16	1.03E-16
14	2.98E-16	∗1.42E-07	∗1.20E-06
15	∗1.23E-07	3.12E-16	1.15E-16
16	3.97E-16	∗3.89E-09	∗2.85E-09
17	∗2.76E-09		

6.3. Deformable ring in contact with a deformable block

The third example is a large deformation and large sliding contact problem. A scheme of the example is shown in Figure 11. The upper body consists of two joined rings of equal thickness but different Neo-Hookean hyperelastic material properties. The material parameters are $E = 10^5$ and $\upsilon = 0.3$ for the inner ring and $E = 10^3$ and $\upsilon = 0.3$ for the outer ring. The problem is 3D, with symmetry boundary condition applied to the frontal plane. The ring thickness is 40 units of length and the block thickness is 50 units of length. The block is linear elastic with material parameters $E = 1000$ and $\upsilon = 0.3$. We solved the problem assuming two materials for the block: a pure elastic behavior and plasticity with yielding limit $S_y = 50$ and plastic hardening $H = 50$. A downward displacement of $Dy = 90$ is applied to the elastic ring. The displacement is applied in 20 steps in the elastic case and 40 steps in the plastic case, with the time ranging from $t = 0$ to $t = 1$. Linear elements were used

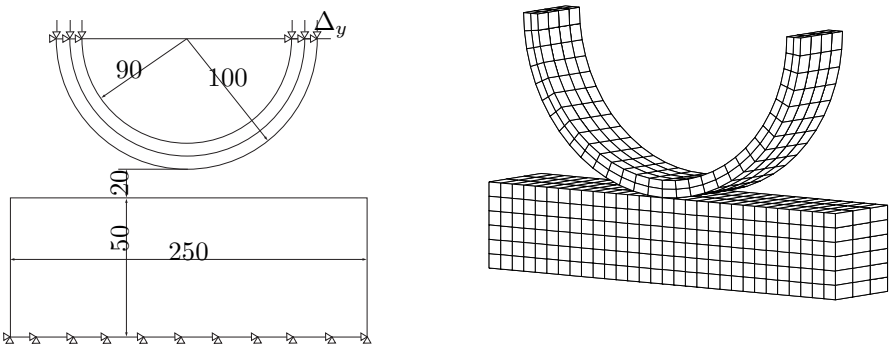

Figure 11: Initial configuration of the elastic ring contact problem.

in the simulation and the number of quadrature points was $n_{pg} = 4 \times 4$. The block contact surface was taken as slave surface where the integration is performed.

Figures 12 and 13 shown some snapshots of the deformed configuration and contact pressure with elastic and plastic behavior of the block. In the first time steps, the deformation of the block is pure elastic and both examples show the same deformed configuration. From $t = 0.65$ plastic deformation occurs in the second case that causes a different deformation of the ring and contact pressure distribution. This effect can also be noticed in Figure 14, where the reaction force is plotted versus the time step for both cases (elastic and elasto-plastic).

In Table 2 we show the convergence of the contact and Richardson iterations for different time steps and both elastic (EL) and elasto-plastic (PL) behavior of the block. The normalized norm of the residual (equation 13) is shown as a function of the iterations. A mark is shown when an augmentation is performed, i.e. the stabilizing stress p_N is updated. The tolerance of the relative error of the residual is set at $1 \cdot 10^{-8}$. As in the linear Example 1 shown above, after 3 or 4 Richardson's iterations the solution has almost converged and the changes in the displacement or contact stresses are very small.

6.4. Bicycle inner tube

The last example is depicted in Figure 15 and shows a quarter of the inner tube of a bicycle tire that is submitted to increasing internal pressure. As the tube deforms, a contact occurs with the tire and the rim. The rim is an elastic material with properties $E = 10^8$ and $\upsilon = 0.3$, the inner tube and the casing are hyper-elastic materials with $E = 1000$ and $\upsilon = 0.3$. The pressure is increased from 0 to $p = 40$ units of pressure. A variable time step increment is applied from $t = 0$ to $t = 1$ in 40 steps. In the front plane of the casing there is a crack that allow the inner tube to escape. The

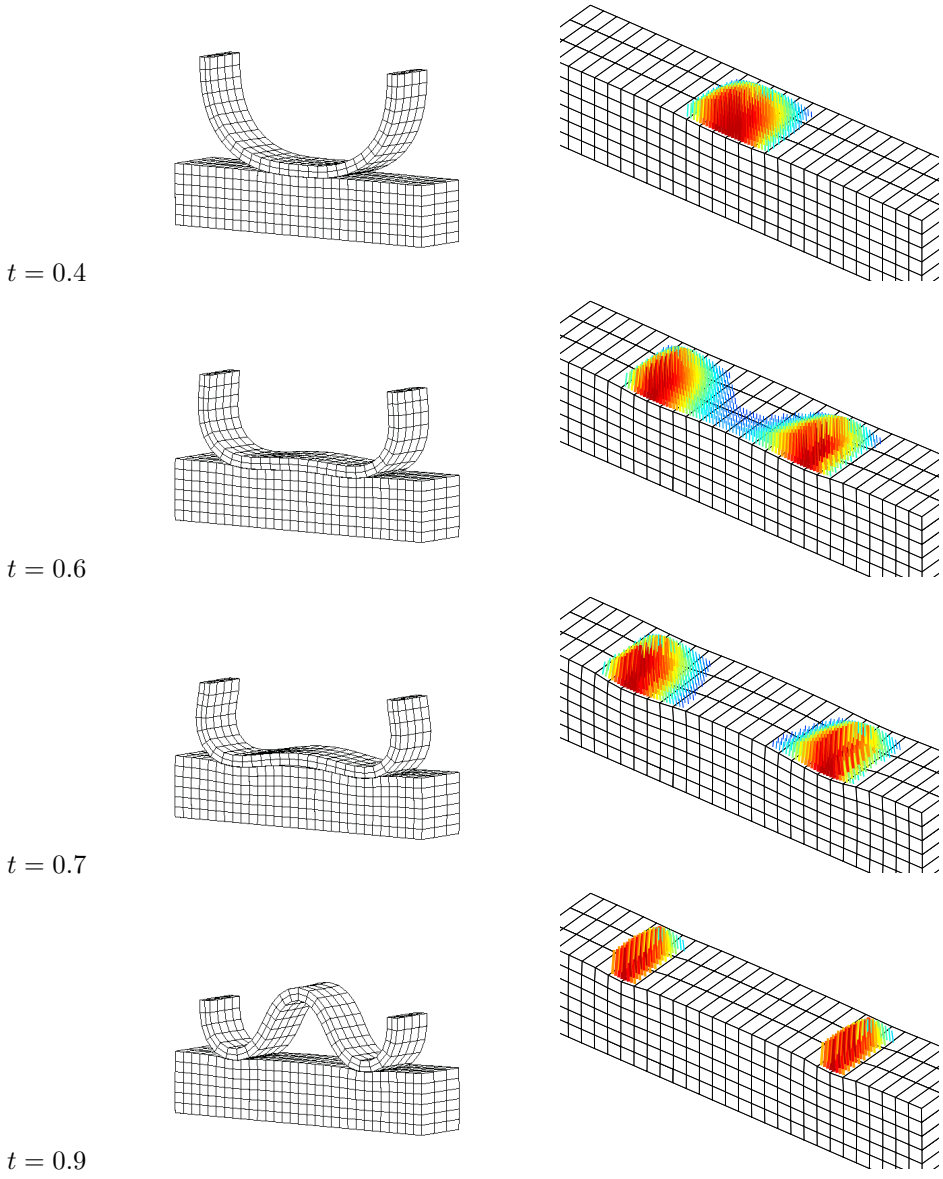

Figure 12: Deformable ring in contact with an elastic block. Deformation and contact pressure for different time steps of the simulation.

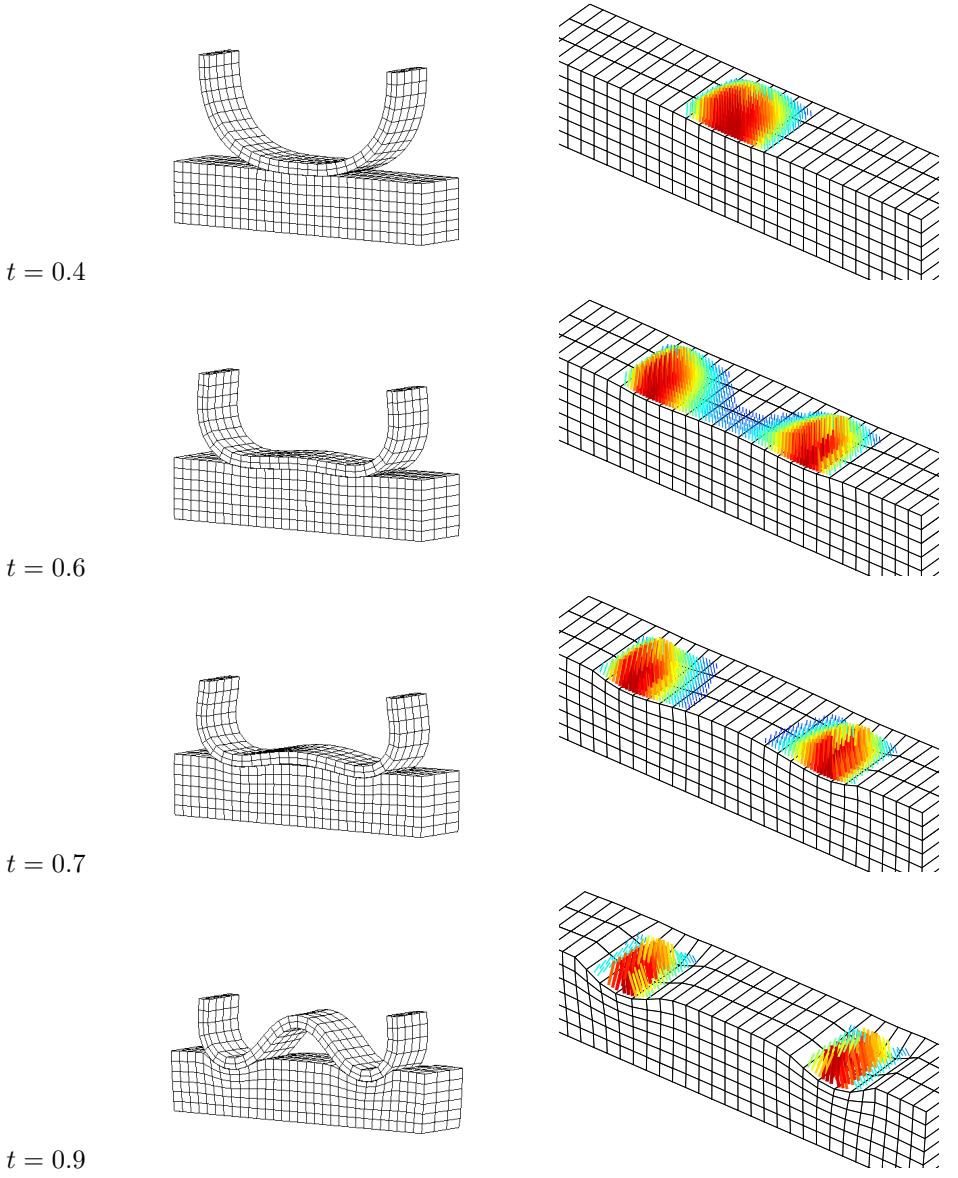

Figure 13: Deformable ring in contact with an elasto-plastic block. Deformation and contact pressure for different time steps of the simulation.

Table 2: Elastic rings in contact with a block. Convergence of the non-linear contact and Richardson iterations. The mark indicates that an augmentation is performed, so the stabilizing stress p_N is updated. The normalized norm of the residual is shown.

Iter	$t = 0.5$, EL	$t = 0.6$, EL	$t = 0.7$, EL	$t = 0.5$, PL	$t = 0.6$, PL	$t = 0.7$, PL
2	8.07E-02	8.74E-02	1.00E-01	4.17E-02	4.44E-02	4.84E-02
3	1.15E-03	9.02E-04	1.89E-03	7.38E-04	7.44E-04	5.19E-03
4	4.58E-05	1.91E-04	5.99E-04	1.63E-05	5.15E-04	1.54E-04
5	1.42E-07	2.32E-06	1.52E-04	4.70E-07	6.99E-06	6.70E-06
6	3.23E-10	1.27E-08	4.11E-05	6.26E-10	3.97E-07	6.39E-08
7	∗3.29E-04	4.39E-11	5.59E-06	∗4.25E-04	1.01E-09	4.05E-10
8	1.53E-06	∗4.68E-04	3.16E-10	4.75E-07	∗8.62E-04	∗1.53E-03
9	3.40E-09	4.09E-06	∗5.88E-04	2.07E-09	1.49E-06	6.09E-06
10	∗1.58E-06	1.08E-08	2.77E-06	∗2.14E-06	1.38E-08	5.81E-08
11	2.20E-09	4.84E-11	2.49E-08	2.85E-09	4.50E-11	3.19E-10
12	∗9.25E-09	∗2.33E-06	1.92E-10	∗1.39E-08	∗5.48E-06	∗1.17E-05
13		5.33E-09	∗3.58E-06	2.36E-11	9.60E-09	5.36E-08
14		∗1.48E-08	1.29E-08	∗1.11E-10	1.94E-11	2.88E-10
15		4.11E-11	8.92E-11		∗4.07E-08	∗1.02E-07
16		1.13E-10	∗2.17E-08		8.48E-11	3.40E-10
17			8.45E-11		∗3.76E-10	∗8.22E-10
18			∗1.36E-10			

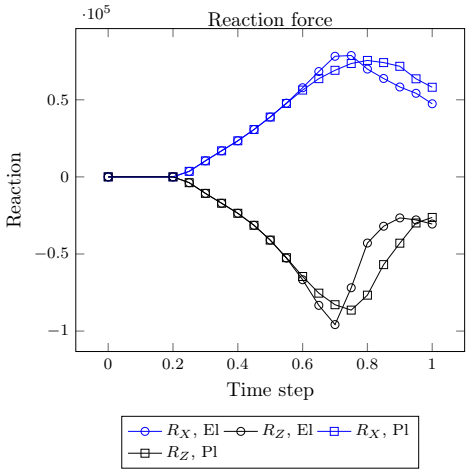

Figure 14: Elastic ring in contact with a block. Reaction force in the ring as a function of the time step.

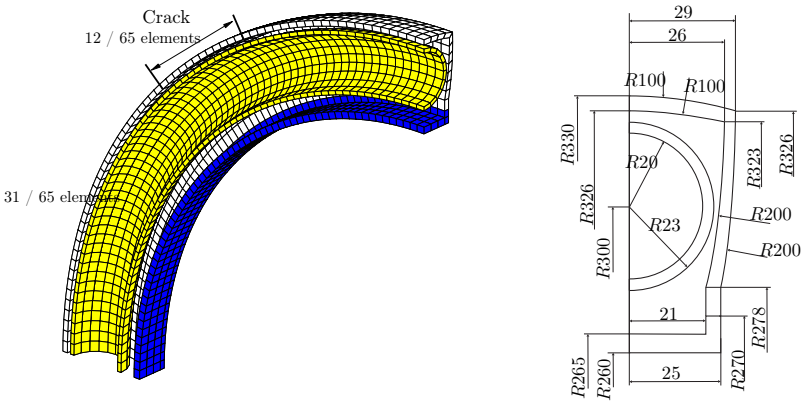

Figure 15: Model of the bicycle tire contact problem. The inner tube is shown in yellow (light grey), the rim in blue (dark grey) and the casing in white.

number of elements in the casing at this plane is 65. The casing is subdivided in 65 equal segments corresponding to the element edge and the crack ranges as depicted in Figure 15. The value of the penalty constant was $\kappa = 10$. The problem was solved using both a double pass and single pass strategies. The deformed configuration is shown in figure 16 for different time steps using the double pass contact. In table 3 a comparison of the residual convergence is shown. In this example, similar behavior is found for both strategies.

Table 3: Inner tube contact problem. Convergence of the non-linear contact and Richardson iterations. The mark indicates that an augmentation was performed in the previous iteration. The normalized norm of the residual is shown.

Iter	DP	SP
2	2.83E-02	2.82E-02
3	4.68E-04	5.17E-04
4	1.34E-08	1.48E-08
5	∗3.86E-03	∗7.72E-03
6	2.03E-08	4.36E-08
7	∗1.34E-06	8.55E-11
8	8.70E-11	∗5.36E-06
9	∗1.34E-09	1.26E-10
10		∗ 9.99E-09

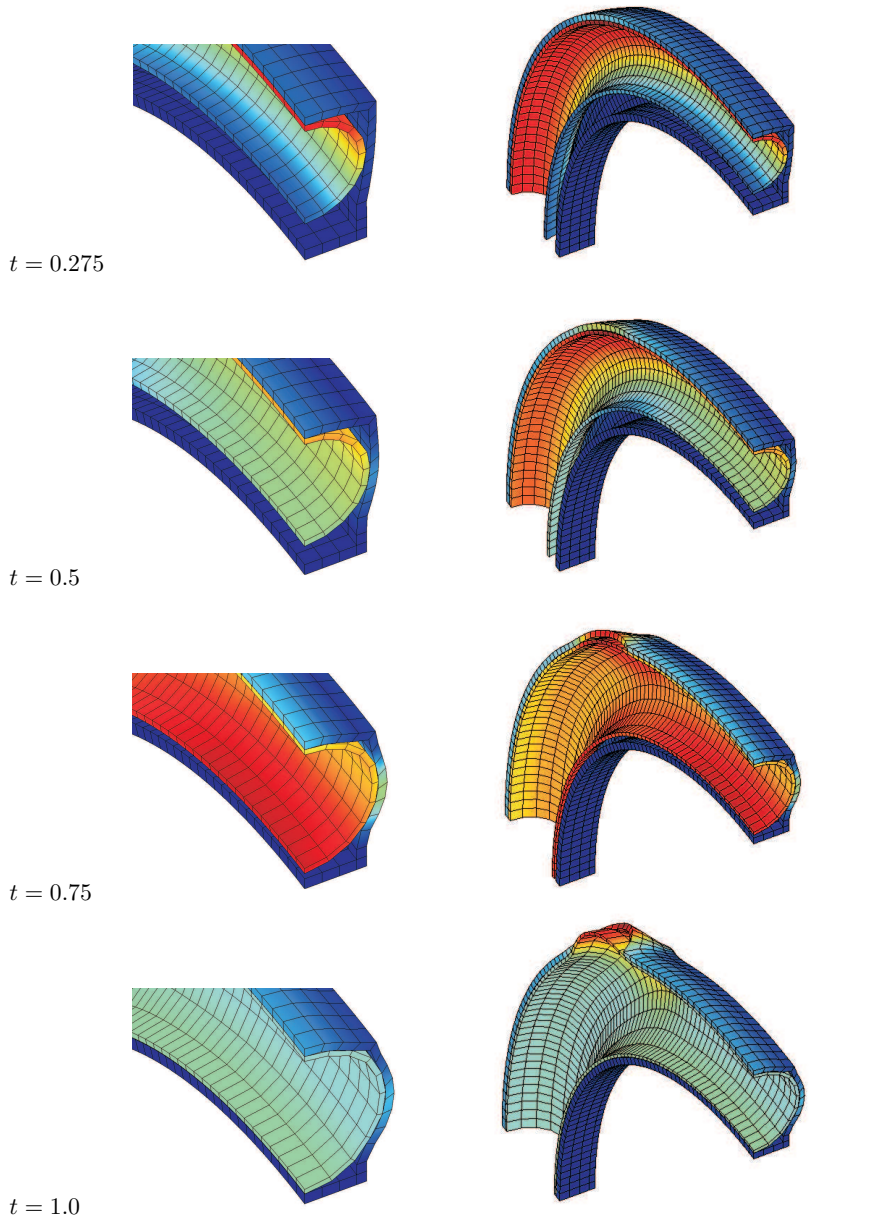

Figure 16: Inner tube contact problem. Comparison of the deformed configuration for different time steps. The colormap is proportional to the modulus of the displacement.

7. Conclusions

This paper proposes a new method for solving contact problems. The formulation is based on the stabilized Nitsche method and after simplifying the equations by condensing the multipliers, a modified penalty formulation is obtained. The method has similarities with the perturbed Lagrangian formulation [47], but with the addition of an extra term that can be computed iteratively and makes the formulation consistent. The proposed method was effectively applied to solving large and small deformation problems implemented with 3D standard 8-node linear and 20-node quadratic elements and with immersed boundary elements in which a Cartesian grid is cut by the real geometry. The method was also tested for materials with elastic, elasto-plastic and hyperelastic behavior. The formulation is robust and simple and can converge to the exact solution with optimal convergence rates.

The results show an optimal convergence rate of the finite element solution for linear elements. For quadratic elements, the integration error can reduce the optimal convergence rate. To overcome this problem, the use of more quadrature points or a double pass strategy has been shown to be effective from the engineering point of view. The method has a user-dependent parameter κ to be defined. In the numerical examples we analyzed a wide range of variation of κ from 10 to 1000 and similar discretization errors and convergence of the iterations were obtained.

A double iterative process is defined to solve contact problems. The first loop is the contact iteration in which the stabilization stress is kept constant and the formulation is a pure penalty method, with κ as penalty constant. The convergence analysis of the method show that a relatively high value of the penalty parameter is needed to guarantee convergence. This value prevents the use of very large time step increments in which the initial penetration of the unconverged solution is very large, and can be considered as a limitation of the method.

Acknowledgements

The authors wish to thank the Spanish Ministerio de Economia y Competitividad for the financial support received through the DPI Project DPI2013-46317-R.

References

[1] Annavarapu, C., Hautefeuille, M., Dolbow, J.: A robust Nitsche's formulation for interface problems. Comput. Method. Appl. M. **228**, 44–54 (2012)

[2] Annavarapu, C., Hautefeuille, M., Dolbow, J.: Stable imposition of stiff constraints in explicit dynamics for embedded finite element methods. Int. J. Numer. Meth. Eng. **92**(2), 206–228 (2012)

[3] Annavarapu, C., Hautefeuille, M., Dolbow, J.: A Nitsche stabilized finite element method for frictional sliding on embedded interfaces. Part II: Intersecting interfaces. Comput. Method. Appl. M. **267**, 318–341 (2013)

[4] Annavarapu, C., Hautefeuille, M., Dolbow, J.: A Nitsche stabilized finite element method for frictional sliding on embedded interfaces. Part I: Single interface. Comput. Method. Appl. M. **268**, 417–436 (2014)

[5] Baiges, J., Codina, R., Henke, F., Shahmiri, S., Wall, W.A.: A symmetric method for weakly imposing Dirichlet boundary conditions in embedded finite element meshes. Int. J. Numer. Meth. Eng. **90**(5), 636–658 (2012)

[6] Barbosa, H.J.C., Hughes, T.J.R.: Circumventing the Babuska-Brezzi condition in mixed finite element approximations of elliptic variational inequalities. Comput. Method. Appl. M. **97**(2), 193–210 (1992)

[7] Bechet, E., Moes, N., Wohlmuth, B.: A stable Lagrange multiplier space for stiff interface conditions within the extended finite element method. Int. J. Numer. Meth. Eng. **78**(8), 931–954 (2009)

[8] Belgacem, F., Hild, P., Laborde, P.: The mortar finite element method for contact problems. Math. Comput. Model. **28 (4-8)**, 263–271 (1998)

[9] Brezzi, F.: On the existence, uniqueness and approximation of saddle-point problems arising from Lagrangian multipliers. ESAIM: Mathematical Modelling and Numerical Analysis - Modélisation Mathématique et Analyse Numérique **8**(R2), 129–151 (1974)

[10] Brezzi, F., Fortin, M.: Mixed and hybrid finite element methods. Springer-Verlag New York, Inc., New York, NY, USA (1991)

[11] Burman, E., Hansbo, P.: Fictitious domain finite element methods using cut elements: I. A stabilized Lagrange multiplier method. Comput. Method. Appl. M. **199**, 2680 – 2686 (2010)

[12] Burman, E., Hansbo, P.: Fictitious domain finite element methods using cut elements: II. A stabilized Nitsche method. Appl. Numer. Math. **62**(4), 328 – 341 (2012)

[13] Chouly, F., Hild, P., Renard, Y.: Symmetric and non-symmetric variants of Nitsche's method for contact problems in elasticity: Theory and numerical experiments. Mathematics of Computation. **84**(293), 1089 – 1112 (2014)

[14] Codina, R., Baiges, J.: Approximate imposition of boundary conditions in immersed boundary methods. Int. J. Numer. Meth. Eng. **80**(11), 1379–1405 (2009)

[15] Coorevits, P., Hild, P., Lhalouani, K., Sassi, T.: Mixed finite element methods for unilateral problems: convergence analysis and numerical studies. Math. Comput. **71 (237)**, 1–25 (2001)

[16] El-Abbasi, N., Bathe, K.J.: Stability and patch test performance of contact discretizations and a new solution algorithm. Comput. Struct. **79** 1473–1486 (2001)

[17] Fischer, K., Wriggers, P.: Frictionless 2D contact formulations for finite deformations based on the mortar method. Comput. Mech. **36**, 226–244 (2005)

[18] Fischer, K., Wriggers, P.: Mortar based frictional contact formulation for higher order interpolations using the moving friction cone. Comput. Method. Appl. M. **195**, 5020–5036 (2005)

[19] Gerstenberger, A., Wall, W.A.: An embedded Dirichlet formulation for 3D continua. Int. J. Numer. Meth. Eng. **82**(5), 537–563 (2010)

[20] Gitterle, M., Popp, A., Gee, M.W., Wall, W.A.: A dual mortar approach for 3D finite deformation contact with consistent linearization. Int. J. Numer. Meth. Eng. **84**(5), 543–571 (2010)

[21] Gravouil, A., Pierres, E., Baietto, M.: Stabilized global-local X-FEM for 3D non-planar frictional contact using relevant meshes. Int. J. Numer. Meth. Eng. **88**(13), 1449–1475 (2011)

[22] Hammer, M.E.: Frictional mortar contact for finite deformation problems with synthetic contact kinematics. Comput. Mech. **51**(6), 975–998 (2013)

[23] Hansbo, P., Lovadina, C., Perugia, I., Sangalli, G.: A Lagrange multiplier method for the finite element solution of elliptic interface problems using non-matching meshes. Numer. Math. **100**, 91–115 (2005)

[24] Hartmann, S., Ramm, E.: A mortar based contact formulation for non-linear dynamics using dual Lagrange multipliers. Finite Elem. Anal. Des. **44**, 245–258 (2008)

[25] Haslinger, J., Renard, Y.: A new fictitious domain approach inspired by the extended finite element method. SIAM J. Numer. Anal. **47**(2), 1474–1499 (2009)

[26] Heintz, P., Hansbo, P.: Stabilized Lagrange multiplier methods for bilateral contact with friction. Comput. Method. Appl. M. **195**, 4323–4333 (2006)

[27] Hild, P.: Numerical implementation of two nonconforming finite element methods for unilateral contact. Comput. Method. Appl. M. **184**, 99–123 (2000)

[28] Hild, P., Laborde, P.: Quadratic finite element methods for unilaterial contact problems. Appl. Numer. Math. **41**, 401–421 (2002)

[29] Hild, P., Renard, Y.: A stabilized Lagrange multiplier method for the finite element approximation of contact problems in elastostatics. Numer. Math. **115**(101-129), 2456 – 2471 (2010)

[30] Hueber, S., Mair, M., Wohlmuth, B.: A priori error estimates and an inexact primal-dual active set strategy for linear and quadratic finite elements applied to multibody contact problems. Comput. Method. Appl. M. **54**, 555–576 (2005)

[31] Hueber, S., Stadler, G., Wohlmuth, B.I.: A primal-dual active set algorithm for three-dimensional contact problems with coulomb friction. SIAM J. Sci. Comput. **30**(2), 572–596 (2008)

[32] Hueber, S., Wohlmuth, B.: A primal-dual active set strategy for non-linear multibody contact problems. Comput. Method. Appl. M. **194**, 3147–3166 (2005)

[33] Laursen, T.: Computational Contact and Impact Mechanics. Springer, Berlin (2002)

[34] Liu, F., Borja, R.I.: Stabilized low-order finite elements for frictional contact with the extended finite element method. Comput. Method. Appl. M. **199**(37–40), 2456 – 2471 (2010)

[35] McDevitt, T., Laursen, T.: A mortar-finite element formulation for frictional contact problems. Int. J. Numer. Meth. Eng. **48**, 1525–1547 (2000)

[36] Nadal, E., Ródenas, J. J., Albelda, J., Tur, M., Tarancón, J. E., Fuenmayor, F. J.:Efficient Finite Element Methodology based on Cartesian grids: Application to structural shape optimization. Abstr. Appl. Anal., 1–19 (2013)

[37] Nistor, I., Guiton, M., Massin, P, Moes, N., Geniaut, S.: An X-FEM approach for large sliding contact along discontinuities Int. J. Numer. Meth. Eng. **78**(12), 1407–1435 (2009)

[38] Popp, A., Gitterle, M., Gee, M.W., Wall, W.A.: Finite deformation frictional mortar contact using a semi-smooth Newton method with consistent linearization. Int. J. Numer. Meth. Eng. **83**(11), 1428–1465 (2010)

[39] Puso, M.: A 3D mortar method for solid mechanics. Int. J. Numer. Meth. Eng. **59**, 315–336 (2004)

[40] Puso, M., Laursen, T.: A mortar segment-to-segment contact method for large deformation solid mechanics. Comput. Method. Appl. M. **193**, 601–629 (2004)

[41] Puso, M., Laursen, T.: A mortar segment-to-segment frictional contact method for large deformations. Comput. Method. Appl. M. **193**, 4891–4913 (2004)

[42] Puso, M., Laursen, T., Solberg, J.: A segment-to-segment mortar contact method for quadratic elements and large deformations. Comput. Method. Appl. M. **197**, 555–566 (2008)

[43] Ródenas, J., Tur, M., Fuenmayor, F., Vercher, A.: Improvement of the Superconvergent Patch Recovery technique by the use of constraint equations: the SPR-C technique. Int. J. Numer. Meth. Eng. **70**, 705–727 (2007)

[44] Saad, Y.: Iterative methods for sparse linear systems, Applied Mathematical Sciences, Society for Industrial and Applied Mathematics, Philadelphia, PA, USA (2003)

[45] Sanders, J.D., Laursen, T.A., Puso, M.: A Nitsche embedded mesh method. Comput. Mech. **49**, 243–257 (2012)

[46] Schott, B., Wall, W.: A new face-oriented stabilized XFEM approach foir 2D and 3D incompressible Navier-Stokes equations Comput. Method. Appl. M. **276**, 233–265 (2014)

[47] Simo, J., Wriggers, P., Taylor, R.: A perturbed Lagrangian formulation for the finite element solution of contact problems. Comput. Method. Appl. M. **50**, 163–180 (1985)

[48] Stenberg, R.: On some techniques for approximating boundary conditions in the finite element method. Journal of Computational and Applied Mathematics **63**, 139–148 (1995)

[49] Strouboulis, T., Copps, K., Babuška, I.: The generalized finite element method: An example of its implementation and illustration of its performance. Int. J. Numer. Meth. Eng. **47**, 1401–1417 (2000)

[50] Tur, M., Fuenmayor, F., Wriggers, P.: A mortar-based frictional contact formulation for large deformations using Lagrange multipliers. Comput. Method. Appl. M. **198**, 2860–2873 (2009)

[51] Tur, M., Albelda, J., Nadal, E., Ródenas, J.J.: Imposing Dirichlet boundary conditions in hierarchical Cartesian meshes by means of stabilized Lagrange multipliers. Int. J. Numer. Meth. Eng. **98**(6), 399–417 (2014)

[52] Tur, M., Albelda, J., Marco, O., Ródenas, J.J.: Stabilized method to impose Dirichlet boundary conditions using a smooth stress field. Comput. Method. Appl. M., Under review (2014)

[53] Wohlmuth, B., Popp, A., Gee, M.W., Wall, W.A.: An abstract framework for a priori estimates for contact problems in 3d with quadratic finite elements. Comput. Mech. **49**, 735–747 (2012)

[54] Wriggers, P.: Computational Contact Mechanics. John Wiley & Sons, Ltd. (2002)

[55] Yang, B., Laursen, T., Meng, X.: Two dimensional mortar contact methods for large deformation frictional sliding. Int. J. Numer. Meth. Eng. **62**, 1183–1225 (2005)

[56] Zavarise, G., Wriggers, P.: A segment-to-segment contact strategy. Mathematical and Computer Modelling **28 (4-8)**, 497–515 (1998)

[57] Zavarise, G., Wriggers, P.: A formulation for frictionless contact problems using a weak form introduced by Nitsche. Comput. Mech. **41**, 407–420 (2008)

[58] Zavarise, G., De Lorenzis, L.: A modified node-to-segment algorithm passing the contact patch test. Int. J. Numer. Meth. Eng. **79**, 379-416 (2009)

[59] Zienkiewicz, O., Zhu, J.: Superconvergent patch recovery techniques and a posteriori error estimation., Part I: The recovery technique. Int. J. Numer. Meth. Eng. **33**, 1331–1364 (1992)

PAPER B

Large deformation frictional contact analysis with immersed boundary method

J.M. Navarro-Jiménez, M. Tur, J. Albelda, and J.J. Ródenas

Computational Mechanics
Published online, January 2018
DOI: 10.1007/s00466-017-1533-x

Abstract

This paper proposes a method of solving 3D large deformation frictional contact problems with the Cartesian Grid Finite Element Method (cgFEM). A stabilized augmented Lagrangian contact formulation is developed using a smooth stress field as stabilizing term, calculated by Zienckiewicz and Zhu Superconvergent Patch Recovery. The parametric definition of the CAD surfaces (usually NURBS) is considered in the definition of the contact kinematics in order to obtain an enhanced measure of the contact gap. The numerical examples show the performance of the method.

Key words

Contact; Friction; Immersed boundary; Ficticious domain; cgFEM; Stabilized

Contents

1. Introduction

The so-called immersed boundary Finite Element (FE) methods have recently acquired notable relevance in the computational mechanics field. The benefits of these methods include: virtually automatic domain discretization, suitability for efficient structural shape optimization and simplicity performing multigrid analysis. The present paper is based on the Cartesian grids Finite Element Method (cgFEM) [1], in which the domain is discretized by Cartesian grids independent of the geometry. The distinguishing feature of cgFEM is its ability to take into account the exact CAD definition of the geometry, given by NURBS. The development of a suitable contact formulation for the immersed boundary framework could be of interest for efficiently solving a number of different problems, e.g. wear simulation or fretting fatigue. In [2] the cgFEM is applied to directly create FE models from medical images. The simulation of the contact interaction between CAD defined prostheses and living tissue, of great interest to the scientific community, can also be solved within this framework. In this work a formulation for solving 3D frictional contact problems under large deformations is proposed, using an immersed boundary method based on Cartesian grids. The novelties of the present work are the use of a smooth stress field to iteratively evaluate the stabilizing term and the inclusion of the NURBS surface in the contact kinematics. The work presented in this paper represents an extension of a previous work [3], in which a stabilized formulation for solving frictionless contact problems was introduced and applied to body-fitted Finite Element meshes.

In the standard Finite Element Method (FEM) the mesh is conforming to the geometry. This means that the boundary is approximated by element faces defined from nodes lying on the boundary. Therefore, the geometry is approximated using the FE approximation (FE interpolation functions) used to define the solution. This provides a simple method of describing the domain in which the accuracy of the surface definition will depend on the level of refinement of the mesh. In this case the normal field is discontinuous between elements, which is an issue to consider when it comes to solving contact problems, as the measures of the gap between contact bodies are strongly influenced by the accuracy of the definition of the surfaces [4, 5]. Some studies have tried to improve the quality of the contact kinematics description using various approaches, such as an averaged normal field [6,7], the construction of smooth surfaces to evaluate the contact gap [4, 5], and the application of the isogeometric analysis [8] to solve contact problems (see e.g. [9–11]). In this paper we include the NURBS surfaces in the contact kinematics to describe the reference configuration and enhance the accuracy of the gap measurements, while keeping the standard Finite Element interpolation for the solution of the problem.

The mortar method [12] has been used to successfully solve large deformation frictional contact problems [6, 7, 9–11, 13–15]. Its main advantage over node-to-segment formulations is that the finite element optimal convergence rate of the solution is guaranteed, as the Brezzi-Babuska *InfSup* condition is fulfilled. However, the mortar

method cannot be directly applied to deal with immersed boundary methods because it is cumbersome to find an appropriate Lagrange multipliers field that fulfills the *InfSup* condition [16]. The Vital Vertex method [17] can be used to find compatible displacement and stress fields, and was applied to 2D large sliding contact with XFEM in [18]. Other attempts to solve frictional contact using immersed boundary methods were in the context of simulating crack propagation with the eXtended Finite Element Method (X-FEM) [19–22]. Stabilized formulations are another alternative to overcoming this problem. Several works on this topic have been published, starting with stabilized Lagrange multipliers formulations for body-fitted meshes to solve small sliding 2D contact [23, 24] and large deformation contact [25, 26] in 2D and 3D.

Stabilized formulations have been recently adapted to embedded domains. In [27] a stabilized augmented Lagrange formulation is developed for frictionless contact. A stabilized formulation based on the Nitsche method is presented in [28, 29] for small sliding contact in 2D and 3D respectively. In both formulations the stabilizing term involves the finite element tractions. All these contributions indicate that developing contact formulations for immersed boundary methods is an active research field. To the authors' knowledge no previous work has considered 3D CAD geometries and large deformation frictional contact for immersed boundary methods. A relevant difference between the proposed formulation and other works is its use of a smooth stress field ($\boldsymbol{\sigma}^*$) as stabilizing term, calculated by the Zienckiewicz and Zhu Superconvergent Patch Recovery [30, 31]. With this choice there are fewer terms to evaluate in the tangent matrix, the formulation is displacement-based and the optimal convergence rate is maintained. It also eases the introduction of plasticity into the problem, as the finite element stress is not involved in the formulation (see [32]). The proposed formulation consists of two nested loops, similar to an Uzawa algorithm: the inner loop evaluates the contact active set and the stabilizing term is updated in an external loop.

The paper is organized as follows: Section 2 describes the continuum formulation to solve the contact problem. The contact kinematics and its features regarding the cgFEM is described in Section 3. The FE stabilized formulation is obtained in Section 4. In Section 5 we propose an iterative scheme to solve the contact problem. Finally, some numerical examples are shown in Section 6. Appendices A and B provide with details of the variation and linearization of some auxiliar terms of the problem formulation.

2. Continuum formulation

Here we describe the continuum formulation of the frictional contact problem and introduce all the notation used through the paper. The basic scheme of the contact between two elastic bodies, is shown in Figure 1. We divide the boundary of each

body $\Gamma^{(i)}$, into the Dirichlet boundary $\Gamma_D^{(i)}$, the Neumann boundary $\Gamma_N^{(i)}$ and the area of the boundary where contact may occur, $\Gamma_C^{(i)}$.

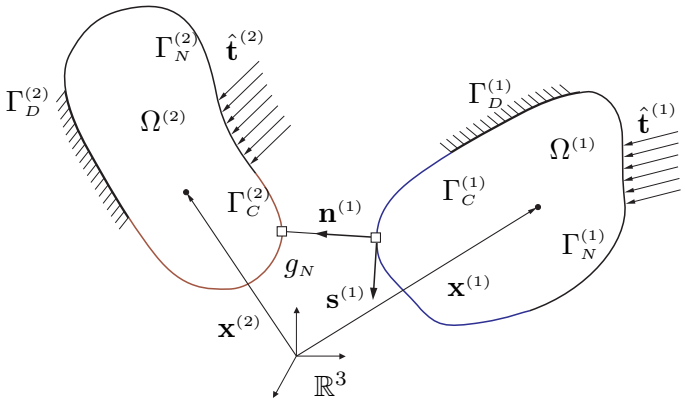

Figure 1: Scheme of two deformable bodies in contact. The red and blue lines depict the contact boundaries $\Gamma^{(i)}$

2.1. Continuum contact kinematics

Let $\mathbf{x}^{(1)}$ be the position of any point in the so called *slave* contact surface, $\Gamma_C^{(1)}$. We use a ray-tracing technique [14, 26] to define the contact point pairs, i.e. we intersect the *master* contact surface $\Gamma_C^{(2)}$ at $\mathbf{x}^{(2)}$ with a line emanating from $\mathbf{x}^{(1)}$ in the direction of the normal vector to the slave surface $\mathbf{n}^{(1)}$. Then the normal contact gap can be defined as

$$g_N = \left(\mathbf{x}^{(2)} - \mathbf{x}^{(1)}\right) \cdot \mathbf{n}^{(1)} \tag{1}$$

In order to enforce frictional contact constraints it is also necessary to define an appropriate relative velocity, from which the increment of the relative movement $\dot{\mathbf{g}}\,dt$ is obtained [33, 34] between the bodies in contact. Details of the calculation are not shown here, as it will be explained in Section 3.3 for the FE discretization using cgFEM.

2.2. Weak formulation for frictional contact

The weak formulation of the Tresca frictional problem can be derived from the augmented Lagrangian functional [24, 26], first proposed by Alart and Curnier [35] and Pietrzak and Curnier [36]:

$$\begin{aligned} opt \Bigg\{ \Pi(\mathbf{u}) + \frac{1}{2\kappa_1} \int_{\Gamma_C^{(1)}} \left(\left[\boldsymbol{\lambda} \cdot \mathbf{n}^{(1)} + \kappa_1 g_N \right]_-^2 - \|\boldsymbol{\lambda}\|^2 \right) d\Gamma + \\ + \frac{1}{2\kappa_1} \int_{\Gamma_C^{(1)}} \| P_{B(n,s)} \left(\boldsymbol{\lambda} - \kappa_1 \dot{\mathbf{g}}\, dt \right) \|^2 \, d\Gamma \Bigg\} \end{aligned} \tag{2}$$

where $\mathbf{u}$ is the displacement field and $\boldsymbol{\lambda}$ is the Lagrange multiplier vectorial field. We assume a hyperelastic material behavior so $\Pi(\mathbf{u})$ represents the potential energy of the bodies, including the external forces applied. $\kappa_1 > 0$ is a penalty constant that keeps the problem solution unchanged. We define the projection operator onto the tangent plane with normal $\mathbf{n}^{(1)}$ as:

$$\mathbf{T}_n = \left(\mathbb{I} - \mathbf{n}^{(1)} \otimes \mathbf{n}^{(1)} \right) \tag{3}$$

We also use the negative part operator

$$[x]_- = \begin{cases} -x & if \quad x \leq 0 \\ \\ 0 & if \quad x > 0 \end{cases} \tag{4}$$

and the projection operator $P_{B(n,s)}(\mathbf{x})$ which is defined as the projection of $\mathbf{x}$ both on the tangent plane $\mathbf{T}_n$ and on a circle of radius s:

$$P_{B(n,s)}(\mathbf{x}) = \begin{cases} \mathbf{T}_n \mathbf{x} & if \quad \|\mathbf{T}_n \mathbf{x}\| \leq s \\ \\ s \frac{\mathbf{T}_n \mathbf{x}}{\|\mathbf{T}_n \mathbf{x}\|} & if \quad \|\mathbf{T}_n \mathbf{x}\| > s \end{cases} \tag{5}$$

The stabilized Coulomb frictional contact formulation proposed in this work will be obtained by modifying the functional in 2. Taking variations in this equation

and assuming a Tresca friction model (i.e. s is constant) we obtain the following expression:

$$\begin{cases} \delta\Pi(\mathbf{u},\delta\mathbf{u}) - \displaystyle\int_{\Gamma_C^{(1)}} \left(\left[\boldsymbol{\lambda}\cdot\mathbf{n}^{(1)} + \kappa_1 g_N \right]_- \delta g_N + P_{B(n,s)}\left(\boldsymbol{\lambda} - \kappa_1 \dot{\mathbf{g}}\, dt\right) \delta\mathbf{g} \right) d\Gamma = 0,\ \forall \delta\mathbf{u} \\ -\frac{1}{\kappa_1} \displaystyle\int_{\Gamma_C^{(1)}} \left(\left[\boldsymbol{\lambda}\cdot\mathbf{n}^{(1)} + \kappa_1 g_N \right]_- \mathbf{n}^{(1)} + \boldsymbol{\lambda} - P_{B(n,s)}\left(\boldsymbol{\lambda} - \kappa_1 \dot{\mathbf{g}}\, dt\right) \right) \delta\boldsymbol{\lambda}\, d\Gamma = 0,\ \forall \delta\boldsymbol{\lambda} \end{cases} \tag{6}$$

where the variations of $\mathbf{g}$, $\dot{\mathbf{g}}dt$, and g_N are a function of $\delta\mathbf{u}$. The first term in the upper equation is the virtual work of the internal and external forces, so the formulation in (6) can be applied to a general class of material behaviour. The contact integral in the first equation in (6) is the virtual work of the contact forces. The second equation contains the Karush-Kuhn-Tucker conditions in normal direction, and the frictional contact behaviour in the tangent plane. We can now modify the projection P_B to consider Coulomb friction, i.e. replacing the friction limit s with $\mu\left[\lambda_N + \kappa_1 g_N\right]_-$, as done in [26].

After defining the weak form of the continuum problem, we replace the displacement and the Lagrange multiplier fields by appropriate finite element approximations, $\mathbf{u}^h \in \mathscr{U}^h$ and $\boldsymbol{\lambda}^h \in \mathscr{M}^h$, to obtain a numerical solution. $\mathscr{U}^h$ is the space of piecewise polynomials of degree $p = 1$ or $p = 2$ in our case. Details on the selection of the Lagrange multiplier approximation space are given in Section 4. For the sake of simplicity of the notation we will omit the superscript h when denoting the finite element variables from now on.

3. Finite Element contact kinematics

In this section we will define all the kinematic variables involved in the solution of the contact problem in the cgFEM, the normal contact gap g_N, the relative displacement $\dot{\mathbf{g}}\, dt$ and the gap vector $\mathbf{g}$, and their respective variations.

In the cgFEM [1,37] the analysis domain Ω is fully embedded in a regular cuboid Ω_h which is much easier to mesh than Ω, see Figure 2. This domain Ω_h is meshed with a sequence of regular Cartesian grids. There will be elements completely inside the domain and elements intersected by the boundary. The elements external to the domain are not considered in the analysis.

The geometry is defined by NURBS surfaces. Figure 3 shows the undeformed configuration of an element intersected by an arbitrary NURBS surface. Three different reference systems appear in the Figure: these are the global reference system

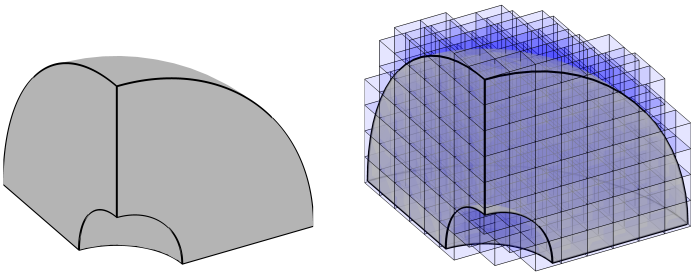

Figure 2: Mesh creation with cgFEM. The analysis domain Ω (left) is embedded in a Cartesian grid Ω_h (right). Elements external to the geometry are not considered in the analysis.

$\mathbf{X}_0 \equiv \{x_0, y_0, z_0\}$, the parametric reference system of the NURBS surface $\boldsymbol{\xi} \equiv \{\xi, \eta\}$ and the local reference system of the finite element $\boldsymbol{\zeta}^e \equiv [\zeta_1^e, \zeta_2^e, \zeta_3^e]$.

Due to the regularity of all the elements in the mesh, the transformation from global coordinates in the undeformed configuration $\mathbf{X}_0$ to element local coordinates $\boldsymbol{\zeta}^e$ of any point is performed with the following affine transformation:

$$\boldsymbol{\zeta}^e = \frac{\mathbf{X}_0 - \mathbf{X}_e}{h/2} \tag{7}$$

where $\mathbf{X}_e$ are global coordinates of the centroid of the element in the initial configuration and h is the size of the element.

We define the position vector $\mathbf{x}^{(i)}$ for any point in $\Omega^{(i)}$ as in equation (8), where $\mathbf{X}_0^{(i)}$ represents the undeformed configuration and the displacement field $\mathbf{u}^{(i)}$ is evaluated using the finite element interpolation.

$$\mathbf{x}^{(i)} = \mathbf{X}_0^{(i)} + \mathbf{u}^{(i)} \tag{8}$$

Equation (8) is valid for the whole domain, including the particular case of the contact surface, $\Gamma_c^{(i)}$. In this work we are interested in enhancing the definition of $\Gamma_c^{(i)}$ using the CAD geometry. We therefore use the NURBS definition of the boundary for the undeformed position for any point located at $\Gamma_c^{(i)}$. NURBS surfaces [38, 39] are rational functions defined in their own parametric space of coordinates $[\xi, \eta]$ as

$$\mathbf{S}^{(i)}(\xi, \eta) = \sum_{i=1}^{n} \sum_{j=1}^{m} \frac{N_i^{(p)}(\xi) M_j^{(q)}(\eta) w_{i,j}}{\sum_{i=1}^{n} \sum_{j=1}^{m} N_i^{(p)}(\xi) M_j^{(q)}(\eta) w_{i,j}} \mathbf{P}_{i,j} \tag{9}$$

These functions are a result of a tensor product between one-dimensional basis functions of order p and q ($N_i^{(p)}, M_j^{(q)}$). The basis functions are defined along two knot vectors with $(n \times m)$ control points and $\mathbf{P}_{i,j}$ coordinates.

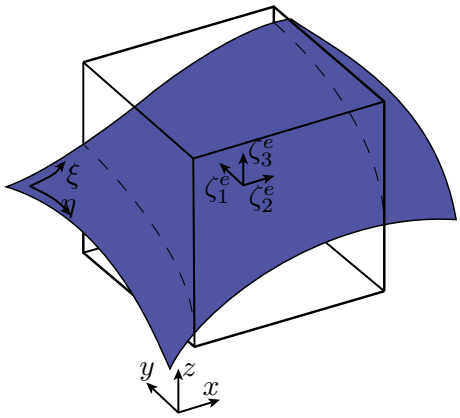

Figure 3: Scheme of the different reference systems involved in the definition of the contact kinematics. The hexahedra represents a finite element cut by an arbitrary NURBS surface.

Finally, the definition of the position vector for any point $\mathbf{x}^{(i)}$ located at $\Gamma_c^{(i)}$ results in:

$$\mathbf{x}^{(i)} = \mathbf{S}^{(i)}\left(\xi,\eta\right) + \sum_j N_j(\boldsymbol{\zeta}^e)\mathbf{u}_j^{(i)} \ , \qquad \mathbf{x}^{(i)} \in \Gamma_c^{(i)} \tag{10}$$

where $N_j\left(\boldsymbol{\zeta}^e\right)$ are the finite element shape functions and $\mathbf{u}_j^{(i)}$ are the nodal displacements of the discretization.

3.1. Normal gap

We recall here the definition of the normal gap g_N, where the position vectors have already been defined in (10):

$$g_N = \left(\mathbf{x}^{(2)}(\boldsymbol{\xi}^{(2)}) - \mathbf{x}^{(1)}\right) \cdot \mathbf{n}^{(1)} \tag{11}$$

A ray-tracing technique is used to find the contact point $\boldsymbol{\xi}^{(2)}$, i.e., given a certain point $\mathbf{x}^{(1)}$ and its surface normal vector $\mathbf{n}^{(1)}$, we solve (11), rearranged as:

$$\mathbf{x}^{(1)} + g_N\mathbf{n}^{(1)} = \mathbf{S}^{(2)}(\boldsymbol{\xi}^{(2)}) + \sum_j N_j(\boldsymbol{\zeta}^e)\mathbf{u}_j^{(2)} \tag{12}$$

This non-linear equation is solved using a Newton-Raphson scheme where the unknowns are $\boldsymbol{\xi}^{(2)}$ and g_N. This solver uses the derivative of (12) with respect to the NURBS local coordinates. The relation between the surface parametric coordinates

and the element local coordinates is obtained considering that for a point located on $\Gamma_c^{(i)}$, $\mathbf{X}_0^{(i)} \equiv \mathbf{S}^{(i)}(\xi,\eta)$, and substituting (9) into (7)

$$\boldsymbol{\zeta}^e = \frac{\mathbf{S}^{(i)}(\xi,\eta) - \mathbf{X}_e}{h/2} \tag{13}$$

and taking derivatives with respect to the NURBS local coordinates $\boldsymbol{\xi} \equiv \{\xi,\eta\}$ we obtain:

$$\frac{\partial \boldsymbol{\zeta}^e}{\partial \xi} = \frac{2}{h}\frac{\partial \mathbf{S}^{(i)}(\xi,\eta)}{\partial \xi}; \qquad \frac{\partial \boldsymbol{\zeta}^e}{\partial \eta} = \frac{2}{h}\frac{\partial \mathbf{S}^{(i)}(\xi,\eta)}{\partial \eta} \tag{14}$$

The calculation of the first derivatives of the NURBS follows a simple procedure (see [39] for example). The first derivatives have a similar definition to (9) with a lower order basis functions. Therefore the surface derivatives can be treated as auxiliary NURBS surfaces, and the evaluation of the NURBS derivatives is reduced to a standard NURBS surface evaluation. The normal vector $\mathbf{n}^{(1)}$ is constructed using the tangent vectors to the surface, $\mathbf{s}_\xi^{(1)}$ and $\mathbf{s}_\eta^{(1)}$ (equations (15), (16) and (17)).

$$\mathbf{n}^{(1)} = \frac{\hat{\mathbf{n}}^{(1)}}{\|\hat{\mathbf{n}}^{(1)}\|}; \qquad \hat{\mathbf{n}}^{(1)} = \mathbf{s}_\xi^{(1)} \times \mathbf{s}_\eta^{(1)} \tag{15}$$

$$\mathbf{s}_\xi^{(1)} = \frac{\partial \mathbf{x}^{(1)}}{\partial \xi} = \frac{\partial \mathbf{S}^{(i)}(\xi,\eta)}{\partial \xi} + \sum_j \left(\frac{\partial N_j}{\partial \zeta_1^e}\frac{\partial \zeta_1^e}{\partial \xi} + \frac{\partial N_j}{\partial \zeta_2^e}\frac{\partial \zeta_2^e}{\partial \xi} + \frac{\partial N_j}{\partial \zeta_3^e}\frac{\partial \zeta_3^e}{\partial \xi} \right) \mathbf{u}_j^{(1)} \tag{16}$$

$$\mathbf{s}_\eta^{(1)} = \frac{\partial \mathbf{x}^{(1)}}{\partial \eta} = \frac{\partial \mathbf{S}^{(i)}(\xi,\eta)}{\partial \eta} + \sum_j \left(\frac{\partial N_j}{\partial \zeta_1^e}\frac{\partial \zeta_1^e}{\partial \eta} + \frac{\partial N_j}{\partial \zeta_2^e}\frac{\partial \zeta_2^e}{\partial \eta} + \frac{\partial N_j}{\partial \zeta_3^e}\frac{\partial \zeta_3^e}{\partial \eta} \right) \mathbf{u}_j^{(1)} \tag{17}$$

3.2. Variation of the normal gap

The contact problem formulation in (6) needs the definition of the normal gap variation. Instead of using the exact variation obtained from (11) we use an approximation which was also used in [6] and [26], and can be written as

$$\delta g_N = \left(\delta \mathbf{u}^{(2)} - \delta \mathbf{u}^{(1)} \right) \cdot \mathbf{n}^{(1)} \tag{18}$$

where for simplicity the following notation has been introduced:

$$\delta \mathbf{u}^{(i)} = \sum_j N_j(\boldsymbol{\zeta}^e) \delta \mathbf{u}_j^{(i)} \tag{19}$$

The exact variation of δg_N also requires the derivatives $\delta\xi$, $\delta\eta$, which will be omitted for the evaluation of the contact force. However, the exact derivative of g_N will be evaluated for the linearization of the problem. The loss of symmetry

and angular momentum conservation that this choice implies is also discussed in references [6, 26].

3.3. Tangent contact

Figure 4 schematically shows the evolution of two bodies in sliding contact from step t to step $t+1$. At time t the *slave* point $\mathbf{x}_t^{(1)}$ is in contact with point $\mathbf{x}_t^{(2)}(\boldsymbol{\xi}_t)$. Since sliding has occurred at time $t+1$ the contact point pair changes from the previous $\boldsymbol{\xi}_t$ to the new location $\boldsymbol{\xi}_{t+1}$. At that moment the position of the previous and the current *master* points are $\mathbf{x}_{t+1}^{(2)}(\boldsymbol{\xi}_t)$ and $\mathbf{x}_{t+1}^{(2)}(\boldsymbol{\xi}_{t+1})$ respectively. This variation of the position is defined as $\Delta^t\mathbf{g}$, which is depicted by the thick blue arrow in Figure 4:

$$\dot{\mathbf{g}}\, dt \approx \Delta^t\mathbf{g} = \left(\mathbf{x}_{t+1}^{(2)}(\boldsymbol{\xi}_t) - \mathbf{x}_{t+1}^{(2)}(\boldsymbol{\xi}_{t+1})\right) \tag{20}$$

This incremental definition of the relative velocity was first proposed in [14] for the 2D case and here we extend the details of its computation for 3D frictional problems and Cartesian grids. Although we skip the h index, this variable is defined for the finite element discretization and can only approximate the continuum variable $\dot{\mathbf{g}}\, dt$, since the time step increments used for the solution are not necessarily small. This definition is objective (frame independent), as proven in [40], and is similar to the one proposed in [7]. For the frictional contact problem we only consider the projection of this relative velocity onto the tangent plane in the current step $\mathbf{T}_n$. We can use the following relation:

$$\mathbf{x}_{t+1}^{(2)}(\boldsymbol{\xi}_{t+1}) = \mathbf{x}_{t+1}^{(1)} + \mathbf{g}_{t+1} \tag{21}$$

and $\mathbf{g}_{t+1}$ is normal to the tangent plane, so:

$$\mathbf{T}_n\, \mathbf{x}_{t+1}^{(2)}(\boldsymbol{\xi}_{t+1}) = \mathbf{T}_n\, \mathbf{x}_{t+1}^{(1)} \tag{22}$$

With this consideration we can use the alternative definition of the projected relative velocity as:

$$\mathbf{T}_n\Delta^t\mathbf{g} = \mathbf{T}_n\left(\mathbf{x}_{t+1}^{(2)}(\boldsymbol{\xi}_t) - \mathbf{x}_{t+1}^{(2)}(\boldsymbol{\xi}_{t+1})\right) = \mathbf{T}_n\left(\mathbf{x}_{t+1}^{(1)} - \mathbf{x}_{t+1}^{(2)}(\boldsymbol{\xi}_t)\right) \tag{23}$$

This definition will provide us with a simpler linearization as it is shown in Appendix B. It is worth noting that, despite using the previous contact coordinates $\boldsymbol{\xi}_t$ to evaluate the relative velocity, only the current configuration is taken into account. Note that in the case of sticking between the solids there is no change of the contact coordinates, then $\boldsymbol{\xi}_{t+1} = \boldsymbol{\xi}_t$ and we can combine the normal gap and the tangent relative velocity:

$$g_n\mathbf{n}^{(1)} - \mathbf{T}_n\Delta^t\mathbf{g} = \mathbf{x}^{(2)}(\boldsymbol{\xi}) - \mathbf{x}^{(1)} = \mathbf{g} \tag{24}$$

This simplification will be useful for the stick contact formulation.

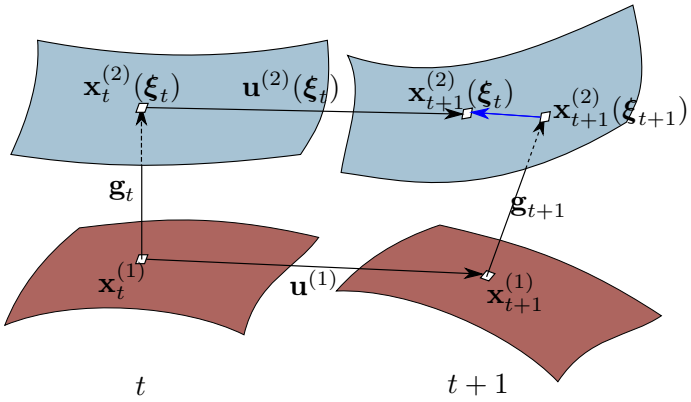

Figure 4: Sliding kinematics scheme. In the configuration t, a point $\mathbf{x}_t^{(1)}$ is in contact with a point with local surface coordinates $\boldsymbol{\xi}_t$. After sliding occurs, the same point $\mathbf{x}_{t+1}^{(1)}$ will be contacting with a point $\mathbf{x}_{t+1}^{(2)}(\boldsymbol{\xi}_{t+1})$.

The variation of the gap vector is also used in the frictional contact formulation for the stick case, and defined with the simple expression:

$$\delta\mathbf{g} = \delta\mathbf{u}^{(2)}(\boldsymbol{\xi}) - \delta\mathbf{u}^{(1)} \tag{25}$$

Again the derivatives $\delta\xi$, $\delta\eta$ will be omitted for the evaluation of the contact force, but will be considered for the linearization of the problem.

4. Finite Element stabilized contact formulation

It is difficult to find a Lagrange multiplier field that fulfills the inf-sup condition in the immersed boundary framework [41]. The different methods of overcoming this problem include new formulations of the contact problem, such as modifications of the Nitsche method and stabilized Lagrangian formulations [27, 42, 43]. Here we extend the frictionless contact formulation first proposed in [3] to deal with frictional contact problems. Our proposed solution combines a stabilized augmented Lagrange formulation with the use of a smooth stress field $\mathbf{T}^* = \boldsymbol{\sigma}^* \cdot \mathbf{n}^{(1)}$ in the stabilizing term. The smooth stress field used to stabilize the formulation must fulfill the following property [32, 44] in order to obtain an optimal FE formulation:

$$\int_{\Gamma_C^{(1)}} \|\mathbf{T}^*\| \leq C \int_{\Omega} \|\boldsymbol{\sigma}^*\|^2 \tag{26}$$

with C independent of the mesh size. This condition states that the norm of the tractions on the boundary must be bounded by the norm of the stress field on the domain. We use the field proposed in [14], which is based on the Zienckiewicz and Zhu Superconvergent Patch Recovery [30, 31]. With this technique a smooth stress field is obtained by solving a small minimization problem at each node of the mesh. Once the displacements are known, the information of the solution at all the elements attached to the node is used to obtain $\boldsymbol{\sigma}^*$. As the stabilizing term has information not only from the boundary elements but also from the surrounding interior elements, it can be proven that the optimal convergence rate for the FE solution is achieved, even if there are elements cut by the boundary with a low ratio between the intersected material volume and the whole element volume. This definition requires an iterative procedure to solve the problem, which will be detailed in Section 5. We modify the augmented Lagrangian functional (2) with the addition of a stabilizing term (the last integral in (27)).

$$\begin{aligned} opt \Bigg\{ \Pi(\mathbf{u}) + \frac{1}{2\kappa_1} \int_{\Gamma_C^{(1)}} \left(\left[\boldsymbol{\lambda} \cdot \mathbf{n}^{(1)} + \kappa_1 g_N \right]_-^2 - \|\boldsymbol{\lambda}\|^2 \right) d\Gamma + \\ + \frac{1}{2\kappa_1} \int_{\Gamma_C^{(1)}} \|P_B \left(\boldsymbol{\lambda} - \kappa_1 \Delta^t \mathbf{g} \right)\|^2 \, d\Gamma - \frac{1}{2\kappa_2} \int_{\Gamma_C^{(1)}} \|\boldsymbol{\lambda} - \mathbf{T}^*\|^2 d\Gamma \Bigg\} \end{aligned} \tag{27}$$

where the simplification $P_B(\mathbf{x}) \equiv P_{B\left(\mathbf{n}^{(1)}, \mu[\lambda_N + \kappa_1 g_N]_-\right)}(\mathbf{x})$ is introduced. This extra term penalizes the difference between the multiplier $\boldsymbol{\lambda}$ and the stress field using a penalty constant $\kappa_2 > 0$. In [32] the penalty constant is defined as $\kappa_2 = C/h$ with h being the mesh size and C a positive constant. It was proved for Dirichlet boundary conditions that, for C greater than a certain value depending only on the material properties and the degree of discretization, the problem is stable and the optimal convergence is reached.

Assuming that $\mathbf{T}^*$ is known, the variation of (27) is now written as:

$$\begin{cases} \delta\Pi(\mathbf{u}, \delta\mathbf{u}) - \displaystyle\int_{\Gamma_C^{(1)}} \left(\left[\boldsymbol{\lambda} \cdot \mathbf{n}^{(1)} + \kappa_1 g_N \right]_- \delta g_N + P_B \left(\boldsymbol{\lambda} - \kappa_1 \Delta^t \mathbf{g} \right) \delta \mathbf{g} \right) d\Gamma = 0, \ \forall \delta\mathbf{u} \\ \\ -\frac{1}{\kappa_1} \displaystyle\int_{\Gamma_C^{(1)}} \left(\left[\boldsymbol{\lambda} \cdot \mathbf{n}^{(1)} + \kappa_1 g_N \right]_- \mathbf{n}^{(1)} + \boldsymbol{\lambda} - P_B \left(\boldsymbol{\lambda} - \kappa_1 \Delta^t \mathbf{g} \right) \right) \delta\boldsymbol{\lambda} \, d\Gamma \\ \\ -\frac{1}{\kappa_2} \displaystyle\int_{\Gamma_C^{(1)}} \left(\boldsymbol{\lambda} - \mathbf{T}^* \right) \delta\boldsymbol{\lambda} \, d\Gamma = 0, \ \forall \delta\boldsymbol{\lambda} \end{cases} \tag{28}$$

Remark: In this paper we will enforce the contact constraint only on surface $\Gamma_C^{(1)}$ for the sake of simplicity. However, [3] shows how to use a double pass strategy

to enforce the contact constraint on both surfaces $\Gamma_C^{(1)}$ and $\Gamma_C^{(2)}$ without additional complexity.

4.1. Lagrange multiplier interpolation

The requirements for the multiplier space to reach optimal convergence is that $\boldsymbol{\lambda}^h$ be a piecewise interpolation in the element of degree at least $p-1$, where p is the interpolation degree used to define $\mathbf{u}^h$. As there is no need to define a continuous piecewise interpolation, we define a multiplier for each of the quadrature points used for the numerical integration. The Lagrange multipliers can the be condensed element by element as described in [3] (or even for every quadrature point), similar to the procedure followed in [45]. This elimination has some advantages: *a)* the number of degrees of freedom of the problem does not increase, and *b)* the system remains positive definite.

Remark: The contact integrals over $\Gamma_C^{(1)}$ are numerically calculated on the integration points where the Lagrange multipliers are defined. This introduces an integration error, which is small if the number of integration points is high enough.

4.2. Frictionless contact formulation

The variational form for the Coulomb frictional contact in (28) can be simplified for the particular case of frictionless contact, yielding the following form:

$$\begin{cases} \delta\Pi(\mathbf{u},\delta\mathbf{u}) - \displaystyle\int_{\Gamma_C^{(1)}} \left[\lambda_N + \kappa_1 g_N\right]_- \delta g_N \, d\Gamma = 0, \ \forall \delta\mathbf{u} \\ \\ -\frac{1}{\kappa_1}\displaystyle\int_{\Gamma_C^{(1)}} \left(\left[\lambda_N + \kappa_1 g_N\right]_- + \lambda_N\right) \delta\lambda_N \, d\Gamma - \frac{1}{\kappa_2}\int_{\Gamma_C^{(1)}} \left(\lambda_N - p_N\right) \delta\lambda_N \, d\Gamma = 0, \ \forall \delta\lambda_N \end{cases} \tag{29}$$

where we have introduced the normal stabilizing stress $p_N = \left(\mathbf{T}^* \cdot \mathbf{n}^{(1)}\right) \cdot \mathbf{n}^{(1)}$. Taking into account the numerical integration, we have one equation for every quadrature point, depicted with the subindex g. Then, the following result can be obtained if we condense the Lagrange multipliers in the second equation in (29):

$$\lambda_{N\,g} = \begin{cases} \kappa_2 g_{N\,g} + p_{N\,g} & if \quad \left[\lambda_{N\,g} + \kappa_1 g_{N\,g}\right]_- \leq 0 \\ \\ 0 & if \quad \left[\lambda_{N\,g} + \kappa_1 g_{N\,g}\right]_- > 0 \end{cases} \tag{30}$$

Substituting the Lagrange multiplier in (29) we will have the following equation to solve the normal contact problem.

$$\begin{aligned} \delta\Pi(\mathbf{u},\delta\mathbf{u}) - \textstyle\sum_g \left(p_{N\,g} + \frac{\kappa E}{h} g_{N\,g}\right) \delta g_{N\,g} \;\; |J_g|\, H_g = 0, \quad if \quad \left[p_{N\,g} + \tfrac{\kappa E}{h} g_{N\,g}\right]_- \leq 0 \\ \delta\Pi(\mathbf{u},\delta\mathbf{u}) = 0, \quad if \quad \left[p_{N\,g} + \tfrac{\kappa E}{h} g_{N\,g}\right]_- > 0 \end{aligned} \tag{31}$$

where H_g and $|J_g|$ are the respective quadrature weight and Jacobian of the transformation, and $\frac{\kappa E}{h} = (\kappa_1 + \kappa_2)$ with E being the Young's modulus and h the mesh size. This result is similar to the one obtained in [27] with the advantage of having less integrals to evaluate as no derivatives of the stabilizing traction are involved in the formulation. Further discussion on the values of the stabilizing term can be found in [3].

4.3. Frictional contact formulation

Here we extend the stabilized formulation to the Coulomb frictional contact case with large deformations. We assume that $\left[p_N + \frac{\kappa E}{h} g_N\right]_- \leq 0$, i.e. the contact condition is active, otherwise the problem equation would remain as the second equation in (31). We can again substitute the value at the quadrature points of λ_N obtained in (30), so that the Coulomb friction limit is written as $\mu \left[p_N + \frac{\kappa E}{h} g_N\right]_-$. It is also possible to condense element-wise the Lagrange multipliers using the second equation in (28). In order to do that, we will distinguish between the different states during frictional contact, the sticking case and the sliding case.

Starting with the stick state, we can substitute in the second equation in (28) the corresponding value $P_B = \mathbf{T}_n \left(\boldsymbol{\lambda} - \kappa_1 \Delta^t \mathbf{g}\right)$:

$$-\frac{1}{\kappa_1}\left(\left[\boldsymbol{\lambda}\cdot\mathbf{n}^{(1)} + \kappa_1 g_N\right]_- \mathbf{n}^{(1)} + \boldsymbol{\lambda} - \mathbf{T}_n\left(\boldsymbol{\lambda} - \kappa_1\Delta^t\mathbf{g}\right)\right) - \frac{1}{\kappa_2}\left(\boldsymbol{\lambda} - \mathbf{T}^*\right) = 0 \tag{32}$$

Hence, (32) can be simplified taking into account that $\boldsymbol{\lambda} = \left(\boldsymbol{\lambda}\cdot\mathbf{n}^{(1)}\right)\mathbf{n}^{(1)} + \mathbf{T}_n\boldsymbol{\lambda}$. Therefore, the Lagrange multiplier can be substituted at each integration point by:

$$\boldsymbol{\lambda}_g = \mathbf{T}^*_g + \kappa_2\left(g_{N\,g}\mathbf{n}^{(1)} - \mathbf{T}_n\Delta^t\mathbf{g}_g\right) \tag{33}$$

After substituting the value in the first equation of (28), and taking into account the simplification of (24) $\mathbf{g} = g_N\mathbf{n}^{(1)} - \mathbf{T}_n\Delta^t\mathbf{g}$ valid only for the stick case, the contact contribution to the problem in the case of stick is written as:

$$\delta\Pi_{C_{St}}(\mathbf{u},\delta\mathbf{u}) = \sum_g \left(\frac{\kappa E}{h}\mathbf{g}_g + \mathbf{T}^*{}_g\right)\cdot\delta\mathbf{g}_g\,|J_g|\,H_g \tag{34}$$

The elimination of the Lagrange multipliers in the frictionless and stick cases allows the problem to be transformed into a modified penalty method, with the advantages mentioned above. However, the elimination of the multipliers for the sliding case is cumbersome, as in this case the second equation in (28) reads as:

$$\begin{aligned} -\tfrac{1}{\kappa_1}\left(\left[\boldsymbol{\lambda}\cdot\mathbf{n}^{(1)}+\kappa_1 g_N\right]_-\mathbf{n}^{(1)}+\boldsymbol{\lambda}+\mu\left(p_N+\tfrac{\kappa E}{h}g_N\right)\tfrac{\mathbf{T}_n\left(\boldsymbol{\lambda}-\kappa_1\Delta^t\mathbf{g}\right)}{\|\mathbf{T}_n(\boldsymbol{\lambda}-\kappa_1\Delta^t\mathbf{g})\|}\right) \\ -\tfrac{1}{\kappa_2}\left(\boldsymbol{\lambda}-\mathbf{T}^*\right)=0 \end{aligned} \tag{35}$$

We can project this equation on the normal direction $\mathbf{n}^{(1)}$ and the tangent plane $\mathbf{T}_n$. The first projection yields the the same equation that was discussed in the frictionless case (30). The projection on the tangent plane leads to the following equation:

$$-\frac{1}{\kappa_1}\left(\mathbf{T}_n\boldsymbol{\lambda}+\mu\left(p_N+\frac{\kappa E}{h}g_N\right)\frac{\mathbf{T}_n\left(\boldsymbol{\lambda}-\kappa_1\Delta^t\mathbf{g}\right)}{\|\mathbf{T}_n\left(\boldsymbol{\lambda}-\kappa_1\Delta^t\mathbf{g}\right)\|}\right)-\frac{1}{\kappa_2}\mathbf{T}_n\left(\boldsymbol{\lambda}-\mathbf{T}^*\right)=0 \tag{36}$$

This is the slip condition that, roughly speaking, (neglecting the stabilizing term, $\boldsymbol{\lambda}=\mathbf{T}^*$) forces the tangent projection of the multiplier to have a modulus $\mu\left(p_N+\frac{\kappa E}{h}g_N\right)$ and the direction of $\mathbf{T}_n\Delta^t\mathbf{g}$. The addition of the stabilization term, if $\mathbf{p}_T=\mathbf{T}_n\cdot\mathbf{T}^*$ is chosen in the direction of $\mathbf{T}_n\Delta^t\mathbf{g}$ and modulus μp_N, becomes again the same constraint, so the equation is redundant.

Only the direction of $\mathbf{T}_n\boldsymbol{\lambda}$ is involved in the first equation in (28). We formulate an alternative approach for the sliding problem that will lead to the same solution by modifying this equation. We consider that the direction of $\mathbf{T}_n\boldsymbol{\lambda}$ is the same as the direction of $\kappa_2\mathbf{T}_n\Delta^t\mathbf{g}+\mathbf{p}_T$, which also has the direction of $\mathbf{T}_n\Delta^t\mathbf{g}$ in the problem solution. In order to avoid convergence problems, the transition between stick and slip has to be continuous. This is achieved with the following substitution:

$$\mathbf{T}_n\boldsymbol{\lambda}=\kappa_2\mathbf{T}_n\Delta^t\mathbf{g}+\mathbf{p}_T \tag{37}$$

Introducing this substitution into the first equation in (28) we obtain the final equation to solve the sliding problem:

$$\begin{aligned} \delta\Pi_{C_{Sl}}(\mathbf{u},\delta\mathbf{u})=\sum_g\Bigg[\left(\frac{\kappa E}{h}g_N+p_N\right)\delta g_N- \\ \mu\left(\frac{\kappa E}{h}g_N+p_N\right)\frac{\mathbf{p}_T-\frac{\kappa E}{h}\mathbf{T}_n\Delta^t\mathbf{g}}{\|\mathbf{p}_T-\frac{\kappa E}{h}\mathbf{T}_n\Delta^t\mathbf{g}\|}\cdot\delta\mathbf{g}\Bigg]\left|J_g\right|H_g \end{aligned} \tag{38}$$

This approximation means the sliding problem can be formulated with a modified penalty method similar to those obtained for the frictionless and sticking cases. The numerical examples in Section 6 show that the convergence is still achieved.

The stabilizing smooth stress field p_N and $\mathbf{p}_T$ are considered independent of the solution $\mathbf{u}$ in the linearization step. The values are iteratively updated in the problem solution as shown in the next Section.

5. Problem solution

The formulation obtained to solve the frictional contact problem can be summarized as:

$$\begin{cases} if\ \left[p_{N\,g} + \frac{\kappa E}{h} g_{N\,g}\right]_- > 0 \\ \qquad \delta\Pi(\mathbf{u}, \delta\mathbf{u}) = 0 \\ otherwise \\ \qquad if\ \|\mathbf{T}_n\left(\mathbf{T}^*_g + \frac{\kappa E}{h}\mathbf{g}_g\right)\| \leq \mu\left(p_{N\,g} + \frac{\kappa E}{h} g_{N\,g}\right) \\ \qquad\qquad \delta\Pi(\mathbf{u}, \delta\mathbf{u}) + \delta\Pi_{C_{St}}(\mathbf{u}, \delta\mathbf{u}) = 0, \\ \qquad if\ \|\mathbf{T}_n\left(\mathbf{T}^*_g + \frac{\kappa E}{h}\mathbf{g}_g\right)\| > \mu\left(p_{N\,g} + \frac{\kappa E}{h} g_{N\,g}\right) \\ \qquad\qquad \delta\Pi(\mathbf{u}, \delta\mathbf{u}) + \delta\Pi_{C_{Sl}}(\mathbf{u}, \delta\mathbf{u}) = 0 \end{cases} \tag{39}$$

The first equation corresponds to the case of no active contact condition. The evaluation of $\delta\Pi_{C_{St}}$ is found in (34), whereas $\delta\Pi_{C_{Sl}}$ is defined in (38).

5.1. Solution algorithm

The choice of the stabilizing term $\mathbf{T}^*$ requires an iterative process to solve (39). The proposed procedure, first introduced in [3] is shown in Algorihm 1. During the *N-R loop* the contact status for each integration point on the contact boundary $\Gamma_C^{(1)}$ is evaluated. When any integration point becomes active, it is set to stick contact for its first iteration. After that, the slip condition is evaluated and the relative velocity is calculated for the sliding integration points. An additional loop is needed for the solution of the problem to update the stabilizing stress field. Here it is called *augmentation loop* because of the similarities with the augmented Lagrange multipliers approach. Our experience shows that the number of augmentations is usually low, so the computational cost of the solution is not substantially increased.

Algorithm 1 Problem resolution scheme

```
Update boundary conditions
Update p_N and p_T from previous converged step
Set all previous contact points to stick state.
ξ_t ← previous step's ξ
while Residual > Tol do Augmentation loop
    while ‖r‖/‖f_int‖ > Tol do N-R loop
        λ_N ← (κE/h) g_N + p_N
        Check active quadrature points. (λ_N < 0)
        for all Active stick points do
            λ_T ← T_n ((κE/h) g + T*)
            if ‖λ_T‖ ≥ μ |λ_N| then
                Change status to Slip
            else
                Evaluate contact using (34) (Stick)
            end if
        end for
        for all Active slip points do
            Evaluate Δ^t g_t
            Evaluate contact using (38) (Slip)
        end for
        Evaluate residual of (39)
        Solve Δu in (39)
    end while
    Update p_N and p_T
    Evaluate residual of (39)
end while
```

5.2. Linearization

The Newton-Raphson solver needs the linearization of the equations that solve the contact problem. This work will only describe the linearization of $\delta\Pi_C$ for both stick and slip cases. The linearization of the contact contribution in the stick case is

$$\Delta\delta\Pi_{C_{Stick}} = \sum_g \left[\frac{\kappa E}{h}\Delta\mathbf{g}\cdot\delta\mathbf{g}\right]|J_g|\,H_g \tag{40}$$

The definition of the linearization $\Delta\mathbf{g}$ is in this case equivalent to its variation (25), as there is no change of contact coordinates during the stick state. The linearization

of the contact contribution in the slip state is shown in (42). For the sake of simplicity, the following definition has been included in the linearization:

$$\Delta^t \mathbf{g}_t = \frac{\mathbf{p}_T - \frac{\kappa E}{h}\mathbf{T}_n \Delta^t \mathbf{g}}{\|\mathbf{p}_T - \frac{\kappa E}{h}\mathbf{T}_n \Delta^t \mathbf{g}\|} \tag{41}$$

$$\begin{aligned}\Delta\delta\Pi_{C_{Slip}} = \sum_g \Bigg[& \frac{\kappa E}{h}\Delta g_N \cdot \delta g_N + \left(\frac{\kappa E}{h} g_N + p_N\right)\Delta\delta g_N - \\ & -\mu\frac{\kappa E}{h}\Delta g_N \left(\Delta^t \mathbf{g}_t \cdot \delta\mathbf{g}\right) - \mu\left(\frac{\kappa E}{h} g_N + p_N\right)\left(\Delta\Delta^t \mathbf{g}_t \cdot \delta\mathbf{g}\right) - \\ & -\mu\left(\frac{\kappa E}{h} g_N + p_N\right)\left(\Delta^t \mathbf{g}_t \cdot \Delta\delta\mathbf{g}\right)\Bigg] \, |J_g| \, H_g\end{aligned} \tag{42}$$

In this case Δg_N, $\Delta\delta g_N$, $\Delta\Delta^t \mathbf{g}_t$ and $\Delta\delta\mathbf{g}$ have to be evaluated. As stated in Section 3.1, the exact derivative must be calculated for the linearization terms. To evaluate Δg_N we rearrange (1) and take variations:

$$\mathbf{x}^{(2)}(\boldsymbol{\xi}^{(2)}) = \mathbf{x}^{(1)} + g_N \mathbf{n}^{(1)} \tag{43}$$

$$\Delta\mathbf{u}^{(2)} + \frac{\partial \mathbf{x}^{(2)}(\boldsymbol{\xi}^{(2)})}{\partial\xi}\Delta\xi + \frac{\partial \mathbf{x}^{(2)}(\boldsymbol{\xi}^{(2)})}{\partial\eta}\Delta\eta = \Delta\mathbf{u}^{(1)} + \Delta g_N \mathbf{n}^{(1)} + g_N \Delta\mathbf{n}^{(1)} \tag{44}$$

Note that as we are using a ray-tracing scheme to define the contact point pairs, the fixed point is located on the slave body, and the coordinates of the master body are variable. This is contrary to the case of using a closest projection scheme to define the contact point pairs. As $\mathbf{n}^{(1)}$ is a unit vector, then $\Delta\mathbf{n}^{(1)} \cdot \mathbf{n}^{(1)} = 0$ and $\mathbf{n}^{(1)} \cdot \mathbf{n}^{(1)} = 1$. Therefore, if we multiply (44) by $\mathbf{n}^{(1)}$

$$\Delta g_N = (\Delta\mathbf{u}^{(2)} - \Delta\mathbf{u}^{(1)}) \cdot \mathbf{n}^{(1)} + \mathbf{s}_\xi^{(2)} \cdot \mathbf{n}^{(1)}\Delta\xi + \mathbf{s}_\eta^{(2)} \cdot \mathbf{n}^{(1)}\Delta\eta \tag{45}$$

where the variables $\Delta\xi$ and $\Delta\eta$ can be calculated solving the linear system of equations (46) resulting from multiplying (44) by vectors $\mathbf{s}_\xi^{(1)}$ and $\mathbf{s}_\eta^{(1)}$, taking into account that $\mathbf{s}_\xi^{(1)} \cdot \mathbf{n}^{(1)} = 0$, $\mathbf{s}_\eta^{(1)} \cdot \mathbf{n}^{(1)} = 0$.

$$\begin{bmatrix} \mathbf{s}_\xi^{(2)} \cdot \mathbf{s}_\xi^{(1)} & \mathbf{s}_\eta^{(2)} \cdot \mathbf{s}_\xi^{(1)} \\ \mathbf{s}_\xi^{(2)} \cdot \mathbf{s}_\eta^{(1)} & \mathbf{s}_\eta^{(2)} \cdot \mathbf{s}_\eta^{(1)} \end{bmatrix} \begin{Bmatrix} \Delta\xi \\ \Delta\eta \end{Bmatrix} = \begin{Bmatrix} g_N \mathbf{s}_\xi^{(1)} \cdot \Delta\mathbf{n}^{(1)} - (\Delta\mathbf{u}^{(2)} - \Delta\mathbf{u}^{(1)}) \cdot \mathbf{s}_\xi^{(1)} \\ g_N \mathbf{s}_\eta^{(1)} \cdot \Delta\mathbf{n}^{(1)} - (\Delta\mathbf{u}^{(2)} - \Delta\mathbf{u}^{(1)}) \cdot \mathbf{s}_\eta^{(1)} \end{Bmatrix} \tag{46}$$

The terms $\Delta\xi$, $\Delta\eta$ are considered for the calculation of $\Delta\delta g_N$ and $\Delta\delta\mathbf{g}$. Therefore, starting from (18) and (25) these increments are respectively written as

$$\Delta\delta g_N = (\delta\mathbf{s}_\xi^{(2)} \cdot \mathbf{n}^{(1)})\Delta\xi + (\delta\mathbf{s}_\eta^{(2)} \cdot \mathbf{n}^{(1)})\Delta\eta + (\delta\mathbf{u}^{(2)} - \delta\mathbf{u}^{(1)}) \cdot \Delta\mathbf{n}^{(1)} \tag{47}$$

$$\Delta\delta\mathbf{g} = (\delta\mathbf{s}_\xi^{(2)} \cdot \mathbf{n}^{(1)})\Delta\xi + (\delta\mathbf{s}_\eta^{(2)} \cdot \mathbf{n}^{(1)})\Delta\eta + (\delta\mathbf{u}^{(2)} - \delta\mathbf{u}^{(1)}) \cdot \Delta\mathbf{n}^{(1)} \tag{48}$$

The details of the calculation of $\delta\mathbf{s}_\xi^{(2)}$, $\delta\mathbf{s}_\eta^{(2)}$ and $\Delta\mathbf{n}^{(1)}$ and $\Delta^t\mathbf{g}_t$ are shown in Appendices A and B. The linearization of the Jacobian is also considered, but not shown in this paper as they are standard terms. Its calculation can be easily performed using the tools developed in Appendix A.

6. Numerical examples

6.1. Contact between plane surfaces

Figure 5 left shows a 2D sketch of the first numerical example, which is the contact simulation between plane surfaces, represented by two elastic cubes. The orientation of the reference system is also shown in the figure, x being the out of plane direction. The separation in the sketch is only for the sake of clarity, as the contact surfaces are overlapping at the initial configuration. A vertical displacement $d = -1.6 \cdot 10^{-6} m$ is applied on the upper face of body 2. The displacements along y direction are constrained on the upper face of body 2 and on the lower face of body 1. Finally, symmetry conditions are applied to the faces parallel to the yz plane, i.e. this problem can also be analyzed as a plane strain problem. The values of the pressure applied on two lateral faces of body 1 are $p_y = 4 \cdot 10^{11}(0.01 - z)z\ Pa$ and $p_z = 10 \cdot 10^{11}(0.01 - z)z\ Pa$. Material properties are common for both bodies, the Young modulus being $E = 115 GPa$ and the Poisson coefficient $\nu = 0.3$.

First we will test the convergence of the solution solving a frictionless contact case. Although there is no analytical solution for this problem, we will use the solution of a 2D overkill mesh from [14] as a reference to measure the discretization error. Non-conforming Cartesian grids are used on both bodies. Figure 6 shows some of the meshes used for the analysis. The initial mesh consists in a $3 \times 3 \times 3$ grid for the upper body and a $4 \times 4 \times 4$ grid for the lower body. In order to avoid nodes over the boundary for this test, the initial grids are built adding a small offset to the cubes. A set of uniformly h-refined meshes is then built by subdividing each element into 8 new elements. Figure 7 shows the relative error in energy norm for a sequence of 5 meshes using linear elements, $\mathscr{H}_8$, and 3 meshes using quadratic elements , $\mathscr{H}_{20}$. The results show that the theoretical convergence rate of the error in energy norm, represented by the triangles, is achieved both for $\mathscr{H}_8$ and $\mathscr{H}_{20}$ elements.

The recovered contact stress p_N is shown in Figure 8 for the solution of the finest mesh. In this figure, positive values of stresses represent compression. The graph on the right shows the evolution of the contact stress on the yz plane (this profile remains constant along the x direction) for meshes 2 to 5. The results show that the values of the contact pressure appropriately converge to the reference solution from [14].

Now the same problem is solved considering frictional contact with a friction coefficient $\mu = 1.0$. In this case we have used non-conforming manually h-adapted

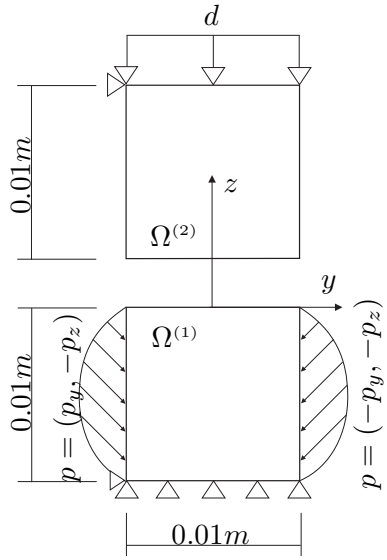

Figure 5: Example 1. Sketch of the contact problem between two elastic cubes in contact.

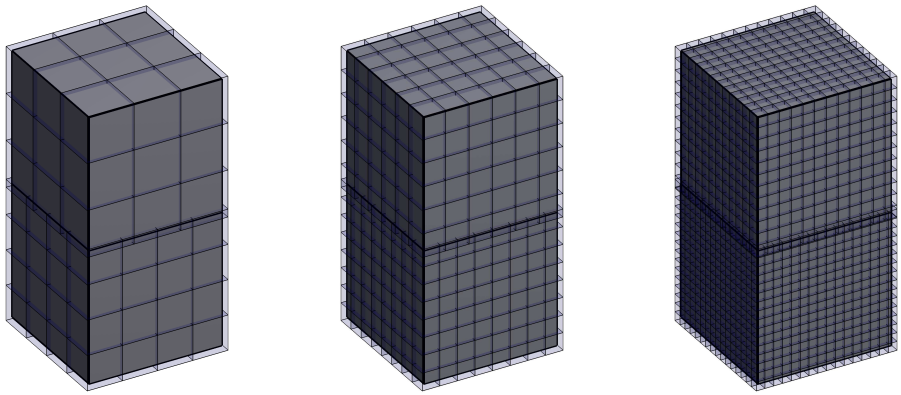

Figure 6: Example 1. Refinement process for the study of the convergence of the solution. Meshes 1 to 3 are shown from left to right.

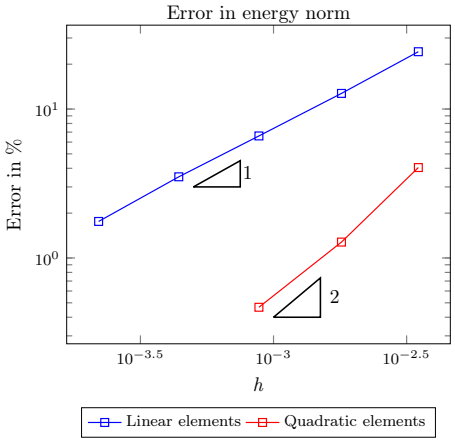

Figure 7: Example 1: Evolution of the error in the energy norm as a function of the element size for the frictionless contact case. Analysis of the convergence of the solution. The element size is referred to the lower body.

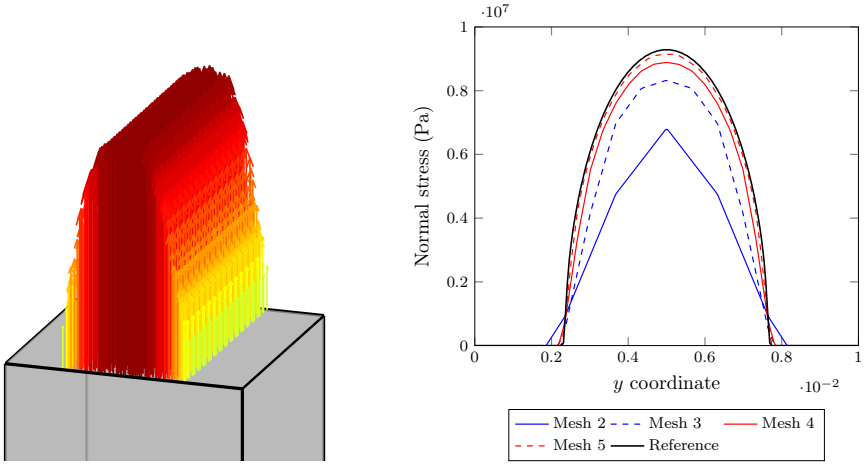

Figure 8: Example 1. Frictionless contact. Left: Normal stress on the contact area (positive values of the stress stand for compression). Right: Evolution of values of the normal stress, along a path that follows the y direction, with mesh refinement.

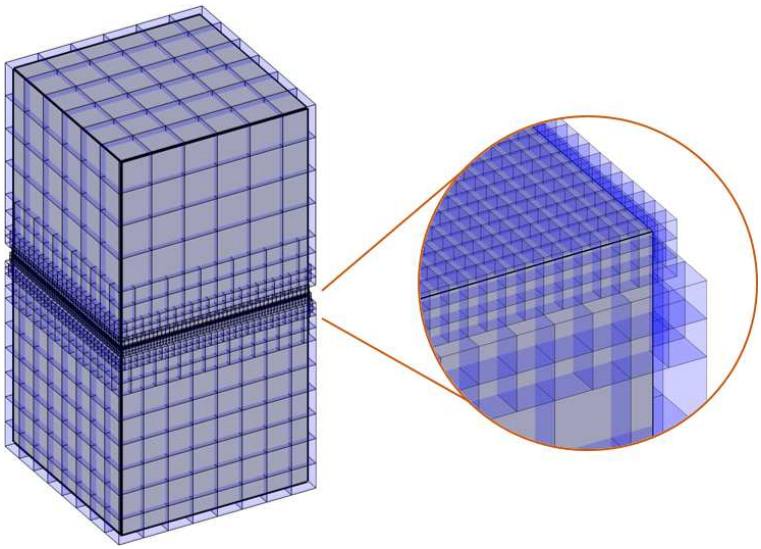

Figure 9: Example 1. Frictional contact h-adapted mesh. The image on the right shows a detail of the refinement of the mesh along the contact surface of the bottom body.

meshes for both bodies, as depicted in Figure 9. Starting with the initial mesh of Figure 5, we refined the elements over the contact surface multiple times. The surrounding elements were refined as well to keep the difference of the refinement level between adjacent elements below or equal to one.

The results of this problem are shown in Figure 10. The graph on the left shows the values of the multipliers $\lambda_N = p_N + \frac{\kappa E}{h} g_N$ and $\boldsymbol{\lambda}_T = \mathbf{p}_T + \frac{\kappa E}{h} \mathbf{g}_T$. The blue dashed line represents the values of $-\lambda_N$. We can observe the slip and stick areas, with $\|\boldsymbol{\lambda}_T\| = \mu\,|\lambda_N|$ over the sliding area and $\|\boldsymbol{\lambda}_T\| \leq \mu\,|\lambda_N|$ over the adhesion area. All these results are similar to those obtained in [14]. The values of the smoothed stress field p_N and $\|\mathbf{p}_T\|$ are represented in the graph on the right. This smoothed field is evaluated without taking into account any constraint, hence the differences between the multiplier values. The imposition of the contact constraints to evaluate this smoothed field to get a better solution using the SPR-C technique [31] will be considered in future work.

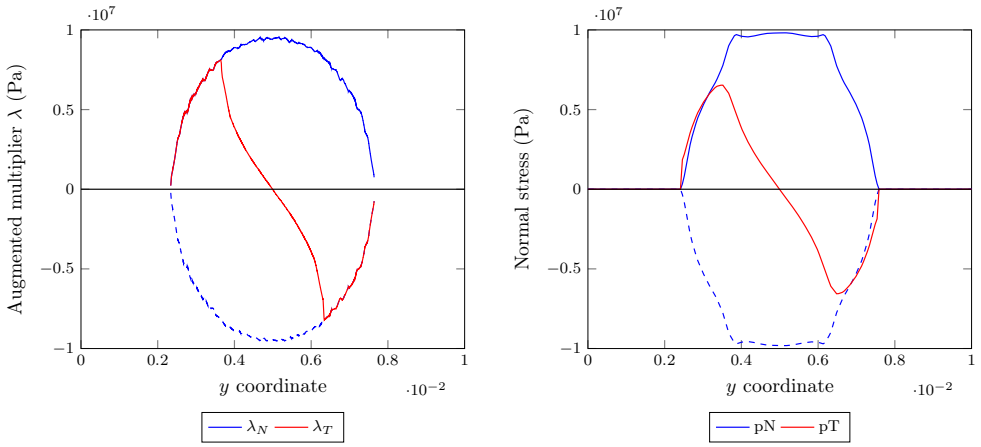

Figure 10: Example 1. Frictional contact along a path that follows the y direction. Left: values of the augmented Lagrange multipliers. Right: smoothed stress field recovered using SPR.

6.2. Hollow sphere under internal pressure

The second example consists of a hollow sphere under internal pressure, which is divided into two independent volumes. In this problem we have curved contact surfaces. We can exactly evaluate the discretization error, as there is an analytical solution. It is easy to express the analytical solution of the problem in spherical coordinates (r, θ, ϕ). The transformation from Cartesian to spherical coordinates is as follows:

$$\begin{aligned} r &= \sqrt{x^2 + y^2 + z^2} \\ \theta &= \arccos \frac{z}{r} \\ \phi &= \arctan \frac{y}{x} \end{aligned} \tag{49}$$

Then, the analytical stress field corresponding to this problem is:

$$\begin{aligned} \boldsymbol{\sigma}_r &= -P \frac{a^3}{b^3 - a^3} \left(\frac{b^3}{r^3} - 1 \right) \\ \boldsymbol{\sigma}_\theta = \boldsymbol{\sigma}_\phi &= P \frac{a^3}{b^3 - a^3} \left(\frac{b^3}{2r^3} + 1 \right) \end{aligned} \tag{50}$$

P being the value of the compression load applied to the internal surface of the sphere, a the inner radius and b the outer radius of the complete hollow sphere. For

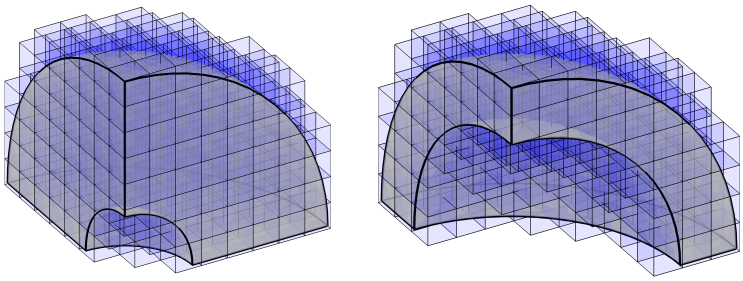

Figure 11: Example 2. First calculation meshes. The sphere is divided into two volumes, which are discretized using non-conforming Cartesian grids.

this example the smaller sphere has an inner radius $a = 5$, the outer radius of the bigger sphere is $b = 20$ and the contact interface is located at radius $c = 15$. One eighth of the hollow spheres with the appropriate symmetry conditions has been used to create the analysis model, as shown in Figure 11. The material properties chosen for the problem are $E = 1000, \nu = 0.3$. The applied internal pressure is $P = 1$.

Following the procedure used in the previous example, a series of non-conforming, uniformly h-refined meshes were solved to test the convergence of the solution. The first calculation mesh is shown in Figure 11. Figure 12 shows the evolution of the relative exact error in energy norm of the solution with $\mathscr{H}_8$ and $\mathscr{H}_{20}$ elements. The optimal convergence rate, depicted by the triangles in the graph, is again achieved for both element types.

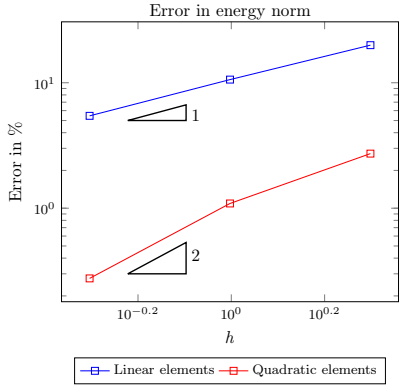

Figure 12: Example 2. Energy norm error of the solution as a function of the element size. Analysis of the convergence of the solution. The optimal convergence rates are depicted by the triangles below the curves.

6.3. Frictional contact under large deformations

The last example in this paper is an ironing problem under large deformations, similar to the ones solved in [14] and [40]. Figure 13 shows the dimensions of the bodies in contact. Material properties and displacements of the problem are shown in Table 1. The ironing block consists of a sphere modelled by four surfaces. The upper surfaces of the sphere are moved towards the slab in 5 time steps, after which a motion along the y direction is applied using 80 time steps. We used a Neo-Hookean material model [46] to consider large deformations of the solids.

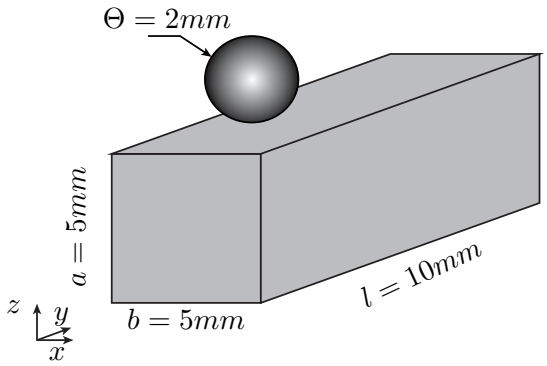

Figure 13: Example 3. Scheme of the ironing problem.

Young modulus of the slab	E_{Slab}	100 (GPa)
Poisson coefficient of the slab	ν_{Slab}	0.3
Young modulus of the sphere	E_{Sphere}	1000 (GPa)
Poisson coefficient of the sphere	ν_{Sphere}	0.3
Vertical displacement of the sphere	Δu_z	-0.3 (mm)
Horizontal displacement of the sphere	Δu_y	5 (mm)
Friction coefficient	μ	0.3

Table 1: Parameters of the ironing problem

This problem was solved with three different meshes. Figure 14 shows the mesh for the first two analyses on the left, with $\mathscr{H}_8$ elements for the first analysis and $\mathscr{H}_{20}$ elements for the second. A manual h-adaptive refinement was performed on the contact surface of the slab to create the third analysis mesh (Figure 14 right), using only $\mathscr{H}_8$ elements this time. Two different meshes with $\mathscr{H}_8$ elements were solved using ANSYS® [47] in order to compare the results. The first of the meshes was created using a discretization similar to the one used in the first mesh in Figure 14. The second was an overkilled mesh which served as a reference.

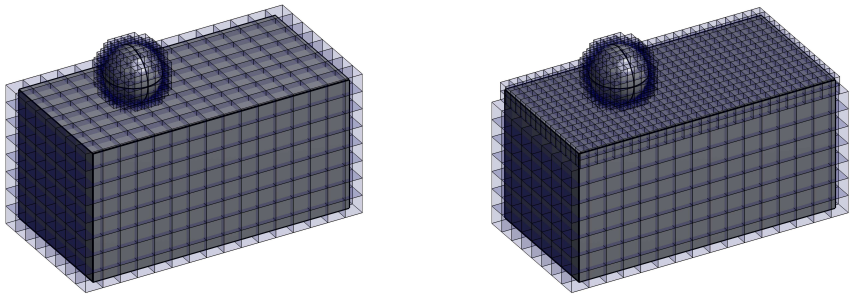

Figure 14: Example 3. Calculation meshes of the ironing problem. Left: uniform initial meshes. Right: manually adapted mesh on the lower body.

Figure 15 shows the sum of the vertical and horizontal reaction forces measured on the lower face of the slab for all the analyses. The results are similar to those obtained with ANSYS®, with the values of the reaction forces tending to the reference value with refinement of the mesh. It should be noted that the use of a coarse mesh with $\mathscr{H}_{20}$ elements provides a smooth evolution of the reaction forces, close to the reference values. This is thanks to the definition of the exact geometry, which is independent of the resolution of the mesh. In all cases the wave lengths of the oscillations that appear in the reaction forces are equal to the size of the mesh and are caused by the interaction of the discretized surfaces, which vary with the element size. The deformed configuration for two different load steps is represented in Figure 16.

7. Conclusions

This paper has extended the formulation first proposed in [3] to the case of large deformation frictional contact. In this method a stabilization term that is iteratively computed is added to an augmented Lagrangian formulation, after which the Lagrange multipliers are condensed for the stick and slide case, ensuring a smooth transition between both states.

The formulation was implemented within the three dimensional version of the Cartesian grid Finite Element Method (cgFEM). For this purpose the deformed configuration was defined as a combination of the NURBS surface definition and the finite element displacement field, which allows the exact definition of the boundaries to be taken into account, an important factor in defining the contact kinematics.

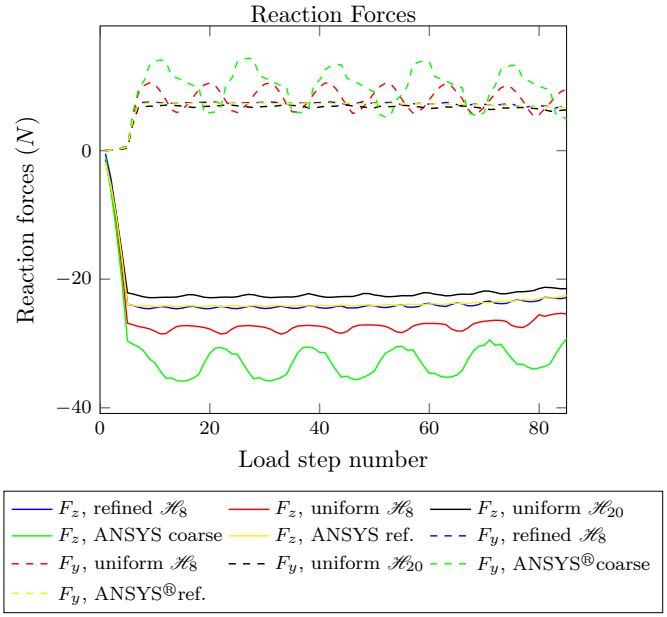

Figure 15: Example 3. Reaction forces on the lower face of the block.

Some numerical examples were solved to test the method, using linear 8-node and quadratic 20-node elements. The results show that the appropriate convergence rates are achieved, and the transition between sticking and sliding states is sufficiently smooth. Although the present work may not outperform the more established body-fitted contact formulations in terms of precision or efficiency, it allows solving large sliding contact problems within the embedded domain framework and would be of interest for the solution of problems like contact wear simulation, fretting fatigue or prosthesis-tissue interaction.

Acknowledgements

The authors wish to thank the Spanish Ministerio de Economia y Competitividad the Generalitat Valenciana and the Universitat Politecnica de Valencia for their financial support received through the projects DPI2013-46317-R, Prometeo 2016/007 and the FPI2015 program.

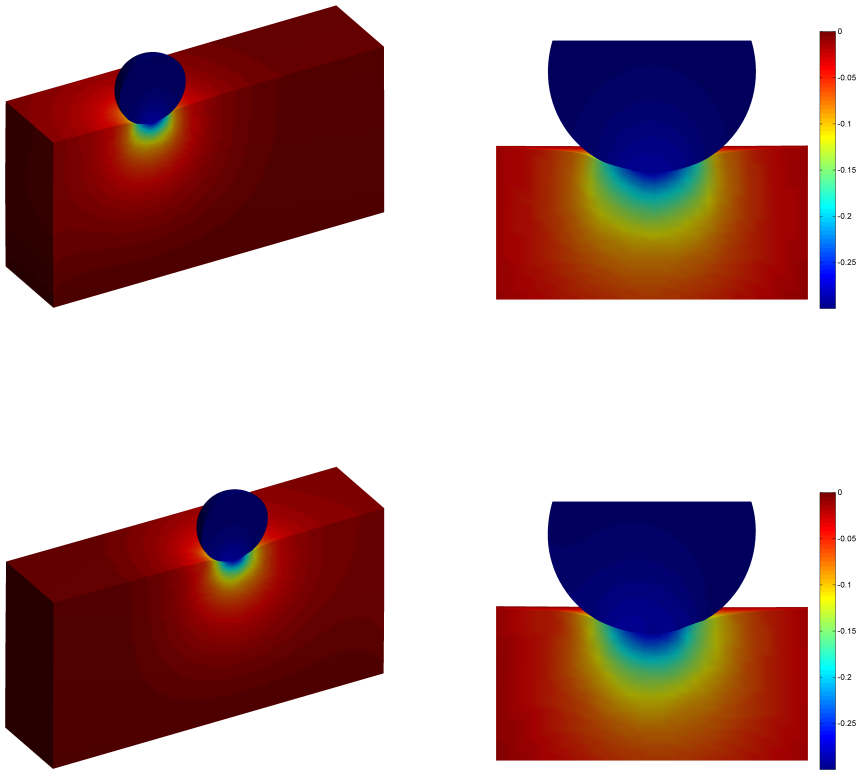

Figure 16: Example 3. Deformed configuration and vertical displacements u_z for the ironing problem for different load steps. On the top, the last load step with only vertical displacement is represented. On the bottom, results from load step 45. These results correspond to the analysis of a coarse mesh using quadratic $\mathscr{H}_{20}$ elements.

A. Variation of normal and tangent vectors

We recall here (15) for the calculation of $\delta\mathbf{n}^{(1)}$.

$$\mathbf{n}^{(1)} = \frac{\hat{\mathbf{n}}^{(1)}}{\|\hat{\mathbf{n}}^{(1)}\|}; \qquad \hat{\mathbf{n}}^{(1)} = \mathbf{s}_\xi^{(1)} \times \mathbf{s}_\eta^{(1)} \tag{51}$$

$$\delta\mathbf{n}^{(1)} = \frac{\delta\mathbf{s}_\xi^{(1)} \times \mathbf{s}_\eta^{(1)} + \mathbf{s}_\xi^{(1)} \times \delta\mathbf{s}_\eta^{(1)}}{\left\|\hat{\mathbf{n}}^{(1)}\right\|} - \frac{\mathbf{n}^{(1)}}{\left\|\hat{\mathbf{n}}^{(1)}\right\|}\left[\mathbf{n}^{(1)} \cdot (\delta\mathbf{s}_\xi^{(1)} \times \mathbf{s}_\eta^{(1)} + \mathbf{s}_\xi^{(1)} \times \delta\mathbf{s}_\eta^{(1)})\right] \tag{52}$$

For the calculation of the variation of the tangent vectors $\mathbf{s}_\xi^{(1)}$ and $\mathbf{s}_\eta^{(1)}$ we start from (16). We will only describe the calculation of $\delta\mathbf{s}_\xi^{(1)}$ as the other term, $\delta\mathbf{s}_\eta^{(1)}$, has an identical procedure:

$$\mathbf{s}_\xi^{(1)} = \frac{\partial\mathbf{x}^{(1)}}{\partial\xi} = \frac{\partial S(\xi,\eta)}{\partial\xi} + \sum_j \left(\frac{\partial N_j}{\partial\zeta_1^e}\frac{\partial\zeta_1^e}{\partial\xi} + \frac{\partial N_j}{\partial\zeta_2^e}\frac{\partial\zeta_2^e}{\partial\xi} + \frac{\partial N_j}{\partial\zeta_3^e}\frac{\partial\zeta_3^e}{\partial\xi}\right)\mathbf{u}_j^{(1)} \tag{53}$$

$$\delta\mathbf{s}_\xi^{(1)} = \delta\left(\frac{\partial\mathbf{x}^{(1)}}{\partial\xi}\right) = \frac{\partial\delta\mathbf{u}^{(1)}}{\partial\xi} = \sum_j \left(\frac{\partial N_j}{\partial\zeta_1^e}\frac{\partial\zeta_1^e}{\partial\xi} + \frac{\partial N_j}{\partial\zeta_2^e}\frac{\partial\zeta_2^e}{\partial\xi} + \frac{\partial N_j}{\partial\zeta_3^e}\frac{\partial\zeta_3^e}{\partial\xi}\right)\delta\mathbf{u}_j^{(1)} \tag{54}$$

The linearization of all these variables has the same structure as the variation, so the variations $\delta\mathbf{n}^{(1)}$, $\delta\mathbf{s}_\xi^{(1)}$ and $\delta\mathbf{s}_\eta^{(1)}$ can be directly substituted for the increments $\Delta\mathbf{n}^{(1)}$, $\Delta\mathbf{s}_\xi^{(1)}$ and $\Delta\mathbf{s}_\eta^{(1)}$.

B. Linearization of $\Delta^t\mathbf{g}_t$

We recall the definition of $\Delta^t\mathbf{g}_t$ here:

$$\Delta^t\mathbf{g}_t = \frac{\mathbf{p}_T - \frac{\kappa E}{h}\mathbf{T}_n\left(\mathbf{x}^{(1)} - \mathbf{x}^{(2)}\left(\boldsymbol{\xi}_t\right)\right)}{\left\|\mathbf{p}_T - \frac{\kappa E}{h}\mathbf{T}_n\left(\mathbf{x}^{(1)} - \mathbf{x}^{(2)}\left(\boldsymbol{\xi}_t\right)\right)\right\|} \tag{55}$$

If we use the simplification of (56), the linearization of $\Delta^t\mathbf{g}_t$ can be expressed as in (57)

$$\Delta^t\mathbf{g}_t = \frac{\hat{\mathbf{d}}}{\|\hat{\mathbf{d}}\|}; \qquad \hat{\mathbf{d}} = \mathbf{p}_T + \frac{\kappa E}{h}\mathbf{T}_n\left(\mathbf{x}^{(2)}\left(\boldsymbol{\xi}_t\right) - \mathbf{x}^{(1)}\right) \tag{56}$$

$$\Delta\Delta^t\mathbf{g}_t = \frac{\Delta\hat{\mathbf{d}}}{\left\|\hat{\mathbf{d}}\right\|} - \frac{\Delta^t\mathbf{g}_t}{\left\|\hat{\mathbf{d}}\right\|}\left[\Delta^t\mathbf{g}_t \cdot \Delta\hat{\mathbf{d}}\right] \tag{57}$$

Finally, for the linearization of $\hat{\mathbf{d}}$ we can rearrange equation (56) as:

$$\hat{\mathbf{d}} = \mathbf{p}_T + \frac{\kappa E}{h}\left\{\left(\mathbf{x}^{(2)} - \mathbf{x}^{(1)}\right) - \left[\left(\mathbf{x}^{(2)} - \mathbf{x}^{(1)}\right) \cdot \mathbf{n}^{(1)}\right]\mathbf{n}^{(1)}\right\} \tag{58}$$

With this definition we have a clearer linearization term, which is the following:

$$\begin{aligned}\Delta\hat{\mathbf{d}} = \frac{\kappa E}{h}\Big\{\Delta\mathbf{u} - \Big[\Delta\mathbf{u}\cdot\mathbf{n}^{(1)} + \left(\mathbf{x}^{(2)} - \mathbf{x}^{(1)}\right)\cdot\Delta\mathbf{n}^{(1)}\Big]\mathbf{n}^{(1)} + \\ \Big[\left(\mathbf{x}^{(2)} - \mathbf{x}^{(1)}\right)\cdot\mathbf{n}^{(1)}\Big]\Delta\mathbf{n}^{(1)}\Big\}\end{aligned} \tag{59}$$

where $\Delta\mathbf{u} = \Delta\mathbf{u}^{(2)}\left(\boldsymbol{\xi}_t\right) - \Delta\mathbf{u}^{(1)}$. Notice that the local coordinates of the *master* body are not unknowns, but the coordinates from the last converged step.

References

[1] O. Marco, R. Sevilla, Y. Zhang, J. J. Ródenas, and M. Tur, "Exact 3D boundary representation in finite element analysis based on Cartesian grids independent of the geometry," *International Journal for Numerical Methods in Engineering*, vol. 103, pp. 445–468, aug 2015.

[2] L. Giovannelli, J. Ródenas, J. Navarro-Jiménez, and M. Tur, "Direct medical image-based Finite Element modelling for patient-specific simulation of future implants," *Finite Elements in Analysis and Design*, vol. 136, 2017.

[3] M. Tur, J. Albelda, J. M. Navarro-Jimenez, and J. J. Rodenas, "A modified perturbed lagrangian formulation for contact problems," *Computational Mechanics*, vol. 55, pp. 737–754, Apr 2015.

[4] M. Tur, E. Giner, F. Fuenmayor, and P. Wriggers, "2d contact smooth formulation based on the mortar method," *Computer Methods in Applied Mechanics and Engineering*, vol. 247–248, pp. 1 – 14, 2012.

[5] D. Neto, M. Oliveira, L. Menezes, and J. Alves, "A contact smoothing method for arbitrary surface meshes using nagata patches," *Computer Methods in Applied Mechanics and Engineering*, vol. 299, pp. 283 – 315, 2016.

[6] M. A. Puso and T. A. Laursen, "A mortar segment-to-segment frictional contact method for large deformations," *Computer Methods in Applied Mechanics and Engineering*, vol. 193, no. 45-47, pp. 4891–4913, 2004.

[7] B. Yang, T. A. Laursen, and X. Meng, "Two dimensional mortar contact methods for large deformation frictional sliding," *International Journal for Numerical Methods in Engineering*, vol. 62, no. 9, pp. 1183–1225, 2005.

[8] T. Hughes, J. Cottrell, and Y. Bazilevs, "Isogeometric analysis: CAD, finite elements, NURBS, exact geometry and mesh refinement," *Computer Methods in Applied Mechanics and Engineering*, vol. 194, pp. 4135–4195, Oct. 2005.

[9] L. De Lorenzis, P. Wriggers, and G. Zavarise, "A mortar formulation for 3D large deformation contact using NURBS-based isogeometric analysis and the augmented Lagrangian method," *Computational Mechanics*, vol. 49, no. 1, pp. 1–20, 2012.

[10] I. Temizer, P. Wriggers, and T. J. R. Hughes, "Three-dimensional mortar-based frictional contact treatment in isogeometric analysis with NURBS," *Computer Methods in Applied Mechanics and Engineering*, vol. 209-212, pp. 115–128, 2012.

[11] M. Dittmann, M. Franke, I. Temizer, and C. Hesch, "Isogeometric Analysis and thermomechanical Mortar contact problems," *Computer Methods in Applied Mechanics and Engineering*, vol. 274, pp. 192–212, 2014.

[12] F. Belgacem, P. Hild, and P. Laborde, "The mortar finite element method for contact problems," *Mathematical and Computer Modelling*, vol. 28, pp. 263–271, aug 1998.

[13] K. A. Fischer and P. Wriggers, "Mortar based frictional contact formulation for higher order interpolations using the moving friction cone," *Computer Methods in Applied Mechanics and Engineering*, vol. 195, pp. 5020–5036, jul 2006.

[14] M. Tur, F. J. Fuenmayor, and P. Wriggers, "A mortar-based frictional contact formulation for large deformations using Lagrange multipliers," *Computer Methods in Applied Mechanics and Engineering*, vol. 198, no. 37-40, pp. 2860–2873, 2009.

[15] M. Gitterle, A. Popp, M. Gee, and W. Wall, "Finite deformation frictional mortar contact using a semi-smooth newton method with consistent linearization," *International Journal for Numerical Methods in Engineering*, vol. 84, pp. 543 – 571, 10 2010.

[16] J. E. Dolbow and a. Devan, "Enrichment of enhanced assumed strain approximations for representing strong discontinuities: addressing volumetric incompressibility and the discontinuous patch test," *International Journal for Numerical Methods in Engineering*, vol. 59, pp. 47–67, Jan. 2004.

[17] É. Béchet, N. Moës, and B. Wohlmuth, "A stable Lagrange multiplier space for stiff interface conditions within the extended finite element method," *International Journal for Numerical Methods in Engineering*, vol. 78, pp. 931–954, may 2009.

[18] I. Nistor, M. L. E. Guiton, P. Massin, N. Moës, and S. Géniaut, "An X-FEM approach for large sliding contact along discontinuities," *International Journal for Numerical Methods in Engineering*, vol. 78, pp. 1407–1435, 2009.

[19] J. Dolbow, N. Moës, and T. Belytschko, "An extended finite element method for modeling crack growth with frictional contact," *Computer Methods in Applied Mechanics and Engineering*, vol. 190, pp. 6825–6846, 2001.

[20] R. Ribeaucourt, M. C. Baietto-Dubourg, and A. Gravouil, "A new fatigue frictional contact crack propagation model with the coupled X-FEM/LATIN method," *Computer Methods in Applied Mechanics and Engineering*, vol. 196, pp. 3230–3247, 2007.

[21] F. Liu and R. I. Borja, "A contact algorithm for frictional crack propagation with the extended finite element method," *International Journal for Numerical Methods in Engineering*, vol. 76, no. June, pp. 1489–1512, 2008.

[22] F. Liu and R. I. Borja, "Stabilized low-order finite elements for frictional contact with the extended finite element method," *Computer Methods in Applied Mechanics and Engineering*, vol. 199, no. 37-40, pp. 2456–2471, 2010.

[23] P. Heintz and P. Hansbo, "Stabilized Lagrange multiplier methods for bilateral elastic contact with friction," *Computer Methods in Applied Mechanics and Engineering*, vol. 195, pp. 4323–4333, jul 2006.

[24] Y. Renard, "Generalized Newton's methods for the approximation and resolution of frictional contact problems in elasticity," *Computer Methods in Applied Mechanics and Engineering*, vol. 256, pp. 38–55, 2013.

[25] J. Oliver, S. Hartmann, J. C. Cante, R. Weyler, and J. A. Hernández, "A contact domain method for large deformation frictional contact problems. Part 1: Theoretical basis," *Computer Methods in Applied Mechanics and Engineering*, vol. 198, pp. 2591–2606, 2009.

[26] K. Poulios and Y. Renard, "An unconstrained integral approximation of large sliding frictional contact between deformable solids," *Computers and Structures*, vol. 153, pp. 75–90, 2015.

[27] P. Hansbo, A. Rashid, and K. Salomonsson, "Least-squares stabilized augmented Lagrangian multiplier method for elastic contact," *Finite Elements in Analysis and Design*, vol. 116, pp. 32–37, 2015.

[28] C. Annavarapu, M. Hautefeuille, and J. E. Dolbow, "A Nitsche stabilized finite element method for frictional sliding on embedded interfaces. Part I: Single interface," *Computer Methods in Applied Mechanics and Engineering*, vol. 268, pp. 417–436, 2014.

[29] C. Annavarapu, R. R. Settgast, S. M. Johnson, P. Fu, and E. B. Herbold, "A weighted nitsche stabilized method for small-sliding contact on frictional surfaces," *Computer Methods in Applied Mechanics and Engineering*, vol. 283, pp. 763–781, 2015.

[30] O. C. Zienkiewicz and J. Z. Zhu, "The superconvergent patch recovery and a posteriori error estimates. Part 1: The recovery technique," *International Journal for Numerical Methods in Engineering*, 1992.

[31] J. J. Ródenas, M. Tur, F. J. Fuenmayor, and A. Vercher, "Improvement of the superconvergent patch recovery technique by the use of constraint equations: The SPR-C technique," *International Journal for Numerical Methods in Engineering*, vol. 70, no. October 2006, pp. 705–727, 2007.

[32] M. Tur, J. Albelda, O. Marco, and J. J. Ródenas, "Stabilized method of imposing Dirichlet boundary conditions using a recovered stress field," *Computer Methods in Applied Mechanics and Engineering*, vol. 296, pp. 352–375, 2015.

[33] P. Wriggers, *Computational contact mechanics*. Springer Science & Business Media, 2006.

[34] T. Laursen, *Computational Contact and Impact Mechanics: Fundamentals of Modelling Interfacial Phenomena In Nonlinear Finite Element Analysis*. Springer, 2003.

[35] P. Alart and A. Curnier, "A mixed formulation for frictional contact problems prone to Newton like solution methods," *Computer Methods in Applied Mechanics and Engineering*, vol. 92, pp. 353–375, nov 1991.

[36] G. Pietrzak and A. Curnier, "Large deformation frictional contact mechanics: continuum formulation and augmented Lagrangian treatment," *Computer Methods in Applied Mechanics and Engineering*, vol. 177, pp. 351–381, jul 1999.

[37] E. Nadal, J. J. Ródenas, J. Albelda, M. Tur, J. E. Tarancón, and F. J. Fuenmayor, "Efficient Finite Element Methodology based on Cartesian grids: Application to structural shape optimization," *Abstract and Applied Analysis*, vol. 2013, pp. 1–19, 2013.

[38] L. Piegl and W. Tiller, *The NURBS Book*. Springer-Verlag, 1995.

[39] D. F. Rogers, *An Introduction to NURBS: with Historical Perspective*. Elsevier, 2001.

[40] M. E. Hammer, "Frictional mortar contact for finite deformation problems with synthetic contact kinematics," *Computational Mechanics*, vol. 51, pp. 975–998, jun 2013.

[41] E. Béchet, N. Moës, and B. Wohlmuth, "A stable Lagrange multiplier space for stiff interface conditions within the extended finite element method," *International Journal for Numerical Methods in Engineering*, vol. 78, pp. 931–954, 2009.

[42] C. Annavarapu, M. Hautefeuille, and J. E. Dolbow, "Stable imposition of stiff constraints in explicit dynamics for embedded finite element methods," *International Journal for Numerical Methods in Engineering*, vol. 92, no. June, pp. 206–228, 2012.

[43] M. Hautefeuille, C. Annavarapu, and J. E. Dolbow, "Robust imposition of Dirichlet boundary conditions on embedded surfaces," *International Journal for Numerical Methods in Engineering*, vol. 90, no. November 2011, pp. 40–64, 2012.

[44] J. Haslinger and Y. Renard, "A New Fictitious Domain Approach Inspired by the Extended Finite Element Method," *SIAM Journal on Numerical Analysis*, vol. 47, pp. 1474–1499, jan 2009.

[45] J. Baiges, R. Codina, F. Henke, S. Shahmiri, and W. A. Wall, "A symmetric method for weakly imposing Dirichlet boundary conditions in embedded finite element meshes," *International Journal for Numerical Methods in Engineering*, vol. 90, pp. 636–658, may 2012.

[46] P. Wriggers, *Nonlinear Finite Element Methods*. Berlin, Heidelberg: Springer Berlin Heidelberg, 2008.

[47] "ANSYS® Academic Research Mechanical, Release 16.2,"

PAPER C

On the effect of the contact surface definition in the Cartesian grid finite element method

J.M. Navarro-Jiménez, M. Tur, F.J. Fuenmayor, and J.J. Ródenas

Advanced Modeling and Simulation in Engineering Sciences 5:12, 2018
DOI: 10.1186/s40323-018-0108-5

Abstract

The definition of the surface plays an important role in the solution of contact problems, as the evaluation of the contact force is based on the measure of the gap between the solids. In this work three different methods to define the surface are proposed for the solution of contact problems within the framework of the 3D Cartesian grid finite element method. A stabilized formulation is used to solve the contact problem and details of the kinematic description for each surface definition are provided. The three methods are compared solving some numerical tests involving frictionless contact with finite and small deformations.

Key words

Contact; Immersed boundary; cgFEM; NURBS

Contents

1. Introduction

In recent years some alternatives to standard Finite Element methods have been developed under the category of immersed boundary methods [1–3], also known as fictitious or embedded domain methods. The common idea in these methods is that the FE mesh is obtained by discretizing a simple domain (usually cuboid) which fully embeds the analysis domain, but is independent of the analysis boundaries, which may be complex. Within this category is the Cartesian grid finite element method (cgFEM) for solving elasticity problems in 2D [4] and 3D [5]. The main differentiating features of cgFEM with respect to other immersed boundary methods are that the cgFEM is able to consider the CAD geometry (represented by NURBS) for the numerical integration and the use of a stabilized Lagrange multiplier method for the imposition of Dirichlet boundary conditions (see [5] and [6] for further details).

In order to solve the contact problem with cgFEM we use a stabilized Lagrangian formulation first presented in [7]. The method has similarities with Nitsche-based formulations proposed in [8–11] with a relevant difference in the stabilizing stress field. In our case we use a smooth field calculated with the Zienkiewicz and Zhu Superconvergent Patch Recovery (SPR) technique [12–14]. In a first approach, the developed contact formulation was applied to cgFEM considering a linear facet discretization of the boundary, based on the intersections between the Cartesian grid with the CAD geometry.

Several attempts to enhance the definition of the contact boundaries have been developed in the framework of body-fitted meshes, usually known as surface smoothing, using diverse techniques such as Hermite, Bezier spline and NURBS interpolations [15–18], Gregory patches [19] or Nagata patches [20]. It is proven in these works that the enhancement of the contact surfaces results in more accurate solutions and increased robustness of the contact algorithm. A relevant contribution in the consideration of CAD geometries is the Isogeometric Analysis [21] (and its applications in contact simulation, e.g. [22, 23]), in which the basis functions for the approximation of the solution are the same used for the CAD definition. There are also NURBS-enriched formulations as in [24, 25], where isogeometric basis functions are included only in the contact elements.

As the cgFEM is able to consider the CAD geometry, it seems appropriate to use this surface definition to improve the gap measure. In [26] the deformed surface is defined as a combination of the undeformed CAD geometry and the finite element displacement field. This paper can be considered as an extension of [26], where we study the effect of the surface definition (hence the contact gap) when solving frictionless contact problems with cgFEM. In addition to the previous approaches, linear facets and a combination of FE solution and NURBS surface, in this work we propose a new method in which the deformed configuration is defined as a NURBS surface, i.e., the control points of the original CAD surface are updated such that the new configuration fits the finite element displacement field of the contact surface.

The paper is structured as follows: in section 2 the kinematic variables of the problem are stated. The different alternatives to define the contact surface are presented in section 3. The formulation used to solve the contact problem is described in section 4. Finally the different methods are compared with some numerical tests in section 5.

2. Contact kinematics

Figure 1 shows the undeformed and deformed configurations of two solids $\Omega^{(i)}$ coming in contact. The indexes $^{(1)}$, $^{(2)}$ represent the so-called *slave* and *master* bodies respectively. $\Gamma_c^{(i)}$ is the part of body (i) that can interact with the other body. Let $\mathbf{X}$ be the initial configuration of a given material point in $\Omega^{(i)}, i = 1, 2$. We describe the motion of $\Omega^{(i)}$ with the mapping $\boldsymbol{\varphi} : \Omega \longrightarrow \mathbb{R}^3$. Therefore $\mathbf{x}^{(i)} = \boldsymbol{\varphi}\left(\mathbf{X}^{(i)}, t\right)$ for a given point at time t. Since we are solving quasi-static problems, we will omit the time variable and assume that the load increments are small enough. Then, the position vector for any point in $\Omega^{(i)}$ is given as

$$\mathbf{x}^{(i)} = \boldsymbol{\varphi}\left(\mathbf{X}^{(i)}\right) \tag{1}$$

To enforce the contact constrain, a pair of points $\mathbf{x}^{(1)}$, $\mathbf{x}^{(2)}$ is defined such that the following equation is fulfilled:

$$\mathbf{x}^{(2)}\left(\boldsymbol{\Theta}^{(2)}\right) = g_N \mathbf{n}^{(1)} + \mathbf{x}^{(1)}\left(\boldsymbol{\Theta}^{(1)}\right); \qquad \mathbf{x}^{(1)} \in \Gamma_c^{(1)}, \quad \mathbf{x}^{(2)} \in \Gamma_c^{(2)} \tag{2}$$

where $\boldsymbol{\Theta}^{(i)} \equiv (\xi, \eta)^{(i)}$ are the convective coordinates of $\Gamma_c^{(i)}$ and g_N is the contact normal gap. The normal vector to the surface is obtained from the tangent vectors to the surface $\mathbf{x}_{,\xi}$ and $\mathbf{x}_{,\eta}$:

$$\mathbf{n}^{(i)} = \frac{\mathbf{x}_{,\xi}^{(i)} \times \mathbf{x}_{,\eta}^{(i)}}{\left\| \mathbf{x}_{,\xi}^{(i)} \times \mathbf{x}_{,\eta}^{(i)} \right\|}; \qquad \mathbf{x}_{,\xi}^{(i)} = \frac{\partial \mathbf{x}^{(i)}}{\partial \xi}, \qquad \mathbf{x}_{,\eta}^{(i)} = \frac{\partial \mathbf{x}^{(i)}}{\partial \eta} \tag{3}$$

We use a ray-tracing scheme to build the contact pair, so, $\mathbf{x}^{(1)}$ remains fixed and equation (2) has the unknowns $\boldsymbol{\Theta}^{(2)}$ and g_N. The method for solving this equation depends on the parametric transformation $\mathbf{x}^{(2)}(\boldsymbol{\Theta}^{(2)})$. Equation (2) can be directly solved for linear facets. However, if the surface is defined using rational transformations (e.g. NURBS) (2) becomes non-linear, so we use a Newton-Raphson scheme.

From now onwards we assume that $(\xi, \eta)^{(2)} \equiv (\xi, \eta)$. We can now take variations in (2):

$$\delta \mathbf{x}^{(2)}(\xi, \eta) = \delta g_N \mathbf{n}^{(1)} + g_N \delta \mathbf{n}^{(1)} + \delta \mathbf{x}^{(1)} \tag{4}$$

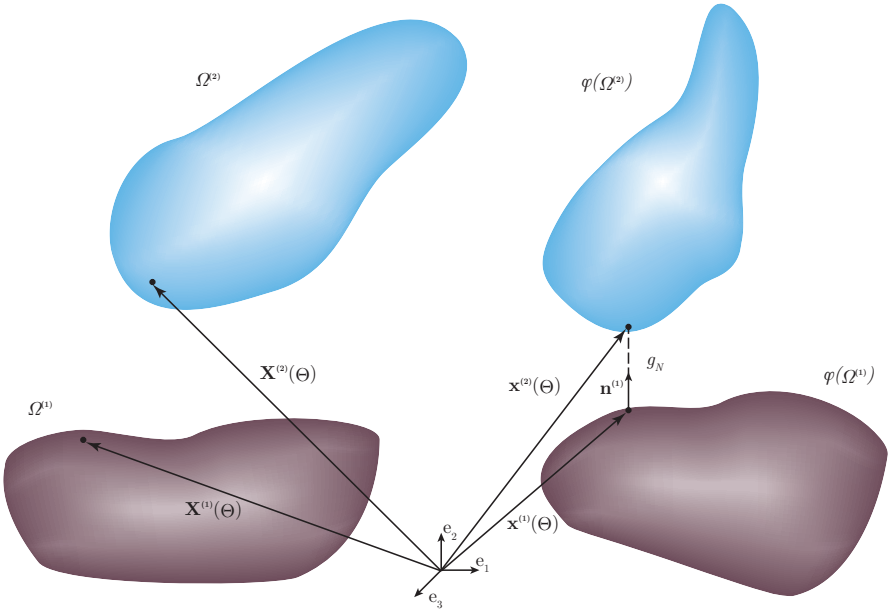

Figure 1: Sketch of two deformable solids getting in contact.

Taking into account that $\delta\mathbf{n}^{(1)} \cdot \mathbf{n}^{(1)} = 0, \mathbf{n}^{(1)} \cdot \mathbf{n}^{(1)} = 1$ and projecting equation (4) into $\mathbf{n}^{(1)}$ we obtain the variation of the normal gap:

$$\delta g_N = \left(\delta\mathbf{x}^{(2)}(\xi,\eta) - \delta\mathbf{x}^{(1)}\right) \cdot \mathbf{n}^{(1)} \tag{5}$$

3. Discretization of contact kinematics

The finite element (FE) approximation of these continuum variables introduces two important sources of error. One is related to the discretization of the analysis domain Ω_h which usually differs from the original Ω. The approximation of the continuum displacement with the FE variable $\mathbf{u}^h$ introduces the discretization error. We define this field from the nodal value $\mathbf{u}$ using linear shape functions, $\mathbf{u}^h = N_k\mathbf{u}_k$, where $\mathbf{u}_k$ is the displacement of node k.

In this work we want to assess the performance of three different alternatives for the definition of $\boldsymbol{\varphi}$. In the first alternative we will consider a linear approximation of Ω. The second alternative, first introduced in [7], includes the CAD definition of $\Gamma_c^{(i)}$ in the reference configuration, combined with the FE approximation of the

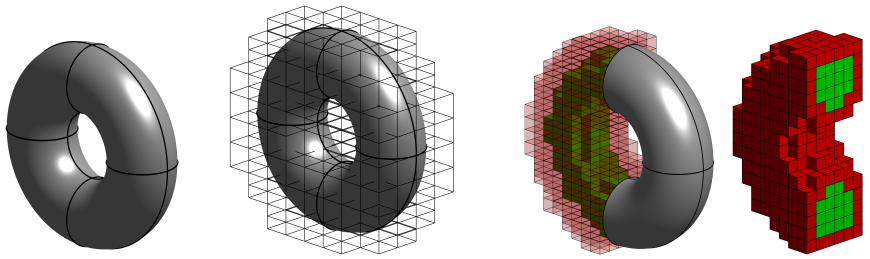

(a) Phys. domain Ω (b) Discretization Ω_h (c) Internal and boundary elements

Figure 2: Disctretization mesh of a torus in cgFEM. In green, elements internal to the domain. In red, elements cut by the boundary (*boundary elements*). Elements completely outside the domain are not considered during the analysis.

displacements. Finally we present an alternative in which the CAD surface is deformed such that it fits the FE solution.

3.1. Previous considerations regarding cgFEM

3.1.1. Surface topology with the *Marching cubes* algorithm

In body-fitted contact FEM formulations the discretized domain Ω_h is created so that there are nodes located at $\Gamma^{(i)}$ and the surface segments are directly faces of the elements in Ω_h. In cgFEM [4, 5] Ω_h is a regular cuboid in which the analysis domain Ω is completely embedded. This embedding domain can be easily meshed with a sequence of regular Cartesian grids (Fig. 2b). Thus, there are no nodes located on $\Gamma^{(i)}$ and there exist elements cut by the boundary, depicted in red in Figure 2c. The consideration of the boundary within these elements is implicitly achieved by only integrating the material part of the intersected element. A 2D sketch of the numerical integration construction procedure for an element cut by the boundary is shown in Figure 3. Given the inside-outside status of the nodes (Fig. 3a), the Marching Cubes algorithm [27] classifies the intersected pattern into 16 unique configurations. Then a tetrahedron (triangles in 2D) topology is created for each configuration. Only the subdomains in the material side are kept (Fig. 3b) for numerical integration. Instead of creating linear surface and volume segments using this topology, cgFEM is able to take into account the NURBS definition of Γ_c, as explained in [5], using a technique based on the work of Sevilla et al. [28]. With this procedure the points used for surface numerical integration are located over the actual CAD definition of the boundary (Fig. 3c), and the volume subdomains account for the actual intersected volume in the element. Other specific methods to obtain the volume and surface subdomains and quadratures for particular cases, such as multiple surfaces within a boundary element, can be found in [5].

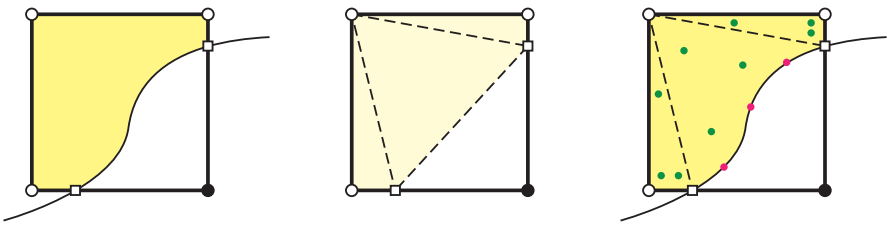

(a) (b) (c)

Figure 3: Surface and volume discretization using the Marching Cubes algorithm and cgFEM. a) Inside-outside test of nodes using intersections data. b) Marching Cubes topology. c) Volume (green) and surface (red) quadratures considering CAD geometry.

3.1.2. Convective to local coordinates transformation

It is worth to remark that for the case of a point lying on $\Gamma^{(i)}$ the reference configuration mapping is described using the surface convective coordinates, whereas the FE solution $\mathbf{u}^h$ is defined with the shape functions of the elements, which are independent of the geometry. Figure 4 shows the coordinate transformations involved in the evaluation of the displacement field for a surface point with convective coordinates $\boldsymbol{\Theta}$, where $\mathbf{B}(\boldsymbol{\Theta})$ represents the surface parametric transformation to the global space, $\mathbf{X} = \mathbf{B}(\boldsymbol{\Theta})$. The reference and deformed configurations are shown in the Figure with coordinates $\mathbf{X}$ and $\mathbf{x}$, and the reference element used to define the shape functions $\mathbf{N}(\boldsymbol{\zeta}^e)$ is depicted on the left. As all the elements in cgFEM are regular hexahedrons the backward mapping from the global space to the local element space $\boldsymbol{\zeta}^e$ is straightforward. For a given point with coordinates $\mathbf{X} = \mathbf{B}(\boldsymbol{\Theta})$ we have:

$$\boldsymbol{\zeta}^e = \frac{\mathbf{B}(\boldsymbol{\Theta}) - \mathbf{X}_e}{h/2} \tag{6}$$

where $\mathbf{X}_e$ is the center and h the size of the element. The partial derivatives of this mapping with respect to the convective coordinates are involved in the kinematic variables definition and can be formulated as:

$$\frac{\partial \boldsymbol{\zeta}^e}{\partial \xi} = \frac{2}{h}\mathbf{B}_{,\xi}; \qquad \frac{\partial \boldsymbol{\zeta}^e}{\partial \eta} = \frac{2}{h}\mathbf{B}_{,\eta} \tag{7}$$

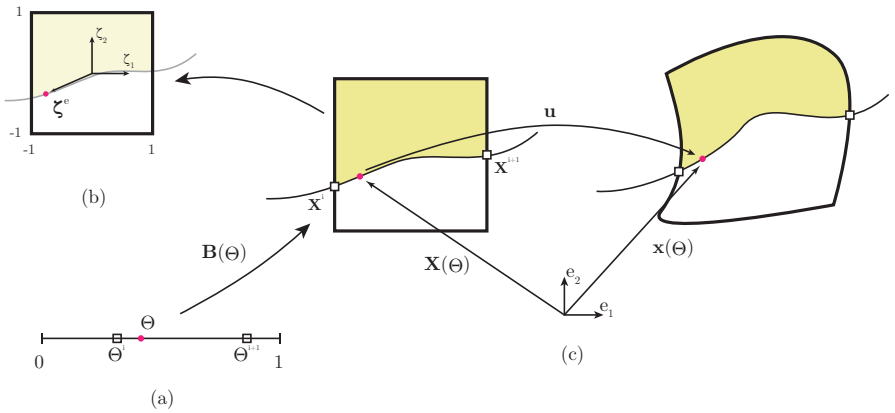

Figure 4: Convective to local coordinates transformation. A point located at $\boldsymbol{\Theta}$ in the surface parametric space (a) is mapped to the reference configuration $\mathbf{X}(\boldsymbol{\Theta})$ on the global coordinates system (c) and then to the local element space (b) with coordinates $\boldsymbol{\zeta}^e$.

3.2. Variation of kinematic variables

In this work we use the exact variation of $\mathbf{x}^{(1)}$ and $\mathbf{x}^{(2)}$, which ensures the symmetry of the formulation and the conservation of the angular momentum. Therefore the variation of the position vector for each body is formulated as:

$$\begin{aligned}\delta\mathbf{x}^{(1)} &= \mathbf{x}^{(1)}_{,u}\ \delta\mathbf{u}\\ \delta\mathbf{x}^{(2)} &= \left(\mathbf{x}^{(2)}_{,\xi}\delta\xi + \mathbf{x}^{(2)}_{,\eta}\delta\eta + \mathbf{x}^{(2)}_{,u}\right)\ \delta\mathbf{u}\end{aligned} \tag{8}$$

The variations $\delta\xi$ and $\delta\eta$ in equation (8) are obtained by projecting equation (4) into $\mathbf{x}^{(1)}_{,\xi}$ and $\mathbf{x}^{(1)}_{,\eta}$. Considering that $\mathbf{x}^{(1)}_{,\xi}\cdot\mathbf{n}^{(1)}=0, \mathbf{x}^{(1)}_{,\eta}\cdot\mathbf{n}^{(1)}=0$, the following system is presented:

$$\begin{bmatrix}\mathbf{x}^{(2)}_{,\xi}\cdot\mathbf{x}^{(1)}_{,\xi} & \mathbf{x}^{(2)}_{,\eta}\cdot\mathbf{x}^{(1)}_{,\xi}\\ \mathbf{x}^{(2)}_{,\xi}\cdot\mathbf{x}^{(1)}_{,\eta} & \mathbf{x}^{(2)}_{,\eta}\cdot\mathbf{x}^{(1)}_{,\eta}\end{bmatrix}\begin{Bmatrix}\delta\xi\\ \delta\eta\end{Bmatrix} = \begin{Bmatrix}g_N\delta\mathbf{n}^{(1)}\cdot\mathbf{x}^{(1)}_{,\xi} - (\mathbf{x}^{(2)}_{,u}-\mathbf{x}^{(1)}_{,u})\cdot\mathbf{x}^{(1)}_{,\xi}\\ g_N\delta\mathbf{n}^{(1)}\cdot\mathbf{x}^{(1)}_{,\eta} - (\mathbf{x}^{(2)}_{,u}-\mathbf{x}^{(1)}_{,u})\cdot\mathbf{x}^{(1)}_{,\eta}\end{Bmatrix} \tag{9}$$

where the last term to calculate is the variation of the normal gap. Starting from (3), the variation is evaluated as:

$$\begin{aligned}\delta\mathbf{n}^{(1)} &= \mathbf{n}^{(1)}_{,u}\delta\mathbf{u}\\ \mathbf{n}^{(1)}_{,u} &= \frac{\mathbf{x}^{(1)}_{,u,\xi}\times\mathbf{x}^{(1)}_{,\eta}+\mathbf{x}^{(1)}_{,\xi}\times\mathbf{x}^{(1)}_{,u,\eta}}{\left\|\hat{\mathbf{n}}^{(1)}\right\|} - \frac{\mathbf{n}^{(1)}}{\left\|\hat{\mathbf{n}}^{(1)}\right\|}\left[\mathbf{n}^{(1)}\cdot\left(\mathbf{x}^{(1)}_{,u,\xi}\times\mathbf{x}^{(1)}_{,\eta}+\mathbf{x}^{(1)}_{,\xi}\times\mathbf{x}^{(1)}_{,u,\eta}\right)\right]\end{aligned} \tag{10}$$

3.3. Surface definition using linear facets

Having the surface segments topology provided by the Marching Cubes algorithm we define a linear mapping $\mathbf{B}^l(\boldsymbol{\Theta})$ from the unit triangle to the segment in the initial configuration, $\mathbf{X} = \mathbf{B}^l(\boldsymbol{\Theta})$. Therefore the position vector in the deformed configuration and its derivatives are defined as:

$$\begin{aligned}
&\mathbf{x} = \mathbf{B}^l(\boldsymbol{\Theta}) + \mathbf{N}\left(\boldsymbol{\zeta}^e\right)\mathbf{u}, \qquad \mathbf{x} \in \Gamma_c \\
&\mathbf{x}_{,u} = \mathbf{N}\left(\boldsymbol{\zeta}^e\right) \\
&\mathbf{x}_{,\xi} = \mathbf{B}^l_{,\xi}(\boldsymbol{\Theta}) + \mathbf{N}_{,\boldsymbol{\zeta}^e}\left(\boldsymbol{\zeta}^e\right)\frac{\partial \boldsymbol{\zeta}^e}{\partial \xi}\mathbf{u} \\
&\mathbf{x}_{,u,\xi} = \mathbf{N}_{,\boldsymbol{\zeta}^e}\left(\boldsymbol{\zeta}^e\right)\frac{\partial \boldsymbol{\zeta}^e}{\partial \xi} \\
&\mathbf{x}_{,\xi,\xi} = \mathbf{N}_{,\boldsymbol{\zeta}^e,\boldsymbol{\zeta}^e}\left(\boldsymbol{\zeta}^e\right)\frac{\partial \boldsymbol{\zeta}^e}{\partial \xi}\frac{\partial \boldsymbol{\zeta}^e}{\partial \xi}\mathbf{u} + \mathbf{N}_{,\boldsymbol{\zeta}^e}\left(\boldsymbol{\zeta}^e\right)\frac{\partial^2 \boldsymbol{\zeta}^e}{\partial \xi^2}\mathbf{u}
\end{aligned} \tag{11}$$

where $\mathbf{N}\left(\boldsymbol{\zeta}^e\right)$, $\mathbf{N}_{,\boldsymbol{\zeta}^e}\left(\boldsymbol{\zeta}^e\right)$ and $\mathbf{N}_{,\boldsymbol{\zeta}^e,\boldsymbol{\zeta}^e}\left(\boldsymbol{\zeta}^e\right)$ are the FE shape functions and its respective derivatives, and $\boldsymbol{\zeta}^e$ is evaluated as a function of $\boldsymbol{\Theta}$ from (6). The partial derivatives with respect to η are evaluated similarly to the terms $\mathbf{x}_{,\xi}$, $\mathbf{x}_{,u,\xi}$ and $\mathbf{x}_{,\xi,\xi}$. As the contact segments are linear, the tangent vectors $\mathbf{x}_{,\xi}$, $\mathbf{x}_{,\eta}$ (and consequently the normal vector $\mathbf{n}^{(1)}$) are constant in a segment, and discontinuous between adjacent segments. This fact can produce a loss of convergence in the search of the contact active set, especially for coarse discretizations of the solids.

3.4. Surface definition using NURBS and FE displacements

In the cgFEM framework it is possible to eliminate the geometry discretization error thanks to the independence between the approximation mesh and the analysis domain. The surface and volume subdomains can be created considering the exact geometry of the domain (Figure 5), provided that it is defined by NURBS surfaces, which is nowadays a standard among the CAD industry. NURBS surfaces are rational functions defined in their own parametric space of coordinates (ξ, η) as

$$\mathbf{Q}\left(\xi,\eta\right) = \sum_{i=1}^{n}\sum_{j=1}^{m}\frac{N_i^{(p)}\left(\xi\right)M_j^{(q)}\left(\eta\right)w_{i,j}}{\sum_{i=1}^{n}\sum_{j=1}^{m}N_i^{(p)}\left(\xi\right)M_j^{(q)}\left(\eta\right)w_{i,j}}\mathbf{P}_{i,j} \tag{12}$$

where $N_i^{(p)}$ and $M_j^{(q)}$ are one-dimensional basis functions of order p and q respectively, each one defined along two knot vectors with n and m control points. $\mathbf{P}_{i,j}$ are the coordinates of the $n \times m$ control points of the surface. Equation (12) can be simplified for further developments as:

$$\mathbf{Q}\left(\xi,\eta\right) = \sum_{i=1}^{n}\sum_{j=1}^{m}S_{i,j}\left(\xi,\eta\right)\mathbf{P}_{i,j} \tag{13}$$

where the term $S_{i,j}(\xi,\eta)$ is the NURBS basis function associated to the control point (i,j):

$$S_{i,j}(\xi,\eta) = \frac{N_i^{(p)}(\xi)\, M_j^{(q)}(\eta)\, w_{i,j}}{\sum_{i=1}^{n}\sum_{j=1}^{m} N_i^{(p)}(\xi)\, M_j^{(q)}(\eta)\, w_{i,j}} \tag{14}$$

We can carefully rearrange the indexation of the control points from (i,j) to the unique index k , hence, we can rewrite the NURBS surface as a vector-matrix multiplication:

$$\mathbf{Q}(\xi,\eta) = \sum_{k=1}^{n\times m} S_k(\xi,\eta)\,\mathbf{P}_k = \mathbf{S}(\xi,\eta)\cdot\mathbf{P} \tag{15}$$

where $\mathbf{S}(\xi,\eta)$ is a row vector containing the $n\times m$ NURBS basis functions, and $\mathbf{P}$ is a $(n\times m)\times 3$ matrix with the coordinates of all the control points of the surface. If we use the NURBS to define the reference configuration of $\Gamma_c^{(i)}$ (1) and its derivatives are rewritten as

$$\begin{aligned}
&\mathbf{x} = \mathbf{Q}(\xi,\eta) + \mathbf{N}(\boldsymbol{\zeta}^e)\,\mathbf{u}, \qquad \mathbf{x}\in\Gamma_c\\
&\mathbf{x}_{,u} = \mathbf{N}(\boldsymbol{\zeta}^e)\\
&\mathbf{x}_{,\xi} = \mathbf{Q}_{,\xi}(\xi,\eta) + \mathbf{N}_{,\boldsymbol{\zeta}^e}(\boldsymbol{\zeta}^e)\,\frac{\partial\boldsymbol{\zeta}^e}{\partial\xi}\mathbf{u}\\
&\mathbf{x}_{,u,\xi} = \mathbf{N}_{,\boldsymbol{\zeta}^e}(\boldsymbol{\zeta}^e)\,\frac{\partial\boldsymbol{\zeta}^e}{\partial\xi}\\
&\mathbf{x}_{,\xi,\xi} = \mathbf{Q}_{,\xi,\xi}(\xi,\eta) + \mathbf{N}_{,\boldsymbol{\zeta}^e,\boldsymbol{\zeta}^e}(\boldsymbol{\zeta}^e)\,\frac{\partial\boldsymbol{\zeta}^e}{\partial\xi}\frac{\partial\boldsymbol{\zeta}^e}{\partial\xi}\mathbf{u} + \mathbf{N}_{,\boldsymbol{\zeta}^e}(\boldsymbol{\zeta}^e)\,\frac{\partial^2\boldsymbol{\zeta}^e}{\partial\xi^2}\mathbf{u}
\end{aligned} \tag{16}$$

Differentiating (12) we can obtain the NURBS derivatives:

$$\mathbf{Q}_{,\xi} = \frac{\partial\mathbf{S}(\xi,\eta)}{\partial\xi}\mathbf{P}; \qquad \mathbf{Q}_{,\eta} = \frac{\partial\mathbf{S}(\xi,\eta)}{\partial\eta}\mathbf{P} \tag{17}$$

3.5. Displacement of the NURBS surface matching the FE solution

The last alternative is a step further in the use of NURBS surfaces to define the position of a point laying on Γ_c. Let $\mathbf{u}$ be the FE displacements obtained for the current iteration during the solution process. Then the following least squares problem is proposed to fit the contact surface (equation (15)) to the solution $\mathbf{u}^h$:

$$\min\left[\frac{1}{2}\int_{\Gamma_c^{(i)}} \left(\mathbf{S}(\xi,\eta)\,\mathbf{V} - \mathbf{N}(\boldsymbol{\zeta}^e)\mathbf{u}\right)^2 d\xi d\eta\right] \tag{18}$$

where $\mathbf{V}$ are the displacements of control points $\mathbf{P}$ such as the NURBS surface matches the displacement field given by the FE solution. Figure 6 illustrates this idea with a simple example. The boundary Γ_c is represented in Figure 6a, with the control points

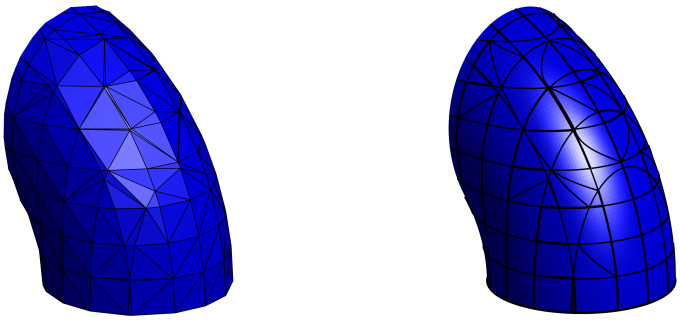

(a) (b)

Figure 5: Surface segments of a regular torus in cgFEM using the same approximation mesh. a) linear facets, b) NURBS surface segments.

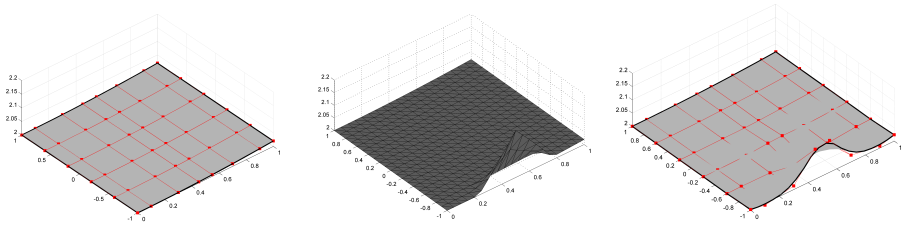

(a) NURBS definition of Γ_c (b) FE solution $\mathbf{u}^h$ (c) NURBS fitting to $\mathbf{u}^h$

Figure 6: Example of NURBS fitting to the FE solution.

net depicted in red. Assuming the solution $\mathbf{u}^h$ evaluated over this surface is as in Figure 6b the NURBS is fitted to that solution (Figure 6c). It is straightforward that the quality of this fitting will strongly depend on the "flexibility" of the surface, this is, the degree and number of knots of the NURBS. To overcome this issue there exist degree elevation and knot insertion algorithms which increase the degrees of freedom without changing the original surface.

The least squares problem in (18) can be solved using numerical integration over Γ_c:

$$\mathbf{V} = \mathbf{M}^{-1}\mathbf{G}\mathbf{u} \tag{19}$$

where

$$\mathbf{M} = \sum_i \mathbf{S}\left(\xi,\eta\right)_i^T \mathbf{S}\left(\xi,\eta\right)_i \left|\mathbf{J}\right|_i H_i \; ; \qquad \mathbf{G} = \sum_i \mathbf{S}\left(\xi,\eta\right)_i^T \mathbf{N}(\boldsymbol{\zeta}_i^e) \left|\mathbf{J}\right|_i H_i \tag{20}$$

If the contact surface is modified such that the FE solution is implicitly included, the position of a given point of Γ_c can be expressed using only the modified NURBS definition:

$$\mathbf{x} = \mathbf{S}\left(\xi,\eta\right)\left(\mathbf{P}+\mathbf{V}\right) = \mathbf{S}\left(\xi,\eta\right)\left(\mathbf{P}+\mathbf{C}\mathbf{u}\right), \qquad \mathbf{x}\in\Gamma_c \tag{21}$$

with $\mathbf{C} = \mathbf{M}^{-1}\mathbf{G}$. Note that $\mathbf{C}$ is a constant matrix which is defined for each different NURBS surface in $\Gamma_c^{(i)}$. These matrices can be calculated once previously and then used during the solving algorithm saving computational cost. For this case the derivatives of the position vector are expressed as:

$$\begin{aligned}
\mathbf{x}_{,u} &= \mathbf{S}\left(\xi,\eta\right)\mathbf{C}\\
\mathbf{x}_{,\xi} &= \mathbf{S}_{,\xi}\left(\xi,\eta\right)\left(\mathbf{P}+\mathbf{C}\mathbf{u}\right)\\
\mathbf{x}_{,u,\xi} &= \mathbf{S}_{,\xi}\left(\xi,\eta\right)\mathbf{C}\\
\mathbf{x}_{,\xi,\xi} &= \mathbf{S}_{,\xi,\xi}\left(\xi,\eta\right)\left(\mathbf{P}+\mathbf{C}\mathbf{u}\right)
\end{aligned} \tag{22}$$

The evaluations of the position vector and all its derivatives becomes considerably easier thanks to the use of a unique NURBS in comparison with a mixed definition using the NURBS and the FE solution. The intersection procedure is also faster, since only surface evaluations must be computed. However, matrix $\mathbf{C}$ couples all the elements in the mesh that contain the same surface, making this method non-viable in terms of computational cost for refined meshes.

Note that in both proposed alternatives the NURBS surface is implicitly considered through the numerical integration, and in the last one the nodes of the Cartesian grid are coupled with the control points of the contact NURBS through the gap definition. However, no additional degrees of freedom are included over the boundary and, in contrast with NURBS-enriched contact formulations as [24], the standard FE interpolation is kept inside the domain.

4. Stabilized Lagrangian contact formulation

This study is focused on the solution of frictionless 3D contact problems using the cgFEM, so we recall the stabilized Lagrange functional presented in [7]. The solution of the contact problem is the displacement field $\mathbf{u}$ and the Lagrange multipliers field λ_N that optimizes the following stabilized Lagrangian:

$$opt\left\{\Pi(\mathbf{u}) + \frac{1}{2\kappa_1}\int_{\Gamma_c^{(1)}}\left(\left[\lambda_N+\kappa_1 g_N\right]_-^2 - \left|\lambda_N\right|^2\right)\,d\Gamma - \frac{1}{2\kappa_2}\int_{\Gamma_c^{(1)}}\left(\lambda_N-p_N\right)^2\,d\Gamma\right\} \tag{23}$$

with $\Pi(\mathbf{u})$ containing all the terms related to the finite strain elasticity, κ_1, κ_2 are penalty constants, and we use the negative part operator which is defined as:

$$[x]_- = \begin{cases} -x & if \quad x \leq 0 \\ \\ 0 & if \quad x > 0 \end{cases} \tag{24}$$

We introduce the normal stabilizing stress $p_N = \mathbf{n}^{(1)} \cdot \boldsymbol{\sigma}^* \cdot \mathbf{n}^{(1)}$, where $\boldsymbol{\sigma}^*$ is a smooth field evaluated using the Zienkiewicz and Zhu Superconvergent Patch Recovery (SPR) technique [12,13]. This term is considered independent of the solution, and an external loop is introduced to re-evaluate it. We experienced that the number of iterations is usually only between 2-4. Taking variations in equation (23) we can assume that $\boldsymbol{\sigma}^*$ is constant and we obtain the following system:

$$\begin{cases} \delta\Pi(\mathbf{u}, \delta\mathbf{u}) - \displaystyle\int_{\Gamma_c^{(1)}} [\lambda_N + \kappa_1 g_N]_- \, \delta g_N \, d\Gamma = 0, \ \forall \delta\mathbf{u} \\ \\ -\dfrac{1}{\kappa_1} \displaystyle\int_{\Gamma_c^{(1)}} \left([\lambda_N + \kappa_1 g_N]_- + \lambda_N \right) \delta\lambda_N \, d\Gamma - \dfrac{1}{\kappa_2} \displaystyle\int_{\Gamma_c^{(1)}} (\lambda_N - p_N) \, \delta\lambda_N \, d\Gamma = 0, \ \forall \delta\lambda_N \end{cases} \tag{25}$$

The Lagrange multipliers in the second equation in (25) can be condensed element-wise [7] when considering the numerical integration, obtaining the following result:

$$\lambda_{Ng} = \begin{cases} \kappa_2 g_{Ng} + p_{Ng} & if \quad \left(\lambda_{Ng} + \kappa_1 g_{Ng} \right) \leq 0 \\ \\ 0 & if \quad \left(\lambda_{Ng} + \kappa_1 g_{Ng} \right) > 0 \end{cases} \tag{26}$$

This is defined for each quadrature point depicted by sub-index g. The substitution of λ_N in the numerical integration of (25) yields the following equation:

$$\begin{gathered} \delta\Pi(\mathbf{u}, \delta\mathbf{u}) - \textstyle\sum_g \left(p_{Ng} + \frac{\kappa E}{h} g_{Ng} \right) \delta g_{Ng} \, |J|_g \, H_g = 0, \quad if \quad \left(p_{Ng} + \frac{\kappa E}{h} g_{Ng} \right) \leq 0 \\ \\ \delta\Pi(\mathbf{u}, \delta\mathbf{u}) = 0, \quad if \quad \left(p_{Ng} + \frac{\kappa E}{h} g_{Ng} \right) > 0 \end{gathered} \tag{27}$$

where $\frac{\kappa E}{h} = (\kappa_1 + \kappa_2)$ is the penalty term, E is the elastic modulus, h is the mesh size, H_g is the quadrature weight and, $|J|_g$ is the Jacobian of the transformation.

4.1. Linearization of kinematic variables

The formulation used above is solved using the Newton-Raphson method, therefore, the linearizations of the kinematic variables in equation (27), i.e., Δg_N and $\Delta\delta g_N$

are needed. The same process performed in (5) can be used to obtain Δg_N. For the linearization $\Delta\delta g_N$ we start from (4) and obtain the following expression:

$$\Delta\delta\mathbf{x}^{(2)}(\xi,\eta) = \Delta\delta g_N \mathbf{n}^{(1)} + \delta g_N \Delta\mathbf{n}^{(1)} + \Delta g_N \delta\mathbf{n}^{(1)} + g_N \Delta\delta\mathbf{n}^{(1)} + \Delta\delta\mathbf{x}^{(1)} \tag{28}$$

which, after multiplying by $\mathbf{n}^{(1)}$, results in:

$$\Delta\delta g_N = \left(\Delta\delta\mathbf{x}^{(2)}(\xi,\eta) - \Delta\delta\mathbf{x}^{(1)}\right)\cdot\mathbf{n}^{(1)} - g_N \Delta\delta\mathbf{n}^{(1)}\cdot\mathbf{n}^{(1)} \tag{29}$$

We can now obtain the linearizations $\Delta\delta\mathbf{x}^{(1)}$, $\Delta\delta\mathbf{x}^{(2)}$ from equation (8):

$$\begin{aligned}\Delta\delta\mathbf{x}^{(2)} &= \delta u\left[\mathbf{x}^{(2)}_{,\xi,\xi}\Delta\xi\delta\xi + \mathbf{x}^{(2)}_{,\eta,\eta}\Delta\eta\delta\eta + \mathbf{x}^{(2)}_{,\xi,\eta}\left(\Delta\xi\delta\eta + \delta\xi\Delta\eta\right) + \mathbf{x}^{(2)}_{,u,\xi}\delta\xi + \right.\\ &\quad \left. + \mathbf{x}^{(2)}_{,u,\xi}\Delta\xi + \mathbf{x}^{(2)}_{,u,\eta}\delta\eta + \mathbf{x}^{(2)}_{,u,\eta}\Delta\eta + \mathbf{x}^{(2)}_{,\xi}\Delta\delta\xi + \mathbf{x}^{(2)}_{,\eta}\Delta\delta\eta\right]\Delta u\\ \Delta\delta\mathbf{x}^{(1)} &= 0\end{aligned} \tag{30}$$

Finally, multiplying (28) by $\mathbf{x}^{(1)}_{,\xi}$ and $\mathbf{x}^{(1)}_{,\eta}$ a system of equations similar to (9) is obtained to compute the variables $\Delta\delta\xi$ and $\Delta\delta\eta$.

5. Numerical examples

5.1. Contact between plane surfaces

In this example, similar to [29,30], a simple analysis of contact between plane surfaces is solved to test the convergence of the FE solution using the different surface definitions described in this paper. The 2D sketch of the solids in contact is depicted in Figure 7, where x is the out-of-plane direction. Both solids have common elastic material properties, $E = 115GPa$ and $\nu = 0.3$. At the initial configuration, the contact surfaces are overlapping and vertical displacement $d = -1.6\cdot 10^{-6}m$ is applied on the upper face of the upper body. Displacements along y direction are constrained on the upper face of body 2 and on the lower face of body 1. We use a 2D plane strain overkill solution from [30] as a reference for the discretization error evaluation, so symmetry conditions are applied to the faces parallel to the yz plane. The lateral faces of body 1 are loaded with $p_y = 4\cdot 10^{11}(0.01 - z)z\ Pa$ and $p_z = 10\cdot 10^{11}(0.01 - z)z\ Pa$.

Non-conforming Cartesian grids are used on both bodies. Figure 8 shows some of the uniformly refined meshes used for the analysis. Starting with the first discretization in Figure 8 each element is subdivided into 8 new elements to build the following mesh. The convergence of the relative error in energy norm is shown in Figure 9 for a sequence of 4 meshes using linear elements, $\mathscr{H}_8$. The results show that, for all the surface definitions, optimal convergence rate of the error in energy norm (represented

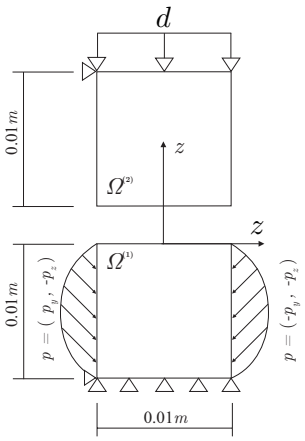

Figure 7: Example 1. Contact between plane surfaces. Sketch of problem.

by the triangle) is achieved. Only two meshes were solved with the fitting NURBS definition due to the high amounts of nodes coupled in the following meshes.

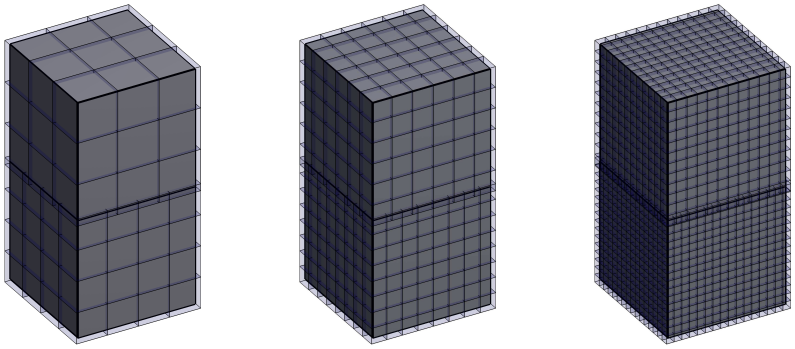

Figure 8: Example 1. Refinement process for the study of the convergence of the solution. Meshes 1 to 3 are shown from left to right.

The original surface definitions consist in linear NURBS for both solids. The degree of the contact surfaces was modified in order to increase the flexibility of the surfaces when performing the NURBS fitting. Figure 10 shows the vertical displacements u_y^h along a line located on the top surface of the lower solid for the cases of linear facets and fitting NURBS definitions, which are very similar. The line in red represents the NURBS surface resulting from the fitting problem (equation (18)).

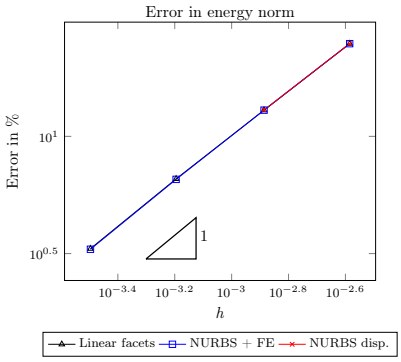

Figure 9: Example 1: Evolution of the error in energy norm with the element size of the lower body. Convergence of the FE solution.

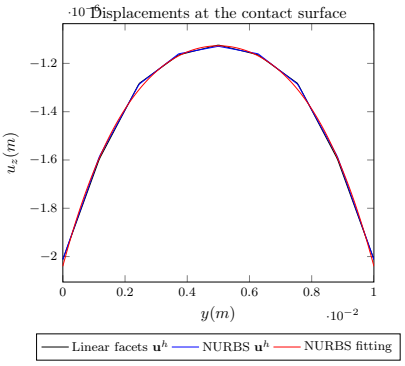

Figure 10: Example 1: FE displacements $\mathbf{u}^h$ over the top surface of the lower solid considering linear facets and NURBS fitting definitions. The curve in red depicts the solution of the NURBS fitting problem.

When the contact occurs between planar surfaces there is practically no difference in the definition of the surfaces using the three presented methods, and the gap measurement is trivial. Therefore, as expected, all methods have results with a similar precision.

5.2. Contact between curved surfaces, finite deformations

The second example considers the contact interaction between elastic solids with a toroidal shape with major radius $R = 2cm$ and minor radius $r = 0.5cm$. Figure 11 shows the initial position of the bodies in contact. A positive displacement is imposed along the y direction over the purple surfaces in 5 incremental steps of $0.1cm$. All the DOFs are constrained over the blue surfaces. A Neo-Hookean material is used with $E = 116GPa$ and $\nu = 0.3$. Three different discretizations have been considered in this case, using the same uniform refinement process described in the previous example. Figure 12 shows the analysis meshes for one of the solids. No results were obtained when using linear facets with the first of the meshes due to loss of convergence caused by the surface discretization being extremely coarse. However, the same coarse mesh had no convergence problems using the other two surface definitions, thanks to the consideration of the exact geometry. The last mesh was not solved using the NURBS displacement method due to the high amount of nodes coupled by each surface, which results in non-viable computational cost.

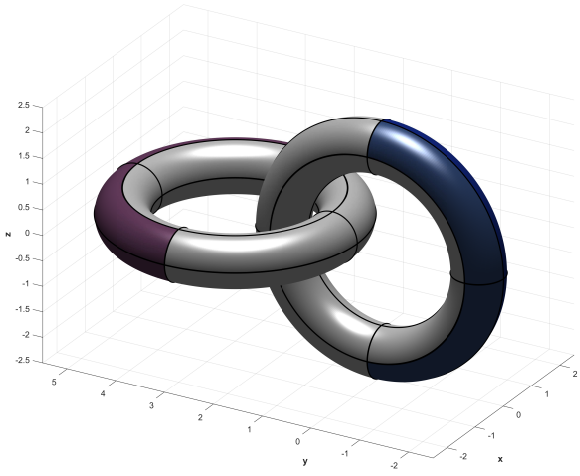

Figure 11: Example 2. Contact simulation between curved surfaces. A positive displacement along the y direction is imposed over the purple surfaces. All the DOFs are constrained over the blue surfaces.

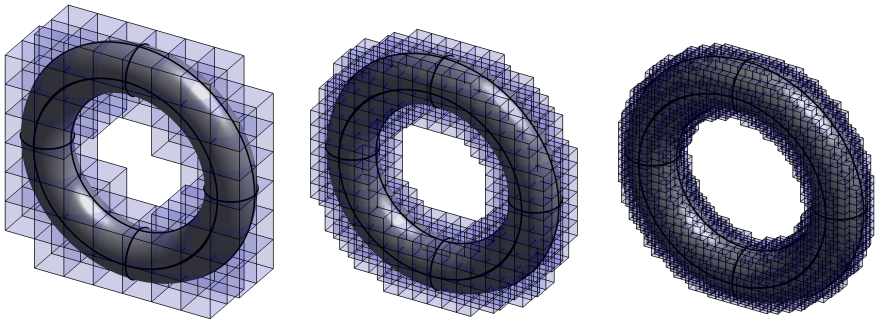

(a) 216 nodes (b) 1052 nodes (c) 5268 nodes

Figure 12: Example 2. Refinement process for the analysis of contact between curved surfaces. Meshes 1 to 3 are shown from left to right. Both solids are meshed with a similar discretization.

Figure 13 shows the evolution of the reaction forces over the constrained surfaces during the load for each analysis. Note that although all analyses have similar results, the reaction forces when solving mesh 2 with linear facets is clearly lower than the rest of the analyses, including the results obtained with NURBS+FE and NURBS fitting

for the coarse mesh. This is mainly due to the lower precision in the gap measurement with linear facets.

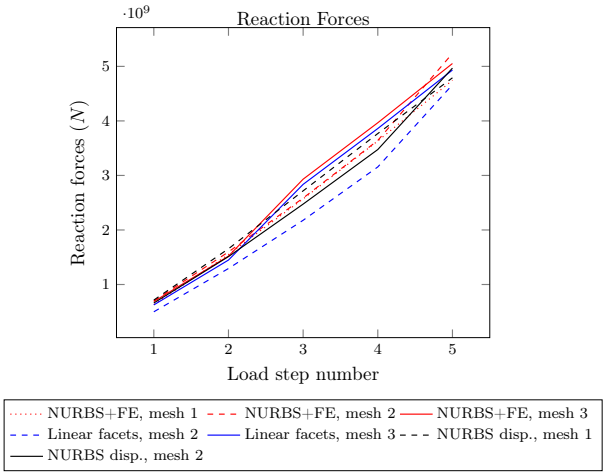

Figure 13: Example 2. Reaction forces on the Dirichlet constrained surfaces during the load.

The values of $\boldsymbol{\sigma}_y$ at the final load step for all the performed analyses is shown in Figure 15. The results are similar for the different methods, with the maximum stress value increasing with the refinement of the mesh.

The same problem was solved using a Neo-Hookean material with $E = 7MPa$, $\nu = 0.45$, and 15 displacement increments of $0.1cm$ along the y direction. Two methods are compared in this test, first the linear facets definition with mesh number 2 (Figure 12b) and the NURBS + FE method with the coarse mesh (Figure 12a). The deformed configuration of the solids for the last load step is shown in Figure 14. It can be seen that despite the use of a coarser discretization, the results with the NURBS + FE method are similar to those obtained with linear facets and a finer mesh.

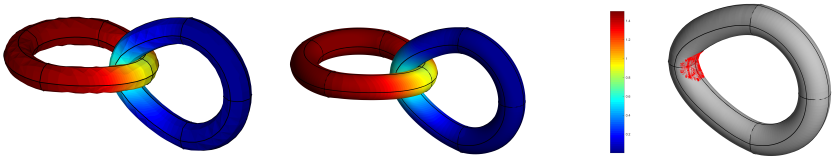

(a) 1052 nodes (b) 216 nodes (c) Contact area

Figure 14: Example 2. Finite deformations with Neo-Hookean material. Deformed shape using a) Linear facets, b) NURBS + FE solution. The color map represents values of $\|\mathbf{u}^h\|$.

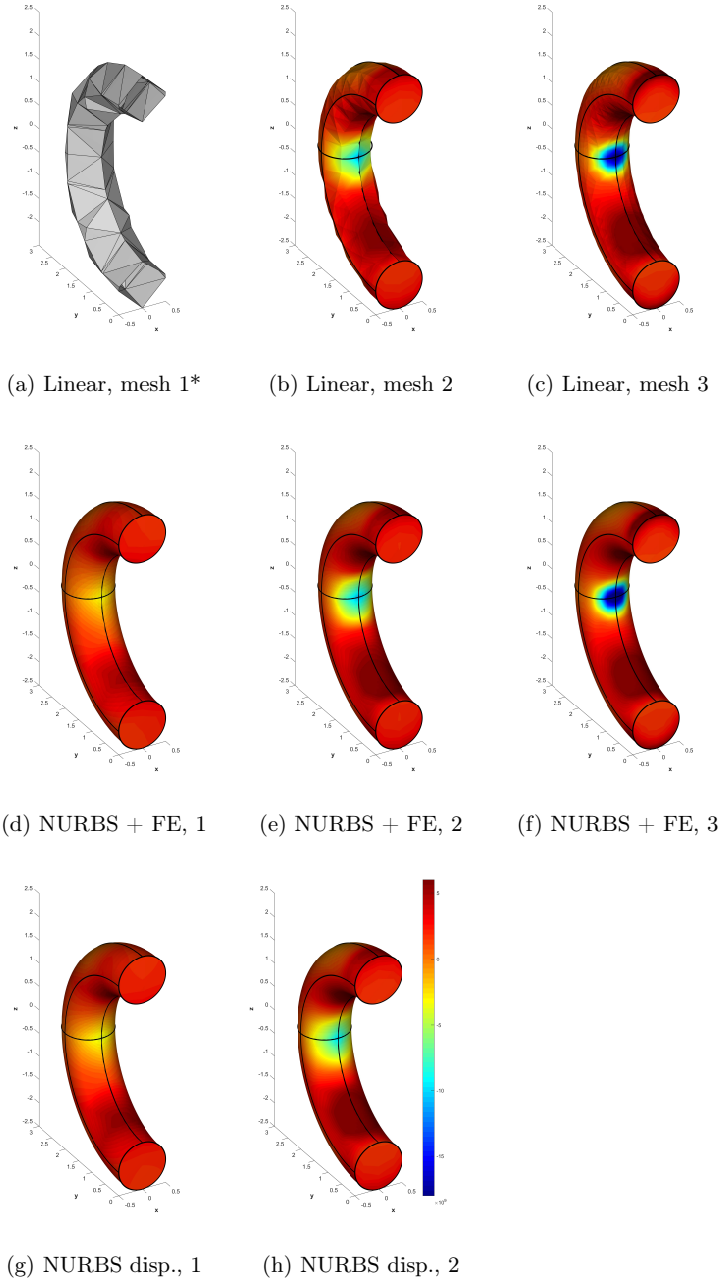

(a) Linear, mesh 1* (b) Linear, mesh 2 (c) Linear, mesh 3

(d) NURBS + FE, 1 (e) NURBS + FE, 2 (f) NURBS + FE, 3

(g) NURBS disp., 1 (h) NURBS disp., 2

Figure 15: Example 2.Values of $\boldsymbol{\sigma}_y$ (Pa) at final load step for all the analyses. *The image in a) shows the coarse surface discretization which led to loss of convergence.

5.3. Contact between curved surfaces, small deformations

The last example consists in a small deformations contact simulation between three torus. The geometric parameters are the same as in the previous example. For this problem a linear elastic material has been considered, with $E = 115GPa$ and $\nu = 0.3$, and only one increment of $0.05cm$ has been applied in the y direction over the purple surfaces, shown in Figure 16. The problem was solved using linear facets and NURBS + FE definition, with the meshes in Figure 12b and 12a respectively.

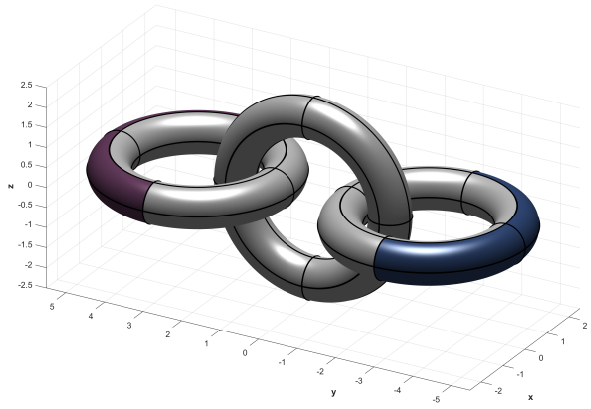

Figure 16: Example 3. Small deformations contact between curved surfaces. A positive displacement along the y direction is imposed over the purple surfaces. All the DOFs are constrained over the blue surfaces.

Figure 17 shows the resulting Von Mises stress at the central solid for both cases. A substantial difference between the maximum stress values can be appreciated in this cases. As the deformations in this problem are small, the stress is mainly due to the contact interaction, and the initial gap measure becomes crucial. With convex contact surfaces the linear facets definition estimates less penetration than the actual geometries have, thus producing lower values of stress, even with a higher number of degrees of freedom than in the case of NURBS contact surfaces.

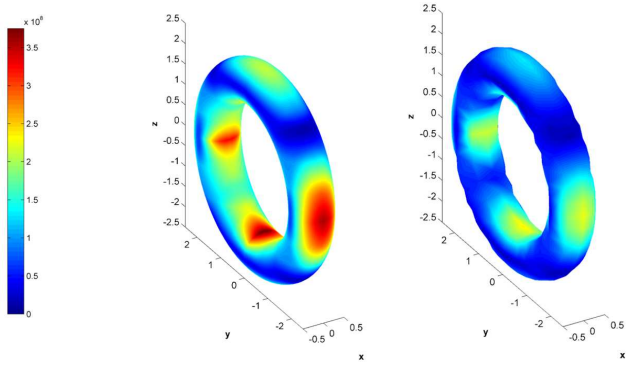

(a) Facets, 216 nodes (b) Facets, 1052 nodes

Figure 17: Example 3. Small deformations contact between three torus. Von Mises stress for the central torus (Pa) with exact geometry consideration and linear facets.

6. Conclusions

Three different alternatives have been presented to define the contact surfaces within the Cartesian grid finite element method: a linear facet representation, a combination of NURBS surface and FE displacements and the fitting of a NURBS surface to the FE displacements. The first option, is the most simple and fastest of all three in terms of procedure and implementation. The surface integration quadratures are based on linear triangles whose rules are well known. The ray-tracing algorithm becomes a linear equation, thus having an analytical solution. Therefore the gap is easily computed. In terms of implementation, the normal vector is constant along a surface subdomain (triangle) reducing the number of terms in the calculation of the kinematic variables. On the other hand, this method has lower precision in the gap measure, which can affect the robustness of the method, specially with coarse discretizations.

The use of NURBS surfaces combined with FE solution provides with better results compared with linear facets, as the actual CAD geometry is considered regardless of the used discretization. In all the tests analysed the precision of the solution computed in terms of energy error or stresses is always greater or equal than that obtained with linear facets. This is specially true for coarse discretizations, due to the enhanced gap measure. Some drawbacks of this method are related to the computational cost of the quadrature rules creation [5] and the solution of the ray-tracing algorithm (non-linear equation). In terms of implementation, more terms are involved in the evaluation of the kinematic variables and its variations. However, the total computational cost is not compromised, as the results obtained with NURBS surfaces and coarse meshes have a similar quality as those obtained with finer meshes and linear facets.

From an analytical point of view, the NURBS fitting definition has interesting features with respect to the mixed NURBS and FE definition. The evaluation of the kinematic variables and the ray-tracing solution are simpler as there is only a NURBS involved. However, the high coupling of degrees of freedom for fine discretizations should be addressed, as the computational cost grows exponentially. For these reasons, the combination of NURBS and FE solution seems to be the most versatile and robust option to define the contact surfaces in the framework of the cgFEM.

Acknowledgements

The authors wish to thank the Spanish Ministerio de Economia y Competitividad the Generalitat Valenciana and the Universitat Politècnica de València for their financial support received through the projects DPI2017-89816-R, Prometeo 2016/007 and the FPI2015 program.

References

[1] A. Düster, J. Parvizian, Z. Yang, and E. Rank, "The finite cell method for three-dimensional problems of solid mechanics," *Computer Methods in Applied Mechanics and Engineering*, vol. 197, pp. 3768–3782, aug 2008.

[2] D. Schillinger and M. Ruess, "The Finite Cell Method: A Review in the Context of Higher-Order Structural Analysis of CAD and Image-Based Geometric Models," *Archives of Computational Methods in Engineering*, vol. 22, pp. 391–455, jul 2015.

[3] E. Burman, S. Claus, P. Hansbo, M. G. Larson, and A. Massing, "CutFEM: Discretizing geometry and partial differential equations," *International Journal for Numerical Methods in Engineering*, vol. 104, pp. 472–501, nov 2015.

[4] E. Nadal, J. J. Ródenas, J. Albelda, M. Tur, J. E. Tarancón, and F. J. Fuenmayor, "Efficient Finite Element Methodology based on Cartesian grids: Application to structural shape optimization," *Abstract and Applied Analysis*, vol. 2013, pp. 1–19, 2013.

[5] O. Marco, R. Sevilla, Y. Zhang, J. J. Ródenas, and M. Tur, "Exact 3D boundary representation in finite element analysis based on Cartesian grids independent of the geometry," *International Journal for Numerical Methods in Engineering*, vol. 103, pp. 445–468, aug 2015.

[6] M. Tur, J. Albelda, O. Marco, and J. J. Ródenas, "Stabilized method of imposing Dirichlet boundary conditions using a recovered stress field," *Computer Methods in Applied Mechanics and Engineering*, vol. 296, pp. 352–375, 2015.

[7] M. Tur, J. Albelda, J. M. Navarro-Jimenez, and J. J. Rodenas, "A modified perturbed Lagrangian formulation for contact problems," *Computational Mechanics*, vol. 55, no. 4, pp. 737–754, 2015.

[8] P. Heintz and P. Hansbo, "Stabilized Lagrange multiplier methods for bilateral elastic contact with friction," *Computer Methods in Applied Mechanics and Engineering*, vol. 195, pp. 4323–4333, jul 2006.

[9] C. Annavarapu, M. Hautefeuille, and J. E. Dolbow, "A Nitsche stabilized finite element method for frictional sliding on embedded interfaces. Part I: Single interface," *Computer Methods in Applied Mechanics and Engineering*, vol. 268, pp. 417–436, 2014.

[10] K. Poulios and Y. Renard, "An unconstrained integral approximation of large sliding frictional contact between deformable solids," *Computers and Structures*, vol. 153, pp. 75–90, 2015.

[11] R. Mlika, Y. Renard, and F. Chouly, "An unbiased Nitsche's formulation of large deformation frictional contact and self-contact," *Computer Methods in Applied Mechanics and Engineering*, vol. 325, pp. 265–288, oct 2017.

[12] O. C. Zienkiewicz and J. Z. Zhu, "The superconvergent patch recovery and a posteriori error estimates. Part 1: The recovery technique," *International Journal for Numerical Methods in Engineering*, 1992.

[13] J. J. Ródenas, M. Tur, F. J. Fuenmayor, and A. Vercher, "Improvement of the superconvergent patch recovery technique by the use of constraint equations: The SPR-C technique," *International Journal for Numerical Methods in Engineering*, vol. 70, no. October 2006, pp. 705–727, 2007.

[14] O. González-Estrada, J. Ródenas, S. Bordas, E. Nadal, P. Kerfriden, and F. Fuenmayor, "Locally equilibrated stress recovery for goal oriented error estimation in the extended finite element method," *Computers & Structures*, vol. 152, pp. 1–10, may 2015.

[15] P. Wriggers, L. Krstulovic-Opara, and J. Korelc, "Smooth c1-interpolations for two-dimensional frictional contact problems," *International Journal for Numerical Methods in Engineering*, vol. 51, no. 12, pp. 1469–1495, 2001.

[16] V. Padmanabhan and T. Laursen, "A framework for development of surface smoothing procedures in large deformation frictional contact analysis," *Finite Elements in Analysis and Design*, vol. 37, pp. 173–198, mar 2001.

[17] M. Tur, E. Giner, F. Fuenmayor, and P. Wriggers, "2d contact smooth formulation based on the mortar method," *Computer Methods in Applied Mechanics and Engineering*, vol. 247–248, pp. 1 – 14, 2012.

[18] M. Stadler, G. A. Holzapfel, and J. Korelc, "Cn continuous modelling of smooth contact surfaces using NURBS and application to 2D problems," *International Journal for Numerical Methods in Engineering*, vol. 57, no. 15, pp. 2177–2203, 2003.

[19] M. A. Puso and T. A. Laursen, "A 3d contact smoothing method using gregory patches," *International Journal for Numerical Methods in Engineering*, vol. 54, no. 8, pp. 1161–1194, 2002.

[20] D. Neto, M. Oliveira, L. Menezes, and J. Alves, "A contact smoothing method for arbitrary surface meshes using nagata patches," *Computer Methods in Applied Mechanics and Engineering*, vol. 299, pp. 283 – 315, 2016.

[21] T. Hughes, J. Cottrell, and Y. Bazilevs, "Isogeometric analysis: CAD, finite elements, NURBS, exact geometry and mesh refinement," *Computer Methods in Applied Mechanics and Engineering*, vol. 194, pp. 4135–4195, oct 2005.

[22] L. De Lorenzis, P. Wriggers, and T. J. Hughes, "Isogeometric contact: a review," *GAMM-Mitteilungen*, vol. 37, pp. 85–123, jul 2014.

[23] M. Dittmann, M. Franke, I. Temizer, and C. Hesch, "Isogeometric Analysis and thermomechanical Mortar contact problems," *Computer Methods in Applied Mechanics and Engineering*, vol. 274, pp. 192–212, 2014.

[24] C. J. Corbett and R. A. Sauer, "NURBS-enriched contact finite elements," *Computer Methods in Applied Mechanics and Engineering*, vol. 275, pp. 55–75, jun 2014.

[25] C. J. Corbett and R. A. Sauer, "Three-dimensional isogeometrically enriched finite elements for frictional contact and mixed-mode debonding," *Computer Methods in Applied Mechanics and Engineering*, 2015.

[26] J. M. Navarro-Jiménez, M. Tur, J. Albelda, and J. J. Ródenas, "Large deformation frictional contact analysis with immersed boundary method," *Computational Mechanics*, vol. 62, pp. 853–870, Oct 2018.

[27] W. E. Lorensen, H. E. Cline, W. E. Lorensen, and H. E. Cline, "Marching cubes: A high resolution 3D surface construction algorithm," in *Proceedings of the 14th annual conference on Computer graphics and interactive techniques - SIGGRAPH '87*, vol. 21, (New York, New York, USA), pp. 163–169, ACM Press, 1987.

[28] R. Sevilla, S. Fernández-Méndez, and A. Huerta, "NURBS-enhanced finite element method (NEFEM)," *International Journal for Numerical Methods in Engineering*, vol. 76, no. February, pp. 56–83, 2008.

[29] S. Hüeber, M. Mair, and B. Wohlmuth, "A priori error estimates and an inexact primal-dual active set strategy for linear and quadratic finite elements applied to multibody contact problems," *Applied Numerical Mathematics*, vol. 54, pp. 555–576, aug 2005.

[30] M. Tur, F. J. Fuenmayor, and P. Wriggers, "A mortar-based frictional contact formulation for large deformations using Lagrange multipliers," *Computer Methods in Applied Mechanics and Engineering*, vol. 198, no. 37-40, pp. 2860–2873, 2009.

PAPER D

On the use of stabilization techniques in the cgFEM framework for iterative solvers

E. Nadal, M. Tur, J.M. Navarro-Jiménez, J. Martínez and J.J. Ródenas

Preprint submitted to International Journal for Numerical Methods in Engineering

Abstract

Fictitious Domain Methods, like the cartesian grid Finite Element Method (cgFEM), are based on the intersection of an octree-mesh with the geometry. This may yield to ill-conditioned system of equations since the stiffness associated to a node could be small, thus poorly contributing to the energy of the problem. This issue makes the use of iterative solvers for large problems difficult. In this work we present a new stabilization technique which preserves the cartesian structure of the mesh. The formulation consists in penalizing the free movement of those nodes by an smooth extension of the solution from the interior of the domain, by means of a post-process of the solution via a displacement recovery technique. The numerical results show an improvement of the condition number and a decrease in the number of iterations of the iterative solver while preserving the problem accuracy and improving the accuracy of the tractions on the Neumann boundaries.

Key words

cgFEM; Iterative solver; Fictitious domain; Condition number

Contents

1. Introduction

During the last decades of the XX^{th} century, a parallel concept to the Finite Element Method (FEM) emerged, the Fictitious Domain Method (FDM). According to [1], a wide amount of variants have been developed since VK Saul'ev published, in Russian, the paper *Solution of certain boundary-value problems on high-speed computers by the fictitious-domain method* (Sibirsk. Mat.Z. 1963.4:912-925). In the FEM framework the geometry of the component to be analysed is conformingly meshed. Therefore, the mesh generation complexity is directly related with the complexity of the geometry. Besides the existence of advanced and automated mesh generators algorithms [2,3], the meshing process is one of the most tedious during the FE analysis. On the contrary, the FDM is based on embedding the problem domain into a fictitius domain, i.e. a square, which is easy to mesh. Then the FDM completely separates the mesh used for solving the Finite Element (FE) problem from the geometry of the component. Therefore the component geometrical complexity is completely unrelated with the mesh generation process, which, in fact, is usually octree-based. Since the FE mesh is not related with the geometry, an special treatment of the geometry is needed in the FDM. This important issue is usually the key ingredient which differentiate the different approaches of the FDM.

Recently the FDM has recovered the interest since problems without a CAD geometry are arising in numerical simulations. This sort of problems embrace, among others, those coming from medical images. In that sense the Finite Cell Method [4,5] and the Cartesian Grid Finite Element Method (cgFEM) [6, 7] have demonstrated their capabilities in these problems [8,9].

Independently of the approach used, most of these methods fails in similar aspects: i.e. imposing the Dirichlet boundary conditions, numerical conditioning, accuracy over the boundary... CutFEM [10] proposes a robust methodology to guarantee the stability when Dirichlet boundaries cut the mesh resulting in very small element sub-regions. cgFEM [11, 12] also uses stabilization methods for imposing Dirichlet boundary conditions guaranteeing the coercivity of the problem. These stabilization procedures are able to guarantee the solvability of the problem at hand for direct solvers. However, when iterative solvers are needed, not only the solvability must be guaranteed but also that the condition number of the system of equations is under control in order improve the performance of the iterative solver. In this sense, Badía *et. al.* [13] implemented a technique that makes aggregates in order to increase the stiffness associated to nodes outside the problem domain.

Since in the FDM framework elements are intersected by the geometry, there are situations in which the nodes are far from the boundary, having a small influence on the energy of the solution. In other words, the value of the solution at these nodes is not relevant in the minimization of the potential energy and therefore elevating the condition number of the system of equations. In this manuscript we propose a technique able to keep under control the solution of these nodes, while keeping the

right convergence rate and accuracy of the solution. This will allow to efficiently use iterative solvers for large problems in the FDM framework. Additionally, the accuracy of the stress field near the boundary will be improved as a direct consequence of the proposed technique.

This paper is structured as follows: after this introduction, the problem model and the formulation of the proposed stabilization terms are introduced in section 2. Section 3 is devoted to recall the recovery procedures used for the stabilization terms and Section 4 contains a convergence analysis of the proposed stabilization terms. Finally the numerical results and final conclusions are in Sections 5 and 6, respectively.

2. Problem Statement

This paper is devoted to solve the 3D linear elasticity problem by means of the cgFEM. The notation used all along the contribution is settled at this point. The Cauchy stress field is denoted as $\boldsymbol{\sigma}$, the displacement field as $\mathbf{u}$, and the strain field as $\boldsymbol{\varepsilon}$, all these fields being defined over the domain $\Omega \subset \mathbb{R}^3$, with boundary denoted by $\partial\Omega$. Prescribed tractions denoted by $\mathbf{t}$ are imposed over the part Γ_N of the boundary, while displacements denoted by $\bar{\mathbf{u}}$ are prescribed over the complementary part Γ_D of the boundary. Body loads are denoted as $\mathbf{b}$.

The linear elasticity problem takes the primal variational form:

$$\begin{aligned} &\text{Find } \mathbf{u} \in (V_\Omega + \{\mathbf{w}\}) : \forall \mathbf{v} \in V_\Omega \\ &a(\mathbf{u},\mathbf{v})_\Omega = l(\mathbf{v})_\Omega \qquad \text{where} \\ &a(\mathbf{u},\mathbf{v})_\Omega = \int_\Omega \boldsymbol{\varepsilon}(\mathbf{u}) : \boldsymbol{\sigma}(\mathbf{v}) \, \mathrm{d}\Omega \\ &l(\mathbf{v})_\Omega = \int_\Omega \mathbf{b}\cdot\mathbf{v} \, \mathrm{d}\Omega + \int_{\Gamma_N} \mathbf{t}\cdot\mathbf{v} \, \mathrm{d}\Gamma, \end{aligned} \tag{1}$$

where $V_\Omega = \{\mathbf{v} \mid \mathbf{v} \in \left[H^1(\Omega)\right]^3, \mathbf{v}|_{\Gamma_D} = \mathbf{0}\}$, $\mathbf{w}$ is a particular displacement field satisfying the Dirichlet boundary conditions and $\boldsymbol{\sigma}(\mathbf{v}) = \mathbf{D} : \boldsymbol{\varepsilon}(\mathbf{v})$, being $\mathbf{D}$ the fourth order tensor relating the stress tensor with the strain tensor, defined as the symmetric gradient of the displacement field. Equation (1) settles the linear elasticity problem for the standard FEM. However, in the cgFEM framework an additional domain, embedding Ω as shown in figure 1, should be introduced: $\Omega^\star$.

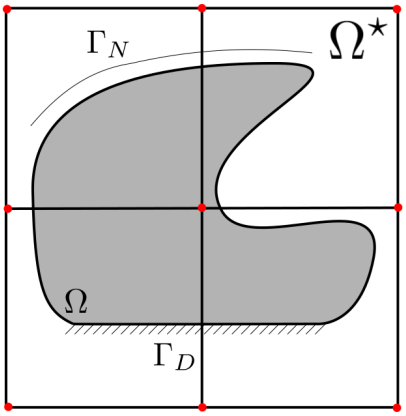

Figure 1: Representation of a problem domain Ω and the embedding domain $\Omega^\star$ in the cgFEM framework.

This modification of the problem domain leads to a formal modification of the problem (1) in the following way:

$$\begin{aligned} &\text{Find } \mathbf{u} \in (V + \{\mathbf{w}\}) : \forall \mathbf{v} \in V \\ &a(\mathbf{u}, \mathbf{v}) = l(\mathbf{v}) \qquad \text{where} \\ &a(\mathbf{u}, \mathbf{v}) = \int_{\Omega^\star} \boldsymbol{\varepsilon}(\mathbf{u}) : \boldsymbol{\sigma}(\mathbf{v}) \, \mathrm{d}\Omega \\ &l(\mathbf{v}) = \int_{\Omega^\star} \mathbf{b} \cdot \mathbf{v} \, \mathrm{d}\Omega + \int_{\Gamma_N} \mathbf{t} \cdot \mathbf{v} \, \mathrm{d}\Gamma, \end{aligned} \tag{2}$$

where $V = \{\mathbf{v} \mid \mathbf{v} \in \left[H^1(\Omega^\star)\right]^3, \mathbf{v}|_{\Gamma_D} = \mathbf{0}\}$. Note that $a(\mathbf{u}, \mathbf{v}) = a(\mathbf{u}, \mathbf{v})_\Omega$ and $l(\mathbf{v}) = l(\mathbf{v})_\Omega$ since $\mathbf{D} \equiv 0$ and $\mathbf{b} \equiv 0$ outside the domain Ω.

2.1. Boundary conditions in cgFEM

When using the cgFEM for numerically solving the problem (2), we find out that the Dirichlet boundary conditions cannot be directly applied as in the standard FEM since, in general, there are not any nodes over the boundary, as can be appreciated in figure 1. As problem (2) is a constrained optimization problem the Lagrange Multipliers technique can be applied. In order to do that, a Lagrange multipliers discretization over the Dirichlet boundaries is needed. The choice of the Lagrange multipliers space is crucial for the well behaviour of the proposed method. This method is well known in the standard FE and the stabilized version [14, 15] was shown to be equivalent to the Nitsche method. In the FDM, other authors [16, 17] propose the Vital Vertex Method which *a prioiri* defines an appropriate discretization

for the Lagrange multiplier space; however this procedure is not trivial for the 3D case. One alternative to the right selection of the Lagrange Multipliers space is the use of stabilized methods such as the ones proposed by Hansbo *et. al.* [18] and Burman and Hansbo [19] which are an adaptation of the Nitsche's method to the FDM framework, using the element traction jumps for stabilization purposes. In the context of the Finite Cell Method, the authors propose the use of a Nitsche's based approach for imposing the essential boundary conditions [9]. More recently Tur *et. al.* [11] propose a stabilization technique which makes use of recovery procedures easing the implementation of the method specially for the 3D case. This last method is adopted in this contribution. To impose the Dirichlet boundary conditions in a weak sense via a mortar method implies the use of Lagrange multipliers. Therefore solving problem (2) is equivalent to solve the following problem:

$$\mathscr{L}_0(\mathbf{v}^h, \boldsymbol{\mu}^h) = \frac{1}{2} a(\mathbf{v}^h, \mathbf{u}^h) + b(\boldsymbol{\mu}^h, \mathbf{v}^h - \bar{\mathbf{u}}) - l(\mathbf{v}^h), \tag{3}$$

where $\mathbf{v}^h \in V^h$ is the discrete counterpart of the space V, $\boldsymbol{\mu}^h \in M^h$ is a suitable discretized space for the Lagrange multipliers and

$$b(\boldsymbol{\mu}^h, \mathbf{v}^h) = \int_{\Gamma_D} \boldsymbol{\mu}^h \cdot \mathbf{v}^h \, \mathrm{d}\Gamma. \tag{4}$$

Note that, in general, the appropriate Lagrange multipliers space is not easy to find since it is problem-dependent and it also depends on the way the mesh and geometry intersect. We follow the approach first presented in [20] which introduces a Lagrange multiplier at each integration point of the surface defining a polynomial approximation (piece-wise discontinuous polynomial approximation). This discretization does not fulfill the Ladyzhenskaya-Babuška-Brezzi (LBB) condition in general, therefore an additional stabilization term is added:

$$\mathscr{L}_S(\mathbf{v}^h, \boldsymbol{\mu}^h) = \mathscr{L}_0(\mathbf{v}^h, \boldsymbol{\mu}^h) - \frac{h}{k_1} \int_{\Gamma_D} \boldsymbol{\mu}^h \cdot (\boldsymbol{\lambda}^h - \mathbf{T}(\hat{\mathbf{u}}^h)) \, \mathrm{d}\Gamma, \tag{5}$$

where k_1 is a parameter defined by the user, h is the characteristic mesh size and $\mathbf{T}(\hat{\mathbf{u}}^h)$ is a smooth stress field depending on the FE solution $\hat{\mathbf{u}}^h$ that will be defined at Section3.1. The interested reader is addressed to [11] for further details.

Expression (5) is similar to the one used in the Nitsche's method in which the operator $\mathbf{T}(\hat{\mathbf{u}}^h)$ represents the tractions over the Dirichlet boundary. Because of that, Nitsche's method results hard to implement. In the proposed approach, the operator $\mathbf{T}(\hat{\mathbf{u}}^h)$ is a postprocess of the solution, guaranteeing the correct convergence of the method [11]. Further details about the evaluation of this operator are given in section 3.1. Problem (5) is already solvable since essential boundary conditions are properly imposed, thanks to the proper stabilization of the Lagrange multipliers field.

However, depending on how the mesh and geometry intersect, it could happen that the problem becomes ill-conditioned. For small problems, this is not an important issue since direct solvers are able to solve them without major difficulties. In the

case of larger problems, iterative solvers are used and their convergence is strongly affected by the condition number of the system to solve [21]. In the case of FDM in general, and in particular in the case of cgFEM, there are some mesh configurations in which the position of the geometry boundary with respect to the nodes, specially the external nodes, causes ill-conditioning issues, preventing the use of iterative solvers, of special interest for large problems. Figure 2a shows an example in which the numerical problem is likely to be ill-conditioned. If the stiffness associated to the nodes outside the domain is small it leads to an ill-conditioning of the system of equations. This is because the solution of those pathological nodes does not affect to the energy of the problem. That is, the global energy remains practically the same regardless of the solution at those nodes. In other words, the sensibility of the energy to the variation of the solution of those nodes is small. Burman [22] found similar issues and addressed them adding an extra term, the ghost penalty, which stabilizes the solution of the pathological nodes by defining a polynomial expansion over a patch containing a sufficient number of elements into the physical domain Ω. However, this effective methodology requires to construct an additional operator build as the L_2 projection of the solution in the patch to a polynomial expansion, which is no standard in the FE set. More recently, Badía *et. al.* [13] propose a method in which they also add stiffness to those external nodes by generating aggregates; i.e. modifying the Cartesian structure of the mesh.

In this contribution we pretend to introduce a new technique based on the use of recovered fields with the aim of, at least, solve the issue, common for the FDM, with the minimal interference on the Cartesian structure of the mesh and avoiding the construction of non-usual operators in the FE set. The proposed technique adds an additional term to the formulation according to equation (6):

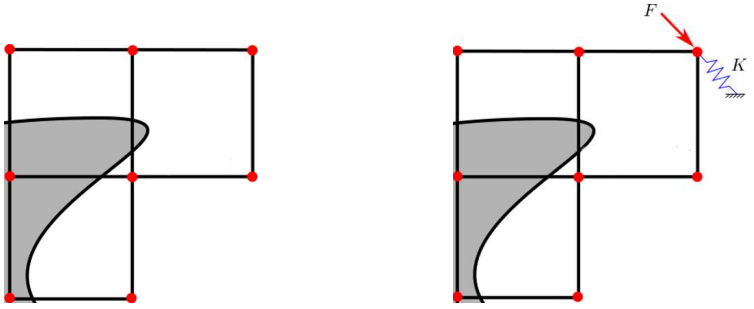

(a) Ill-conditioning issue due to mesh-geometry intersection.

(b) Effect of the additional term.

Figure 2: Scheme of an element subjected to ill-conditioning issues. The stiffness of the nodes far from the domain (in grey) is small.

$$\mathscr{L}(\mathbf{v}^h, \boldsymbol{\mu}^h) = \mathscr{L}_0(\mathbf{v}^h, \boldsymbol{\mu}^h) - \frac{h}{k_1} \int_{\Gamma_D} \boldsymbol{\mu}^h \cdot (\boldsymbol{\lambda}^h - \mathbf{T}(\hat{\mathbf{u}}^h)) \, \mathrm{d}\Gamma - \mathscr{S}(\mathbf{v}^h, \mathbf{u}^h), \qquad (6)$$

where

$$\mathscr{S}(\mathbf{v}^h, \mathbf{u}^h) = \frac{\kappa_2 E}{h^2} \int_{\hat{\Omega}^\star} \mathbf{v}^h \cdot (\mathbf{u}^h - \mathbf{S}(\hat{\mathbf{u}}^h)) \, \mathrm{d}\Gamma, \qquad (7)$$

where E is the Young's modulus, $k_1 = \kappa_1 E$ and $\kappa_2 > 0$ is also a user defined parameter (for the numerical examples $\kappa_2 = 10^{-3}$). Note that $\hat{\Omega}^\star = \bigcup_{\mathrm{p}} \Omega_{\mathrm{p}} \cap \Omega^\star$, being Ω_{p} the domain of an element p containing at least one pathological node, i.e. a node with a small stiffness associated. The additional term, $\mathscr{S}(\mathbf{v}^h, \mathbf{u}^h)$, in equation (6) penalises the "free" displacement of those pathological nodes. In fact, it introduces and artificial stiffness which is compensated with an artificial force as shown in figure 2b. In this term, the integration domain $\hat{\Omega}^\star$ corresponds to the elements containing pathological nodes, not to the surface but to the volume. Thus, the integration domain now considers also the part of the element falling outside the problem domain. The operator $\mathbf{S}(\hat{\mathbf{u}}^h)$ corresponds to a displacements field obtained as a postprocess of the FE solution $\mathbf{u}^h$. Further details of operator $\mathbf{S}$ are in Section 3.2. Note that one of the most important benefits of the method is that the additional term can be constructed as a lumped mass matrix, standard in the FE set.

2.2. Iterative solver

Note that for solving problem (6) an iterative process is required since operators $\mathbf{T}$ and $\mathbf{S}$ depends on the current solution. In this contribution the Richardson's method is implemented, considering $\mathbf{T} = \mathbf{S} = 0$ for the first iteration. Once the first iteration is obtained, the operators $\mathbf{T}$ and $\mathbf{S}$ are obtained as explained in Section 3, considering $\hat{\mathbf{u}}^h$ the solution obtained in the previous iteration step. The convergence of this iterative process is demonstrated in Section 4.2.

3. Recovery techniques

Recovery procedures arise from error indicators techniques developed during the last decades [23–29], just to cite some. Among them we can highlight the Superconvergent Patch Recovery technique developed by Zienkiewicz and Zhu [24] which provides a robust, efficient and easy-to-implement error indicator. The recovery procedure used in this error indicator proposed by Zienkiewicz and Zhu is at the base of the recovery techniques proposed in this contribution for the evaluation of the operators $\mathbf{S}$ and $\mathbf{T}$ used in Section 2 for the stabilization terms. In this section we

will introduce the proposed technique and the construction of the operators $\mathbf{T}$ and $\mathbf{S}$ introduced in Section 2.

The recovered field of an arbitrary vector field $\boldsymbol{\Upsilon}$ at each patch of elements i, $\hat{\boldsymbol{\Upsilon}}_i$, is obtained by minimizing the following functional:

$$\mathcal{F}_i(\hat{\boldsymbol{\Upsilon}}_i) = \int_{\hat{\Omega}_i} (\boldsymbol{\Upsilon}^h - \hat{\boldsymbol{\Upsilon}}_i)^2 \, \mathrm{d}\Omega, \tag{8}$$

where the field $\boldsymbol{\Upsilon}^h$ is a given FE interpolation of the field $\boldsymbol{\Upsilon}$ (i.e. displacements, strains, stresses, ...) and the field $\hat{\boldsymbol{\Upsilon}}_i$ is a polynomial expansion of a higher order than the FE interpolation (usually one order higher). A patch of elements $\hat{\Omega}_i$ consists of the elements attached to the node i, also called *assembly node*. Note that in this case the domain of the patch $\hat{\Omega}_i$ is not restricted to the physical domain Ω since it may include the part of the element falling outside the physical domain. Additionally, we can also add extra terms which improve the quality of the recovered field at each patch, depending on the needs such as static admissibility for the error estimator case, see for instance [26, 30] or [31] for error upper bounds.

After obtaining the recovered field at each patch of elements, valid only in the patch surrounding the node i, the recovered field in the whole domain $\Omega^\star$ is obtained by using the Conjoint Polynomial Enhancement [25], which is nothing but the weighted sum of the contribution of each patch at a given position $\mathbf{x} \in \Omega^\star$:

$$\hat{\boldsymbol{\Upsilon}} = \sum_{j=1}^{Nvn} N(\mathbf{x})_j \hat{\boldsymbol{\Upsilon}}_j(\mathbf{x}), \tag{9}$$

where Nvn is the number of vertex nodes in a element and the weighting functions are the linear shape functions of the elements.

3.1. Operator T

The operator $\mathbf{T}$ is the projection of the recovered stress field to the boundary. That is, $\boldsymbol{\Upsilon}^h = \boldsymbol{\sigma}^h$, $\hat{\boldsymbol{\Upsilon}}_i = \hat{\boldsymbol{\sigma}}_i$ and $\hat{\boldsymbol{\Upsilon}} = \hat{\boldsymbol{\sigma}}$. Therefore:

$$\mathbf{T}(\mathbf{u}^h) = \hat{\boldsymbol{\sigma}} \cdot \mathbf{n}. \tag{10}$$

Note that operator $\mathbf{T}$ is only considered along the Dirichlet boundaries (5). This implies that the reconstruction of the stress field via the minimization of the functional (8) and the use of the Conjoint Polynomial Enhancement (9) is only required at patches cut by the boundary, which has a reduced computational cost.

3.2. Operator S

The operator $\mathbf{S}$ corresponds to the recovered displacement field obtained with the minimization of the functional (8), where in this case $\boldsymbol{\Upsilon}^h = \mathbf{u}^h$ and $\hat{\boldsymbol{\Upsilon}}_i = \hat{\mathbf{u}}_i$.

Therefore:

$$\mathbf{S}(\mathbf{u}^h) = \hat{\mathbf{u}}_i. \tag{11}$$

In this case the operator $\mathbf{S}$ is only required along the part of the boundary influenced by pathological nodes, which makes possible to consider this procedure computationally inexpensive. In contrast with operator $\mathbf{T}$, operator $\mathbf{S}$ is evaluated at each node i (only the nodal value is retained), thus avoiding the use of the Conjoint Polynomial Enhancement (9).

4. Convergence study

In this section we study the different aspects of the convergence to the exact solution of the proposed approach. First we study the *a priori* error estimates to demonstrate the right convergence of all the operators involved. Then, we demonstrate the convergence of the iterative algorithm for the resolution of the problem and finally the improvement of the condition number thanks to the addition of the term $\mathscr{S}(\mathbf{v}^h, \mathbf{u}^h)$.

4.1. A priori error estimates

In this section we show that the additional term defined in equation (7) does not affect the convergence of the approximated solution to the exact solution as the mesh is uniformly refined, i.e. it has at least the same convergence rate than the strain energy [32], according to the following proposition.

Proposition 1. *The term defined in equation* (7) *vanishes with* h^{2p} *as the mesh is refined, being* p *the order of the polynomial interpolation, that is:*

$$\frac{\kappa_2 E}{h^2} \int_{\hat{\Omega}^\star} \mathbf{e}^h \cdot (\mathbf{e}^h - \mathbf{S}(\hat{\mathbf{e}}^h)) \, \mathrm{d}\Gamma \approx \mathcal{O}(h^{2p}), \tag{12}$$

with $\mathbf{e}^h = \mathbf{u} - \mathbf{u}^h$, *being* $\mathbf{u}$ *the exact solution.*

Proof. The additional term can be bounded by using the Cauchy-Schwarz inequality:

$$\frac{\kappa_2 E}{h^2} \int_{\hat{\Omega}^\star} \mathbf{e}^h \cdot (\mathbf{e}^h - \mathbf{S}(\hat{\mathbf{e}}^h)) \, \mathrm{d}\Gamma \lesssim h^{-2} \|\mathbf{e}^h\|_{L_2(\hat{\Omega}^\star)} \|\mathbf{e}^h - \mathbf{S}(\hat{\mathbf{e}}^h)\|_{L_2(\hat{\Omega}^\star)}, \tag{13}$$

with symbol $\lesssim$ indicating that the inequality holds up to a certain positive constant. Using the triangular inequality for the last norm in equation (13):

$$\|\mathbf{e}^h - \mathbf{S}(\hat{\mathbf{e}}^h)\|_{L_2(\hat{\Omega}^\star)} \lesssim \left(\|\mathbf{e}^h\|_{L_2(\hat{\Omega}^\star)} + \|\mathbf{S}(\hat{\mathbf{e}}^h)\|_{L_(\hat{\Omega}^\star)} \right). \tag{14}$$

Finally combining equation (14) in (13) we obtain that:

$$\frac{\kappa_2 E}{h^2}\int_{\hat{\Omega}^\star}\mathbf{e}^h\cdot(\mathbf{e}^h-\mathbf{S}(\hat{\mathbf{e}}^h))\,\mathrm{d}\Gamma\lesssim h^{-2}\|\mathbf{e}^h\|_{L_2(\hat{\Omega}^\star)}\left(\|\mathbf{e}^h\|_{L_2(\hat{\Omega}^\star)}+\|\mathbf{S}(\hat{\mathbf{e}}^h)\|_{L_2(\hat{\Omega}^\star)}\right). \quad (15)$$

In order to check the convergence, we pay attention to the term $\|\mathbf{S}(\hat{\mathbf{e}}^h)\|_{L_2(\hat{\Omega}^\star)}$. This term is built as the L_2-projection to a local and richer space, i.e. a higher order polynomial space, thus the convergence of $\|\mathbf{S}(\hat{\mathbf{e}}^h)\|_{L_2(\hat{\Omega}^\star)}$ is the same as the convergence of $\|\mathbf{e}^h\|_{L_2(\hat{\Omega}^\star)}$, then:

$$\frac{\kappa_2 E}{h^2}\int_{\hat{\Omega}^\star}\mathbf{e}^h\cdot(\mathbf{e}^h-\mathbf{S}(\hat{\mathbf{e}}^h))\,\mathrm{d}\Gamma\lesssim h^{-2}\|\mathbf{e}^h\|^2_{L_2(\hat{\Omega}^\star)}\approx\mathcal{O}(h^{2p}). \quad (16)$$

□

4.2. Iterative solver convergence

As observed in equation (6), the RHS of the system of equations depends on the solution of the same system. Then, the Richardson's method is used for solving linear system of equations.

In matrix notation, equation (6) can be expressed as follows:

$$\mathbf{A}\mathbf{d}^i=\mathbf{c}+\mathbf{B}\mathbf{d}^{i-1} \quad (17)$$

being $\mathbf{d}^i$ the solution at iteration i. The matrix $\mathbf{A}$ is obtained from:

$$a(\mathbf{v}^h,\mathbf{v}^h)+\frac{\kappa_1 E}{h}\int_{\Gamma_D}\mathbf{v}^h\cdot\mathbf{v}^h\,\mathrm{d}\Gamma+\frac{\kappa_2 E}{h^2}\int_{\hat{\Omega}^\star}\mathbf{v}^h\cdot\mathbf{v}^h\,\mathrm{d}\Gamma, \quad (18)$$

and matrix $\mathbf{B}$ is obtained from

$$\int_{\Gamma_D}\mathbf{v}^h\cdot\mathbf{T}(\hat{\mathbf{v}}^h)\,\mathrm{d}\Gamma+\frac{\kappa_2 E}{h^2}\int_{\hat{\Omega}^\star}\mathbf{v}^h\cdot\mathbf{S}(\hat{\mathbf{v}}^h)\,\mathrm{d}\Gamma, \quad (19)$$

which in practice will never be assembled, where $\hat{\mathbf{v}}^h$ is the solution of iteration $i-1$. The Richardon's method is proved to converge if the spectral radius of the matrix $\mathbf{A}^{-1}\mathbf{B}$ is smaller than one.

Proposition 2. *The spectral radius of* $\mathbf{A}^{-1}\mathbf{B}$ *is smaller than 1, that is* $\rho(\mathbf{A}^{-1}\mathbf{B})\leq 1$*, for appropriate values of* κ_1 *and* κ_2*, independent of* h*.*

Proof. In this case, any eigenvalue λ fulfills:

$$\mathbf{A}^{-1}\mathbf{B}\mathbf{d}=\lambda\mathbf{d}. \quad (20)$$

Moving matrix $\mathbf{A}^{-1}$ to the RHS and pre-multiplying both sides by $\mathbf{d}^T$ we obtain:

$$\mathbf{d}^T\mathbf{B}\mathbf{d} = \lambda \mathbf{d}^T\mathbf{A}\mathbf{d}. \tag{21}$$

It can be appreciated that the LHS of equation (21) corresponds to the stabilization terms for a given field $\mathbf{v}^h$, then:

$$\mathbf{d}^T\mathbf{B}\mathbf{d} = \int_{\Gamma_D} \mathbf{v}^h \cdot \mathbf{T}(\mathbf{v}^h)\, \mathrm{d}\Gamma + \frac{k_2}{h^2}\int_{\hat{\Omega}^\star} \mathbf{v}^h \cdot \mathbf{S}(\mathbf{v}^h)\, \mathrm{d}\Gamma. \tag{22}$$

In the same way:

$$\mathbf{d}^T\mathbf{A}\mathbf{d} = a(\mathbf{v}^h, \mathbf{v}^h) + \frac{\kappa_1}{h}\int_{\Gamma_D} \mathbf{v}^h \cdot \mathbf{v}^h\, \mathrm{d}\Gamma + \frac{k_2}{h^2}\int_{\hat{\Omega}^\star} \mathbf{v}^h \cdot \mathbf{v}^h\, \mathrm{d}\Gamma \tag{23}$$

Then, after some algebra and applying the Cauchy-Schwarz inequality, we obtain:

$$\lambda \mathbf{d}^T\mathbf{A}\mathbf{d} = \mathbf{d}^T\mathbf{B}\mathbf{d} \leq \|\mathbf{v}^h\|_{L^2(\Gamma_D)}\|\mathbf{T}(\mathbf{v}^h)\|_{L^2(\Gamma_D)} + \frac{k_2}{h^2}\|\mathbf{v}^h\|_{L^2(\Omega^\star)}\|\mathbf{S}(\mathbf{v}^\mathbf{h})\|_{L^2(\Omega^\star)} \tag{24}$$

According to [11], the term $\|\mathbf{T}(\mathbf{v}^h)\|_{L^2(\Gamma_D)}$ can be bounded by the energy norm of the problem, thus the first term of the RHS in equation (24) can be bounded by the energy norm as follows:

$$\|\mathbf{v}^h\|_{L^2(\Gamma_D)}\|\mathbf{T}(\mathbf{v}^h)\|_{L^2(\Gamma_D)} \leq \|\mathbf{v}^h\|_{L^2(\Gamma_D)}\left(\frac{C_E C_p C_r}{h}\right)^{\frac{1}{2}}\|\mathbf{v}^h\|_E. \tag{25}$$

where $\|\mathbf{v}^h\|_E$ stands for the energy norm, $C_E = \frac{E}{1+2\nu}$, C_p stands for the Poincaré inequality and C_r is the constant relating a recovered field with the FE field into a bounded domain, i.e. $\|\mathbf{T}(\mathbf{v}^h)\|^2_{L^2(\cdot)} \leq C_r\|\boldsymbol{\sigma}(\mathbf{v}^h)\|^2_{L^2(\cdot)}$. We remark that C_E, C_p and C_r are independent of the mesh size. For the interested reader, further details on these constants can be found in [11].

Finally, applying the triangular inequality ($2xy \leq \frac{x^2}{2} + \frac{y^2}{2}$) we obtain:

$$\|\mathbf{v}^h\|_{L^2(\Gamma_D)}\|\mathbf{T}(\mathbf{v}^h)\|_{L^2(\Gamma_D)} \leq \|\mathbf{v}^h\|^2_E + \frac{C_E C_p C_r}{4h}\|\mathbf{v}^h\|^2_{L^2(\Gamma_D)}. \tag{26}$$

On the other hand, we also need to bound the second term of the RHS in equation (24). Considering the relation between a recovered solution and the corresponding FE solution is $\|\hat{\boldsymbol{\Upsilon}}^h_i\|^2_{L^2(\cdot)} \leq \|\boldsymbol{\Upsilon}^h\|^2_{L^2(\cdot)}$, due to the orthogonality between the both fields, we can write:

$$\|\mathbf{v}^h\|_{L^2(\hat{\Omega}^\star)}\|\mathbf{S}(\mathbf{v}^h)\|_{L^2(\hat{\Omega}^\star)} \leq \|\mathbf{v}^h\|^2_{L^2(\hat{\Omega}^\star)} \tag{27}$$

Finally, substituting (26) and (27) in (24) we can write:

$$\lambda \mathbf{d}^T\mathbf{A}\mathbf{d} \leq \|\mathbf{v}^h\|^2_E + \frac{C_E C_p C_r}{4h}\|\mathbf{v}^h\|^2_{L^2(\Gamma_D)} + \frac{k_2}{h^2}\|\mathbf{v}^h\|^2_{L^2(\hat{\Omega}^\star)} \tag{28}$$

Considering that:

$$\mathbf{d}^T\mathbf{A}\mathbf{d} = \|\mathbf{v}^h\|_E^2 + \frac{k_1}{h}\|\mathbf{v}^h\|_{L^2(\Gamma_D)}^2 + \frac{k_2}{h^2}\|\mathbf{v}^h\|_{L^2(\hat{\Omega}^\star)}, \tag{29}$$

it suffices in taking $k_1 > \frac{C_E C_p C_r}{4h}$ for any value of k_2 to ensure that $\lambda < 1$.

□

4.3. Improvement of the condition number

In the standard, conforming, Finite Element set, the condition number grows with h^{-2}. Therefore, in this section we show that the proposed method provides a condition number which grows in the same way than in the standard FE case.

Proposition 3. *The condition number of the system of equations resulting from equation* (6) *grows with* h^{-2}.

Proof. The condition number is the ratio between λ_{min} and λ_{max}, being the smaller and higher eigenvalues, $\kappa = \frac{\lambda_{max}}{\lambda_{min}}$, . In this case we need to proof *i)* $\lambda_{min} > 0$ independently of h and *ii)* λ_{max} is proportional to h^{-2}.

i) $\lambda_{min} > 0$ *independently of* h

For this part of the proof we need to check the coercivity, i.e. there exists $C_1 > 0$, independent of h, such that:

$$C_1\|\mathbf{v}^h\|_{L^2(K)}^2 \leq h^2\left(a_{K\cap\Omega}(\mathbf{v^h},\mathbf{v^h}) + \frac{k_1}{h}\int_{\partial K\cap\Gamma_D}\mathbf{v}^h\cdot\mathbf{v}^h\,\mathrm{d}\Gamma + \frac{k_2}{h^2}\int_K \mathbf{v}^h\cdot\mathbf{v}^h\,\mathrm{d}\Gamma\right) \tag{30}$$

where $K \in \Omega^\star$ represents a single finite element of size h. Equation (30) follows from the mesh-dependent norm definition, see lemma 4.5.3 in [33]. Under the cgFEM framework, the effective domain falling into one element $(K \cap \Omega)$ does not depend on h but on the way the geometry intersects the mesh. Therefore the effective domain is bounded above by K and bounded below by $\emptyset$, i.e. $\emptyset \subseteq K \cap \Omega \subseteq K$, then:

$$a_{K\cap\Omega}(\mathbf{v^h},\mathbf{v^h}), \qquad \text{and} \qquad \frac{k_1}{h}\int_{\partial K\cap\Gamma_D}\mathbf{v}^h\cdot\mathbf{v}^h\,\mathrm{d}\Gamma \tag{31}$$

can eventually tend to zero. That would prevent from fulfilling the coercivity property. However, by taking use of the last term in equation (30), since it does not depend on the physical domain Ω (i.e. it does not depend on how the mesh and geometry intersect), in the eventual case that the two first terms are close to zero, there will be possible to find a proper constant $C_1 > 0$ which ensures the coercivity. Since the problem is coercive, the norm of the minimum eigenvalue is higher than 0, $\lambda_{min} > 0$.

ii) $\lambda_{max} \propto h^{-2}$

On the other hand, according to the lemma 4.5.3 in [33] and summing up all the elements we have:

$$a(\mathbf{v}^h, \mathbf{v}^h) + \frac{k_1}{h} \int_{\Gamma_D} \mathbf{v}^h \cdot \mathbf{v}^h \, \mathrm{d}\Gamma + \frac{k_2 E}{h^2} \int_{\hat{\Omega}^\star} \mathbf{v}^h \cdot \mathbf{v}^h \, \mathrm{d}\Gamma \leq C_2 h^{-2} \|\mathbf{v}^h\|^2_{L^2(\Omega^\star)}. \tag{32}$$

According to the definition of spectral radius we have that $\lambda_{max} \propto C_2 h^{-2}$. Finally, combining the two results: $\lambda_{min} > 0$ and $\lambda_{max} \propto C_2 h^{-2}$ we have that:

$$\kappa = \frac{\lambda_{max}}{\lambda_{min}} \propto h^{-2} \tag{33}$$

□

5. Numerical results

In this section a series of numerical test are carried out in order to check the improvements on the condition number and in the solution when using the proposed approach, and therefore, in the performance of the cgFEM. Additionally we also give some details about the algorithm used for obtaining the numerical solution when combined the Richardson's method and the iterative solver.

5.1. Solution algorithm

In each one of the iterations of the Richardson's method, for a given field $\hat{\mathbf{u}}^h$ the linear system of equations obtained from (6) must be solved. We assume that at Richardson's iteration i, $\hat{\mathbf{u}}^h_{i-1}$ is known, then we proceed as follows:

1. Evaluate the stabilization terms for $\hat{\mathbf{u}}^h_{i-1}$.
2. Solve problem (6).
3. Evaluate the new $\hat{\mathbf{u}}^h_i$.
4. Evaluate $\epsilon^R_i = ||\hat{\mathbf{u}}^h_i - \hat{\mathbf{u}}^h_{i-1}||_2$
5. If $\epsilon^R_i < Tol$ stop the iterations, else go to step 1.

This Richardson's method is initialized with $\hat{\mathbf{u}}_0^h = \mathbf{0}$. Note that step 3 implies the to solve several times a system of equations with the same coefficient matrix, allowing use to factorize it in order to speed up the computations. For large system of equations, when iterative solvers are required, the iterative method uses the solution of the previous Richardson's iteration and the tolerance of the iterative solver decreases proportionally to ϵ_i^R, i.e. $\epsilon_i^I \propto \epsilon_i^R$. This nested procedure for both iterative method will increase the performance of the solver.

5.2. Numerical example 1

The first numerical example consists in a 3D model of an infinite plate under traction at the infinite with a central hole. The analytical solution for the plane strain case is known (34). The aim of using this problem is to show the convergence of the proposed approach to a non-polynomial analytical solution. Using a cylindrical reference system (r, θ), centred in the hole, the stress field is described by the following expressions:

$$\begin{cases} \sigma_{xx}(r,\theta) = \sigma_0 \left(1 - \left(\frac{a}{r}\right)^2 (1.5\cos(2\theta) + \cos(4\theta)) + 1.5\left(\frac{a}{r}\right)^4 \cos(4\theta)\right) \\ \sigma_{yy}(t,\theta) = \sigma_0 \left(-\left(\frac{a}{r}\right)^2 (0.5\cos(2\alpha) - \cos(4\alpha)) - 1.5\left(\frac{a}{r}\right)^4 \cos(4\alpha)\right) \\ \sigma_{zz}(t,\theta) = \nu\left(\sigma_x x(t,\theta) + \sigma_y y(t,\theta)\right) \\ \tau_{xy}(r,\theta) = \sigma_0 \left(-\left(\frac{a}{r}\right)^2 (0.5\sin(2\alpha) + \sin(4\alpha)) + 1.5\left(\frac{a}{r}\right)^4 \sin(4\alpha)\right) \\ \tau_{xz}(r,\theta) = \tau_{yz}(r,\theta) = 0 \end{cases} \tag{34}$$

where $\nu = 0.3$ is the Poisson's ratio, $\sigma_0 = 1$ units of pressure is the traction at the infinite and the Young's modulus considered is $E = 1000$ units of pressure. The 3D model is represented in figure 3 with an example of a mesh of level 6 (2^6 divisions per direction in the octree-mesh) provided by the cgFEM. Three symmetry conditions are considered (rear, left and bottom planes), and appropriate Neumann boundary conditions are applied following (34) on the rest of the surface. For this problem $Q8$ linear elements are considered.

The first study consists in the analysis of the convergence of the iterative solver, considering both situations: with and without the new stabilization term (7) introduced in this publication. The iterative solver is the PCG solver implemented in Matlab® configured with a null initialization solution and an incomplete Cholesky factorization as preconditioner, with the same configuration in both cases. As it can be observed in figure 4a, the number of iterations required when the proposed stabilization term is not used is always higher. This fact is strongly influenced by the condition number, which in this case for the mesh of 65058 degrees of freedom is

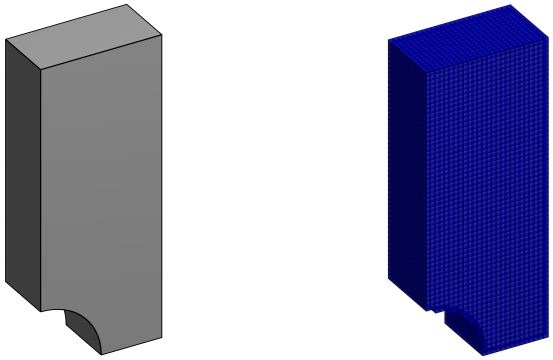

Figure 3: Domain and mesh example for problem 1.

$5.55 \cdot 10^8$ when no stabilization is considered and $2.19 \cdot 10^5$ when it is considered. Note that for this problem there is not an important difference on the condition number (only two orders of magnitude) since the geometry is mainly built with flat surfaces and the intersection patterns do not yield many pathological nodes. Additionally, figure 4b shows that the the relative exact error in energy norm during the uniform refinement process for both cases. It can be observed that the convergence remains unadulterated keeping a convergence rate of $\frac{1}{3}$, the theoretical one for linear elements.

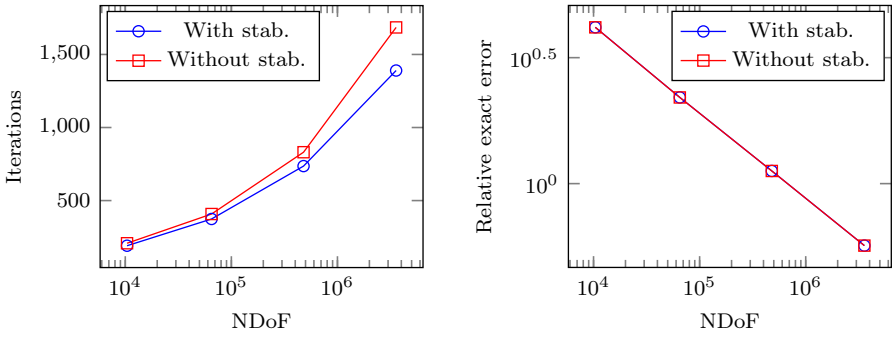

(a) Convergence of the iterative solver. Number of iterations required for a relative tolerance of 10^{-7}.

(b) Convergence of the solution, considering the relative exact error in energy norm.

Figure 4: Numerical example 1. Convergence analysis.

5.3. Numerical example 2

In the second example a toroidal volume is analysed. The curvatures in this shape provide with a variety of cutting patterns between the analysis domain and the discretization mesh. Figure 5 shows the toroidal volume on the left, with major and minor radius of $R = 1.5$, $r = 0.5$ length units respectively and the meshed model with mesh level 6 at the right. The material model for this problem is the same as in the previous example.

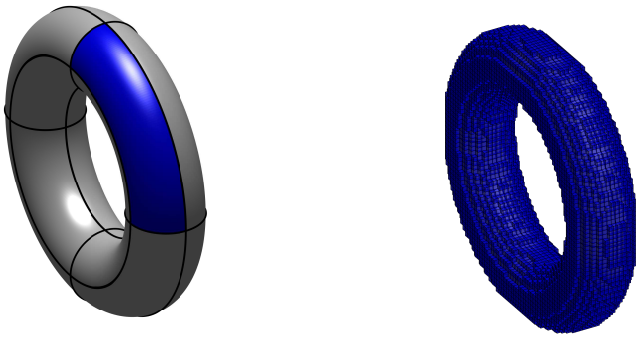

Figure 5: Domain and mesh example for numerical example 2. All displacements are constrained on the blue patches. Neumann boundary conditions are applied on the rest of the surface.

The analytical displacement field for this problem is defined in expression (35). The corresponding stress field and body forces field can be easy derived by using the analytical elasticity equations. For the numerical analysis the coloured octant in figure 5 is under Dirichlet boundary conditions dictated by (35), while the rest of the boundary is under the corresponding Neumann boundary conditions also derived from (35). Finally the required body forces are also applied.

$$\begin{cases} u(x,y,z) = x^4 + 3yx^3 - 2xz^2 + yxz \\ v(x,y,z) = 7x^2y + y^4 - 2zy^3 \\ w(x,y,z) = -3x^2z^2 + 2yxz + z^3 \end{cases} \tag{35}$$

In this case the arbitrary cutting patterns easily generates ill-conditioning problems in the system of equations. This fact is clearly observed in the condition number of the system of equations for the mesh of Q8 linear elements of level 6 with 118020 degrees of freedom. When the proposed term is not utilized, the condition number is $5.67 \cdot 10^{25}$, but when the proposed stabilization term is used this number decreases to $5.69 \cdot 10^{5}$, similar to that of the previous example for a similar mesh.

First, we analyse the performance of cgFEM regarding the behaviour of the PCG iterative solver. Figure 6a shows that the number of iterations are always considerably lower due to the improvement of the condition number and the increase on the number of iterations when the proposed stabilization is not used increase faster with the number of degrees of freedom. Additionally, figure 6 shows the savings in the computational time for each resolution of the iterative solver.

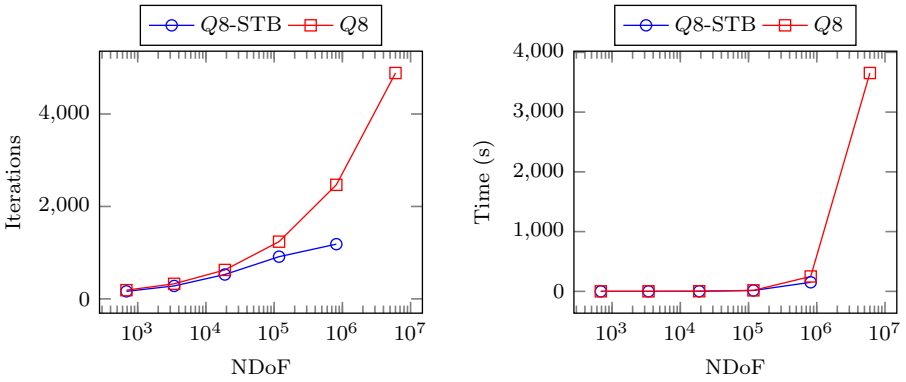

(a) Convergence of the iterative solver. Number of iterations required for a relative tolerance of 10^{-9}.

(b) Computational cost of the iterative solver.

Figure 6: Numerical example 2. Analysis of the convergence of the iterative solver.

Figure 7 shows the convergence to the exact solution of the error in energy norm. As you can observe the convergence rate remains unaltered for Q8 elements and the convergence rate when the asymptotic rate is achieves is around $\frac{1}{3}$, the theoretical one for linear elements.

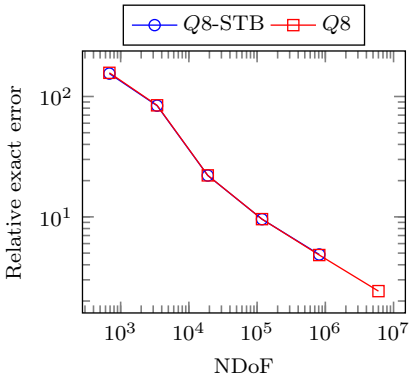

Figure 7: Numerical example 2. Convergence to the exact solution.

6. Conclusions

This contribution tries to address the common issue of the FDM, in particular the cgFEM, when mesh-geometry cutting patters yields to ill-conditioned system of equations. The proposed approach is naturally included during the solving loop and the evaluation of the additional terms is inexpensive since only requires a post-process of the solution along the boundary, while preserving the Cartesian structure of the cgFEM framework. The results show a independence of the condition number with respect to the mesh-geometry intersection, yielding, speeding up the solving process while preserving the consistency of the formulation.

Acknowledgements

The authors wish to thank the Spanish Ministerio de Economia y Competitividad the Generalitat Valenciana and the Universitat Politècnica de València for their financial support received through the projects DPI2017-89816-R, Prometeo 2016/007 and the FPI2015 program.

References

[1] E. Burman and P. Hansbo, "Fictitious domain finite element methods using cut elements: I. A stabilized Lagrange multiplier method," *Computer Methods in Applied Mechanics and Engineering*, vol. 199, no. 41-44, pp. 2680–2686, 2010.

[2] E. Ruiz-Girons and J. Sarrate, "Generation of structured hexahedral meshes in volumes with holes," *Finite Elements in Analysis and Design*, vol. 46, pp. 792–804, oct 2010.

[3] C. Geuzaine and J.-F. Remacle, "Gmsh: a three-dimensional finite element mesh generator with built-in pre-and post-processing facilities," *International Journal for Numerical Methods in Engineering 79(11)*, vol. 0, pp. 1309–1331, 2009.

[4] J. Parvizian, A. Düster, and E. Rank, "Finite cell method," *Computational Mechanics*, vol. 41, pp. 121–133, sep 2007.

[5] A. Düster, J. Parvizian, Z. Yang, and E. Rank, "The finite cell method for three-dimensional problems of solid mechanics," *Computer Methods in Applied Mechanics and Engineering*, vol. 197, pp. 3768–3782, aug 2008.

[6] E. Nadal, J. J. Ródenas, J. Albelda, M. Tur, J. E. Tarancón, and F. J. Fuenmayor, "Efficient Finite Element Methodology Based on Cartesian Grids: Application to Structural Shape Optimization," *Abstract and Applied Analysis*, pp. 1–19, 2013.

[7] E. Nadal, *Cartesian grid FEM (cgFEM): High performance h adaptive FE analysis with efficient error control . Application to structural shape optimization.* PhD thesis, Universitat Politècnica de València, 2014.

[8] L. Giovannelli, J. Ródenas, J. Navarro-Jiménez, and M. Tur, "Direct medical image-based Finite Element modelling for patient-specific simulation of future implants," *Finite Elements in Analysis and Design*, vol. 136, pp. 37–57, nov 2017.

[9] D. Schillinger and M. Ruess, "The Finite Cell Method: A Review in the Context of Higher-Order Structural Analysis of CAD and Image-Based Geometric Models," *Archives of Computational Methods in Engineering*, vol. 22, no. 3, pp. 391–455, 2015.

[10] E. Burman, S. Claus, P. Hansbo, M. G. Larson, and A. Massing, "CutFEM: Discretizing geometry and partial differential equations," *International Journal for Numerical Methods in Engineering*, vol. 104, pp. 472–501, nov 2015.

[11] M. Tur, J. Albelda, O. Marco, and J. J. Ródenas, "Stabilized method of imposing Dirichlet boundary conditions using a recovered stress field," *Computer Methods in Applied Mechanics and Engineering*, vol. 296, pp. 352–375, aug 2015.

[12] M. Tur, J. Albelda, E. Nadal, and J. J. Ródenas, "Imposing Dirichlet boundary conditions in hierarchical Cartesian meshes by means of stabilized Lagrange multipliers," *International Journal for Numerical Methods in Engineering*, vol. 98, pp. 399–417, may 2014.

[13] S. Badia, F. Verdugo, and A. F. Martín, "The aggregated unfitted finite element method for elliptic problems," sep 2017.

[14] H. J. C. Barbosa and T. J. R. Hughes, "The finite element method with Lagrange multipliers on the boundary: circumventing the Babu??ka-Brezzi condition," *Computer Methods in Applied Mechanics and Engineering*, vol. 85, no. 1, pp. 109–128, 1991.

[15] H. J. C. Barbosa and T. J. R. Hughes, "Boundary Lagrange multipliers in finite element methods: Error analysis in natural norms," *Numerische Mathematik*, vol. 62, pp. 1–15, dec 1992.

[16] E. Béchet, N. Moës, B. Wohlmuth, É. Béchet, N. Moës, and B. Wohlmuth, "A stable Lagrange multiplier space for stiff interface conditions within the extended finite element method," *International Journal for Numerical Methods in Engineering*, vol. 78, pp. 931–954, may 2009.

[17] M. Hautefeuille, C. Annavarapu, and J. E. Dolbow, "Robust imposition of Dirichlet boundary conditions on embedded surfaces," *International Journal for Numerical Methods in Engineering*, vol. 90, pp. 40–64, apr 2012.

[18] P. Hansbo, C. Lovadina, I. Perugia, and G. Sangalli, "A Lagrange multiplier method for the finite element solution of elliptic interface problems using non-matching meshes," *Numerische Mathematik*, vol. 100, pp. 91–115, mar 2005.

[19] E. Burman and P. Hansbo, "Fictitious domain finite element methods using cut elements: II. A stabilized Nitsche method," *Applied Numerical Mathematics*, vol. 62, no. 4, pp. 328–341, 2012.

[20] A. Gerstenberger and W. Wall, "An eXtended Finite Element Method/Lagrange multiplier based approach for fluid-structure interaction," *Computer Methods in Applied Mechanics and Engineering*, vol. 197, no. 19-20, pp. 1699–1714, 2008.

[21] O. Axelsson, "Iterative Solution Methods," 1994.

[22] E. Burman, "La pénalisation fantôme," *Comptes Rendus Mathematique*, vol. 348, no. 21-22, pp. 1217–1220, 2010.

[23] O. C. Zienkiewicz and J. Z. Zhu, "A simple error estimator and adaptive procedure for practical engineering analysis," *International Journal for Numerical Methods in Engineering*, vol. 24, no. 2, pp. 337–357, 1987.

[24] O. C. Zienkiewicz and J. Z. Zhu, "The superconvergent patch recovery and a posteriori error estimates. Part 1: The recovery technique," *International Journal for Numerical Methods in Engineering*, vol. 33, no. 7, pp. 1331–1364, 1992.

[25] T. Blacker and T. Belytschko, "Superconvergent patch recovery with equilibrium and conjoint interpolant enhancements," *International Journal for Numerical Methods in Engineering*, vol. 37, no. 3, pp. 517–536, 1994.

[26] P. Díez, J. J. Ródenas, O. C. Zienkiewicz, D. Pedro, P. Díez, J. J. Ródenas, and O. C. Zienkiewicz, "Equilibrated patch recovery error estimates : simple and accurate upper bounds of the error," *International Journal for Numerical Methods in Engineering*, vol. 69, no. August 200610, pp. 2075–2098, 2007.

[27] Q. Z. Xiao and B. L. Karihaloo, "Statically admissible stress recovery using the moving least squares technique," in *Congress in Computational Structures Technology* (B. H. V. Topping and C. A. M. Soares, eds.), (Stirling, Scotland), pp. 111–138, Saxe-Coburg Publications, 2004.

[28] J. J. Ródenas, M. Tur, F. J. Fuenmayor, and A. Vercher, "Improvement of the superconvergent patch recovery technique by the use of constraint equations: the SPR-C technique," *International Journal for Numerical Methods in Engineering*, vol. 70, no. 6, pp. 705–727, 2007.

[29] Z. Zhang, "A posteriori error estimates on irregular grids based on gradient recovery," *Advances in Computational Mathematics*, vol. 15, pp. 363–374, 2001.

[30] O. A. González-Estrada, E. Nadal, J. J. Ródenas, P. Kerfriden, S. P. a. Bordas, and F. J. Fuenmayor, "Mesh adaptivity driven by goal-oriented locally equilibrated superconvergent patch recovery," *Computational Mechanics*, vol. 53, pp. 957–976, oct 2013.

[31] E. Nadal, P. Díez, J. J. Ródenas, M. Tur, and F. J. Fuenmayor, "A recovery-explicit error estimator in energy norm for linear elasticity," *Computer Methods in Applied Mechanics and Engineering*, vol. 287, pp. 172–190, 2015.

[32] D. J. Alan, *The Finite Element Method*. 1980.

[33] S. C. Brenner and L. R. Scott, *Mathematical Theory of Finite Element Methods*. Springer Berlin Heidelberg, 1994.

PAPER E

Superconvergent patch recovery with constrains for 3D contact problems within the Cartesian grid Finite Element Method

J.M. Navarro-Jiménez, H. Navarro-García, M. Tur, and J.J. Ródenas

Preprint submitted to International Journal for Numerical Methods in Engineering

Abstract

The Superconvergent Patch Recovery technique with constraints (SPR-C) consists in improving the accuracy of the recovered stresses obtained with the original SPR technique by considering known information about the exact solution, like the internal equilibrium equation, the compatibility equation or the boundary equilibrium, during the recovery process. In this paper the SPR-C is extended to consider the boundary equilibrium around the contact area when solving contact problems with the Cartesian grid Finite Element Method (cgFEM). In the method presented, the Finite Element stress fields of both bodies in contact are considered during the recovery process and the boundary equilibrium is enforced by means of the continuity of tractions along the contact surface.

Key words

Superconvergent Patch Recovery; Contact; Cartesian grid; Immersed boundary

Contents

1. Introduction

The mechanical contact problem is present in several classical industrial applications such as tyre-road, wheel-rail interactions, pin-on-disc wear or fretting. The contact problem is also being introduced in novel research areas like the patient specific study of the interaction between living tissue and prosthetic devices. The formulation of the problem at hand, the contact between two linear elastic domains $\Omega^{(i)}, i = 1, 2$, can be written as follows:

$$\begin{aligned} &\operatorname{div} \boldsymbol{\sigma} + \mathbf{b} = 0 \\ &\boldsymbol{\sigma} = \boldsymbol{\sigma}(\boldsymbol{\epsilon}) \\ &\boldsymbol{\epsilon} = \boldsymbol{\epsilon}(\mathbf{u}) \\ &\mathbf{u}(\mathbf{x}) = \mathbf{u}_d(\mathbf{x}) \qquad \mathbf{x} \in \Gamma_D \\ &\mathbf{n} \cdot \boldsymbol{\sigma} = \hat{\mathbf{t}} \qquad \mathbf{x} \in \Gamma_N \\ &g_N \geq 0 \qquad \mathbf{x} \in \Gamma_C \end{aligned} \tag{1}$$

where the displacements are represented by $\mathbf{u}$, the strain and stress tensors are $\boldsymbol{\epsilon}, \boldsymbol{\sigma}$ respectively, $\mathbf{D}$ is the linear elasticity constitutive relation and $\mathbf{b}$ denotes the volume forces. The boundaries of the analysis domains are divided in three non-overlapping regions $\{\Gamma_D, \Gamma_N, \Gamma_C\}$ where the Dirichlet, Neumann and contact constrains are imposed. The last constrain in (1) only accounts for the non-penetrability condition. Sliding contact can also be considered using frictional laws as the Coulomb model [1].

The use of the Finite Element method to obtain an approximated solution of (1) has become a standard. In this framework the *a posteriori* error estimation of the approximated solution can be very useful in different aspects like error-driven mesh adaptation or error estimations in quantities of interest. A complete study of such methods can be found in [2]. The first developments in *a posteriori* error estimators for contact problems were in the context of node-to-node formulations. For example, an h-adaptive refinement strategy was guided by a residual based estimator in [3] and a stress recovery estimator in [4]. A posteriori errors have also been developed to guide hp-adatpive refinements as in [5]. Since then, several error estimators have been proposed for contact problems involving non-matching meshes [6], using locally equilibrated fluxes [7] and mixed formulations [8] to cite some.

Zienkiewicz and Zhu [9] proposed the ZZ error estimator to estimate the disctretization error in energy norm, which is widely used within the FE community. The ZZ estimator can be formulated as:

$$\|\mathbf{e}_{es}\| = \int_{\Omega} \left(\boldsymbol{\sigma}^* - \boldsymbol{\sigma}^h\right)^t \mathbf{D}^{-1} \left(\boldsymbol{\sigma}^* - \boldsymbol{\sigma}^h\right) \, d\Omega \tag{2}$$

where Ω can be the whole analysis domain or a subdomain of it, $\boldsymbol{\sigma}^h$ is the FE stress field and $\boldsymbol{\sigma}^*$ is usually named as *smooth stress* or *recovered stress* field. The most

extended method to evaluate this field is the Superconvergent Patch Recovery, also developed by Zienkiewicz and Zhu [10], which is simple, robust and requires a considerably low computational cost. The ZZ estimator has been adapted to contact problems with different approaches. Some works in this direction are the use of the global version of the ZZ estimator for Coulomb's frictional contact [11] and the combination with multigrid methods in [12].

The Cartesian grid Finite Element Method (cgFEM) [13,14] is an immersed boundary method developed for solving 2D [13] and 3D [14] elasticity problems. The main characteristic of the method is the use of approximation meshes with regular quadrilaterals (2D) or hexaedrons (3D) that are independent of the domain. The cgFEM features an efficient hierarchical data structure based on the use of nested Cartesian grids together with a special numerical integration procedure that enables to capture the exact boundary definition through the use of NURBS. This method has been recently extended to solve 3D frictional contact problems [15] with a stabilized Lagrangian formulation in which the stabilization term is calculated with the SPR stress field. Moreover, the cgFEM features an h-adaptive refinement strategy based on the ZZ estimator and the SPR technique [16]. The accuracy of the ZZ estimator relies directly on that of the smooth field $\boldsymbol{\sigma}^*$ [9]. Therefore, in this work we aim to improve the accuracy of the smooth field $\boldsymbol{\sigma}^*$ for contact problems to serve as stabilization stress and to efficiently guide the h-adaptive refinement.

Upon the publication of the SPR technique, several attempts to enhance the accuracy of the recovered field were proposed. A thorough revision of the different modifications of the SPR is presented in [17]. The same work proposes the SPR with constrains (SPR-C), which is based in the enforcement of known equilibrium equations of the 2D elasticity problem at a patch level. This work represents an extension of the SPR-C technique in which the contact constrain is weakly imposed for 3D elastic contact problems. The paper is structured as follows: section 2 features a brief review of the SPR and SPR-C methods, and some special features regarding the use of cgFEM are presented. In section 3 the contact condition constrain is included in the SPR-C. Finally, section 4 shows how the performance of the technique with some numerical examples.

2. Superconvergent Patch Recovery with constrains: SPR-C

The idea behind the Superconvergent Patch Recovery [10] for computing the smooth field $\boldsymbol{\sigma}^*$ is the following: having a FE mesh, a recovery patch Ω_p^k is defined for each node k in the mesh, which is composed by all the elements containing the given node. Then, for each FE stress component σ_i^h a polynomial field $\sigma_i^{*,k}(\mathbf{x}) = \mathbf{p}(\mathbf{x})\ \mathbf{a}_i^k$ is fitted at Ω_p^k. The polynomial expansion $\mathbf{p}(\mathbf{x}) = \{1, x, y, z, ...\}$ is usually of the

same degree as the FE interpolation and the coefficients $\mathbf{a}_i^k$ are obtained solving a minimization problem:

$$\min \left[\sum_{g}^{\Omega_p^k} \left(\sigma_i^{*,k}(\mathbf{x}_g) - \sigma_i^h(\mathbf{x}_g) \right)^2 \right] \tag{3}$$

where g stands for all the integration points in Ω_p^k. After having all patches in the mesh solved, a smooth field $\boldsymbol{\sigma}^*$ is evaluated by the FE interpolation of the nodal recovered values $\sigma_i^{*,j}(\mathbf{x}_j)$ using the shape functions $N_j(\mathbf{x})$ associated to the j nodes of the element:

$$\sigma_i^*(\mathbf{x}) = \sum_j N_j(\mathbf{x}) \sigma_i^{*,j}(\mathbf{x}_j) \tag{4}$$

A straight-forward idea to enhance the accuracy of $\boldsymbol{\sigma}^{*,k}$ consists in considering known information of the exact solution of the elasticity problem in equation (3). Following this idea, the Superconvergent Patch Recovery with constrains (SPR-C, [17]) is a modified version where the fulfillment of the internal and boundary equilibrium, are enforced at each patch by means of adding constrains to equation (3). As these equations involve the six components of the stress tensor $\{\sigma_1^{*,k}, ..., \sigma_6^{*,k}\}$ this version requires the simultaneous solving of all stress components. Therefore the smooth stress field is now defined with the block matrix $\mathbf{P}(\mathbf{x})$ and the column vector $\mathbf{A}^k$, which are written as:

$$\begin{aligned} &\boldsymbol{\sigma}^{*,k}(\mathbf{x}) = \mathbf{P}(\mathbf{x}) \mathbf{A}^k \\ &\mathbf{P}(\mathbf{x}) = diag\left(\mathbf{p}(\mathbf{x}), ..., \mathbf{p}(\mathbf{x})\right) \ ; \qquad \mathbf{A}_k = \left\{\mathbf{a}_1^k, ..., \mathbf{a}_6^k\right\} \end{aligned} \tag{5}$$

Instead of the discrete approach of the standard SPR, an adaptation of the SPR-C technique to the X-FEM framework [18] considered a continuous formulation of the minimization problem (3). This approach provides better results for patches with different quadrature point densities in the elements, which is the case both in X-FEM and cgFEM [14], as the values at integration points are weighted [19]. Therefore, the modified minimization problem is the following:

$$\begin{aligned} &\min \left[\int_{\Omega_p^k} \left(\mathbf{P}(\mathbf{x}) \mathbf{A}^k - \boldsymbol{\sigma}^h \right)^2 d\Omega \right] \\ &\text{subject to } \mathbf{C}\mathbf{A}^k = \boldsymbol{\Lambda} \end{aligned} \tag{6}$$

where the additional constraints (to be defined later) have been included using a generic equation. Solving this problem applying Lagrange Multipliers we obtain the following linear system of equations expressed in matrix form:

$$\begin{bmatrix} \mathbf{M} & \mathbf{C}^T \\ \mathbf{C} & \mathbf{0} \end{bmatrix} \begin{Bmatrix} \mathbf{A}^k \\ \boldsymbol{\lambda} \end{Bmatrix} = \begin{Bmatrix} \mathbf{H} \\ \boldsymbol{\Lambda} \end{Bmatrix} \tag{7}$$

where

$$\mathbf{M} = 2 \int_{\Omega_p^k} \mathbf{P}(\mathbf{x})^T \, \mathbf{P}(\mathbf{x}) d\Omega \; ; \qquad \mathbf{H} = 2 \int_{\Omega_p^k} \mathbf{P}(\mathbf{x})^T \, \boldsymbol{\sigma}^h d\Omega \tag{8}$$

A numerical integration scheme is used to evaluate the SPR coefficient matrix and vector defined in equation (8), using the integration quadratures built for the FE analysis. Now we will define the constrain terms $\{\mathbf{C}, \boldsymbol{\Lambda}\}$ for the fulfillment of the internal equilibrium equation and the Neumann boundary equilibrium. The details of the Lagrange multipliers enforcement will be discussed in section 2.1.3 and the contact constrain will be presented in section 3.

The **internal equilibrium** equation corresponds to the first equation in (1), and identifying terms we obtain:

$$\nabla \cdot \mathbf{P}(\mathbf{x}) \; \mathbf{A}^k = -\mathbf{b}(\mathbf{x}) \qquad \Rightarrow \qquad \mathbf{C}^{iee} = \nabla \cdot \mathbf{P}(\mathbf{x}) \; ; \qquad \boldsymbol{\Lambda}^{iee} = -\mathbf{b}(\mathbf{x}); \qquad \mathbf{x} \in \Omega_p^k \tag{9}$$

The SPR-C is also able to enforce the tractions equilibrium at patches containing any loaded or free boundary Γ_p^k. In case of enforcing the **boundary equilibrium**, the following constraint contributions to matrix $\mathbf{C}$ and vector $\boldsymbol{\Lambda}$ are added to problem (7):

$$\mathbf{R}(\mathbf{x})\mathbf{P}(\mathbf{x}) \; \mathbf{A}^k - \mathbf{t}(\mathbf{x}) = \mathbf{0} \qquad \Rightarrow \qquad \mathbf{C}^{ext} = \mathbf{R}(\mathbf{x})\mathbf{P}(\mathbf{x}) \; ; \qquad \boldsymbol{\Lambda}^{ext} = \mathbf{t}(\mathbf{x}); \qquad \mathbf{x} \in \Gamma_p^k \tag{10}$$

where $\mathbf{R}(\mathbf{x})$ is an operator that obtains the tractions vector from the stress components using the normal vector to the surface, and $\mathbf{t}(\mathbf{x})$ are the applied tractions ($\mathbf{t}(\mathbf{x}) = \mathbf{0}$ for free surfaces).

Finally, the computation of $\boldsymbol{\sigma}^*$ is now performed by means of the *conjoint polynomials* technique proposed in [20]. This method, instead of interpolating the recovered nodal values, computes the recovered magnitude at any point $\mathbf{x}$ in an element by interpolating each SPR polynomial $\sigma_i^{*,j}(\mathbf{x})$ of the vertex nodes using the linear shape functions $N_j^v(\mathbf{x})$ associated to these nodes, such that:

$$\sigma_i^*(\mathbf{x}) = \sum_j N_j^v(\mathbf{x}) \sigma_i^{*,j}(\mathbf{x}) \tag{11}$$

Note that although obtaining local internal and boundary equilibrium in each patch, the process of interpolating a global smooth stress field introduces a lack of equilibrium of these constrains. As shown in ref. [21], if we evaluate the internal equilibrium for the smooth field $\boldsymbol{\sigma}^*$ taking into account equation (11) we obtain:

$$\nabla\boldsymbol{\sigma}^*(\mathbf{x}) = \sum_j \nabla N_j^v(\mathbf{x})\boldsymbol{\sigma}_j^* + \sum_j N_j^v(\mathbf{x})\nabla\boldsymbol{\sigma}_j^* \tag{12}$$

Considering the constraint in equation (9) and the partition of unity property of the shape functions, the second sum in equation (12) is equivalent to the volumetric forces $\mathbf{b}(\mathbf{x})$. Therefore the internal equilibrium of the smooth field results in:

$$\nabla\boldsymbol{\sigma}^*(\mathbf{x}) + \mathbf{b}(\mathbf{x}) = \mathbf{S}(\mathbf{x}) \neq 0 \tag{13}$$

where $\mathbf{S}(\mathbf{x}) \neq 0$ represents the lack of equilibrium. Ref. [22] proved that this term can be used to obtain accurate asymptotic upper error bounds of the FE solution using recovery techniques. It is straight forward to obtain a similar term related to the boundary equilibrium in equation (10).

2.1. cgFEM 3D features regarding SPR-C

In the cgFEM the mesh is independent of the domain. Thus, there are some nodes outside the domain at the elements cut by the geometry (called boundary elements from now on) as well as elements completely inside the domain (internal elements). We can also distinguish between internal and boundary patches: internal patches contain only internal elements whereas boundary patches are those containing at least one boundary element. The internal equilibrium constrain will be enforced at both internal and boundary patches. Boundary patches cut by the Neumann boundary will also include the boundary equilibrium constrain. In this section we will detail the enforcement of such constrains and show some features that improve the efficiency of the SPR technique within the cgFEM.

2.1.1. Boundary patch enlargement

The arbitrary intersection between the Cartesian grids and the analysis domain may produce some elements with a low volume of material inside, as in the example shown in Figure 1a. In that case the stiffness associated to the external node colored in red becomes very small, which results in an ill-conditioning of the FE formulation [23] and also a poor quality of the FE stress field computed at those *pathological* elements. In the classical SPR procedure the patch Ω_p^k associated to the red node in Figure 1a would consist only in that pathological element. So, the smooth field $\boldsymbol{\sigma}^*$ would, eventually, have a lower quality in that region. In order to avoid these situations we measure the ratio between material and element volume for each boundary patch (all internal patches will have a 100% ratio). If the patch volume ratio is under a

certain threshold, the patch is enlarged by including the adjacent elements, as shown in Figure 1b. All the tests in this paper were carried out with a threshold value of 25%, with acceptable results.

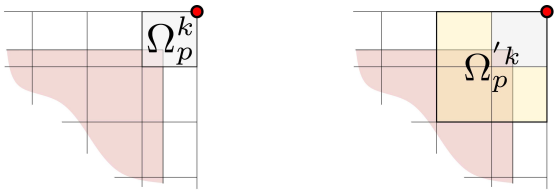

(a) Original patch (b) Enlarged patch

Figure 1: Example of boundary patch enlargement. The patch Ω_p^k associated to the red node has a low material/element volume ratio. Hence a bigger patch $\Omega_p^{'k}$ that also includes the surrounding elements is considered.

2.1.2. Patch coding

In order to reduce numerical problems while solving equation (7) a normalized local coordinate system centred at the patch node is used instead. Therefore, for a given node with coordinates $\mathbf{x}_N$, the local coordinate system built for its recovery patch is defined as:

$$\mathbf{x}_{local} = \frac{\mathbf{x} - \mathbf{x}_N}{h_p} \tag{14}$$

where h_p is a representative size of the patch, e.g. the biggest element size in the patch. Taking into account this variable change, the coefficient matrix $\mathbf{M}$ in equation (7) only depends on the relative position of the integration points inside the patch. This implies that patches with the same shape will share the coefficient matrix, and only one matrix inversion for each different patch topology is needed to calculate the SPR coefficients.

Only one level difference is allowed between adjacent elements in cgFEM h-adapted meshes. Hence, since all the elements in the cgFEM are quadrilaterals/hexahedrons there is a finite number of internal patch topologies. Figure 2a shows all possible patch configurations that exist in a 2D cgFEM mesh.

However, there are still hundreds of possible patch topologies in a cgFEM 3D mesh (some examples are shown in Figure 2b). Instead of manually coding all the configurations we have designed an efficient automatic coding of the patches based on the relative size of the elements within the patch. Then, given a FE mesh, all internal patch topologies in the mesh are detected, and the coefficient matrix $\mathbf{M}$ is evaluated and inverted once only for the present topologies. Figure 3 shows an example of the automatic coding for 2D patches. The bigger element in the patch is defined as

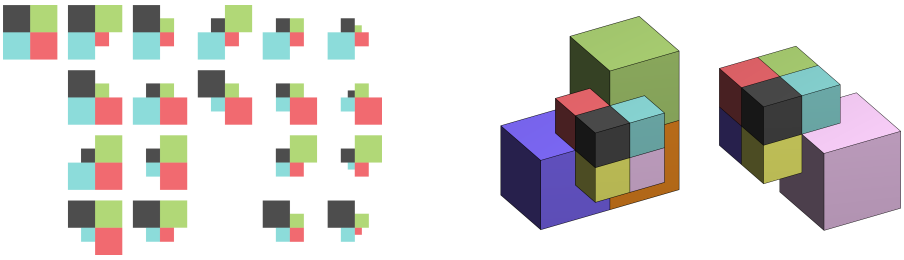

(a) (b)

Figure 2: Patch topologies that can appear in a cgFEM analysis. All 19 possible configurations for cgFEM 2D (a), and examples of possible configurations for cgFEM 3D (b).

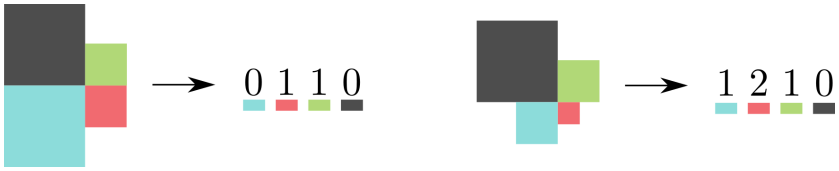

Figure 3: 2D example of SPR patch coding. The patch on the left has code number 0110 and the patch on the right is number 1210.

level 0 and smaller elements have increasing values. A decimal number for the patch topology is obtained by concatenating all levels in the patch (4 digits for 2D patches, 8 digits for 3D patches).

Despite not being compact, this coding avoids manual classification and coding of all possible 3D patches that may exist in a cgFEM 3D analysis. With this procedure the computational cost of the recovery process for the internal patches can be neglected if compared with the evaluation at boundary patches, as these must be solved individually. This could be seen as a $(d-1)$-dimensional computational cost associated to the recovery procedure.

2.1.3. SPR-C constraints enforcement

The recovered field $\boldsymbol{\sigma}^*$ cannot satisfy the enforced equilibrium equations for all points in the domain (or boundary) in the general case. For instance, if $\boldsymbol{\sigma}^*$ is a polynomial of degree 2 the internal equilibrium equation (9) is only fulfilled for linear volumetric forces $\mathbf{b}(\mathbf{x})$. Similarly, it is not possible to strongly enforce the boundary equilibrium for generic tractions and/or curved boundaries. A possible alternative is the strong enforcement of the constrain equations at a set of points in the patch to provide a number of linearly independent equations equal to the number of constrains. However, the location of such points in 3D results to be arbitrary and cumbersome.

We propose the weak enforcement of the equilibrium constrains using a pseudoinverse approach. For the case of the internal equilibrium, equation (9) is now written as the following numerical integration, where the subscript g denotes each quadrature point:

$$\sum_g \nabla \cdot \mathbf{P}(\mathbf{x}_g) w_g \mathbf{A}^k = -\sum_g \mathbf{b}(\mathbf{x}_g) w_g \tag{15}$$

with the quadrature weights w_g. Matrix $\mathbf{C}^{iee}$ and a vector $\mathbf{\Lambda}^{iee}$ are built such that each row represents the enforced constrain (15) written as $\mathbf{C}_g^{iee}\mathbf{A}_k = \mathbf{\Lambda}_g^{iee}$ for each quadrature point $\mathbf{x}_g \in \Omega_p^k$. Then the set of linearly independent columns $\mathbf{C}^{*iee}$ is selected from the constraint matrix, and the constrain block of equations included in problem (6) is:

$$\mathbf{C}^{*iee'}\mathbf{C}^{iee}\mathbf{A}_k = \mathbf{C}^{*iee'}\mathbf{\Lambda}^{iee} \tag{16}$$

This generic approach is applied independently for any type of constrain included in problem (6), then the resulting blocks of constrain equations are concatenated to form $\mathbf{C}, \mathbf{\Lambda}$ in the system (7). For example, a boundary patch that contains a loaded surface will have the following blocks of constrain equations:

$$\mathbf{C} = \begin{Bmatrix} \mathbf{C}^{*iee'}\mathbf{C}^{iee} \\ \mathbf{C}^{*ext'}\mathbf{C}^{ext} \end{Bmatrix} \; ; \qquad \mathbf{\Lambda} = \begin{Bmatrix} \mathbf{C}^{*iee'}\mathbf{\Lambda}^{iee} \\ \mathbf{C}^{*ext'}\mathbf{\Lambda}^{ext} \end{Bmatrix} \tag{17}$$

3. Contact condition constrain

Consider two elastic bodies $\Omega^{(1)}$ and $\Omega^{(2)}$ becoming in contact, and let $\Gamma_C^{(i)} \equiv \partial\Omega^{(i)},\ i = 1, 2$ be the fraction of the boundary that is likely to come into contact. When both solids are in equilibrium the deformed boundary $\Gamma_C^{(i)_d}$ will comprise all point pairs from both bodies that are actually in contact. The stress distribution corresponding to the exact solution must fulfil the equilibrium equation over the contact boundary $\Gamma_C^{(i)_d}$, this is:

$$\mathbf{t}^{(1)}(\mathbf{x}) + \mathbf{t}^{(2)}(\mathbf{x}) = \mathbf{0} \tag{18}$$

where, similarly to the boundary equilibrium, $\mathbf{t}^{(i)}(\mathbf{x})$ are given by

$$\mathbf{R}^{(i)}(\mathbf{x})\mathbf{P}^{(i)}(\mathbf{x})\ \mathbf{A}^{(i)} = \mathbf{t}^{(i)}(\mathbf{x})\ , \qquad \forall \mathbf{x} \in \Gamma_C^{(i)_d}\ , \qquad i = 1, 2 \tag{19}$$

therefore we can rewrite the equilibrium equation at the contact boundary as:

$$\mathbf{R}^{(1)}(\mathbf{x})\mathbf{P}^{(1)}(\mathbf{x})\ \mathbf{A}^{(1)} + \mathbf{R}^{(2)}(\mathbf{x})\mathbf{P}^{(2)}(\mathbf{x})\ \mathbf{A}^{(2)} = \mathbf{0} \tag{20}$$

Note that the coefficients $\mathbf{A}^{(i)}$ of the SPR are defined at nodes of each FE mesh. However, the meshes are non-conforming when solving the contact problem within the cgFEM, and the association between the nodes of both bodies in contact is unclear. Our approach is the following: we define a *main* body (e.g $\Omega^{(1)}$) where the SPR-C will be performed, and the *auxiliary* body in contact (e.g. $\Omega^{(2)}$). For a patch at the main body with active contact points in it we associate a region of the auxiliary body, we define another SPR-C problem at the auxiliary region and couple both problems with equation (20). Finally the system of equations that will be solved for a patch at the main body is an expansion of equation (7):

$$\begin{bmatrix} \mathbf{M}^{(1)} & \mathbf{C}^{(1)T} & \mathbf{0} & & \mathbf{C}^{cont\ T} \\ \mathbf{C}^{(1)} & \mathbf{0} & & & \\ & \mathbf{0} & \mathbf{M}^{(2)} & \mathbf{C}^{(2)T} & \\ & & \mathbf{C}^{(2)} & \mathbf{0} & \\ & \mathbf{C}^{cont} & & & \mathbf{0} \end{bmatrix} \begin{Bmatrix} \mathbf{A}^{(1)} \\ \boldsymbol{\lambda}^{(1)} \\ \mathbf{A}^{*(2)} \\ \boldsymbol{\lambda}^{(2)} \\ \boldsymbol{\lambda}^{cont} \end{Bmatrix} = \begin{Bmatrix} \mathbf{H}^{(1)} \\ \boldsymbol{\Lambda}^{(1)} \\ \mathbf{H}^{(2)} \\ \boldsymbol{\Lambda}^{(2)} \\ \mathbf{0} \end{Bmatrix} \tag{21}$$

where the block in red corresponds to the stress field at the main body, the green block corresponds to the stress field at the auxiliary domain, and the contact constraint $\mathbf{C}^{cont}$ enforces the continuity of both fields over the contact interface. As the problem considered for the auxiliary body is not associated with a particular node of its mesh, the coefficients $\mathbf{A}^{*(2)}$ cannot be used to create a recovered stress field. Therefore, when solving the system in (21) we obtain two sets of coefficients, $\mathbf{A}^{(1)}$ and $\mathbf{A}^{*(2)}$, but only those regarding the *main* body are considered for the evaluation of the smooth stress field. An analogous procedure exchanging the *main* and *auxiliary* roles is followed to obtain the coefficients $\mathbf{A}^{(2)}$. With these considerations the recovered stress fields will not fulfill equation (20) at each patch, which we find assumable since the calculation of the smooth stress $\boldsymbol{\sigma}^*$ already introduces a lack of equilibrium (shown in section 2).

Once the equilibrium equation at the contact surface has been presented, we need to define a procedure to assign an auxiliary domain within the *auxiliary* body to each patch of the *main* body. One possible approach is shown in Figure 4. The contact zone is defined over the *main* body, which is approximated by means of the minimum-area convex polygon that encompasses all the contact points in the patch (Figure 4a). The auxiliary region is obtained projecting that contact area towards the interior of the auxiliary body following the normal direction to the deformed surface. This direction is calculated as the weighted arithmetic mean of the normal vector to the deformed surface at the active contact points (Figure 4b). The values used to weight the vectors are those of the surface numerical integration. Finally, we must establish the depth of the auxiliary region. In this regard, we extend the projection considering the volume of the *auxiliary* body included in the contour elements (Figure 4c). With this procedure we obtain an auxiliary region with enough information to get a representative stress distribution after applying the smoothing technique.

Let us consider a contact problem in 2D solved with Cartesian elements having 4 vertex nodes like that presented in Figure 5. The procedure to obtain the recovered stress fields at a given element K located on this contour involves solving four different

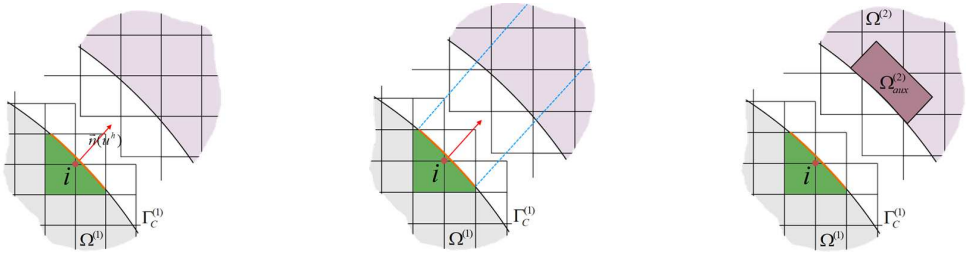

(a) SPR patch with active contact condition. The contact area is depicted in red.

(b) Projection of the contact area towards the supporting body following an averaged normal vector.

(c) The boundary elements inside the projection define the auxiliary domain.

Figure 4: Definition of the auxiliary domain for the evaluation of the recovered stress field.

patches. All of them contain points in contact and, therefore, an auxiliary region must be associated for the solution of SPR-C patches $i_1, ..., i_4$. These auxiliary domains depend only on the boundary elements contained in each patch and, since each element is usually contained in several patches, the auxiliary domains will be overlapped. To eliminate redundant calculations, we propose an alternative approach which splits the procedure to define the auxiliary domains into two stages. First, we evaluate the portion of the *auxiliary* body associated to each element cut by the contact zone. Then, the auxiliary domain of the patch is built as the union of the auxiliary domains of the elements in the patch.

4. Numerical examples

In this section three contact problems are solved to test the proposed recovery procedure. The quality of the presented SPR-C with contact constrains is evaluated in different aspects like the equilibrium of the contact tractions between bodies, the effectivity of the error estimator and the suitability for h-adaptive refinement.

4.1. Example 1. Contact test between elastic solids

An analysis of the differences between the recovered field calculation with and without contact constrains is performed in the following problem of two elastic solids in contact. A 2D sketch of the problem is shown in Figure 6 left. At the initial

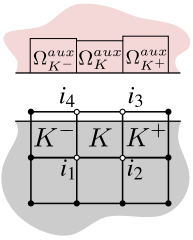

(a) Assignment of auxiliary regions at element level

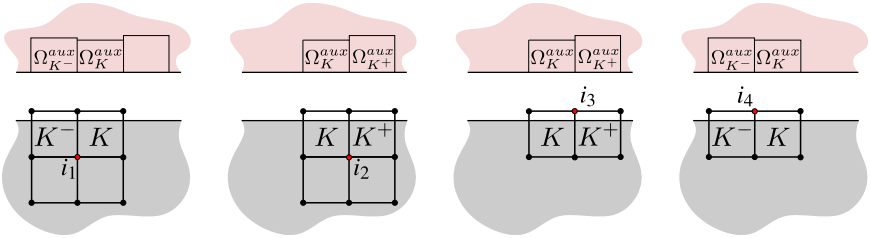

(b) Auxiliary regions associated to the vertex nodes of the element K

Figure 5: Auxiliary region assignment for SPR-C patches.

configuration both contact surfaces are overlapping (there is no such space between solids), and vertical displacement $d = -1.6 \cdot 10^{-6} m$ is applied on the upper face of body 2. Symmetry conditions are applied to the faces parallel to the yz plane, and displacements along y direction are constrained in a point to avoid rigid body motions. Two lateral faces of body 1 are loaded with $p_y = 4 \cdot 10^{11}(0.01 - z)z\ Pa$ and $p_z = 10 \cdot 10^{11}(0.01 - z)z\ Pa$. The material properties, common for both solids, are $E = 115GPa$ and $\nu = 0.3$. Three non-conforming uniformly h-refined meshes (Figure 6) were solved in the analysis, using the standard recovery technique (SPR) and the constrained version including contact constrains (SPR-C). We also considered a reference solution coming from a 2D overkilled mesh analysis.

The contact pressure $p_N = \mathbf{n} \cdot \boldsymbol{\sigma}^* \cdot \mathbf{n}$ evaluated at a path along x direction is shown in Figure 7a for the upper solid. An improvement of the recovered field can be appreciated in two different aspects. First, the maximum contact pressure estimation is much closer to the reference values. Furthermore, the enforcement of boundary equilibrium also ensures null normal tractions over non-contact regions. The results show that both effects have a higher impact on the recovered field as the mesh is coarser.

As a consequence of these improvements, it might be seen that there is a better estimation of the end-of-contact area. However, is not possible to provide with accurate estimates of the end-of-contact point (line in 3D) using regular polynomials for the recovered stress field given the regularity of the exact solution. Although there is a considerably enhanced estimation of the stress gradient, the location of this area

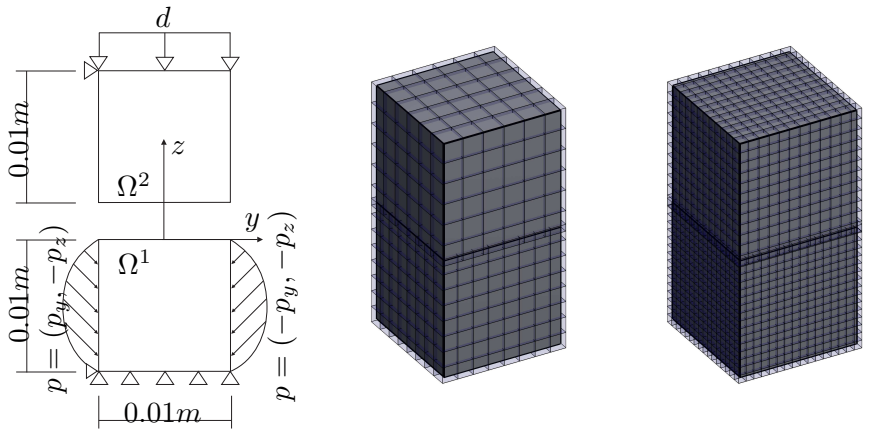

Figure 6: Example 1. Sketch of the problem and two analysis meshes. A third mesh obtained by dividing the right-most mesh was also used in the analysis.

is still highly influenced by the mesh. This is illustrated with the results shown in Figure 7b. The contact pressure is evaluated at both bodies and the difference is normalized with respect to the maximum contact pressure obtained at the reference solution ($9.49MPa$). The vertical discontinuous lines represent the end-of-contact points for the reference solution. Note that the addition of contact constrains in the SPR-C results in a considerably lower lack of equilibrium inside the contact area. However, there is no such improvement in the end-of-contact area. As the analysis meshes are non-conforming the recovery process estimates these areas at a different location for each body, thus locally increasing the lack of equilibrium. The results also show that this local error is alleviated with the h-refinement of the meshes.

Note that the ZZ-estimator (2) becomes the exact error in energy norm $\|\mathbf{e}_{ex}\|$ if the considered problem had an analytical solution (which is usually not available). In that case, we can define the effectivity index Θ of the error estimator as $\Theta = \|\mathbf{e}_{es}\| \,/\, \|\mathbf{e}_{ex}\|$. A good error estimator should converge to $\Theta = 1$ as the mesh is refined. Figure 8 shows the effectivity of the ZZ-estimator in this problem using the standard SPR and the proposed SPR-C, assuming the overkilled solution as reference. Although the error estimator is evaluated at all the domain there is a substantial improvement in the effectivity values, especially for coarse meshes. In order to evaluate the local improvement of the estimator around the contact area, the integrand of equation (2) is evaluated at the quadrature points on the contact surface of the lower body calculating the smooth field $\boldsymbol{\sigma}^*$ with SPR, SPR-C and the reference solution. This comparison allows to qualitatively evaluate the accuracy of the recovered field on the contact area. Results show that the SPR-C estimator detects error due to the end-of-contact and free surface areas, whereas the SPR based estimator is not able to

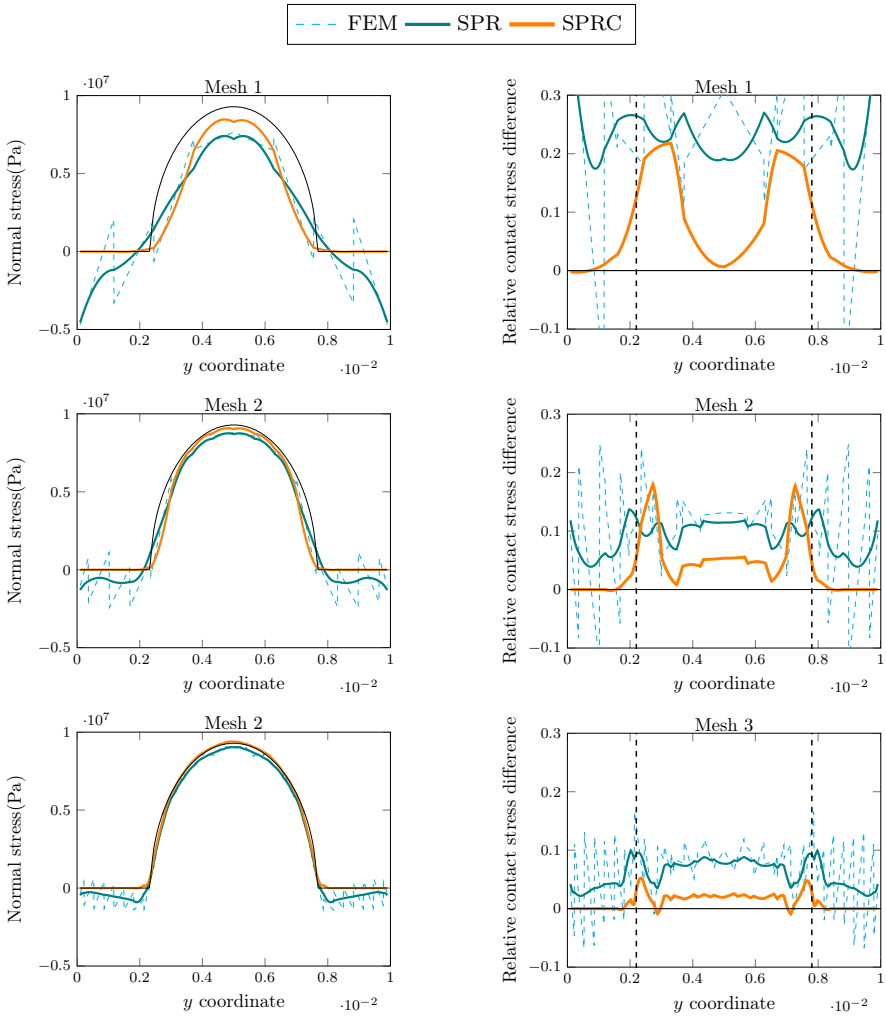

(a) Distribution of the normal stress evaluated at the upper body. Positive values of the stress stand for compression.

(b) Contact stress difference between the two bodies ($\sigma^2\mathbf{n}^2 - \sigma^1\mathbf{n}^1$). Values are normalized with the reference maximum contact stress. The contact area lies between the vertical discontinuous lines.

Figure 7: Example 1. Evolution of the different magnitudes along a path that follows the y direction

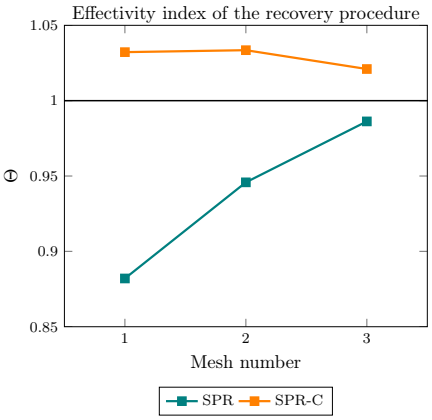

Figure 8: Example 1. Effectivity of the error estimation using SPR and SPR-C taking the overkilled mesh solution as reference.

capture those errors. It can also be seen that the error in the end-of-contact area is underestimated by the SPR-C.

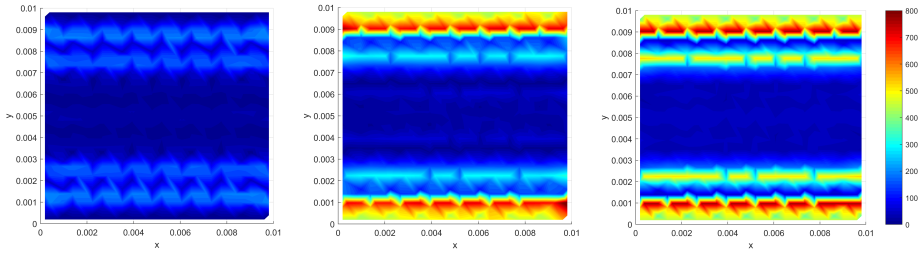

(a) $\boldsymbol{\sigma}^*_{SPR} - \boldsymbol{\sigma}^h$ (b) $\boldsymbol{\sigma}^*_{SPR-C} - \boldsymbol{\sigma}^h$ (c) $\boldsymbol{\sigma} - \boldsymbol{\sigma}^h$

Figure 9: Example 1. Evaluation of the error estimation integrand $\left(\boldsymbol{\sigma}^* - \boldsymbol{\sigma}^h\right) \mathbf{D}^{-1} \left(\boldsymbol{\sigma}^* - \boldsymbol{\sigma}^h\right)$ over the contact surface at the lower body using different stress fields. Results correspond to the first analysis mesh.

4.2. Example 2. Cylinder-plane contact

In the second example a block with cylindrical surface becomes in contact with a plain block. The geometric model of the problem is depicted in Figure 10a, with the dimensions $L = 4mm$ and $R = 50mm$. A linear elastic material is used for both bodies with properties $E = 115GPa$ and $\nu = 0.32$. A vertical displacement $d = -1.77e-05$

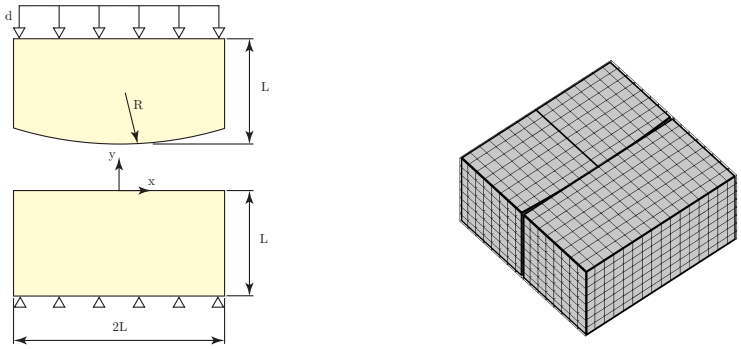

(a) (b)

Figure 10: Example 2. (a) Geometry model for the cylinder-plane contact problem. (b) Initial analysis mesh, containing 8262 degrees of freedom.

is applied on the upper face of the cylindric body and vertical displacements are constrained on the lower face of the plain block.

Symmetry conditions are applied on the surfaces perpendicular to the z axis and rigid body motions are properly constrained along x. Both bodies are initially meshed with non-conforming uniform grids of size $h \approx 0.5mm$ as shown in Figure 10b. Two different analysis are compared in this example. First a sequence of three uniformly h-refined are solved, with the finest containing 135045 degrees of freedom. In the second test an automatic h-adaptive refinement procedure based on the ZZ-error estimator is used [24], and the SPR-C presented in this work is used as the smooth stress field. Figure 11 shows the sequence of meshes obtained with this procedure for the cylinder body. Similar meshes are obtained on the other body in the analysis. It is worth to remark that the refinement algorithm automatically adapts the mesh around the end-of-contact area, where the highest gradient of the solution arises. A 2D overkilled solution has been solved again to serve as a reference and compare the error of both strategies. Tho conclusions can be extracted from the results of Figure 12. First, the optimal convergence rate is obtained for the uniform refinement analysis, and secondly the automatic adaptive refinement strategy is more efficient in the sense that it can provide similar accuracy results with approximately a quarter of the DOFs in this particular problem.

Finally, the effectivity of the ZZ-error estimator is compared again between the use of SPR and SPR-C. The effectivity index Θ presented in the previous example can also be calculated element-by-element to have for a local assesment of the quality of the estimator. However, this index does not provide clear representations of the recovery performance because the values are not balanced, this is, "underestimation"

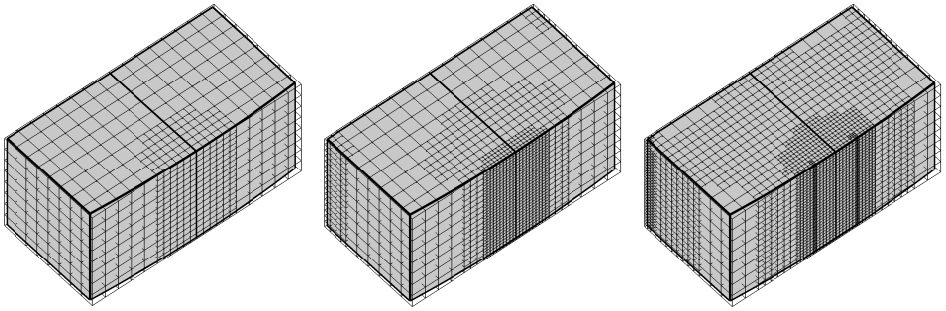

(a) 15468 DOF (b) 46140 DOF (c) 135045 DOF

Figure 11: Example 2. Sequence of three meshes obtained through error-based h-adaptive refinement. Detail of body 2. For each mesh the DOF number of the complete problem is shown.

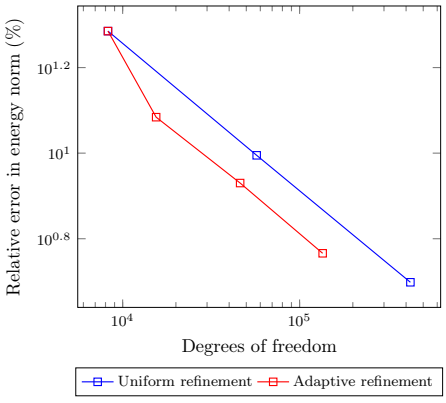

Figure 12: Example 2. Comparison of the error in energy norm with uniform and adaptive h-refinement using SPR-C in the ZZ-estimator.

efficiencies range between $(0, 1]$ and "overestimation" efficiencies are in the $(1, +\infty]$ range. To overcome this issue, the *local effectivity* index is defined as:

$$\begin{cases} D = \Theta - 1 \ ; & \Theta \geq 1 \\ D = 1 - \dfrac{1}{\Theta}; & \Theta < 1 \end{cases} \tag{22}$$

Using the last mesh of the adaptive refinement sequence we have compared the accuracy of the SPR and SPR-C by means of the local effectivity index D. This index is evaluated in Figure 13 at the elements cut by the cylinder surface, where we can distinguish the contact area where the elements are more refined. In the color map a red color denotes overestimation of the error and blue colors indicate underestimation of the error. It is clearly seen that the SPR without constrains underestimates the error around the end-of-contact area, whereas the SPR-C has an overall better performance on the contact area. It is also worth to remark that the performance of the estimator is considerably deteriorated far from the contact zone because the discretization is coarser, and the discretization is coarse due to the low strain energy in the area.

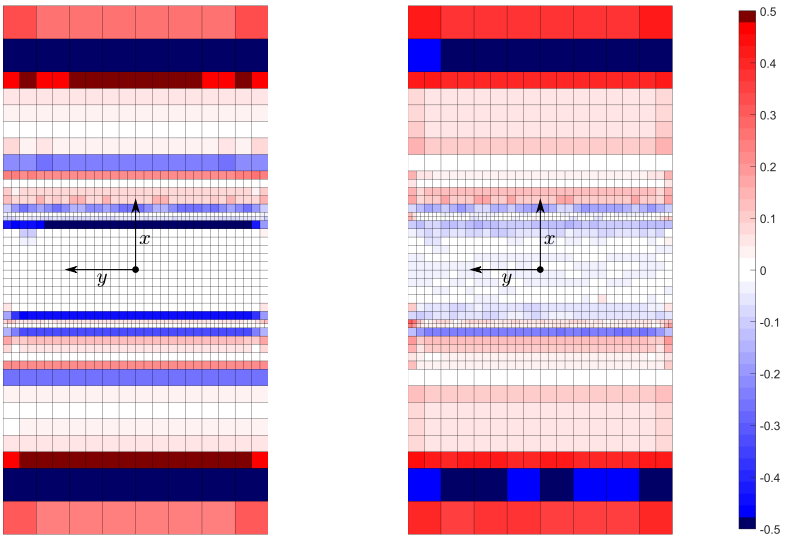

(a) (b)

Figure 13: Example 2. Color map of the local effectivity D evaluated at the contact surface for the finest h-adapted mesh using SPR (a) and SPR-C (b).

4.3. Example 3. Frictional contact between curved surfaces

In this example a frictional contact problem involving curved surfaces is solved. Both solids have a toroidal shape with the same geometrical parameters, major and minor radius of $R = 1.5cm$ and $r = 0.5cm$ respectively. The initial configuration of the problem is shown in Figure 14a, where the blue colored surfaces are clamped and a constant displacement along y direction of $0.05cm$ is applied on the orange colored surfaces. The problem is solved considering a Coulomb frictional model with a friction coefficient of $\mu = 1$ and linear elastic material with $E = 115GPa, \nu = 0.3$. We have conducted again two different h-refinement strategies in this example, the uniform and the automatic adaptive using the ZZ-error estimator and the SPR-C smoothed stress. The error estimation results, presented in Figure 15, show that the FE convergence rate is kept once again for the unform refinement and that the adaptive strategy is more efficient in terms of computational cost for a prescribed error.

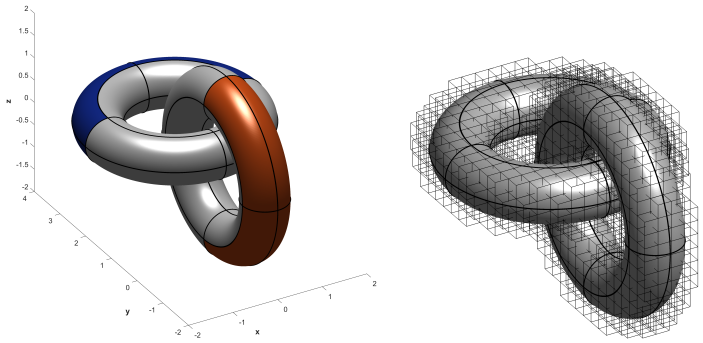

(a) Problem scheme (b) Analysis mesh

Figure 14: Example 3. Model of the contact problem between curved solids. Lengths in cm. Surfaces in blue are clamped, and a constant displacement $u_y = -0.05cm$ is applied on the orange surfaces. The initial mesh is a non-conforming uniform grid with element size of $h \approx 0.25cm$ for both bodies.

Figure 16 shows a detail around the contact area in one of the bodies for all the discretization meshes in the refinement sequence. In order to highlight the discretization of the surface, only the intersection cuts between the Cartesian grid and the surface are shown. Note that the mesh is again automatically refined around the contact area, which in this case has a circular shape. The contact area can be distinguished in Figure 16, which represents the values of the normal component of the surface tractions, $(\mathbf{n} \cdot \boldsymbol{\sigma})\mathbf{n}$, using the FE stress field and the smooth stress obtained with the SPR-C. The negative values represent compression stress, and the color map has been modified so that positive values of normal traction, which are physically unfeasible since the surfaces are not loaded, are represented in black. It can be seen that be-

sides smoothing the FE stress field, which is discontinuous, the positive tractions are removed on the recovered solution thanks to the additional constrains of the SPR-C.

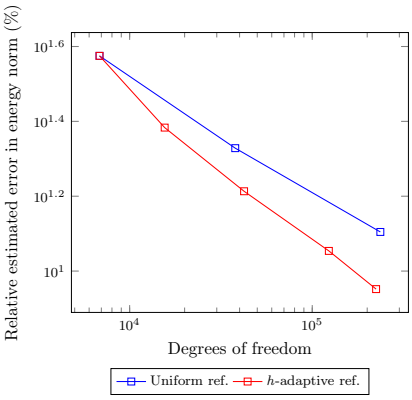

Figure 15: Example 3. Comparison of the error in energy norm with uniform and adaptive h-refinement using the ZZ-estimator and the SPR-C smooth stress field.

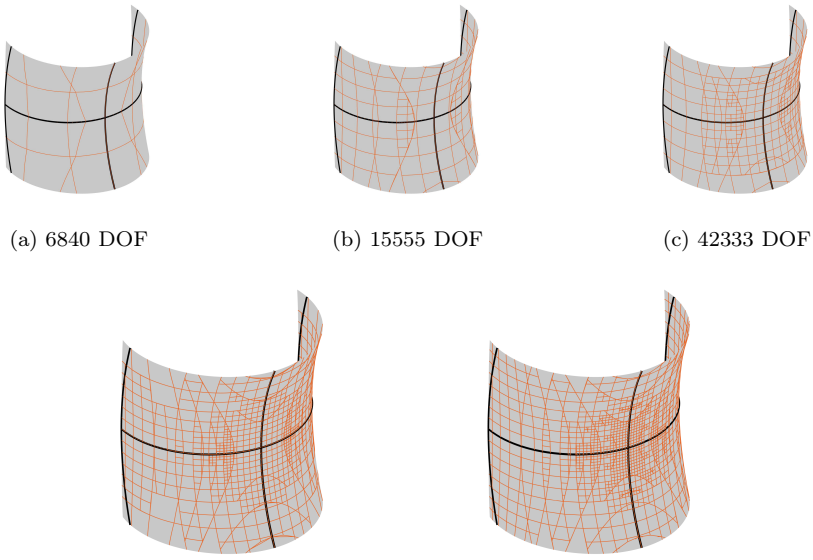

(a) 6840 DOF (b) 15555 DOF (c) 42333 DOF

(d) 123306 DOF (e) 223743 DOF

Figure 16: Example 3. Sequence of five meshes obtained through error-based h-adaptive refinement. Detail of the intersection between the discretization mesh and geometry around the contact area.

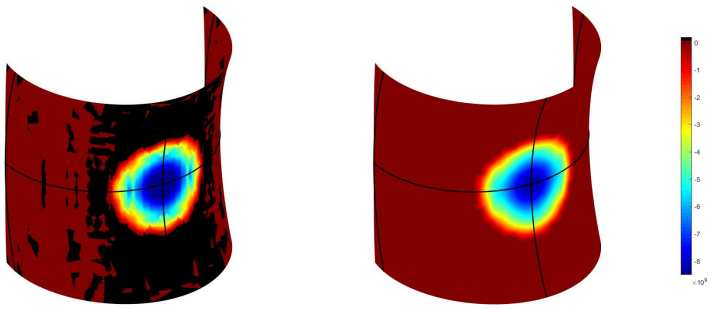

Figure 17: Example 3. Surface normal tractions $(\mathbf{n} \cdot \boldsymbol{\sigma})\mathbf{n}$ using the FE solution (left) and the smooth stress obtained with the SPR-C (right) for the last h-adapted mesh. Negative values represent compression stress. Positive values (physically unfeasible) are colored in black.

5. Conclusions

We have presented a modified version of the constrained Superconvergent Patch Recovery (SPR-C) that includes the boundary equilibrium at the contact area for frictionless and friction problems. For each patch containing active contact points, an auxiliary SPR problem with information of both contacting bodies is used. The constrains are enforced in a weak sense to avoid ill-conditioning of the systems to solve at each SPR patch. The non-conforming nature of the meshes in the cgFEM prevents the direct coupling of SPR patches between bodies in contact. However, the results show that the contact pressure equilibrium is greatly improved with the SPR-C, especially inside those elements completely contained within the contact zone. The use of polynomials to build the recovered stress field prevents to capture the pressure discontinuity that appears at the end of the contact area. Nevertheless, the accuracy of the resulting contact stress distribution is clearly enhanced when the SPR-C technique is considered.

The numerical examples show that the definition of the smooth field $\boldsymbol{\sigma}^*$ and the effectivity of the ZZ estimator are clearly improved when including the contact boundary equilibrium in the SPR-C. Finally, we have combined the ZZ estimator with an automatic h-adaptive refinement procedure that increases the efficiency of 3D contact problems resolution requiring fewer degrees of freedom to reach a prescribed error level. The h-adaptive procedure guided by the accurate recovery-based error estimator is able to locate the limit of the contact area and adequately refine the mesh in these regions, providing a better spatial discretisation to capture the end of the contact zone.

Acknowledgements

The authors want to thank Generalitat Valenciana (PROMETEO/2016/007), the Spanish Ministerio de Economía, Industria y Competitividad (DPI2017-89816-R), the Spanish Ministerio de Ciencia, Innovación y Universidades (FPU17/03993) and Universitat Politècnica de València (FPI2015) for the financial support to this work.

References

[1] P. Wriggers, *Computational contact mechanics, second ed., Springer*. 2006.

[2] M. Ainsworth and J. T. Oden, *A posteriori error estimation in finite element analysis*. Wiley, 2000.

[3] P. Wriggers and O. Scherf, "Adaptive finite element techniques for frictional contact problems involving large elastic strains," *Computer Methods in Applied Mechanics and Engineering*, vol. 151, no. 3-4, pp. 593–603, 1998.

[4] P. Wriggers and O. Scherf, "Different a Posteriori error estimators and indicators for contact problems," *Mathematical and Computer Modelling*, vol. 28, no. 4-8, pp. 437–447, 1998.

[5] C. Lee and J. Oden, "A posteriori error estimation of h-p finite element approximations of frictional contact problems," *Computer Methods in Applied Mechanics and Engineering*, vol. 113, pp. 11–45, mar 1994.

[6] P. Coorevits, P. Hild, and J.-P. Pelle, "A posteriori error estimation for unilateral contact with matching and non-matching meshes," *Computer Methods in Applied Mechanics and Engineering*, vol. 186, pp. 65–83, may 2000.

[7] B. I. Wohlmuth, "An a Posteriori Error Estimator for Two-Body Contact Problems on Non-Matching Meshes," *J Sci Comput*, vol. 33, pp. 25–45, 2007.

[8] F. Kuss and F. Lebon, "Error estimation and mesh adaptation for Signorini–Coulomb problems using E-FEM," *Computers & Structures*, vol. 89, pp. 1148–1154, jun 2011.

[9] O. C. Zienkiewicz and J. Z. Zhu, "A simple error estimator and adaptive procedure for practical engineerng analysis," *International Journal for Numerical Methods in Engineering*, vol. 24, no. January 1986, pp. 337–357, 1987.

[10] O. C. Zienkiewicz and J. Z. Zhu, "The superconvergent patch recovery and a posteriori error estimates. Part 1: The recovery technique," *International Journal for Numerical Methods in Engineering*, 1992.

[11] A. Becheur, A. Tahakourt, and P. Coorevits, "An a posteriori error indicator for Coulomb's frictional contact," *Mechanics Research Communications*, vol. 35, pp. 562–575, dec 2008.

[12] H. Liu, I. Ramière, and F. Lebon, "On the coupling of local multilevel mesh refinement and ZZ methods for unilateral frictional contact problems in elastostatics," *Computer Methods in Applied Mechanics and Engineering*, vol. 323, pp. 1–26, aug 2017.

[13] E. Nadal, J. J. Ródenas, J. Albelda, M. Tur, J. E. Tarancón, and F. J. Fuenmayor, "Efficient Finite Element Methodology Based on Cartesian Grids: Application to Structural Shape Optimization," *Abstract and Applied Analysis*, vol. 2013, pp. 1–19, apr 2013.

[14] O. Marco, R. Sevilla, Y. Zhang, J. J. Ródenas, and M. Tur, "Exact 3D boundary representation in finite element analysis based on Cartesian grids independent of the geometry," *International Journal for Numerical Methods in Engineering*, vol. 103, pp. 445–468, aug 2015.

[15] J. M. Navarro-Jiménez, M. Tur, J. Albelda, and J. J. Ródenas, "Large deformation frictional contact analysis with immersed boundary method," *Computational Mechanics*, vol. 62, pp. 853–870, oct 2018.

[16] O. Marco, J. Ródenas, J. Navarro-Jiménez, and M. Tur, "Robust h-adaptive meshing strategy considering exact arbitrary CAD geometries in a Cartesian grid framework," *Computers and Structures*, vol. 193, 2017.

[17] J. J. Ródenas, M. Tur, F. J. Fuenmayor, and A. Vercher, "Improvement of the superconvergent patch recovery technique by the use of constraint equations: The SPR-C technique," *International Journal for Numerical Methods in Engineering*, vol. 70, no. October 2006, pp. 705–727, 2007.

[18] J. Ródenas, O. González-Estrada, P. Díez, and F. Fuenmayor, "Accurate recovery-based upper error bounds for the extended finite element framework," *Computer Methods in Applied Mechanics and Engineering*, vol. 199, pp. 2607–2621, aug 2010.

[19] E. Nadal Soriano, *Cartesian grid FEM (cgFEM): High performance h-adaptive FE analysis with efficient error control. Application to structural shape optimization.* PhD thesis, Universitat Politècnica de València, Valencia (Spain), jan 2014.

[20] T. Blacker and T. Belytschko, "Superconvergent patch recovery with equilibrium and conjoint interpolant enhancements*," *International Journal for Numerical Methods in Engineering*, vol. 37, no. December 1992, pp. 517–536, 1994.

[21] P. Díez, J. José Ródenas, and O. C. Zienkiewicz, "Equilibrated patch recovery error estimates: simple and accurate upper bounds of the error," *International Journal for Numerical Methods in Engineering*, vol. 69, pp. 2075–2098, mar 2007.

[22] E. Nadal, P. Díez, J. Ródenas, M. Tur, and F. Fuenmayor, "A recovery-explicit error estimator in energy norm for linear elasticity," *Computer Methods in Applied Mechanics and Engineering*, vol. 287, pp. 172–190, apr 2015.

[23] S. Badia, F. Verdugo, and A. F. Martín, "The aggregated unfitted finite element method for elliptic problems," *Computer Methods in Applied Mechanics and Engineering*, vol. 336, pp. 533 – 553, 2018.

[24] F. J. Fuenmayor and J. L. Oliver, "Criteria to achieve nearly optimal meshes in the h-adaptive finite element mehod," *International Journal for Numerical Methods in Engineering*, vol. 39, no. January, pp. 4039–4061, 1996.